JOHANNES GUTENBERG
UNIVERSITÄT MAINZ

Ice Formation Pathways in Warm Conveyor Belts

Dissertation
zur Erlangung des Grades
"Doktor der Naturwissenschaft"

am Fachbereich Physik, Mathematik und Informatik
der Johannes Gutenberg-Universität in Mainz

Tim Lüttmer
geboren in Rüsselsheim

Mainz, Mai 2024

Die Annahme dieser Dissertation wurde empfohlen von

1. Berichterstatter: Prof. Dr. Peter Spichtinger
2. Berichterstatterin: Prof. Dr. Annette Miltenberger

Die **mündliche Prüfung** fand am **4. September 2024** statt.

Zusammenfassung

Reine Eiswolken in der Erdatmosphäre in Höhen zwischen 7 und 12 Kilometer werden allgemein als 'Cirrus' bezeichnet. Wir unterscheiden zwischen zwei thermodynamischen Entstehungswegen für natürlichen Cirrus, einen nahe und einen unter Sättiung im Bezug auf Wasser. Unterhalb des Dreiphasenpunkts (0 °C) gefrieren Wassertropfen nahe Sättigung für gewöhnlich durch Interaktionen mit einem geeigneten Aerosolpartikel (Eiskeim), welches den Gefrierprozess initiiert. Ohne Eiskeime können Wassertropfen bis zu ≈ -35 °C unterkühlt werden bis sie durch spontane Fluktuationen homogen gefrieren. Entsteht der Cirrus durch Gefrieren von Wassertropfen wird der Entstehungsweg als 'liquid origin' bezeichnet. Ist die Luft untersättigt im Bezug auf Wasser können Eiskristalle bei hoher Eisübersättigung auch direkt aus der Gasphase entstehen. Dies geschieht zum Beispiel durch die Deposition von Dampf direkt auf die Oberfläche eines Aerosolpartikeles, welche Eisnukleationseigenschaften besitzt, wie zum Beispiel Staub. Dieser Entstehungsweg wird als 'in-situ' bezeichnet.
Messungen deuten daraufhin, dass Cirrus charakteristische Eigenschaften je nach Entstehungsweg aufweist. So nehmen wir an, dass 'liquid origin' Cirrus für gewöhnlich höhere Eisanzahlkonztrationen und größere Eiskristalle als 'in-situ' Cirrus zeigt. Dies beeinflusst die Strahlungseigenschaften des Cirrus, also ob er im Schnitt wärmend oder kühlend wirkt. Es ist also wichtig, dass wir unser physikalischen Verständnis der Cirrus Entstehung verbessern um ihren Einfluss auf die Energiebilanz der Erde einschätzen zu können. Dies ist besonders wichtig für die großflächigen Cirruswolkenfelder, die im Outflow von Warm Conveyor Belts (WCB) entstehen. Warm Conveyor Belts sind häufig auftretende synoptische Wettererscheinungen, die im Warmsektor von außertropischen Zyklonen entstehen. Diese gewaltigen atmosphärischen Strömungen heben Wolkentropfen und feuchte Luft aus der Grenzschicht bis in die obere Troposphäre wodurch sie Cirruswolken erzeugen. Jedoch besteht kein Konsens darüber ob dabei der 'liquid origin' oder 'in-situ' Entstehungsweg präferiert wird.
Im erstem Teil dieser Doktorarbeit stellen wir ein neues Mikrophysikmodell, das 'Eismodenschema', vor, welches erlaubt in atmosphärischen Simulationen den Entstehungsprozess von Eiskristallen zu erfassen. Damit teilen wir die Eiskristalle in 'Eismoden' auf. Mit dieser Herangehensweise lässt sich die Herkunft von Cirren klassifizieren.
Zunächst wird dieses neue Mikrophysikmodell in idealisierten Simulationen von hochreichender Konvektion getestet und mit Referenzsimulationen verglichen. Als Nächstes wird das Eismodenschema in einer Fallstudie eingesetzt um die Eisentstehungswege in einem WCB zu untersuchen und mit einem etablierten Algorithmus zur Cirrusklassifizierung zu vergleichen. Die Cirruseigenschaften beider Klassifizierungsmethoden werden mit Klimatologien aus Beobachtungsdaten verglichen.
Als Nächstes wird der Einfluss verschiedener heterogener Eisnukleations Parametrisierun-

gen auf die Eisentstehungswege und Cirrusklassifizierung untersucht. Als Letztes wird diese Analyse der Eisentstehungswege für ein Ensemble von WCB Fallstudien wiederholt. Dort wird die Beziehung von dem präferierten Eisentstehungsweg zu den atmosphärischen Startbedingungen der WCB Luftströme untersucht.

Abstract

Pure ice clouds occurring on altitudes between 7 and 12 kilometer in Earth's atmosphere are commonly referred to as 'cirrus'. We distinguish between two thermodynamical pathways to form natural cirrus clouds, one close to and one below water saturation. Water droplets freeze below the triple point (0 °C) close to water saturation due to interaction with aerosol particles or unaided, once the droplets are sufficiently supercooled ($\approx -35\,°C$) . This formation process is referred to as 'liquid origin'. In air subsaturated with respect to water but supersaturated with respect to ice, ice crystals can also form directly from the water vapor phase. Usually by deposition of vapor directly onto aerosol particles, that show ice nucleating qualities, for example dust, or onto aqueous solution droplets. This formation process is referred to as 'in-situ'.
Observations suggest that cirrus of each formation pathway show characteristic properties. In general we assume that liquid origin cirrus contains higher ice mass concentrations and larger ice crystals than in-situ cirrus. This impacts the radiative effects of cirrus clouds, e.g., if there are net warming or cooling. It is important to increase our physical understanding of cirrus formation pathways to asses their influence on Earth's energy budget.
This is especially important for large cirrus cloud fields occurring in the outflow of Warm Conveyor Belts (WCB). Warm Conveyor Belts originate in the warm sector of extratropical cyclones and are a frequent occurrence. These massive, coherent air streams transport droplets and moist air from the planetary boundary layer into the upper troposphere where they form cirrus. However, whether the liquid origin or in-situ formation pathway is preferred remains unclear.
In the first part of the thesis a novel microphysics scheme is introduced, that allows to distinguish between ice crystals stemming from different formation pathways, referred to as 'ice modes', in atmospheric simulations. This new approach allows for classification of cirrus origin.
First the new ice modes scheme is tested for idealised simulations of deep convection and compared to reference simulations. Next the ice modes scheme is used to investigate the ice formation pathways in a WCB case study and compared to an established method of classifying cirrus origin. The cirrus properties of both classification schemes are compared to climatologies from observations.
Next the impact of different heterogeneous ice nucleation setups on the ice formation pathways and cirrus classification is evaluated. Lastly the analysis of ice formation pathways with the ice modes scheme is applied to an ensemble of WCB cases. There the relation of favoured ice formation pathways to environmental starting conditions of the WCB air streams is investigated.

Contents

List of publications

Several publications that were part of my PhD project are in the process of being submitted. A list of these publications with my contributions and their position in this dissertation is provided here.

- Lüttmer et al. [2024a]
  Lüttmer, T., Spichtinger, P.: **A two-moment cloud microphysics for the investigation of ice formation pathways**, Atmos. Chem. Phys.,

  I performed the majority of the model development and implementation. The simulations as well well as the postprocessing and data analysis were performed by me. I wrote the manuscript as lead author.
  Excerpts of this work appear in Chapters 1, 2 and 3.

- Lüttmer et al. [2024b]
  Lüttmer, T., Spichtinger, P., Miltenberger, A.: **Liquid vs in-situ formation in WCB outflow**, Atmos. Chem. Phys.,

  I designed the experiments and methods. The simulation and data analysis were performed by me. I wrote the manuscript as lead author.
  Excerpts of this work appear in Chapters 1 and 4.

- Lüttmer et al. [2024c]
  Lüttmer, T., Spichtinger, P., Miltenberger, A.: **Sensitivity of liquid vs in-situ formation to choice of parametrisation**, Atmos. Chem. Phys.,

  I designed the experiments and methods. The simulation and data analysis were performed by me. I wrote the manuscript as lead author.
  Excerpts of this work appear in Chapter 5.

1. Introduction

Water is an important constitute of the Earth-Atmosphere system. In its gaseous phase, water vapor is a potent greenhouse gases strongly affecting the radiative energy balance of the Earth. In its liquid (droplets) and solid phase (ice), water forms clouds. They cover a large part of the planet and are omnipresent in the lower atmosphere. In this work 'hydrometeor' is used as a collective term for all cloud particles (liquid and solid). Clouds affect the Earth-Atmosphere system in many ways. They influence the hydrological cycle and distribution of moisture in the atmosphere, e.g., by forming precipitation and atmospheric transport of hydrometeors in weather systems.
The phase changes of water by forming or dissipating liquid and ice clouds result in thermal energy being 'released' or 'removed' creating or modifying major atmospheric circulation and weather patterns (Lamb and Verlinde, 2011). In atmospheric dynamics this effect is often investigated by evaluating the effect of cloud related latent heat releases on Potential Vorticity (PV) distributions. This dynamic variable is conserved under certain assumptions (e.g. dry, adiabatic, inviscid flow) and is useful in physical understanding of atmospheric flows. The diabatic modification of PV from cloud processes is especially relevant for extratropical cyclones (Reed et al., 1992).
The chemical composition of the atmosphere is also influenced by clouds. Hydrometeors collect ('scavenge') trace gases and aerosol (solids and liquids suspended in the atmosphere) transporting or removing them entirely. They also serve as chemical reactors transforming trace components into other compounds or remove them by multi-phase processes (see, e.g., Solomon et al., 1997; Tost et al., 2006).
Atmospheric electrification and electric charge separation are an essential process for the formation of thunderstorms and occurrence of lightning. Lightning does not only affect the biosphere directly but is also important for atmospheric chemistry with tropospheric production of NOx (Price et al., 1997). Collisions of ice crystals, snow and graupel, are the leading mechanism for charge separation and formation of dipoles in convective mixed-phase clouds (Saunders, 1993).
Lastly clouds affect the Earth system's energy budget by interaction with solar and thermal radiation. Incoming solar radiation is partly scattered and reflected back to space (albedo effect) whereas the Earth's outgoing infrared radiation is partly absorbed and re-emitted at a different temperature (greenhouse effect). Hence clouds can have a warming and a cooling effect on the earths surface. The IPCC report 2021 states that the overall cloud feedback on climate is positive, hence enhancing global warming. However, there are still many cloud regimes with large uncertainties regarding their impact on the global energy budget (Forster et al., 2021). In particular, pure ice clouds could have net warming or cooling effects.

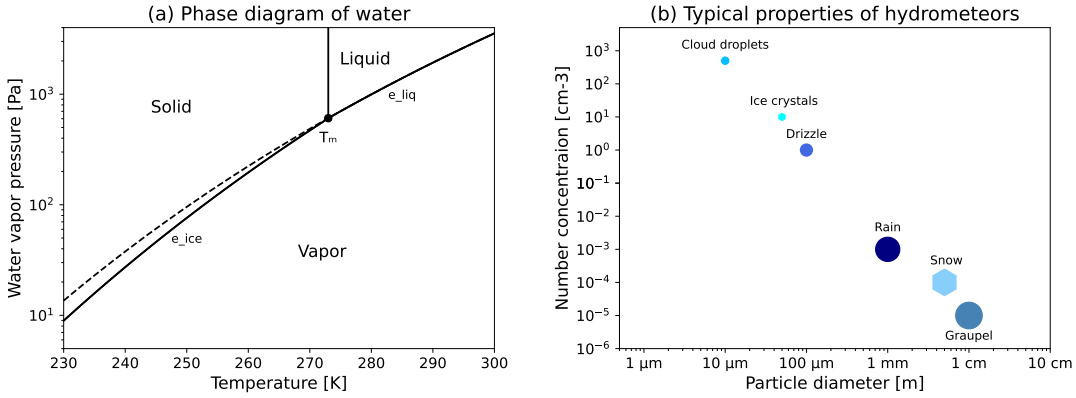

Figure 1.1.: (a) Phase diagram of water with saturation pressure over liquid water e_{liq} and ice e_{ice}, respectively. T_m is the triple point. The dashed line represents e_{liq} for the metastable phase of supercooled liquid water. (b) Overview of typical diameters and number concentrations of hydrometeor types.

1.1. Clouds and hydrometeors

Water vapor is a constituent gas of air. With the good approximation of air as an ideal gas, we can describe vapor with the ideal gas law

$$e = q_v R_v T = \frac{N}{V} k_b T \tag{1.1}$$

with the vapor pressure e (Pa), mass density of vapor q_v ($\mathrm{kg\,m^{-3}}$), the (air) temperature T (K) and the specific gas constant of water R_v ($\mathrm{J\,kg^{-1}\,K^{-1}}$). The second term expresses e as a function of number of water molecules N per volume of air V ($\mathrm{m^{-3}}$), temperature T (K) and the Boltzmann constant k_B ($\mathrm{J\,K^{-1}}$)

A body of liquid water or ice (hydrometeor) suspended in air interacts with the surrounding water vapor. Water molecules (randomly) strike the surface of the hydrometeor and have a chance of integrating themselves into the liquid (or ice phase). Conversely water molecules can leave the hydrometeor into the surrounding vapor phase. The ratio of the molecular fluxes of water entering and leaving, determines if the liquid (/ice phase) is growing, evaporating (/sublimating) or if it is in a state equilibrium. Physical change of waters phase results in warming (by condensation, freezing and deposition) or cooling (by evaporation, melting and sublimation) of air. This is called the latent heat of phase change caused by conversion of molecular potential energy into molecular kinetic energy (and vice versa) (Lamb and Verlinde, 2011).

We can relate this molecular concept of equilibrium to the thermodynamic quantity of vapor pressure e as the molecular concentration $\frac{N}{V}$ is proportional to e for ideal gases (see Equation (1.1)) When e exceeds the saturation pressure e_{sat} over an (even) surface of water (or ice), we describe air as supersaturated as more water molecules integrate themselves into the liquid (or ice) phase then leaving it. If e is lower than e_{sat}, more

water molecules leave the liquid (or ice) phase, thus the air is subsaturated. We define the supersaturation S for ice and liquid phase, respectively, as

$$S_i = \frac{e}{e_{sat,i}(T)} \quad \text{and} \quad S_l = \frac{e}{e_{sat,l}(T)} \tag{1.2}$$

Saturation pressure is a function of temperature and differs (slightly) whether the surface is water or ice (Murphy and Koop, 2005). For $S_{i/l} = 1$ the vapor and ice/liquid phase are in equilibrium. For $S_{i/l} > 1$ or $S_{i/l} < 1$ the air is supersaturated or subsaturated, respectively.

Panel (a) in Figure 1.1 shows the phase diagram of water for atmospheric conditions relevant in this work. Saturation pressure with respect $e_{sat,l}$ to water separate the vapor liquid phase. Saturation pressure with respect to ice $e_{sat,i}$ separates the vapor and solid phase. In the atmosphere, along e_{sat} are vapor and the respective phase in equilibrium. On the triple point of water $T_m = 273.16\,\mathrm{K}$ all three phases can coexist in equilibrium. T_m also separates the liquid and ice phase of water as the melting temperature line.

Liquid water is metastable when cooled below T_m. Although ice is the more stable phase below this temperature, water requires a thermodynamic 'push' to enter the ice phase (Lamb and Verlinde, 2011). This can occur due to interaction with an aerosol that shows ice nucleating (surface) properties. Pure supercooled liquid droplets can also freeze spontaneously which is a stochastic process. However, below the homogeneous freezing threshold $T_c = 235\,\mathrm{K}$ all liquid droplets will have frozen homogeneously.

The dashed line in Panel (a) of Figure 1.1 represents the saturation pressure $e_{sat,l}$ for supercooled liquid water. We notice that $e_{sat,l}$ is higher than $e_{sat,i}$. This has an important ramification for the evolution of clouds containing both ice and liquid water. At vapor pressures between $e_{sat,l}$ and $e_{sat,i}$ the air is subsaturated with respect to water $S_l < 1$ and supersaturated with respect to ice $S_i > 1$. Provided q_v is sufficiently high, the ice phases continues to grow, while the liquid phase diminishes. This leads to the glaciation of clouds and is part of the Bergeron–Findeisen process.

We can discriminate between two thermodynamic regimes for clouds containing the ice phase. In the temperature regime $235\,\mathrm{K} \leq T \leq 273.16\,\mathrm{K}$ super-cooled liquid droplets as well as ice particles can co-exist; clouds containing both, liquid and ice phase, are called mixed-phase clouds. At lower temperatures, only the solid phase exists, i.e. we find pure ice clouds. High-altitude (7 - 12 km) pure ice clouds below temperatures of 235 K are referred to as cirrus clouds.

There exist no universal definition of what constitutes a cloud on a macrophysical level. In this work we define that a cloud is present if the mass mixing ratio of liquid or frozen cloud particles in a standard volume of air exceeds $0.1\,\mathrm{mg\,kg^{-1}}$. Based on observations of clouds in the atmosphere and theoretical considerations, we can distinguish several cloud particle (hydrometeor) types. Figure 1.1 (b) shows an overview for a common classification of hydrometeor types. The markers indicate typical diameters and number concentrations of the respective hydrometeor found in clouds.

Liquid droplets are usually classified as either cloud droplets or raindrops. Cloud droplets are spherical and small ($\sim 10\,\mu\mathrm{m}$) but appear in high number concentrations ($\sim 100-1000\,\mathrm{cm^{-3}}$) (Lamb and Verlinde, 2011). They constitute warm and mixed-phase

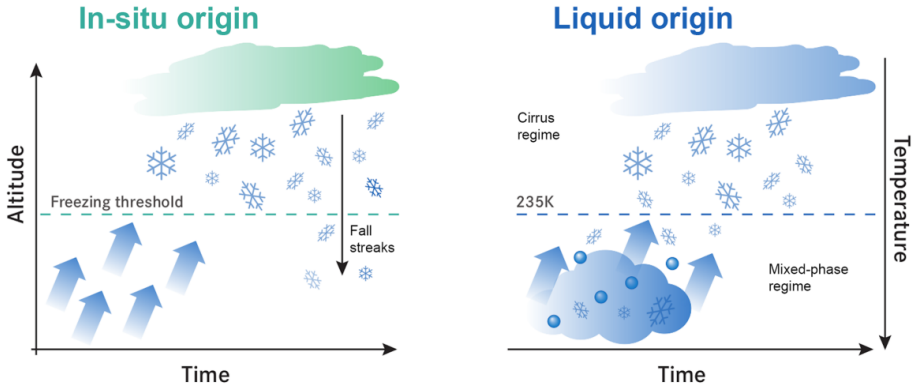

Figure 1.2.: Conceptual overview of the two cirrus formation pathways. In-situ origin: direct ice formation from vapor below water saturation. Liquid origin: freezing of pre-existing cloud droplets close to water saturation. This figure is adapted from Luebke et al. (2016).

clouds. Raindrops on the other hand are several orders of magnitude larger ($\sim 1000\,\mu m$) but show comparatively low number concentrations ($\sim 0.001\,cm^{-3}$) (Lamb and Verlinde, 2011). Raindrops show a size depended shape and are the most common form of precipitation. Drizzle droplets sit in the range between cloud droplets and raindrops with a size of $\sim 100\,\mu m$ (Lamb and Verlinde, 2011).
The other form of precipitation consists of solid ice. The term cloud ice describes (pure) ice crystals that have grown by diffusion of water vapor onto the ice surface in ice supersaturated environments (Pruppacher et al., 2010). The shape of the ice crystal ranges from spheres, plates, columnar crystals to more complex and branching dendritic forms. Their growth habit depends on temperature and supersaturation (Magono and Lee, 1966). However, their formation pathway is also important, e.g., if the ice crystal originated from a frozen droplet or from nucleation. Snow (or 'aggregates') are formed by collisions and aggregation of ice crystals. The sticking efficiency of the ice crystals is an important parameter and strongly depended on temperature with a peak around 258 K (Phillips et al., 2015). Analogous to liquid droplets, cloud ice shows small diameters ($\sim 10 - 100\,\mu m$) and high number concentrations ($\sim 0.1 - 100\,cm^{-3}$) while snow is larger ($\sim 1\,mm - 1\,cm$) with low number concentrations ($0.0001\,cm^{-3}$) (Lamb and Verlinde, 2011).
In mixed-phase clouds ice particles also grow by collecting super-cooled droplets ('riming'). This process strongly affects the mass, diameter and shape of the hydrometeor. With continued riming the ice particle eventually grows to graupel ($\sim 1\,cm$) or even hail ($> 1\,cm$) (Lamb and Verlinde, 2011). However, for the latter the ice particle needs to spend on average 15 min in a storm cell (Allen et al., 2020).

1.2. Ice formation pathways

They are three requirements for forming clouds in the atmosphere: a adequate supply of water vapor, sufficiently low temperatures and aerosol particle to aid in the condensation or deposition of water vapor (Lamb and Verlinde, 2011). In particular for ice crystals it is quite difficult to determine their formation pathway. The different formation mechanisms were summarized and classified in the following ways [see, e.g., Krämer et al. (2016) and Wernli et al. (2016)]:

- Formation pathways related to freezing of pre-existing cloud droplets (i.e. in the mixed-phase temperature regime and close to water saturation) are termed liquid origin formation.
- Formation pathways related to direct formation of ice crystals from vapor at (liquid or solid) aerosols at low temperatures and below water saturation are termed in situ formation.

A conceptual visualization of the two formation pathways is provided in Figure 1.2. There are some indications, e.g., from airborne in-situ observations, that we might be able to use ice particle properties for a classification of the formation pathways. Liquid origin cirrus are 'thicker' than in-situ cirrus. They are associated with high Ice Water Content (IWC) and larger ice crystals (see, e.g., Luebke et al., 2016; Wolf et al., 2018). It also seems to be probable that liquid origin ice clouds consist of much more ice particles than in situ formed ice clouds. This can be explained by the formation process. Liquid origin ice particles stem from pre-existing cloud droplets; the number concentration of water droplets in liquid clouds is usually in the order of some hundreds of particles per cubic centimeter and thus much larger than the amount of available ice nuclei at low temperatures.
This also relates to their radiative properties as summarized by Krämer et al. (2020): The optical depth of liquid origin cirrus is large and they exhibit a strong net cooling effect. For in-situ cirrus the average optical depth likely depends on the updraft speed that drove their formation. Slow updrafts ($< 10\,\mathrm{cm\,s^{-1}}$) cirrus are characterized by few large crystals from deposition of vapor onto solid aerosols. These clouds show a small optical depth with a small net warming effect. In-situ cirrus from fast updraft is associated with homogeneous freezing of small liquid aerosols which caused the formation of many small ice crystals. They can show a small net warming or cooling effect depending on their altitude. The radiative characteristics of in-situ cirrus are still not fully understood.
Imaging techniques also provide some hints as to the shape of the ice crystal depending on the formation pathway (Wolf et al., 2018). Complex shapes and large particle sizes are most probable for liquid origin ice crystals, whereas in-situ formed ice crystals remain small and their shapes remain simple (quasi-spherical or columnar shapes). This can be explained by the available water vapor, which can be used for diffusional growth. At the mixed phase regime, more water vapor is available leading to larger and more complex shapes, whereas at low temperatures the amount of water vapor is very limited leading to small sized and simple shaped ice crystals.
There have been several studies classifying cirrus clouds and investigating their proper-

ties. Luebke et al. (2016) used airborne, in-situ measurements of IWC, cloud ice numbers concentration (n_i) and ice crystal size (D_i) to demonstrate the differences between liquid origin and in-situ formed cirrus. Wolf et al. (2018) used balloon-borne, in-situ observations to investigate ice crystal size distributions in Arctic cirrus clouds. Both studies utilized the CLaMS-Ice microphysics model (Spichtinger and Gierens, 2009) to simulate the cirrus cloud development. The model was run along Lagrangian backward trajectories originating from the geographic information of the in-situ measurement. ECMWF operational analysis data was used to drive the trajectory model. The observed cloud was classified as in-situ if cloud ice did (first) appear below the homogeneous freezing threshold (or cirrus temperature level) ($T_c = 235\,\mathrm{K}$). Below T_c water and ice phase cannot coexist, thus the ice formation has to be in-situ. The cloud was classified as liquid origin if the temperature at the first occurrence of cloud ice was above T_c and the measurement was taken at pressure levels less than 500 hPa.
Another method for cirrus origin classification is to utilize retrievals from remote sensing to estimate cirrus properties and then search for signatures that match the characteristics of the cloud types. Urbanek et al. (2017) used backscatter ratio lidar from atmospheric cross sections to identify in-cloud and cloud-free regions. With ice supersaturation (S_i) from synergistic lidar measurements and temperature fields derived from ECMWF model data, they determined the cloud type by application of S_i threshold values. Huo et al. (2020) utilized 4 years of ground based radar measurements in Beijing to obtain cloud properties. They classified the cirrus origin by cloud temperature and reflectivity to match proposed cloud properties of previous studies (e.g. Krämer et al., 2016; Luebke et al., 2016). Krämer et al. (2020) used 10 years of remote sensing observations from satellites (CALIPSO and CloudSat) to estimate cloud properties. They then derived a global climatology of ice concentrations n_i based on the agreement between remote sensing and in-situ measurements. The data of n_i coupled with cloud temperatures gave indications of the cirrus origin.
Gasparini et al. (2018) compared cloud patterns from global simulations of the ECHAM-HAM general circulation model to CALIPSO satellite data. As in Luebke et al. (2016) they used a temperature based criterion to distinguish between liquid origin and in-situ cirrus. Ice clouds which cloud bases extended to 238 K were classified as liquid origin and all other cirrus clouds as in-situ. Wernli et al. (2016) developed an algorithm that investigated backward trajectories originating from cirrus clouds until the air parcel contained no ice. If the segment contained any liquid water content (LWC), it was classified as liquid origin or in-situ, otherwise. They applied this classification to 12 years of ERA-interim data for the North Atlantic storm track. They found a dynamic linkage between the occurrence frequency of cloud types to altitude. Liquid origin frequency decreased with altitude. More than 80 % of liquid origin ice clouds were topped with an in-situ cloud.
These approaches have their limitations. For classification with observations, measured cloud properties are compared with characteristic values of the cloud type. However, remote sensing methods do not report on the history of the cloud and cloud processes like ice crystal growth, aggregation and sedimentation. These can blurr the differences after the formation process (Krämer et al., 2020). Further can a temperature based clas-

sification misidentify the cloud type when the horizontal dimension of the cloud is not considered (Gasparini and Lohmann, 2016). Classification with in-situ measurements requires the analysis of air mass origin with lagrangian backward trajectories. This introduces uncertainty if the dynamical data driving the trajectory model does not adequately resolve convection and meso-scale temperature fluctuations. Simulations with high resolutions can help mitigate these issues (Wernli et al., 2016). Further running a parcel microphysics model like CLaMS-Ice along the trajectory path to investigate the cloud history might fail to take sedimentation of cloud ice from other regions into account correctly. Trajectory-based classification can be 'confused' if cloud ice from different formation pathways mixes through sedimentation and cloud turbulence thus altering the cloud properties (Wernli et al., 2016).
So although there are some indications that we might be able to use the particle's properties themselves for a classification of the formation pathway, such evaluations are mostly based on single cases of measurements together with trajectory calculations and have an inherit uncertainty, which cannot be quantified. Therefore, a complementary viewpoint from the modeling perspective is necessary in order to give a more rigorous insight into the different formation mechanism in cloud systems, especially in vertically extending systems as convective clouds or Warm Conveyor Belts.

1.3. Secondary ice

We already introduced two primary pathways in which ice crystals can form in the atmosphere. Either by freezing of liquid droplets or directly by deposition of water vapor onto an ice nucleating particle (INP). However, observations suggest that sometimes higher ice crystals concentrations are measured than the concentration of available INP, responsible for most of the primary ice formation, would indicate. The difference could be explained by secondary ice particles (SIP). Several mechanisms of ice multiplication and ice production apart from primary nucleation have been suggested (Korolev et al., 2020):

- Rime splintering (RS)
- Frozen droplet fragmentation (DS)
- Ice–ice collisional breakup (BR)
- Ice fragmentation during thermal shock
- Ice fragmentation during sublimation

The latter two mechanisms have not yet been thoroughly studied in pertinent literature and will only be mentioned here (Korolev et al., 2020).
Only the parameterisation of one specific secondary ice process has been commonly included in many cloud physic models: rime splintering (RS), based on the laboratory studies of Hallett and Mossop (1974). However, model applications of collisional breakup and droplet fragmentation have been of great interest in recent years.
They have been several model studies simulating secondary ice production using existing or introducing new parametrisations. In general most secondary ice studies compare observations from field campaigns, where both INP and ice concentrations were measured

or estimated, with simulations including secondary ice mechanisms to explain the discrepancy between estimated primary nucleation and observed ice concentrations. Thus either estimating the amount of SIPs indirectly or evaluate the enhancement of total ice content through the contribution of SIPs.
Sullivan et al. (2017) studied the sensitivity of secondary ice enhancement from rime splintering and graupel breakup under various dynamical conditions and graupel nonsphericity with a mixed-phase parcel model. Sullivan et al. (2018b) added frozen droplet fragmentation (DS) as an additional secondary ice process and investigated the sensitivity of the parameterisations on thermodynamic and parameter perturbations. Sullivan et al. (2018a) implemented collisional breakup (BR) and droplet fragmentation into the atmospheric model COSMO and performed simulations of a cold frontal rainband.
Phillips et al. (2017a) developed a ice-ice collisional breakup parametrisation and implemented it into a hybrid bin–bulk microphysics scheme to perform simulations of a convective storm. A empirical droplet fragmentation was developed by Phillips et al. (2018) and employed in a parcel model validating it with observations from a case of tropical maritime convection.
Dedekind et al. (2021) simulated a passing of a cold front on Gotschnagrat peak with parameterisations for RS, BR and DS and compared them with observations from the RACLETS field campaign. They focused on the impact of SIPs on precipitation and its sensitivity to different configurations of the SIP parametrisations. Sotiropoulou et al. (2020) evaluated the impact of secondary ice production on Arctic stratocumulus finding that both RS and BR were needed to explain observed ice concentrations. Sotiropoulou et al. (2020) also expanded the collisional breakup scheme of Sullivan et al. (2018a) with particle size-depended scaling coefficients.
Miltenberger et al. (2020) investigated rime splintering in idealised simulations of a deep convective cloud system using Lagrangian analysis with online trajectories emphasizing the significance of transport processes for secondary ice.
In this work we will investigate the relevance of several secondary ice mechanisms, in particular, rime splintering, collisional breakup and droplet fragmentation as additional ice formation pathways.

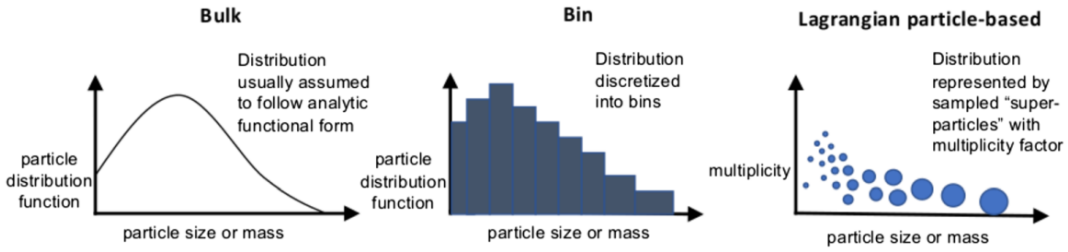

Figure 1.3.: Conceptual overview of three approaches to represent microphysics: bulk (left), spectral (middle) and super particle (right). This figure is adapted from Morrison et al. (2020).

1.4. Microphysic models

Modelling clouds is challenging. Hydrometeors are subject to a large number of complex processes: particle formation, collision and collection mechanisms, growth by water vapor deposition, freezing, melting and more. Additionally the interaction of hydrometeors with other components of the earth-atmosphere system such as change in thermal energy due to phase change, transport within atmospheric circulation, radiation and aerosols needs to be considered. 'Microphysics' refers to these physical and chemical processes (Morrison et al., 2020). Microphysic models simulate these processes usually within the framework of an atmospheric model or prescribed atmospheric flows.
The most complete microphysic model would be to directly simulate all hydrometeors within a volume of air and their interactions directly (Morrison et al., 2020). However, individual hydrometeors exist on a scale from submicrometers to centimeters (see overview in Figure 1.1), while atmospheric flows are resolved on a scale from meters to 10000 kilometers (Morrison et al., 2020). Simulation of large scale (synoptic) weather systems like cyclones and associated Warm Conveyor Belts presented in this work use effective grid scales in the range of $\Delta x =\sim 1.5 - 13\,\mathrm{km}$. Even high spatial resolution simulations of turbulent flow (large eddy simulations) use effective grid scales of $\Delta x =\sim 10\,\mathrm{m}$, which are several orders of magnitude larger than hydrometeors. Moreover, some cloud processes like the growth of hydrometeors by deposition of vapor introduced in Section 1.1 would need to be effectually resolved on the molecular scale. Thus simulating the large number concentration of hydrometeors that make up clouds ($\sim 1000\,\mathrm{cm}^{-3}$) directly is unfeasible.
Unfortunately even our physical understanding of many relevant and dominant cloud processes is still quite limited, especially for clouds containing ice particles. Fundamentally, many cloud process rates can not (yet) be quantified or constrained neither with observations nor laboratory studies. Not even the degree uncertainty of most microphysic schemes can be quantified systematically (Morrison et al., 2020). Nevertheless, numerous advances in representing clouds in (numerical) atmospheric simulations have been made in the last decades. We will present the common approaches of modelling cloud microphysics here.

Instead of simulating each hydrometeor, microphysical process rate equations affecting an ensemble of hydrometeors are formulated. A description of this ensembles must include at least the integrated mass of hydrometeors within a grid volume of the atmospheric model. Most microphysics model also predict the number of hydrometeors within a grid volume and further provide a size distribution, which gives the number density of hydrometeors of a given size. Size is usually expressed as mass or diameter of the hydrometeor. There are three approaches of representing these hydrometeor ensembles. Bulk models assume a analytical functional form of the size distribution. Spectral (or bin) models use a discretization of the size distribution into bins. Lagrangian based particle models use a large number of 'super particles' within a grid volume, where each super particle represents a number (multiplicity) of hydrometeor with the same size. Figure 1.3 provides a conceptual overview of the three approaches adapted from Morrison et al. (2020). In the following we will review these three approaches individually.
Bulk models are a commonly used model approach to parameterize cloud physics in large scale atmospheric models with spatial resolutions of several kilometers but have also have been utilized in high resolution large eddy simulations and, on the other end of the spatial and temporal scale, climate models. Bulk models were first introduced by Kessler (1969).
In Kessler's original scheme cloud particles are grouped into a set of classes e.g., cloud droplets and rain. Cloud droplets being small, spherical liquid droplets (see Section 1.1) with low fallspeeds and thus mostly being kept aloft by vertical updrafts. Whereby rain is larger (and often no longer spherical) with significant fallspeeds resulting in perception. Beginning with the work of Lin et al. (1983) classes for ice crystals, snow, graupel and hail were added in more advanced bulk schemes.
For each particle class a measure of particle size, either mass or diameter and a type of distribution have to be chosen. Generally particle size distributions are unimodal and have an analytical functional form. They rise sharply from low sizes towards a single maximum and then gently decline towards larger sizes (tail) (Pruppacher and Klett, 1998). Commonly, empirically motivated choices are exponential, log-normal and generalized gamma distributions. Integrating over the entire size distribution within a grid volume one obtains a moment of the size distribution. Microphysical process rates equations are formulated to predict the change of distribution moments. From the prognostic moments the shape and scale parameters of the distributions can be (re)calculated. We will provide an in-depth review of this method in Chapter 2.
The number of predicted moments determines the order of the scheme: one-moment schemes only consider mass density while two-moment schemes also predict number density and three-moment schemes additionally calculate a moment that is related to radar reflectivity (Khain et al., 2015). Higher order bulk schemes provide more realistic results and better resolve microphysical processes like size sorting through sedimentation. However, higher order schemes also have a higher computational cost.
Bulk schemes have several drawbacks: preset distribution types, while empirically motivated, fail to represent the complex nature of multi modal cloud particle ensembles. Especially liquid droplets within clouds are usually bi-modal with small 'cloud' droplets and larger 'rain' drops. In Kessler (1969) and subsequent schemes these are separate

classes. This rigid classification gives rise to unphysical conversion processes like autoconversion, defined as the collision of cloud droplets resulting in a raindrop, and accretion, defined as the collection of cloud droplets by raindrops.
Another problem is the artificial separation of cloud particles into a set of classes while in nature there is a continuous microphysical range between particles of different types like ice, snow and graupel. For example a snow particle might 'slowly' rime by collision with supercooled droplets, gradually changing its shape and mass density. Only until its original shape is no longer apparent would it be classified as graupel.
Some bulk schemes introduce additional hydrometeor classes like Sant et al. (2015), who included a drizzle droplet class to better represent the size spectra of liquid droplets.
There are bulk scheme approaches that moved away from preset classification of ice particles like the P3 scheme (Morrison and Milbrandt, 2015), which instead features ice classes that can freely evolve into any ice particle type. This scheme prognoses four bulk properties including rime fraction and volume, than partitions the ice particle size distribution dynamically into segments, where each segment represents a certain particle type, e.g., pristine ice and graupel. An extension of the P3 scheme allows for multiple free ice categories with different properties to coexist (Milbrandt and Morrison, 2016).
The second approach to represent ensemble of cloud particles are spectral (bin) methods. Most bin models still utilize the concept of particle classes similar to a bulk schemes but do not require a prescribed distribution type and instead aim to resolve the entire size range by discretization of the size distribution. Each bin describes the number of particles within the size range of the bin, usually as a uniform distribution, with at least one prognostic variable, the number density. This approach is similar to the bulk approach in the sense that microphysical rate equations for the number density of each bin need to be formulated.
This approach allows for a more realistic representation of multi-modal size distributions as they are observed in nature. However, the computational cost is much higher compared to bulk schemes because differential equations of usually one or two prognostic variables have to be solved for each of the 30 to 50 bins of each particle class in each model grid point. The complexity is further increased since the prognostic variables are not only depended on the environment, but also on the prognostic variables of other bins. This requires between 5 to 20 times more computational time than traditional bulk schemes (Khain et al., 2015).
Another approach are particle models, sometimes labeled as 'super droplet methods'. They utilize the concept of 'super particles' where the properties of a single simulated particle represent the state of an ensemble of usually between 10^1 to 10^4 members. These particles move freely through the model domain in a Lagrangian sense and in general do not belong to a certain preset class but instead are able to evolve dynamically depending on environmental conditions and their interaction with other particles. Similar to spectral (bin) models, it is required to solve differential equations for each prognostic variable of each super particle within a grid volume.
Most particle models have been developed for specialized applications: warm cloud physics (Shima et al. (2009)), natural and contrail cirrus (Sölch and Kärcher (2010) and Unterstrasser and Sölch (2010)), aqueous-phase chemistry (Jaruga and Pawlowska

(2018)) or aggregation and riming of ice particles (Brdar and Seifert (2018)). While particle based models are valuable for process understanding as the history of each particle can be tracked they demand a high computational cost and the use of high-resolution atmospheric models.

1.5. Cloud dynamics

We discussed the microscale of primary and secondary ice formation in the atmosphere and its dependence on temperature and, especially, supersaturation. To form and maintain clouds on a macrophysical scale, atmospheric flows and interactions with other components of the Earth system need to create regions of supersaturation. We will be reviewing the dynamics of macrophysical cloud formation from a Lagrangian viewpoint, that is following the movement of cloud forming air masses in the atmosphere.
(Super)saturation S with to respect to water or ice is the ratio of the partial pressure to the saturation pressure of water vapor (see Equation (1.2)). The saturation pressure of water vapor is depended on temperature T and the partial pressure of water vapor is depended on quantity of water vapor q_v in the air and T. The change of S can be expressed as

$$\frac{dS}{dt} = \left(\frac{\partial S}{\partial T}\frac{dT}{dt} + \frac{\partial S}{\partial p}\frac{dp}{dt}\right)_{therm} + \left(\frac{\partial S}{\partial q_v}\frac{dq_v}{dt}\right)_{phase,source} \tag{1.3}$$

where the first term describes the change of S due to thermodynamics affecting air temperature and air pressure. Cooling of air is the most important way of increasing supersaturation in the lower atmosphere. The second term in Equation (1.3) describes the change of S due to phase change of water and sources of water vapor in the Earth system. Section 2.3.3 contains an example of an adiabatically rising air parcel, thus without exchanging heat and mass with its environment, describing ice cloud formation by homogeneous freezing of solution droplets. In summary, supersaturation in an air parcel is achieved by either cooling or by a source of water vapor.
Both volcanic eruptions and biomass burning (Parmar et al., 2008) release water vapor into the atmosphere. However, both sources are unlikely to contribute consistently to the formation of ice clouds on a synoptic scale. Combustion in aircraft jet engines also introduces water vapor and soot (which can serve as an INP) into the upper atmosphere, which leads to a frequent occurrence of contrail cirrus. Although the life time of contrails strongly depends on the synoptic situation (Kärcher, 2018).
For the formation of natural occurring ice clouds, the primary process to achieve supersaturations, is cooling of (moist) air. Possible mechanisms are adiabatic cooling by expansion during uplift of air, radiation or mixing (Lamb and Verlinde, 2011). The latter process is e.g., relevant for contrail formation. Natural ice formation initiated by radiative cooling has been studied, but is likely only occurring under specific circumstances, e.g., very calm environments like in the antarctic polar vortex (Fusina and Spichtinger, 2010). So the most common mechanism to create thermodynamic conditions for ice formation in the atmosphere is uplifting of (moist) air. They are several ways of lifting air

masses that lead to cloud formation from the micro- ($< 1\,\mathrm{km}$), meso- ($< 1000\,\mathrm{km}$) to the synoptic scale ($> 1000\,\mathrm{km}$). We provide several examples although not an exhaustive list here.

Air masses get lifted from the lower troposphere by streaming over mountains or other elevated terrain features. The warm, mixed-phase or ice clouds they form are referred to as orographic clouds. The type, horizontal and vertical extension, position of the cloud base, lifetime, and precipitation (if any) of the cloud on the windward side vary strongly by the specifics of the terrain features, e.g., altitude and slope (Houze and Robert, 2012). They are also influenced by the specifics of the air mass, e.g., direction of flow, temperature, moisture and aerosol concentrations (see, e.g., Siler and Roe, 2014; Sandvik et al., 2018; Thomas et al., 2023).

We also observe clouds on the leeward side. A stable, stratified flow streaming over mountains can induce internal gravity waves. As the air mass moves upward to the wave crest, it cools adiabatically and a cloud can form. As the wave moves downward towards its equilibrium point (and beyond by overshooting) the air warms and the cloud can dissipate. Hence air masses following this gravity wave can create characteristic patterns of cloud and clear air regions.

These 'lee waves' can also propagate upward forming clouds on many vertical levels, sometimes simultaneously, and even exceeding the altitude of the mountain (range) by several times its height. This is strongly depended on the vertical structure of the background atmosphere. Lee waves can also travel long distances down stream depending on synoptic conditions and form long bands of parallel cloud bands. Gravity waves can also be triggered by several other mechanisms that lift (stable) air masses, e.g., by flowing over storm cells, jets and frontal passages (see, e.g., Ming et al., 2010; Plougonven and Zhang, 2014). In general, cirrus clouds formation in air masses moved by gravity waves, occurs due to the creation of ice supersaturated regions in the upper troposphere (Spichtinger et al., 2005). Thus the cirrus are of in-situ origin.

Atmospheric convection occurs if an air mass shows anomalous higher temperatures compared to its environment, resulting in lower density than the surrounding air and thus buoyancy. This temperature anomaly can be caused by a source of heat or surface inhomogeneities, e.g., if surfaces show different properties in absorbing solar radiation. Convection can also be initiated by topography or (horizontal) pressure gradients. The strength and duration of the upward lift depends on the lapse rate, the change of temperature with altitude, of the air mass compared to the lapse rate of the surrounding atmosphere. The latter is depended on the atmospheric stability, which can enhance or limit convection. As the air mass ascends, it expands and cools adiabatically. When the temperature reaches the dew point (depending on the moisture) the air mass is saturated and a cloud forms.

In general, we distinguish between two types of convection (Yano and Plant, 2012). Shallow convection describes convective clouds, which cloud top is near the planetary boundary layer. Shallow convection clouds also produces no or only weak precipitation. Deep convective produces cloud that reach the upper troposphere and might even penetrate the tropopause. They are associated with strong precipitation. Multiple convective cells can form a complex systems of convection, which can span multiple hundred

kilometers. These mesoscale convective systems are responsible for much of Earth's precipitation (Houze, 2018). The life cycle, vertical and horizontal extension of convective cells and interaction with the atmospheric environment is complicated (Lamb and Verlinde, 2011). Deep convection clouds are characterized by mixed-phase cloud processes, which can lead to graupel and even hail formation. Deep convection are also associated with the formation of pure ice clouds at or near cloud top. These ice clouds take the form of anvils, overshoots and thin cirrus outflows. As we will investigate in Chapter 3, ice formation in deep convection is in general of liquid origin due to high number concentrations and upward transport of cloud droplets.
Warm Conveyor Belts (WCB) are large air streams that extend from the planetary boundary layer to the upper troposphere. They originate from the warm sectors of extratropical cyclones and are a frequent occurrence on the Northern Hemisphere for all seasons, mainly beginning there ascent over the ocean (Madonna et al., 2014). The large scale upward transport and subsequent cooling of moist air from the boundary leads to many microphysical processes occurring along the ascent and sees the formation of warm, mixed-phase and ice clouds. Convective clouds can also be embedded in the WCB. Diabatic modification of PV due to latent heat released from cloud processes, can influence the flow downstream of the WCB significantly (Grams et al., 2011; Rodwell et al., 2018; Grams et al., 2018). WCBs are responsible for a large part of precipitation of cyclones and of the extratropics in general (Pfahl et al., 2014). The vast cloud fields that are formed due to WCBs are very relevant for cloud radiative forcing in storm tracks (Joos, 2019). Hence its important to improve our understanding of cloud formation in WCBs to investigate their radiative impact on the Earth-Atmosphere system.
Usually, lagrangian-based methods are employed to investigate the dynamical structure of WCBs and trace meteorological variables along the ascent (see, e.g., Wernli and Davies, 1997; Wernli and Schwierz, 2006; Madonna et al., 2014). As WCB transport both, moist air and cloud droplets, into the upper troposphere, both cirrus formation pathways, 'liquid origin' and 'in-situ', are possible. It is inherently difficult to determine which ice formation pathway is favoured from observations alone. Wernli et al. (2016) investigated origin of ice clouds in 12 years of ERA-Interim data. They suggest that ice clouds attributed to WCB outflows stem from complex and potential inhomogeneous formation pathways. Thus ice clouds from different formation pathways might be layered above each other and mix due to sedimentation and turbulence.
The investigation of ice formation in WCBs using the atmospheric model ICON and a complex microphysics scheme is a major focus of this thesis.

1.6. Scope

We developed a novel microphysics bulk scheme to investigate ice formation pathways. Instead of a single ice class, common for bulk schemes, we introduce five ice classes ('ice modes') - each stemming from a unique ice formation mechanism. Each 'ice mode' features two moment, mass content and number concentrations, as prognostic variables in the model. This new bulk scheme allows us to address the in-situ vs liquid origin

research question in a novel way.
In Chapter 2 we will describe the ice modes microphysics scheme. This chapter includes an introduction to the theory of bulk schemes, ice formation pathways and the microphysical processes governing the bulk properties of cloud ice, e.g., sedimentation, growth by diffusion of water vapor and collision with other hydrometeors.
The first results of the ice modes schemes, employing it in idealized simulations using a warm bubble setup, will be presented in Chapter 3. These tests will demonstrate the capabilities of the scheme to determine the dominant ice formation pathways in a deep convection cloud and show its value for testing and comparing heterogeneous ice nucleation parametrisations. This test case also serves as an opportunity to validate the scheme by comparison to the established and widely used two-moment scheme of Seifert and Beheng (2006).
The first application of the ice modes scheme for a Warm Conveyor Belt (WCB) case study is featured in Chapter 4. There we will investigate the liquid origin vs in-situ formation in cirrus outflow of a WCB. We will also compare the cirrus cloud classification of our new scheme to the work of Wernli et al. (2016) and evaluate if bulk ice properties of determined cirrus types match climatologies derived from observations.
In Chapter 5 we will investigate the sensitivity of in-situ vs liquid origin formation to the choice of ice formation schemes. Using the same model setup as in the previous chapter we compare various heterogeneous ice parameterisations introduced in Chapter 2 and their impact on composition of ice modes in cirrus and mixed-phase clouds. We also show results from ensemble simulations to investigate the impact of different assumptions regarding the number concentrations of ice nucleating particles (INP) on the ice formation pathways.
In Chapter 6 we present an algorithm to group and evaluate average cirrus properties of WCB outflow features in the ECMWF Reanalysis v5 (ERA5) dataset. Using this feature tracking we calculated a 10 year climatology of average Ice Water Path (IWP) for cirrus in the start of WCB outflow. Using this climatology we chose 10 WCB case studies for ensemble simulations to a obtain a broader insight of the liquid origin vs in-situ formation research question for different initialisations of thermodynamic starting conditions and dynamical developments of WCB ascent.
Finally we will summarize our results and provide some further ideas to investigate the liquid origin vs in-situ formation research question in Chapter 7.

2. Model description

2.1. Introduction

The basis for our model development is the double-moment scheme of Seifert and Beheng (2006) (SB hereafter). The original SB scheme distinguished between six classes of cloud particles: cloud droplets, rain, (cloud) ice, snow, graupel and hail. While the formulation for the liquid droplet's treatment in the model remains unchanged, we reformulate the ice microphysics, and also the interaction of ice and water particles in terms of collision processes. In the following the new scheme is described.

2.2. General settings

The model formulation relies on the usual approach of a bulk model with two (general) moments. Instead of computing the temporal and spatial evolution of a (maybe multivariate) mass distribution with a Boltzmann-type evolution equation, we use the integrated version, i.e., the evolution equations for moments of the underlying mass distribution of the respective class of hydrometeors. The moments are defined in the usual way, i.e.

$$M_i^k := \int_0^\infty x^k \, f_i(x) \mathrm{d}x \tag{2.1}$$

with the mass of particles x for the respective class i of hydrometeors. The mass distribution is normalized by the total number concentration of particles n_i. For a meaningful closure of the systems of equations, we have to choose a suitable type of mass distribution. We generally assume that the particle mass distributions can be represented by generalized Gamma-distributions (see also Seifert and Beheng, 2006) of the form

$$f_i(x) = A_i x^{\nu_i} \exp(-\lambda_i x^{\mu_i}) \tag{2.2}$$

where the shape parameters ν_i and μ_i are prescribed, λ_i and A_i are linked to the zeroth and first distribution moments, the number concentration n_i and the mass content q_i

$$n_i = M_i^0 = \int_0^\infty f(x) \, \mathrm{d}x = \frac{A}{\mu \lambda^{\frac{\nu+1}{\mu}}} \Gamma\left(\frac{\nu+1}{\mu}\right) \tag{2.3}$$

$$q_i = M_i^1 = \int_0^\infty f(x) x \, \mathrm{d}x = \frac{A}{\mu \lambda^{\frac{\nu+2}{\mu}}} \Gamma\left(\frac{\nu+2}{\mu}\right) \tag{2.4}$$

See Appendix A.1 for details on the properties of the gamma distribution and the analytical solution of the integrals.

For the formulation of single particle processes (e.g. growth or sedimentation), we have to introduce size-mass relations and velocity-mass relations of the form

$$D_i(x) = a_i x^{b_i}, \quad v_i(x) = \alpha_i x^{\beta_i} \tag{2.5}$$

with the (generalized) size D_i and the terminal velocity v_i for a particle of mass x within a class i, respectively. These relations represent the different shapes of particles from different classes. The remaining classes of hydrometeors are labeled by indices, i.e. c for cloud droplets, r for rain drops, s for snow, g for graupel, and h for hail, respectively. The old class cloud ice is now splitted into five classes. For details of the formulation and the determination of the shapes for the used hydrometeor classes we refer to Seifert and Beheng (2006).
For our newly introduced ice modes we use the same parameters of the distribution (2.2) and the relations (2.5) for all classes. While the formation pathway of an ice crystal might have an impact on its shape, the morphology of the particle is mainly determined by the environmental conditions encountered during its growth, e.g., temperature and humidity (see, e.g., Magono and Lee, 1966; Kobayashi, 1967; Libbrecht, 2005; Pruppacher et al., 2010), which is not accounted for in the SB scheme. Using the same coefficients and parametrisations for each ice mode apart from its source also has the advantage that it allows a more concise interpretation on the impact of the individual ice formation pathways on the cloud evolution.
The time evolution of the kth-moment M_i^k of an ice mode i (or another class of hydrometeors) is governed by

$$\frac{\partial M_i^k}{\partial t} + \boldsymbol{\nabla} \cdot \left[\vec{v} M_i^k\right] + \frac{\partial \bar{v}_{i,k} M_i^k}{\partial z} - \boldsymbol{\nabla} \cdot \left[K_h \boldsymbol{\nabla} M_i^k\right] = \text{Source/Sink} \tag{2.6}$$

The terms on the left-hand side describe the effects of advection with the mean wind velocity $\vec{v}$, sedimentation with the weighted mean fall-speed $\bar{v}_{i,k}$ and turbulent mixing with the mean turbulent diffusivity of heat K_h, respectively. On the right-hand side are the source and sink terms for the particle formation, which is unique for each ice mode, deposition of water vapor and evaporation and a number of collisions processes, most importantly aggregation and riming, respectively. Actually, these equations must be coupled with a model for atmospheric flows, as, e.g., suitable approximations of the Navier-Stokes equations within the ICON model.
In the following we will focus on the description of the ice related physics and refer to Seifert and Beheng (2006) for an in-depth description of the warm- and mixed-phase microphysics.

2.3. Ice formation pathways

For the treatment of ice particles, we introduce new classes of ice particles, discriminated by their formation mechanisms. The ice modes scheme features five independent ice classes instead of a single one (former class “cloud ice”), called ice modes in this work, each with their unique formation pathway. For each new ice mode, we introduce number

concentrations and mass content, respectively. The other classes (graupel, hail and snow) remain unchanged; however, we have to reformulate the processes of interactions between the former class "cloud ice" and other variables (e.g. for collision processes, see below). The new classes are as follows:

- Homogeneous freezing of cloud droplets n_{frz}, q_{frz}
- Immersion freezing of cloud and rain droplets n_{imm}, q_{imm}
- Freezing of solution droplets (homogeneous nucleation) n_{hom}, q_{hom}
- Deposition nucleation n_{dep}, q_{dep}
- Secondary ice from rime splintering n_{sec}, q_{sec}

The sum of all ice modes represent all ice crystals present (n_{tot}, q_{tot}).

2.3.1. Ice cloud classification due to formation pathway

The basis for the classification of ice clouds formation by different pathways is given by the thermodynamic properties of water. Liquid water is the stable phase at temperature above the triple point $T_m = 273.16\,\mathrm{K}$. Below this temperature, pure liquid water is meta stable, i.e., it can be supercooled down temperatures around $T \sim 235\,\mathrm{K}$; at lower temperatures, liquid droplets freeze almost instantaneously to form the stable phase in the regime $T < T_m$, i.e. the solid phase of hexagonal ice.
Ice formation is always triggered by the formation of a nucleation germ. The germ could either form spontaneously by fluctuations within the liquid phase as a small cluster of molecules, which is then growing to the stable ice phase. This type of ice formation is called homogeneous freezing or homogeneous nucleation, since only liquid phases are involved. On the other hand, the surface of a solid aerosol particle, so called ice nucleating particle (INP) can serve as an ice nucleus, triggering ice formation. This type of ice formation is called heterogeneous nucleation (since another phase is involved). We distinguish between two ice modes of heterogeneous nucleation: immersion freezing and deposition nucleation. Immersion freezing is the initiation of droplet freezing by an INP located inside the droplet (Vali et al., 2015). Deposition nucleation on the other hand describes the deposition of supersaturated water vapor directly onto the INP and following formation of an ice crystal (Vali et al., 2015). There is a huge variety of experimental studies investigating different substances about their ice nucleating properties. However, we lack of theoretical understanding of the different formation mechanisms on a molecular basis, thus until now it is still quite unclear why some substances are good INP and why some others not. For an overview we refer to Hoose and Möhler (2012).
While this kind of classification might be relevant for investigating ice formation in laboratory studies, it is not quite meaningful for investigations of clouds and cloud systems. Therefore we use a different classification, as introduced by Krämer et al. (2016) and Wernli et al. (2016), which is more related to the usual description of clouds.

- Liquid origin: Once a cloud consisting of water particle has formed, it can only exist at or close water saturation. If these cloud droplets are cooled down below the triple point and freeze to ice particles, this pathway is called "liquid origin". Thermodynamically, the system is well characterized as close to water saturation (but supersaturated with respect to ice) and in the temperature range $235 \leq T \leq T_m$.

- In situ formation: If there are no pre-existing cloud particles available, in an environment which is supersaturated with respect to ice (but subsaturated with respect to water), ice particles can form either from aqueous solution droplets (i.e. liquid aerosol droplets) by spontaneous freezing or by deposition of water vapor on available solid aerosol particles (deposition nucleation). Both formations mechanisms are subsummed by the term in situ formation.

In regards to this classification scheme of ice clouds (liquid origin vs. in situ formation), homogeneous and deposition nucleation contributes to in-situ cirrus and homogeneous as well as immersion freezing of cloud droplets and rain to liquid origin cirrus. Ice particles formed by secondary ice production can not be attributed to either due to secondary ice production's intrinsic link to multiple other ice particle formation pathways, e.g., aggregation and riming.

2.3.2. Homogeneous freezing of cloud droplets

Cloud droplets are considered to be pure water droplets, thus freezing homogeneously at temperatures below the triple point T_m but at water saturation. Homogeneous freezing of cloud droplets is the source for the FRZ ice mode with the bulk quantities q_{frz} and n_{frz}. The stochastic process of homogeneous freezing is described by a nucleation rate J_{hom} ($\mathrm{m^{-3}s^{-1}}$), which depends on temperature only (since existence of cloud droplets requires water saturation), thus the change in number and mass concentrations of the ice mode can be described by

$$\frac{\partial n_{frz}}{\partial t} = J_{hom} q_c, \quad \frac{\partial q_{frz}}{\partial t} = J_{hom} q_c \overline{x}_c \frac{\nu_c + 2}{\nu_c + 1} \tag{2.7}$$

using the mass mixing ratio of cloud droplets q_c, the mean mass of cloud droplets $\overline{x}_c$ and the distribution shape parameter ν_c of the cloud mass distribution (generalized gamma distribution), respectively. For the formulation of the homogeneous freezing coefficient of cloud droplets in $\mu\mathrm{kg^{-1}s^{-1}}$, we use the fit of Cotton and Field (2002) to the formulation of Jeffery and Austin (1997):

$$\log\left(\frac{J_{hom}}{\rho_w}\right) = \begin{cases} -243.4 - 14.75T - 0.307T^2 - 0.00287T^3 - 1.02 \cdot 10^{-5} T^4 & \text{for } T \leq -30\,^\circ\mathrm{C} \\ -7.63 - 2.996(T + 30) & \text{for } T > -30\,^\circ\mathrm{C} \end{cases} \tag{2.8}$$

whereas ρ_w denotes the liquid water density. The direct numerical integration is possible since due to saturation adjustment for the cloud droplets (see SB), the system stays at

water saturation permanently.
Homogeneous freezing of raindrops in the SB scheme is omitted, since raindrops freeze rapidly by heterogeneous freezing before reaching temperature levels close to the homogeneous freezing temperature.

2.3.3. Homogeneous freezing of solution droplets

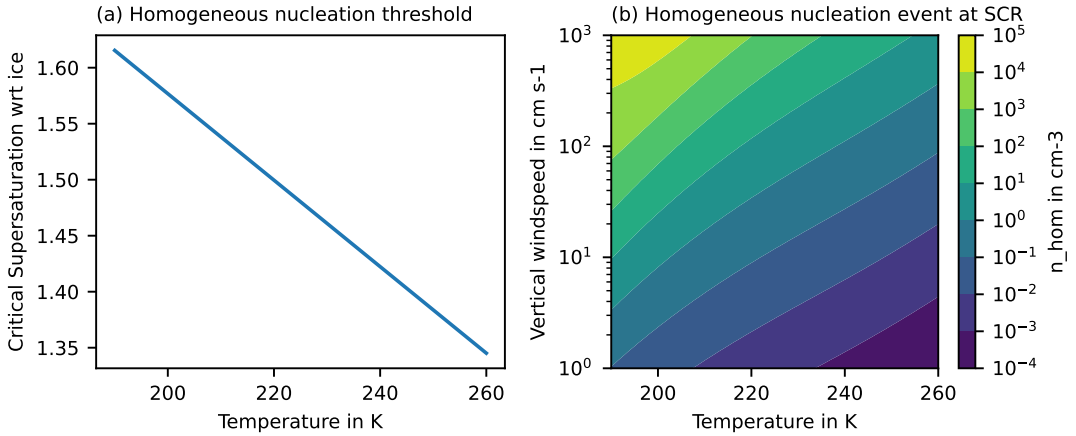

Figure 2.1.: Homogeneous nucleation following Kärcher et al. (2006) for no pre-existing ice. (a) Critical supersaturation serves as a nucleation threshold and (b) number of ice crystals after an homogeneous nucleation event at S_{cr}.

Aequeous solution droplets, i.e. liquid aerosol particles can be supercooled to lower temperatures than pure liquid droplets. The solute obviously impedes the establishment of a critical cluster. Koop et al. (2000) showed that the effect of solutes on the freezing temperature is driven by their thermodynamic (equilibrium) quantities, which can be expressed in terms of water activity, that is defined as the water saturation vapor pressure ratio between the solution and pure water $a_w = e_{sol}/e_{liq}$. When we assume that the solution droplet is in a thermodynamic equilibrium with its environment than the freezing temperature is independent of the choice of chemical droplet composition, at least for inorganic compounds. This translates into a nucleation rate for solution droplets, which solely depends on the environmental conditions, i.e. temperature and supersaturation with respect to ice, but not on the substance in the water drops. The nucleation rate can be formulated using a threshold of critical supersaturation, as could be shown by Spichtinger et al. (2023), e.g., using the formulation by Ren and MacKenzie (2005)

$$S_{\mathrm{cr}} = 2.349 - T/259. \tag{2.9}$$

Panel (a) in Figure 2.1 shows that quite high supersaturations ($S_i > 1.4$) are necessary for homogeneous nucleation events to occur, especially in low temperature regimes ($T < 230\,\mathrm{K}$) where freezing of pure water droplets is no longer possible and homogeneous nucleation commonly observed. This ice formation process is called homogeneous

nucleation and the source term for the HOM ice mode with the bulk properties n_{hom} and q_{hom}. Generally, we would obtain similar equations for the change in n, q as for the freezing of cloud droplets (see Section 2.3.2). However, since the system is in a non-equilibrium state and there is no boundary condition (like the assumption of water saturation as above), we would have to represent the evolution of the saturation ratio, changed also by diffusional growth; this would require a small timestep for the numerical scheme and thus is not feasible.
Therefore, we use the parameterisation by Kärcher and Lohmann (2002), which describes the homogeneous nucleation event in an ascending air parcel. When an air parcel ascends adiabatically supersaturation is generated by adiabatic cooling. When the critical supersaturation S_{cr} is reached, homogeneous nucleation is triggered. The newly nucleated ice crystals deplete supersaturation by depositional growth. The competition between generating supersaturation by adiabatic cooling and depleting supersaturation by depositional growth in a adiabatically ascending air parcel, driven by a constant wind velocity w can be described as

$$\frac{dS}{dt} = a_1 S w - (a_2 + a_3 S) R_i(t) \tag{2.10}$$

with the parameters

$$a_1 = \frac{L_s M_w g}{c_p R T^2} - \frac{M_a g}{RT},\ a_2 = \frac{T k_b}{e_{sat,i}},\ a_3 = \frac{L_s^2 M_w m_w}{c_p p T M_a} \tag{2.11}$$

a_1 describes the effect of adiabatic cooling, where a_2, a_3 and R_i describe the depletion of supersaturation by depositional growth as a function of time. The parameters and process of depositional growth will be further explained in Section 2.5.1.
If the air parcels continues to rise, aqueous solution droplets continue too freeze. When the newly nucleated ice crystals deplete more supersaturation than is being generated by adiabatic cooling, the maximum value of the supersaturation S_* is reached. The supersaturation is depleted and once it reaches S_{cr} the freezing of solution droplets stops. The integrated number of solution droplets frozen within the freezing time interval t_* described the number of ice crystals from the homogeneous nucleation event. Numerical simulations suggest that the freezing time interval t_* is short and the maximum value of supersaturation S_* is approximately equal to S_{cr} (Kärcher et al., 2006). Thus the number concentration of ice particles in a homogeneous nucleation event can than be estimated as

$$n_{hom} = w \frac{a_1 S_{\mathrm{cr}}}{a_2 + a_3 S_{\mathrm{cr}}} \frac{1}{R_{im}(r_0)} \tag{2.12}$$

R_{im} is the analytical approximation of the integral that describes the growth of the solution droplet within the freezing time interval where we refer to Kärcher et al. (2006) for a detailed derivation. $r_0 = 27.2\,\mathrm{nm}$ is the radius of the monodisperse aqueous solution droplets. We obtain the bulk mass of the newly nucleated homogeneous ice mode as

$$q_{hom} = \frac{4}{3}\pi\rho_i \left(\frac{r_0(1 + b_{KH} r_0) - 1}{b_{KH}} \right)^3 n_{hom} \tag{2.13}$$

with the parameter $b_{KH} = \frac{\alpha_d v_{th}}{4 D_v}$. α_d is the deposition coefficient, v_{th} is the mean molecular velocity of water vapor, and D_v denotes the diffusivity.
Panel (b) in Figure 2.1 shows the number concentration of ice n_i after a homogeneous nucleation event at critical supersaturation S_{cr} for vertical windspeeds ranging from synoptic velocities (up to $10\,\mathrm{cm\,s^{-1}}$), gravity waves (up to $100\,\mathrm{cm\,s^{-1}}$) and convection (up to $1000\,\mathrm{cm\,s^{-1}}$). Homogeneous nucleation is strongly sensitive to the model level vertical windspeed and large nucleation events can only be represented if vertical windspeeds are resolved, and no other nucleation mechanisms disturbs the effect of homogeneous nucleation. Nucleation events at synoptic vertical windspeed will be more common in the model and nucleate up to $1\,\mathrm{cm^{-3}}$ ice crystals. Note that the parametrisation of Kärcher et al. (2006) does not explicitly scale with the microphysics time step as it describes an entire nucleation event and not a nucleation rate. Shorter time steps might lead to higher number concentrations because newly nucleated ice crystals have less time to deplete the supersaturation until a new event is allowed to trigger. However, the homogeneous ice mass content is still constrained by the the availability of supersaturation, i.e. by thermodynamics.
The ice modes scheme uses the extension of Kärcher et al. (2006) where the effect of pre-existing ice depleting supersaturation is taken into account as an equivalent to a fictitious downdraft velocity w_{pre}

$$w' = w - w_{pre} = w - \frac{a_2 + a_3 S_i}{a_1 S_i} R_{i,pre} \tag{2.14}$$

with w as the model level vertical wind speed and $R_{i,pre}$ as the mean radius of the pre-existing ice. Pre-existing ice usually originates from a heterogeneous ice mode or a prior homogeneous nucleation event, as we will see in our simulation results.

2.3.4. Heterogeneous nucleation

In the new scheme we use the two nucleation pathways, i.e. immersion freezing and deposition nucleation. Both ice formation pathways depend on temperature, supersaturation and properties of the INP like effectiveness and number of sites causing nucleation per unit surface area (Vali et al., 2015). Both immersion freezing of raindrops and cloud droplets are considered in this model.
We obtain the number density for immersion freezing as the sum of freezing cloud and rain droplets as

$$\frac{\partial n_{imm}}{\partial t} = C_{IMM}|_c - n_{inact} + \frac{\partial n_{imm}}{\partial t}|_r \tag{2.15}$$

and the mass density as

$$\frac{\partial q_{imm}}{\partial t} = \frac{\partial n_{imm}}{\partial t}|_c x_c + \frac{\partial q_{imm}}{\partial t}|_r \tag{2.16}$$

with the mean cloud droplet mass x_c. Similarly for deposition nucleation

$$\frac{\partial n_{dep}}{\partial t} = C_{DEP} - n_{inact} \tag{2.17}$$

$$\frac{\partial q_{dep}}{\partial t} = \frac{\partial n_{dep}}{\partial t} x_{i,min} \tag{2.18}$$

with the minimum mass of ice crystals in the model $x_{i,min}$. C_{IMM} and C_{DEP} describe the number concentration (m^{-3}) of activated INPs for immersion freezing (of cloud droplets) and deposition nucleation, respectively. The model does not feature an explicit model for INP or aerosols in general. Instead the number of activated INPs n_{inact} (m^{-3}) is tracked and advected along with the other ice bulk properties. In further nucleation events n_{inact} is subtracted from the INP number. n_{inact} relaxes back to zero in an ice free environment.

$$\frac{\partial n_{inact}}{\partial t} = \begin{cases} -\frac{n_{inact}}{\tau_{inact}} & \text{if } q_{tot} = \frac{\partial n_{imm}}{\partial t} = \frac{\partial n_{dep}}{\partial t} = 0 \\ \frac{\partial n_{imm}}{\partial t} + \frac{\partial n_{dep}}{\partial t} & \text{else} \end{cases} \tag{2.19}$$

with the relaxation time scale $\tau_{inact} = 600\,\mathrm{s}$ and the total ice content (as the sum of all ice modes) q_{tot}.
First, we describe immersion freezing for rain droplets, i.e. for large water droplets. Bigg (1953) performed laboratory studies investigating the freezing of supercooled purified water in the presence of INP and estimated the probability of a raindrop freezing depending on temperature and droplet volume. Using this results the freezing rate of rain can be expressed as

$$\frac{\partial n_{imm}}{\partial t}|_r = -J_{bigg} q_r = -A_{imm} \rho_w^{-1} \exp(B_{imm}(T_m - T) - 1) q_r \tag{2.20}$$

where we use the coefficients $A_{imm} = 200\,\mathrm{m}^{-3}\mathrm{s}^{-1}$ and $B_{imm} = 0.65\,\mathrm{K}^{-1}$ for rain water due to Barklie and Gokhale (1959). We obtain the mass of frozen raindrops as

$$\frac{\partial q_{imm}}{\partial t}|_r = -A_{imm} \rho_w^{-1} \exp(B_{imm}(T_m - T) - 1) q_r \overline{x}_r Z_r \tag{2.21}$$

with the second moment of the rain mass distribution $Z_r = M_r^2$ and the melting temperature T_m. The mass and number density of frozen raindrops is partitioned into the immersion freezing ice mode (IMM), graupel and hail depending on its diameter. Raindrops smaller than 0.5 mm freeze into ice, raindrops with sizes between 0.5 mm and 1.25 mm are shifted into the graupel class, and raindrops larger than 1.25 mm are considered as hail.
Second, we present the nucleation schemes for immersion freezing of cloud droplets and deposition nucleation, respectively, resulting into changes in the ice modes n_{imm}, q_{imm} (immersion freezing) and n_{dep}, q_{dep} (deposition nucleation).
The ice mode scheme offers the choice between the three heterogeneous nucleation schemes, i.e. Hande et al. (2015), Ullrich et al. (2017), Phillips et al. (2008). Hande et al. (2015) (HA15) considered dust as the main source for INPs over Europe. They used the COnsortium for Small-scale MOdelling (COSMO) meteorological model coupled to the MUlti-Scale Chemistry Aerosol Transport (MUSCAT) to simulate Sahara dust outbreaks for the year 2008. From the statistics of simulated dust concentrations HA15 calculated atmospheric profiles of potential INPs. Since Sahara dust outbreaks shows a

strong seasonal variability HA15 provided mean profiles for each season. The number of active INPs for immersion freezing was than parameterised using the laboratory results of Niemand et al. (2012) for dust particles

$$C_{IMM}(T) = A_H \cdot \exp\Big[-B_H(T - T_{H,min})^{C_H}\Big] \tag{2.22}$$

valid for the temperature range from $T_{H,min} = 237.15\,\mathrm{K}$ to $261.15\,\mathrm{K}$ with the set of coefficients $A_H, B_H, C_H, T_{H,min}$ being chosen depending on the season (see Table 1 in Hande et al. (2015)). The number concentration of active INPs for deposition nucleation was estimated using the parametrisation of Steinke et al. (2015)

$$C_{DEP}(T, S_i) = C_{IMM}(T) \cdot (a_H \arctan(b_H(\mathrm{RH_i} - 100) + c_H) + d_H) \tag{2.23}$$

for temperatures between $T_{H,min} = 220\,\mathrm{K}$ and $253\,\mathrm{K}$. Again, the coefficients depend on the season (see Table 1 in Hande et al. (2015)).
Ullrich et al. (2017) (UL17) used 11 years of data from ice nucleation experiments in the Aerosol Interaction and Dynamics in the Atmosphere (AIDA) cloud chamber to develop a empirical parametrisation for both immersion freezing and deposition nucleation. Dust and soot samples of different types, collected in various locations of the world were analysed in AIDA. The data set includes the results published in Niemand et al. (2012), which where also used in the HA15 parametrisation. However, their are some differences in their approach to calculate the density of active surfaces sites (see Ullrich et al. (2017)) resulting in a light shift to higher densities. In this study we only consider the dust mode. We obtain the number of active INP for immersion freezing and deposition nucleation, respectively, for dust by

$$C_{IMM/DEP}(T, S_i) = n_a\big(1 - \exp\big[-n_{s,IMM/DEP}(T, S_i)SA_a\big]\big) \tag{2.24}$$

with the aerosol number concentration n_a (m^{-3}), the aerosol surface area concentration SA_a and the ice nucleating active surface site density $n_{s,IMM/DEP}$ (m^{-2}) for immersion freezing and deposition nucleation, respectively. The ice nucleating active surface site density for immersion freezing follows a simple exponential temperature profile

$$n_{s,IMM} = \exp[150.577 - 0.517T] \tag{2.25}$$

and for deposition nucleation

$$n_{s,DEP} = \exp\Big[\alpha(S_i - 1)^{1/4}\cos(\beta(T - \gamma))^2 \operatorname{arccot}(\kappa(T - \lambda))\Big] \tag{2.26}$$

where the fixed coefficients α, β, γ, κ and λ can be found in Ullrich et al. (2017). For dust size distribution we use a sum of three lognormal distribution modes. The distribution parameters were chosen such that the immersion freezing temperature profile for UL17 is similar to HA15.
Phillips et al. (2008) (PH08) developed a empirically derived framework for heterogeneous nucleation of multiple aerosol species.

INP are grouped into three basic types: dust/metallic aerosols, inorganic black carbon and insoluble biological aerosol like bacteria and pollen. The basic assumption is that the ice nucleating activity of insoluble aerosol depends on its number of sites causing nucleation (active sites) and hence is proportional to the total aerosol surface area. The number concentration of active INP for a aerosol group X was parameterised as

$$C_{INP,X} = \int_{D_{X,min}}^{\infty} (1 - \exp[-\mu_X(D_X, T, S_i)]) f_X(D_X)\, \mathrm{d}D_X \tag{2.27}$$

where μ_X is the Poisson distributed average of the number of activated INPs for each aerosol particle of size D_X. μ_X was empirically determined by using observational and laboratory data (Phillips et al., 2008). The ice mode schemes uses a simple lookup table and 2D interpolation to determine the fraction of activated INPs as function of temperature and supersaturation for each aerosol type. Lognormal size distributions are assumed for all aerosol types. The number of INPs is the sum over all three aerosol types with the associated number concentration n_X and active fraction $C_{INP,X}$

$$C_{INP} = \sum_X C_{INP,X}(T, S_i) n_X \tag{2.28}$$

where we obtain the number of INPs for immersion freezing at and for deposition nucleation below saturation wrt to water. The initial number concentration of soot particles and biological aerosol is fixed and the number concentration of dust varies with altitude z following a prescribed background profile

$$n_{\mathrm{dust}}(z) = n_{\mathrm{dust},0} \exp\left[\frac{z_{\mathrm{dust},0} - z}{z_{\mathrm{dust},e}}\right] \tag{2.29}$$

Unless otherwise noted we only consider the dust mode for PH08 in this work. We chose $z_{\mathrm{dust},0}$ such that the maximum number of INPs activated for immersion freezing is the same as for HA15.
Panel (a) in Figure 2.2 shows the temperature profiles for immersion freezing parametrisations (IMM) and contour plots of deposition nucleation (c-d). PH08 uses geometric altitude as a coordinate for dust concentration. We transform the altitude into a temperature coordinate using the ICAO Standard Atmosphere. The profile labeled PH08+ considers also soot and biological aerosols in addition to dust. The exponential profiles of immersion freezing for HA15 and UL17 are very similar starting both close to 260 K and being capped at the homogeneous freezing temperature threshold. It is not surprising that we only observe minor differences since INP activation in both parametrisations is based on mostly the same laboratory studies. On the other hand immersion freezing for PH08 starts a higher temperatures but increases less steeply past 260 K. For convectively driven clouds this means an earlier onset of ice formation and has potentially strong effects on the evolution of the ice phase in mixed-phase clouds. PH08+ shows activation of INP at even higher temperature caused by soot and biological aerosol. However, since we did not tune this version of the PH08 scheme to HA15 the maximum number of active INP is lower.

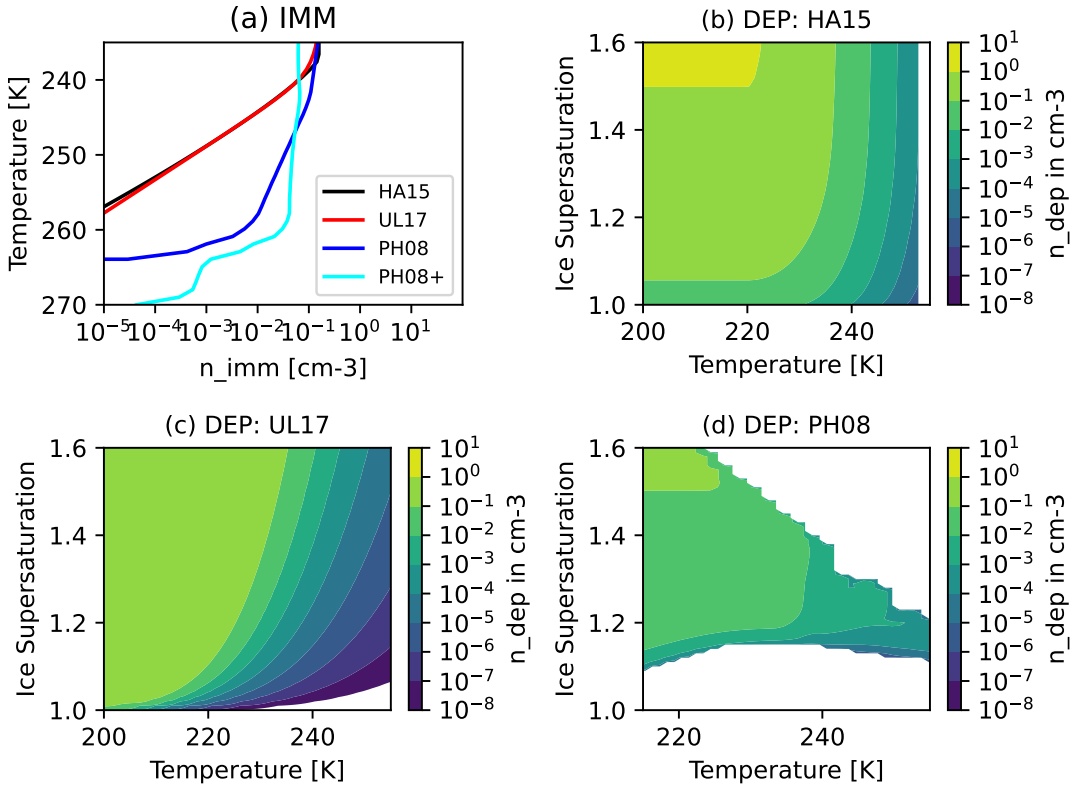

Figure 2.2.: Number concentration of activated INPs for (a) Immersion freezing with profiles for HA15, UL17, PH08 and PH08+ schemes and (b-d) deposition nucleation as a function of T and S_i for (b) HA15, (c) UL17, (d) PH08.

Deposition nucleation shows larger differences between all parametrisations. HA15 (Fig. 2.2 (b)) activates INPs even for small S_i up to 253 K. The number of nucleated ice crystals lies between 0.1 to 1 cm^{-3} for most of the T-S_i space. The UL17 parametrisation shows mostly the same features as HA15 with the major exception that for temperatures above 253 K nucleation is much weaker for low S_i . The number of activated INPs also has a stronger dependency on S_i than HA15. PH08 in contrast shows no active INP at all below $S_i < 1.1$ and overall nucleation is less potent by an order of magnitude compared to the other parametrisations. In general all three parametrisations show large differences for deposition nucleation despite the efforts to adjust them towards similar dust concentrations and immersion freezing profiles. This illustrates that there are still large uncertainties concerning the physical understanding of heterogeneous ice nucleation. However, INP are still limited by the number of activated INPs n_{inact} for all parametrisations.

2.4. Secondary ice

There are three secondary ice mechanisms we consider in this work: rime splintering (RS), frozen droplet fragmentation/shattering (DS) and ice–ice collisional breakup (BR). All mechanisms contribute to the same SEC ice mode. The number density of SEC ice can be obtained as the sum over all secondary ice mechanisms

$$\frac{\partial n_{sec}}{\partial t} = \left(\frac{\partial n_{sec}}{\partial t}\right)_{\mathrm{RS}} + \left(\frac{\partial n_{sec}}{\partial t}\right)_{\mathrm{DF}} + \left(\frac{\partial n_{sec}}{\partial t}\right)_{\mathrm{BR}} \tag{2.30}$$

and the mass density

$$\frac{\partial q_{sec}}{\partial t} = \left(\frac{\partial q_{sec}}{\partial t}\right)_{\mathrm{RS}} + \left(\frac{\partial q_{sec}}{\partial t}\right)_{\mathrm{DF}} + \left(\frac{\partial q_{sec}}{\partial t}\right)_{\mathrm{BR}} \tag{2.31}$$

In the following sections we will discuss the individual parametrisation options of these secondary ice mechanisms.

2.4.1. Rime splintering

Supercooled droplets colliding with ice particles (riming), especially graupel and hail, can throw off small ice splinters, which can grow into ice crystals. This phenomenon was first investigated by Macklin (1960). Various physical mechanism have since been suggested: Macklin (1960) reported that riming caused the growth of fine ice structures that would break to create secondary ice splinters while Choularton et al. (1978) suggested that shattering of freezing droplets produces the ice splinters. The latter would suggest that rime splintering is a sub-process of droplet fragmentation, a secondary ice mechanism we discuss in detail in Section 2.4.2. Hallett and Mossop (1974) counted ice crystals in a light-beam beneath a metal rod, which moved through the cloud chamber and sweeped up water droplets causing riming. By comparing the enhanced number of ice crystals to the background number of the cloud chamber they derived a profile depending on cloud temperature. The standard parametrisation for RS is based on this study and often referred to as the the Hallett-Mossop process. Emersic and Connolly (2017) investigated riming events using high-speed cameras concluded that even small ice crystals and not only large rimers like graupel could potentially produce a significant amount of secondary ice fragments. Seidel et al. (2024) investigated rime splintering with high-speed video microscopy, IR thermography and a custom-build ice counter. They could not reproduce the results of Hallett and Mossop (1974). In general they found only insignificant amounts of SIP production during riming, which can not explain the amount of SIP expected in convective and frontal clouds.
Overall Korolev and Leisner (2020) found no consistency in measured or estimated rime splintering rates between various groups and attributed the discrepancy to different laboratory setups and techniques. Despite RS being the most commonly included secondary ice mechanism in numerical cloud models, the physical understanding is severely lacking and thus the development of a physically based parameterisation seems unfeasible at the moment (Korolev and Leisner, 2020). Still we will use the parameterisation of RS based

on the dataset of Hallett-Mossop extensively in this work as it part of the standard SB scheme.
In Hallett and Mossop (1974) rime splintering occurred within a narrow temperature range of $T_{rs,min} = 265\,\mathrm{K}$ and $T_{rs,max} = 270\,\mathrm{K}$. A fit onto their dataset is used as a function of temperature and rimed mass q_{rime} (kg) as it is implemented in SB

$$\left(\frac{\partial n_{sec}}{\partial t}\right)_{\mathrm{RS}} = q_{rime} C_{RS} \frac{T - T_{rs,min}}{T_{rs,opt} - T_{rs,min}} \frac{T - T_{rs,max}}{T_{rs,opt} - T_{rs,max}}$$
$$\left(\frac{\partial q_{sec}}{\partial t}\right)_{\mathrm{RS}} = \left(\frac{\partial n_{sec}}{\partial t}\right)_{\mathrm{RS}} x_{i,min} \tag{2.32}$$

with the multiplication factor $C_{RS} = 3.5 \cdot 10^8\,\mathrm{kg}^{-1}$ as well as the optimal temperature $T_{rs,opt} = 268\,\mathrm{K}$, the minimum temperature $T_{rs,min} = 265\,\mathrm{K}$ and the maximum temperature for splintering $T_{rs,max} = 270\,\mathrm{K}$. The triangular profile is centered at $T_{rs,opt}$ and ejects up to 350 splinters per mg rimed ice mass. The fragments are initialized as ice splinters of the minimum ice mass $x_{i,min} = 10^{-12}\,\mathrm{kg}$.

2.4.2. Frozen droplet fragmentation

In the last fifty years they have been several laboratory studies investigating the freezing process of water droplets and their ejection of fragments during freezing and by breakup. We will discuss a selection of these works here to illustrate the physical mechanisms and sensitivity to parameters as well as to discuss the opportunities and problems in developing parameterisations of this process for cloud models.
Many laboratory studies have been conducted to study the freezing process of droplets in detail. However, the laboratory setups, techniques and limitations vary between the groups. Droplets were placed in a near-vacuum chamber (Wildeman et al., 2017), levitated in particle-free air at ice saturation (Lauber et al., 2018) or exposed to a laminar air stream to simulate a droplet falling in a real cloud (Keinert et al., 2020). The freezing events were observed and analysed using high-speed camera recordings. Both, droplet temperature ($-30\,^{\circ}\mathrm{C}$ to $-1\,^{\circ}\mathrm{C}$) and humidity were controlled in this studies. However, each study only investigated a small sample and range of droplet sizes: millimeter-sized droplets in Wildeman et al. (2017), 45 to 765 µm in Takahashi (1975), 300 to 350 µm in Lauber et al. (2018) and Keinert et al. (2020). Freezing was triggered by using a tip silver iodide (Wildeman et al., 2017) or contact with a small particle (Lauber et al. (2018), Keinert et al. (2020)).
It is evident from that studies that contact induced freezing leads to the formation of an outer ice shell. While the ice shell radially expands inwards the internal pressure of the still liquid core increases, which results in a number of pressure-release mechanisms:

1. Formation of a spicule
2. Cracking of the ice shell
3. Bursting of bubbles
4. Jetting of liquid water
5. Breakup

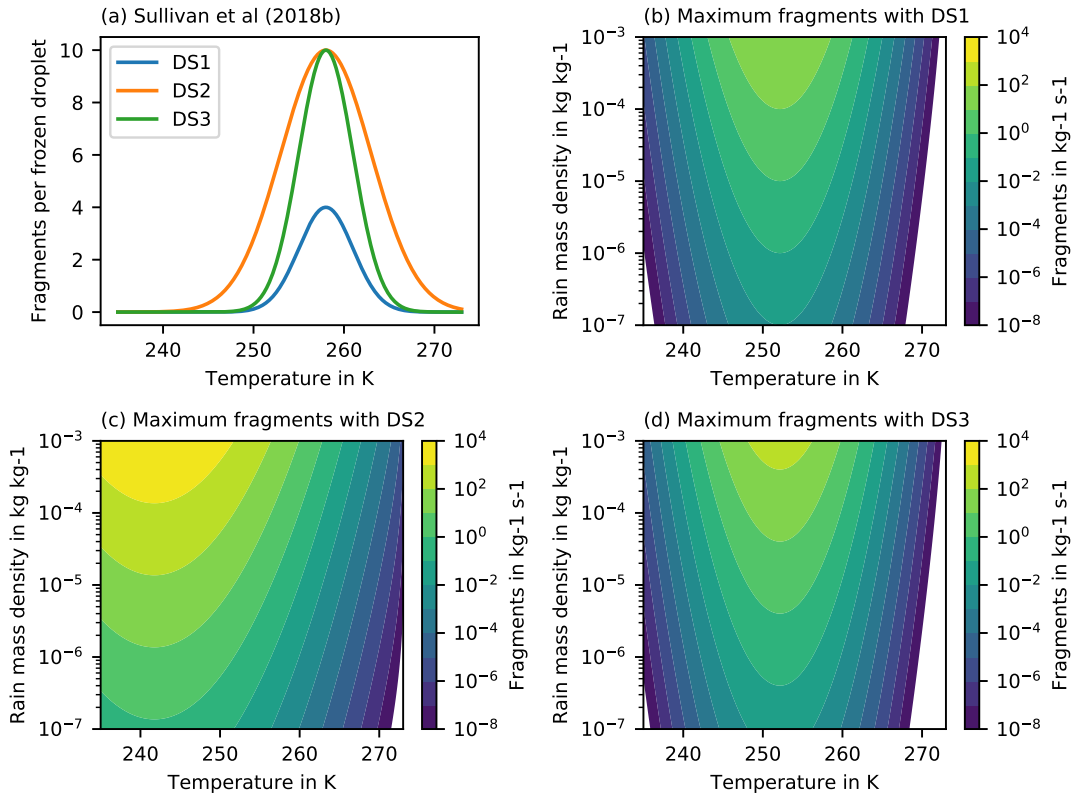

Figure 2.3.: (a) SEC ice rate from freezing droplets with a constant fragment number for three sets of coefficients SU18. (b) to (d) show the maximum rate of SEC ice fragments ejected from frozen droplet shattering using the profiles shown in (a) with the rain freezing rate of Bigg (1953)

In general a sequence of fracturing and healing events is observed that release internal pressure and can eject liquid water as well as ice fragments.
One of the most notable pressure-release mechanism is the formation of a spicule that growths to a size comparable to the droplet diameter. Lauber et al. (2018) observed jetting of liquid water through the spicule although it is unknown if the jet included frozen splinters.
The internal pressure leads also to the formation of cracks in the ice shell, which are filled by water that gradually freezes and mends the cracks (Wildeman et al., 2017). Lauber et al. (2018) observed that such cracks eject an unknown number of ice splinters.
Another frequent occurrence especially for the case of large droplets ($\approx 310\,\mu m$) is the formation of bubbles on the ice shell surface and subsequent bursting accompanied by an ejection of splinters.
Wildeman et al. (2017) focused in their study on the breakup and explosion of the droplets, estimating the fragment velocities and showed that these fragments can induce

freezing in nearby droplets. This is what we define as ice multiplication. This process accelerates the glaciation of a mixed-phased clouds. While it affects the temporal evolution of the cloud particles it inherently does not change the number for frozen particles directly. There exists currently no parameterisation for bulk schemes that describes the effect of frozen droplet shattering onto the freezing rate of nearby droplets. Wildeman et al. (2017) found through theoretical considerations that droplets below a critical radius of 50 µm can not shatter since the energy required to form the new surface area is higher that the elastic energy released by the breakup.
This matches with the findings of Lauber et al. (2018) that pure water droplets of size 85 µm do not breakup or eject ice splinters. However, the addition of solid inclusions into the droplet lead to maximum of 10 % breakup events at around −15 °C. Large droplets (310 µm) showed a maximum of breakup and cracking events of 40 % occurrence between −15 °C and −10 °C, while for higher temperatures ejection events dominate. The inclusion of solids enhanced the occurrence of breakup up to 80 %, which is probably caused by the reduction of mechanical stability of the ice shell (Lauber et al., 2018). Lauber et al. (2018) also investigated the effect of sea salt which suppresses breakup or fragment ejection during freezing, however the typical salt concentrations in cloud droplets are too low to have a significant effect.
The freezing time of a droplet is thus controlled by the transport rate of latent heat to the environment, e.g., convection. Keinert et al. (2020) observed that ventilation of the droplet e.g. when the droplet falls through a cloud at its terminal velocity increases the occurrence of breakup by an order of magnitude. Thus ventilation enhances the heat transfer and accelerates the freezing process. This increases the mechanical stress on the ice shell since it has less time to adapt and hence droplet breakup becomes more likely (Keinert et al., 2020).
In general the number of fragments ejected during freezing or breakup is a function of droplet size, ventilation, chemical composition and the thermodynamic variables that control the freezing process most importantly temperature. Additionally air pressure, dissolved gases and droplet nucleating temperature and other parameters characterizing droplet freezing could be important (Korolev and Leisner, 2020). The sensitivity of the freezing process and fragmentation on these parameters remain poorly understood and the laboratory studies show a large diversity of results (Korolev and Leisner, 2020). Hence, it remains difficult to formulate a rigorous parameterisation for the contribution from freezing droplets to secondary ice (Sullivan et al., 2018a).

Parameterisation developments

A parameterisation should describe the probability of breakup and occurrence of splinter ejection as well as the total number of ice fragments created and ejected. Many microphysic schemes use particle mass as a parameter of size distributions. Droplet diameter, shape and the ventilation coefficient are often directly derived from the particle mass. In the model we only consider raindrops for droplet shattering since cloud droplets are to small to produce a significant number of fragments. The freezing rate of rain is governed

by Bigg (1953) and depends on the temperature and rain mass density.
Sullivan et al. (2018a) (SU18 hereafter) parameterized the number of secondary ice fragments ejected from freezing raindrops as the product of a fragment number F_{DS} and shattering probability p_{DS}, where p_{DS} is given as a normal distribution centered at $T_\mu = 258\,\mathrm{K}$ with a standard deviation of σ and limited by the maximum shattering probability $p_{DS,max}$

$$\begin{aligned} p_{DS}(T,\sigma) &= \frac{1}{\sqrt{2\pi}\sigma}\exp\left(\frac{-(T-T_\mu)^2}{2\sigma^2}\right) \\ N_{DS} &= F_{DS}\frac{p_{DS,max}}{max(p_{DS}(T,\sigma))}p_{DS}(T,\sigma) \end{aligned} \tag{2.33}$$

SU18 used a simplified approach and choose the fragment number as a constant, thus making the number of ice fragments being ejected only depend on temperature.
Three sets of coefficients for the standard deviation σ and constant fragment number (DS1 to DS3) were provided and the profiles are shown in Figure 2.3 Panel (a). This parametrisation produces up to 10 fragments following a Gaussian distribution centered at the ideal temperature of $T_\mu = 258\,\mathrm{K}$ and is active between 250 and 265 K for $\sigma = 3$ (DS1 and DS3) or in a much broader temperature range of 245 to 273 K for $\sigma = 5$ (DS2).
Panels (b) to (d) in Figure 2.3 shows the maximum rate of secondary ice fragments that can be obtained using the profiles DS1 to DS3 with Bigg (1953) rain freezing rate provided there is a sufficient number of liquid droplets available. We observe a large variability of the fragment rate spanning many magnitudes both in terms of temperature and droplet mass. DS1 and DS3 provide only significant number of fragments in a narrow temperature range and for rain mass mixing ratios larger than $10^{-5}\,\mathrm{kgkg}^{-1}$. DS2 shows in general larger rates even for small rain mass mixing ratios but only at cold temperatures ($T < 255\,\mathrm{K}$). We will use the DS2 coefficient set for simulations of droplet fragmentation when using a constant fragment number.
Sullivan et al. (2018b) used a formulation of the fragment number depending on droplet size

$$F_{DS} = 2.5 \cdot 10^{13}\,\mathrm{r}_r^4 \tag{2.34}$$

with the droplet radius r_r. This fourth-power polynomial was determined by Lawson et al. (2015) using comparisons between observations and simulations of a convective cloud utilizing a bin microphysics model but has thus far not been confirmed by laboratory studies. Panel (a) in Figure 2.4 shows the number of secondary ice using this fragment number with the same shattering probability used for DS1 ($\sigma = 5$). The freezing of small droplets produce almost no fragments, only at a radius of at least 400 µm do we observe fragment numbers comparable to the profiles in figure 2.3. However, droplets radii near the millimeter scale eject a number fragments several magnitudes higher than the parametrisations with the constant fragment number.
Sullivan et al. (2018b) also provided a sigmoidal fragment number dependency on the droplet radius r_r

$$F_{DS} = \frac{\alpha_{DS}}{1+\exp[\beta_{DS}(2r_r - \gamma_{DS}]} \tag{2.35}$$

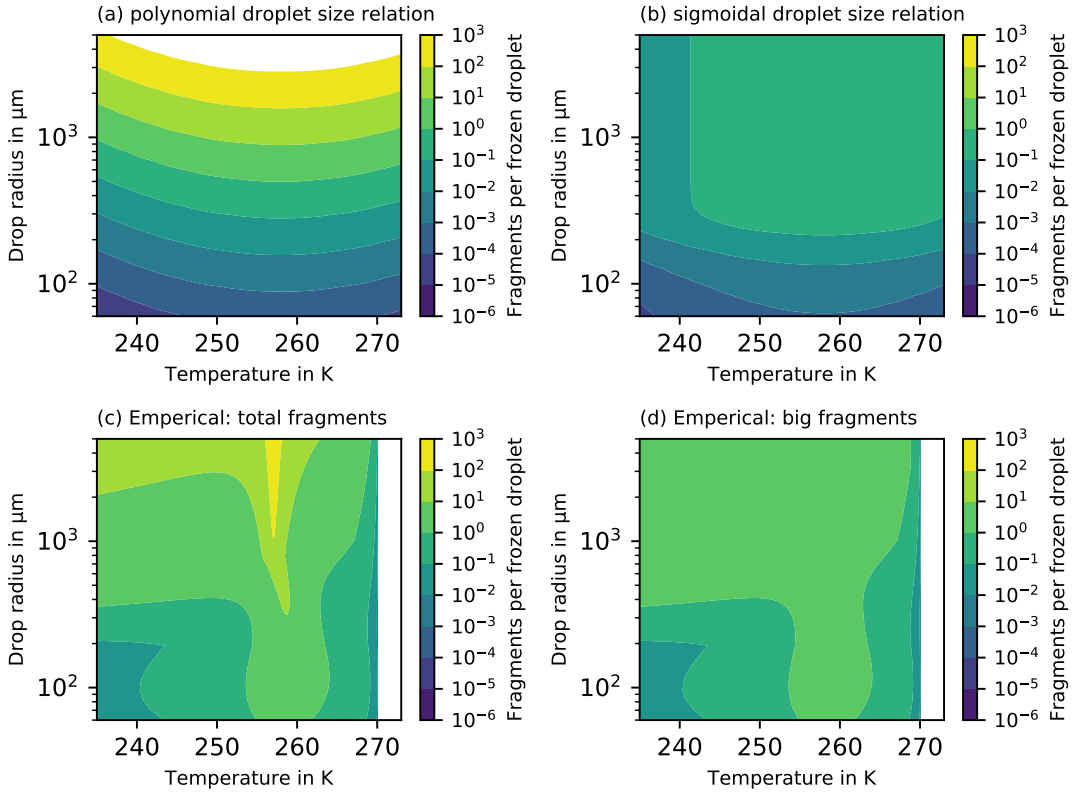

Figure 2.4.: Secondary ice fragments ejected from freezing droplets with (a) polynomial droplet size dependency and (b) sigmoidal droplet size dependency using the a Gaussian shattering probability with $\sigma = 10$ and the empirical parametrisation for (c) total fragements (d) only large fragments.

The results using this relation are shown in Figure 2.4 Panel (b). In general we see a less stark variability of the fragment number with a large plateau for temperatures warmer than 245 K and droplets larger than 300 µm.
Phillips et al. (2018) (PH18 hereafter) choose a rigorous and physical detailed approach for developing a empirical parametrisation of droplet fragmentation. Beginning by fitting a Lorentzian on pooled datasets from selected laboratory studies they obtained the total fragment number as

$$N_{\mathrm{DS}} = \Xi(D)\Omega(T)\left[\frac{\zeta\eta^2}{(T-T_0)^2+\eta^2} + \beta T\right] \tag{2.36}$$

with the droplet diameter D and the temperatures T. For a description of the polynomials $\zeta(D)$, $\eta(D)$ and $T_0(D)$ see PH18. $\Xi(D)$ describes the onset of fragmentation for

smaller droplets as a linear interpolation

$$\Xi(D) = \begin{cases} 0 & \text{for } D < 50\,\mu\text{m} \\ \frac{D-50\,\mu\text{m}}{60\,\mu\text{m}} & \text{for } 50 < D < 110\,\mu\text{m} \\ 1 & \text{for } D \geq 110\,\mu\text{m} \end{cases} \tag{2.37}$$

Similarly the decline of fragmentation for temperatures near the melting temperature is described with

$$\Omega(T) = \begin{cases} 0 & \text{for } T > 270\,\text{K} \\ \frac{270\,\text{K}-T}{3\,\text{K}} & \text{for } 267 < T < 270\,\text{K} \\ 1 & \text{for } T \leq 267\,\text{K} \end{cases} \tag{2.38}$$

Both the number for fragments from ejection of ice splinters and the occurrence of larger fragments from breakup are estimated. The latter is obtained again as a function of droplet diameter D and the temperatures T

$$N_{\text{DS},B} = \Xi(D)\Omega(T)\left[\frac{\zeta_B \eta_B^2}{\left(T - T_{B,0}\right)^2 + \eta_B^2}\right] \tag{2.39}$$

For a description of the parameter functions $zeta(D)$, $\eta(D)$ and $T_{B,0}$ see PH18. The number of small fragments is simply the difference $N_{\text{DS},S} = N_{\text{DS}} - N_{\text{DS},B}$. PH18 also estimated the mass of large and small fragments, respectively, as

$$x_{\text{DS},B} = \frac{x_r}{2.5} \tag{2.40}$$

$$x_{\text{DS},S} = \rho_i \frac{\pi D_S^3}{6} \tag{2.41}$$

with the droplet mass x_r and $D_S = 60\,\mu\text{m}$. Figure 2.4 shows the fragmentation of spherical droplets using this empirical parametrisation as the number of total fragments (c) and large fragments (d). The relationship of fragment number to droplet size and temperature is more complex than in the previously shown parametrisations. We still observe a spike in fragment number around 258 K especially through the ejection of small fragments for droplet sizes in the millimeter regime. At low temperatures near the homogeneous freezing temperature the number of fragments also remains low but overall we observe higher fragment numbers for a larger area without reaching the extreme numbers of the fourth-power polynomial in Equation (2.34).
Whichever parametrisation for the fragment number is used the contribution to the secondary ice mode is obtained as the product of the fragment number and the heterogeneous freezing rate of raindrops

$$\left(\frac{\partial n_{sec}}{\partial t}\right)_{\text{DS}} = N_{\text{DS}}\left(\frac{\partial n_r}{\partial t}\right)_{frz} \tag{2.42}$$

with the raindrop freezing rate obtained with the formula of Bigg (1953). We obtain the mass contribution to the secondary ice mode as

$$\left(\frac{\partial q_{sec}}{\partial t}\right)_{\mathrm{DS}} = x_{\mathrm{DS}} N_{\mathrm{DS}} \left(\frac{\partial n_r}{\partial t}\right)_{frz}$$
$$\left(\frac{\partial q_{sec}}{\partial t}\right)_{\mathrm{DS}} = (x_{\mathrm{DS},S} N_{\mathrm{DS},S} + x_{\mathrm{DS},B} N_{\mathrm{DS},B}) \left(\frac{\partial n_r}{\partial t}\right)_{frz} \tag{2.43}$$

Note that we distinguish between individual masses of large $x_{DS,B}$ and tiny fragments $x_{DS,S}$ for the PH18 parametrisation but only use fragments of the minimal ice mass $x_{\mathrm{DS}} = x_{i,min}$ for the SU18 formulas.

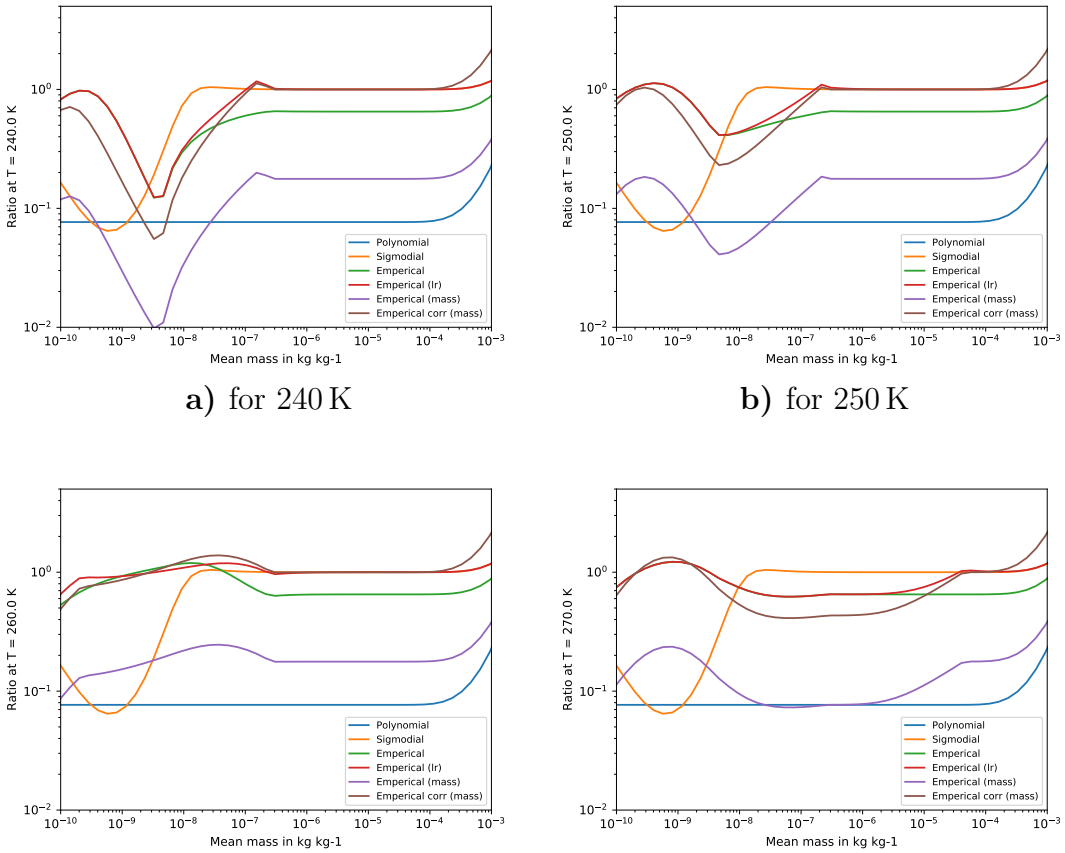

a) for 240 K **b)** for 250 K

c) for 260 K **d)** for 270 K

Figure 2.5.: Relative Error as the ratio of using mean bulk properties and a simulated bin approach for droplet fragmentation. Shown are the polynomial and sigmodial approach of SU18 and the total and large fragment number as well as the fragment mass from the empirical PH18 parametrisation.

Bulk vs emulated bin approach

As noted fragmentation of freezing droplets strongly depends on the size of the droplets. However, since the ice mode model is a 2-moment bulk scheme, we can only consider bulk properties like the mean diameter of the raindrop population when estimating the number of fragments. Thus we could overestimate or underestimate the number of fragments depending on the shape and parameters of the rain size distribution. A better solution would be to use an emulated bin approach. We create a mass grid and populate the bins by evaluating the truncated moments of the rain mass distribution for each bin. Then we calculate the number of fragments from droplet fragmentation for each bin individually and obtain the bulk number density of secondary ice fragments simply by summation over all bins. However, this can be quite difficult in implementation and costly in computational time for a bulk microphysics scheme that is used in large scale simulations.

To estimate the error of using mean bulk properties only instead of an emulated bin approach we created a logarithmic grid of 100 mass bins from 10^{-12} to 10^{-2} kg and populated them for the range of raindrop number and mass densities using truncated moments of the generalized gamma distribution (see Appendix A.4). We than compared the total number and mass of fragments of the emulated bin and mean bulk properties approach for different temperatures.

Figure 2.5 shows the relative error as the ratio of both results for each of the parametrisations, where we consider the emulated bin approach as the true value. The fragments from the empirical P18 parametrisation show a small error, hence the ratio stays close to 1, at least for the range of mean mass from 10^{-7} to 10^{-4} kg. Since the empirical mass is mostly depended on the number of large fragments (see Equation (2.41)) the relative error also shows the same trend but underestimates the mass by an order of magnitude. However, we can apply a constant scaling factor to correct the empirical mass so that the error is comparable to the ones for the fragment number. We determined this scaling coefficient by fitting the relative error of the empirical mass to the one of large fragments using the method of least squares.

We also show the deviations of the SU18 parametrisations although they were intended for use in bulk models, which means they might perform worse when employed in an emulated bin approach. The error of the SU18 polynomial parametrisation is mostly constant and relatively large because the fourth order dependency on radius emphasizes the splintering of large droplets which are underrepresented if only the mean droplet radius is used. The SU18 sigmodial parametrisation shows a good agreement between both approaches except for small mean rain mass ratios. This was to expected since Figure 2.4 showed that the parametrisations shows a constant fragment number for a large part of the mass-number density domain since they land on the sigmodal plateau. Considering the high uncertainty associated with freezing droplet fragmentation and the general error ranges of bulk schemes the empirical as well as the sigmodial parametrisations can be used without an emulated bin approach. While the underestimated fragment mass is a concern, the error can be reduced by employing a simple scaling coefficient.

2.4.3. Ice–ice collisional breakup

Collisions between ice particles, e.g. ice crystals, snow and graupel can lead to breakup and the production of fragments that contribute to secondary ice. There have been only few laboratory experiments that investigate the fragmentation mechanisms due to collision of the various types of ice particles and multitude of collision types between them. Vardiman (1978) studied the fragmentation of graupel and dendritic ice crystals in various stages of riming by taking photographs of natural ice particles impacting a fixed mesh. The number of fragments generated was determined as a function of change in momentum. Vardiman (1978) found unrimed dendrites to produce almost no fragments while rimed crystals produced up to 35 fragments per collision. This was likely caused by their greater terminal velocity and increased fragility. Graupel on the other hand was inefficient in producing fragments.
Takahashi et al. (1995) studied the collision of fixed ice spheres, representing large graupel or hail, and the resulting fragmentation in a laboratory experiment. The graupel were grown either or both by deposition of water vapor and riming. The results showed an average of 200 fragments per collision and exponential increase of ejected ice fragments as a function of collision force which approaches a limit at 450 fragments. The fragment number also varies with ambient temperature to a factor of 3 with a peak at 258 K. This was attributed to the breaking of dendritic ice branches which grow on rimed ice particles in this temperature range. Takahashi et al. (1995) found that extended depositional and riming growth times enhanced fragment generation.
Korolev and Leisner (2020) noted that graupel grown in the experimental set-up of Takahashi et al. (1995) were likely more fragile and significantly larger compared to free-falling graupel formed in natural clouds and thus possible overestimating the fragment number. In general Korolev and Leisner (2020) found it hard to judge the consistency and applicability earlier laboratory studies due their different experimental setups and environmental conditions. More laboratory studies for different types of free-falling ice particles would be required to develop parametrisations for ice-ice collisional breakup. Nevertheless ice-ice collisional breakup is likely an important SIP mechanisms and we will introduce two parameterisations for the fragment number N_{BR} here. N_{BR} in general depends on the growth history of the particle, which is linked to ambient temperature and rime fraction, as well as the collision dynamics, where diameter, mass and velocity of the colliding particles are important parameters.

Parametrisation developments

For their collisional breakup parametrisation Sullivan et al. (2018a) (SU18) focused solely on the temperature dependency, which controls the dendritic growth and thus fragility of the ice particle. A normal distribution was fitted onto the data of Takahashi et al. (1995) for colliding graupel at a collision force of 500 dynes

$$N_{BR} = \frac{F_{BR}}{\alpha_{BR}}(T - T_{br,min})^{1.2} \exp[-(T - T_{br,min})/\gamma_{BR}] \tag{2.44}$$

with the minimum temperature $T_{br,min}$, below which no breakup occurs, the fragment number decay rate γ_{BR} and a constant leading coefficient F_{BR}. These coefficients were varied for different colliding particles in Sullivan et al. (2018a) and a sensitivity analysis in Sullivan et al. (2018b). Note that the data basis for this parameterisation were large graupel ($> 2\,\mathrm{cm}$) at maximum collision force and thus would be overestimating the number of fragments for smaller graupel. Sotiropoulou et al. (2020) introduced a scaling factor α_{BR} for the fragment number based on the diameter of the particle

$$\alpha_{BR}(D) = \begin{cases} 100 & \text{for } D < 500\,\mu\mathrm{m} \\ 50 & \text{for } 500\,\mu\mathrm{m} \leq D < 1\,\mathrm{mm} \\ 10 & \text{for } 1\,\mathrm{mm} \leq D < 1\,\mathrm{cm} \\ 1 & \text{for } D \geq 1\,\mathrm{cm} \end{cases} \tag{2.45}$$

This parametrisation is only valid for collisions with graupel.
Phillips et al. (2017b) (PH17 hereafter) developed a theoretical framework to quantify the fragment number from breaking of branches and asperities due to collisions between two ice particles. The approach is based on conservation of energy during a collision

$$K_0 = K_1 + \Delta S + K_{th} \tag{2.46}$$

with the initial kinetic energy $K_0 = \frac{1}{2}\frac{m_1 m_2}{m_1+m_2}(v_1 - v_2)^2$, the final kinetic energy K_1, the change in surface adhesion ΔS and the energy available for inelastic deformation K_{th}. Only part of the non-thermal loss of kinetic energy is available for breaking off branches and asperities $\delta K_{th} = b_{br,2} K_{th} < K_{th}$. PH17 approximated $\delta K_{th} \approx K_0(1 - q^2)$ with the coefficient of restitution q. Further they assumed K_{th} to be equally distributed in the region of contact.
An important particle property is the number density of breakable branches and asperities in the contact area

$$N_{contact} = \pi D_s^2 G_{branch}(D, T, \Psi_{rime}) \tag{2.47}$$

with the equivalent spherical diameter D_s of the smaller colliding particle. $G_{branch}(\mathrm{m}^{-2})$ describes the distribution of breakable asperities on the surface of the ice particle. G_{branch} in general depends on its growths history as well as the collision dynamics, but can be approximated as a function of temperature, maximum collision diameter, rime fraction and supersaturation

$$G_{branch}(D, T, \psi) = a_g(T, \Psi_{rime}) + b_g(T, \Psi_{rime}) D^{-1.5} \tag{2.48}$$

with the air temperature T and rime fraction Ψ_{rime}. $a_g(T, \Psi_{rime})$ and $b_g(T, \Psi_{rime})$ depend on the collision type and use the coefficients and the diameter from the smaller particle since it is considered to be more fragile. This parametrisation is valid for particle diameters in the range of 500 to 5000 µm and uses the nearest value outside these range. PH17 estimated C and G_{branch} for collisions between graupel and large frozen droplets from the data of Takahashi et al. (1995) and for collisions with snow and dendretic ice

crystals with data from Vardiman (1978).
PH17 set the width of asperities to be exponentially distributed

$$\Xi_{asp} = \frac{1}{\langle \Xi_{asp} \rangle} \exp\left[-\frac{\Xi_{asp}}{\langle \Xi_{asp} \rangle} \right] \tag{2.49}$$

with the mean width $\langle \Xi_{asp} \rangle$. It was further assumed that the work required to break a asperity is proportional to its cross-section

$$\Xi_{asp} \approx b_{br,3} G_{break}^{\gamma_{asp}} \tag{2.50}$$

Hence the width Ξ_{asp} can be used as a measure for the probability of breaking a asperity upon impact. The energy available to break a asperity, which is distributed equally in the surface area, is limited $G_{break} \leq \frac{\delta K_{th}}{N_{contact}}$.
Thus asperities wider than $\Xi_0 = b_{br,3}\left(\frac{\delta K_{th}}{N_{contact}}\right)^{\gamma_{asp}}$ cannot be broken. So the probability of breaking an asperity is the same as this asperity being smaller than Ξ_0

$$\begin{aligned}
P\left(G_{break} \leq \frac{\delta K_{th}}{N_{contact}}\right) &= P(\Xi_{asp} \leq \Xi_0) \\
&= \frac{1}{\langle \Xi_{asp} \rangle} \int_0^{\Xi_0} \exp\left[-\frac{\Xi_{asp}}{\langle \Xi_{asp} \rangle} \right] \mathrm{d}\Xi_{asp} \\
&= 1 - \exp\left[-\frac{\Xi_0}{\langle \Xi_{asp} \rangle} \right] \\
&= 1 - \exp\left[-\frac{b_{br,3}\left(\frac{\delta K_{th}}{N_{contact}}\right)^{\gamma_{asp}}}{\langle \Xi_{asp} \rangle} \right] \\
&= 1 - \exp\left[-\left(\frac{K_0 b_{2,br}(1-q)^2}{N_{contact}} \right)^{\gamma_{asp}} \frac{b_{3,br}}{\langle \Xi_{asp} \rangle} \right] \\
&= 1 - \exp\left[-\left(\frac{K_0 b_{2,br}(1-q)^2}{\pi D_s^2 G_{branch}} \right)^{\gamma_{asp}} \frac{b_{3,br}}{\langle \Xi_{asp} \rangle} \right]
\end{aligned} \tag{2.51}$$

PH17 used the expressions for energy available for deformation K_{th} and breaking of asperities δK_{th} as well as the branch number density and width distribution from equations (2.47) and (2.49) respectively.
The number of fragments is obtained as the product of the number of breakable asperities in the contact area (Equation (2.47)) and the probability of breaking these asperities (Equation (2.44))

$$\chi_{BR} = \pi D_s^2 G_{branch} \left(1 - \exp\left[-\left[\frac{C K_0}{D_s^2 G_{branch}} \right]^{\gamma_{asp}} \right] \right) \tag{2.52}$$

with the asperity-fragility coefficient

$$C = \frac{b_{2,br}(1-q)^2 (b_{3,br} \langle \Xi_{asp} \rangle)^{1/\gamma_{asp}}}{\pi b_{br,1}} \tag{2.53}$$

The asperity-fragility coefficient depends on the collision type and dynamics as well as the mean width of asperities and $\langle \Xi_{asp} \rangle$ and the growths history of the particle. PH17 found that there is a lack of observations and measurements to resolve the full dependencies of C on these parameters. For practical applications C is given as an empirical, average value for each hydrometeor class.
The contribution to the number density of the secondary ice mode from collisional breakup can be summarized as

$$\left(\frac{\partial n_{sec}}{\partial t}\right)_{BR} = \sum_{i}^{N}\sum_{j}^{N}\int_{0}^{\infty}\int_{0}^{\infty} f_i(x_i) f_j(x_j) K_{ij}(x_i, x_j) N_{BR,ij}\, \mathrm{d}x_j\, \mathrm{d}x_i$$
$$\left(\frac{\partial q_{sec}}{\partial t}\right)_{BR} = \left(\frac{\partial n_{sec}}{\partial t}\right)_{BR} x_{i,min} \tag{2.54}$$

with N as the number of hydrometeor classes that produce fragments upon collision within their own and with other classes. For PH17 we included all ice modes, snow, graupel and hail and for SU18 only collisions that include graupel as a partner. Fragments are initiated with the minimum ice mass $x_{i,min}$. K_{ij} is the collision kernel and $N_{BR,ij}$ the number of fragments from a collision between two particles of class i and j. The collision kernel is defined as

$$K_{ij}(x_i, x_j) = \epsilon (D_i(x_i) + D_j(x_j))^2 E_{ij} |v_i(x_i) - v_j(x_j)| \tag{2.55}$$

with the collision efficiency E_{ij} (Seifert and Beheng, 2006).
When using the SU18 parametrisation solving the double integral in (2.54) analytically is simply the collision rate multiplied by equation (2.44). However, it is more difficult for the PH17 parametrisation, since the expression in equations (2.52) and (2.48) can not be rearranged in a such a way that the integrands are of the form $y^{\zeta} \exp(-\eta y)$. Hence we can not can use the relations for the (incomplete) Gamma functions to solve the integral analytically. Therefor we opt to approximate the integral numerically using Gauss-Laguerre quadrature (see Appendix A.5) with 20 nodes.

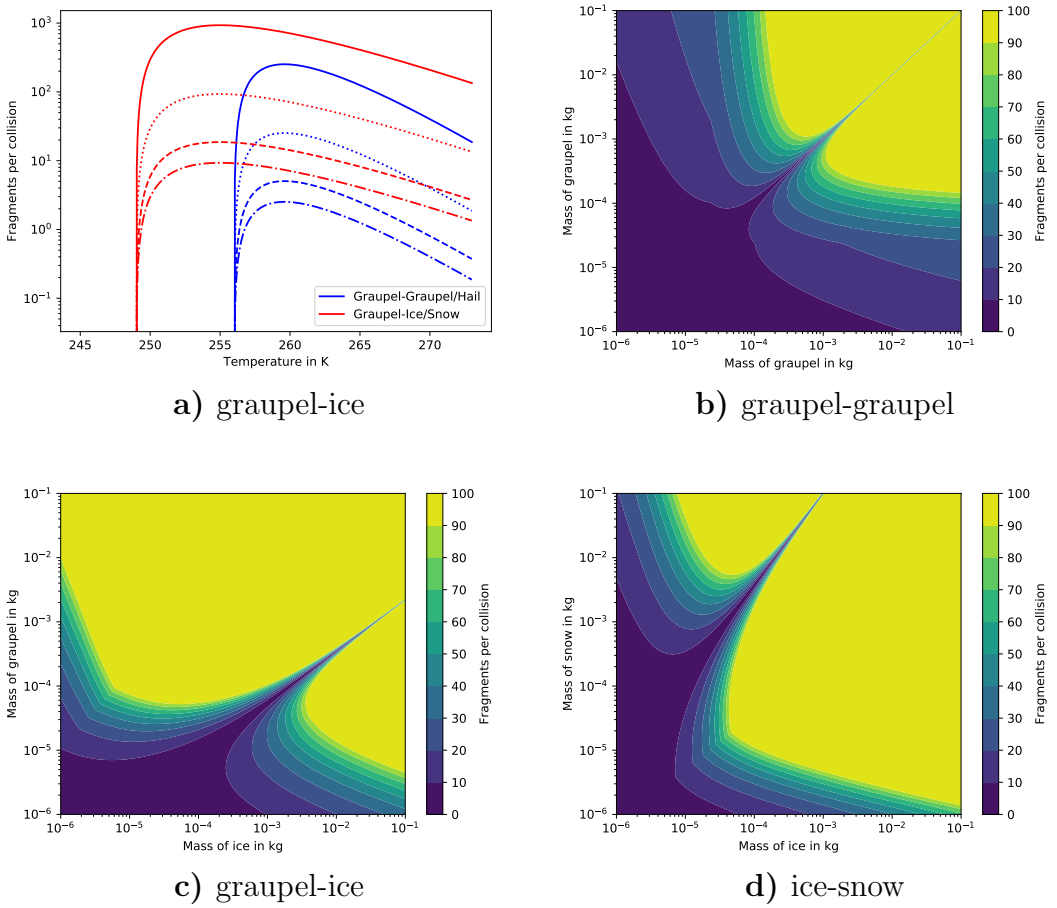

a) graupel-ice **b)** graupel-graupel

c) graupel-ice **d)** ice-snow

Figure 2.6.: Secondary ice fragments per collision of two ice particles for the parametrisation of (a) SU18 with scaling coefficients and (b) to (d) PH17 at $T = 253\,\mathrm{K}$ and $p = 800\,\mathrm{hPa}$. Note that we only show a selection of collision pairs for the PH17 parametrisation.

Figure 2.6 shows an overview of the secondary ice fragments per collision, where panel (a) shows the SU18 parametrisation for both collision types without (continuous line) and with scaling coefficients. Collision of graupel with any other graupel or hail particle produce up to 900 at 256 K fragments per collision for a large temperature range from 273 to 249 K. Collision of graupel with ice and snow produces much less, only up to a maximum of 250 fragments at 259 K and for a narrower temperature range. Ice particles smaller than 1 cm reduce the number of fragments by an order of magnitude (dotted line), smaller than 1 mm by almost two orders of magnitude (dashed line) and the smallest particles ($< 500\,\mu\mathrm{m}$) lead to only up to 8 fragments.
We only show a selection of collision pairs in the Figure 2.6 panels b) graupel-graupel, c) graupel-ice and d) ice-snow. The number of fragments is shown as a function of both

particle masses for a set temperature of 253 K. As expected we see a strong dependency on particle mass, especially on the mass of the larger collision partners graupel and snow, respectively. For collision of particles of the same type we of course obtain a symmetric fragment distribution with an gap at the same mass, since the velocity difference is zero at this point. Interestingly, graupel-graupel collisions are ineffective until the combined mass exceeds 10^{-3} kg by a fair amount. However, for collision with more fragile particles like ice and snow, smaller particles suffice to produce a larger amount of fragments.
Since the PH17 parameterisation is limited to 100 fragments, except for hail-hail collisions, we expect an overall lower fragment number than with the SU18 parameterisation without scaling coefficients (continuous line). This is especially true since this parametrisations is sensitive to the shape of the particle mass distributions. If a majority of the particles are smaller than 10^{-4} kg there we will be much less fragments produced than with the flat rate of the SU18 parametrisation.

2.5. Microphysical processes

There are several microphysical processes modifying the bulk properties of ice mode classes after initial ice formation.

2.5.1. Depositional growth of water particles

Deposition of water vapor onto a cloud particle in a supersaturated environment is the most fundamental growth process for all cloud particles. The SB scheme uses saturation adjustment for the water phase, hence whenever the environment is supersaturated wrt water ($S_w > 1$) at the beginning of a mircophysical time step, S_w is relaxed to water saturation (i.e. $S_w \equiv 1$) and the change of water vapor q_v is converted to cloud water q_c, considering latent heat release (using a Newton-Raphson scheme). However, supersaturation wrt ice (i.e. $S_i > 1$) is explicitly resolved. The mass growth of an ice particle by deposition of water vapor can be described by formulating the flux of vapor and heat between the particle and the environment considering mass and energy conservation, than integrating this fluxes over the particle surface and evaluating the effect of latent heat of sublimation on the particle surface temperature. Assuming that the temperature difference between the particle surface and the environment is small we can derive the general growth equation of a single ice particle with mass x using the Clausius-Clapeyron relation (Pruppacher and Klett, 1998)

$$\left.\frac{\partial x}{\partial t}\right|_{dep} = \frac{4\pi C(x)(S_i - 1)F_v(x)}{\frac{TR_v}{D_v e_{si}} + \frac{L_s\left(\frac{L_s}{R_v T} - 1\right)}{K_a T}} \tag{2.56}$$

with the saturation ratio wrt to ice $S_i = \frac{e}{e_{si}(T)}$, the ventilation coefficient F_v and the capacitance C accounting for the enhancement of the depositional growth by the flow field and the non-spherical shape, respectively. The left term in denominator represents the mass flux relation with the diffusion coefficient D_v and water vapor saturation pressure wrt ice $e_{si}(T)$; the right term describes the heat flux with the thermal conductivity of air K_a and the latent heat of sublimation L_s. The capacitance can be related to the maximum diameter $C(x) = D(x)/c$ with c_k depending on the class of the particle k. Integrating (2.56) over the entire particle distribution for an ice mode k we obtain

$$\begin{aligned} g_{dep,k} &= \left.\frac{\partial q_k}{\partial t}\right|_{dep} = \int_0^\infty \left.\frac{\partial x_k}{\partial t}\right|_{dep} \mathrm{d}x_k \\ &= \frac{4\pi(S_i - 1)c_k^{-1}}{\frac{TR_v}{D_v e_{si}} + \frac{L_s\left(\frac{L_s}{R_v T} - 1\right)}{K_a T}} \int_0^\infty D(x_k)F_v(x_k)f(x_k)\,\mathrm{d}x_k \\ &= \frac{4\pi(S_i - 1)c_k^{-1}}{\frac{TR_v}{D_v e_{si}} + \frac{L_s\left(\frac{L_s}{R_v T} - 1\right)}{K_a T}} D(\overline{x_k})\overline{F_v} \end{aligned} \tag{2.57}$$

with the mean particle mass $\overline{x_k}$ and averaged ventilation coefficient $\overline{F_v}$; for details, see calculations in the Appendix of SB.

However, we must consider that all ice particle classes compete for water vapor. Thus we follow Morrison et al. (2005) semi-analytic approach to estimate the depositional growth rate with a exponential relaxation towards equilibrium. The change of mass density of ice particle class k within a physical time step is

$$\left.\frac{\Delta q_k}{\Delta t}\right|_{dep} = \frac{\delta_i X}{\tau_k}(1 - \exp\left(-\frac{\Delta t}{X}\right)) \tag{2.58}$$

with $\delta_i = q_v - q_{si}$ expressing the supersaturation wrt ice and the microphysical time step Δt. τ_k is defined as the depositional time scale

$$\tau_k^{-1} = \frac{g_{dep,k}}{\delta_i} \tag{2.59}$$

X is the conjoined relaxation time needed to describe the competition between the ice particle classes as a sum of the individual relaxation time scales

$$X = \left[\sum_j^N \tau_j^{-1}\right]^{-1} \tag{2.60}$$

where we consider graupel, hail, snow as well as all five ice modes. For a derivation and application of this method to resolve supersaturation see, e.g., Khvorostyanov (1995), Morrison et al. (2005), Köhler and Seifert (2015).

2.5.2. Sedimentation of cloud particles

For the sedimentation of ice particles, we use the mass-velocity relation (2.5) for ice crystals; these relations were used for all new ice modes. For the use in the evolution equation of moments (2.6), an averaged sedimentation velocity must be calculated via a weighted integration, i.e.

$$\bar{v}_{i,k} = \frac{1}{M_i^k}\int_0^\infty x^k f_i(x) v_i(x) \mathrm{d}x \tag{2.61}$$

Using the analytical results for generalized gamma-distributions, this results into the expression

$$\bar{v}_{i,k} = \alpha_i \frac{\Gamma\left(\frac{k+\nu_i+\beta_i+1}{\mu_i}\right)}{\Gamma\left(\frac{k+\nu_i+1}{\mu_i}\right)} \left[\frac{\Gamma\left(\frac{\nu_i+1}{\mu_i}\right)}{\Gamma\left(\frac{\nu_i+2}{\mu_i}\right)}\right]^{\beta_i} \bar{x}_i^{\beta_i} \tag{2.62}$$

see also Section 3.7 in SB.

2.5.3. Collision processes of cloud particles

Collision is an important process for producing large cloud particles. For the formation of large raindrops, collision is essential. However, considering the formation of rain via the ice phase, again collisions between water and ice particles play an important role.

In the presented scheme, the rates for collisions between liquid particles (cloud droplets and raindrops) remain unchanged. However, the collision rates for ice particles must be reconsidered.
As formulated in the SB scheme, we have the following conceptual treatment for sorting new particles stemming from the collision of ice particles with others:

- Collision between an cloud ice particle and a cloud droplet leads to a larger ice particle or to a graupel particle, depending on the size of the ice particle (riming)
- Collision between two cloud ice particles leads to a snow particle (self-aggregation)
- Collision between an cloud ice particle and a snow particle leads to a snow particle (aggregation)

This concept must be adapted for ice particles from the five different ice modes. Especially, the collision of ice particles from different ice modes must be taken into account as a new process, extending the existing formulation of self-aggregation of ice particles. In the following the changes are documented.

Collision of liquid and solid particles

We adapt the formulation by SB of riming (ice particle collides with cloud droplet or raindrop) for all new ice modes. Analog to the implementation for a single ice class in SB, all ice modes can be collected by graupel, hail or snow and contribute to riming.

Aggregation of ice particles

There is no separate treatment for each ice mode regarding aggregation, all collisions between ice modes as well as self collection within a single ice mode contribute to the same snow class. We will only present a condensed derivation of the collision growth equation here. The full derivation can be found in Appendix A.2.
The collision processes between two ice classes i and j leads to the formation of snow s can be described as

$$\left.\frac{\partial f_i(x)}{\partial t}\right|_{coll,ij} = -\int_0^\infty f_i(x) f_j\big(x'\big) K_{ij}\big(x, x'\big)\,\mathrm{d}x' \tag{2.63}$$

$$\left.\frac{\partial f_j(x)}{\partial t}\right|_{coll,ij} = -\int_0^\infty f_i\big(x'\big) f_j(x) K_{ij}\big(x, x'\big)\,\mathrm{d}x' \tag{2.64}$$

$$\left.\frac{\partial f_s(x)}{\partial t}\right|_{coll,ij} = \int_0^x f_i\big(x'\big) f_j\big(x - x'\big) K_{ij}\big(x', x - x'\big)(x - x')\,\mathrm{d}x' \tag{2.65}$$

The collection kernel is defined as

$$K_{ij}(x_i, x_j) = A_{ij} E_{coll} |v_i(x_i) - v_j(x_j)| \tag{2.66}$$

where A_{ij} is the cross section of the sweep out volume, E_{coll} is the mean sticking efficiency and $v_{i,j}$ are the terminal velocities. Let D_i and D_j donate the maximum diameters of ice crystals and we obtain for A_{ij}

$$A_{ij}(x_i, x_j) = \frac{\pi}{4}(D_i(x_i) + D_j(x_j))^2 \tag{2.67}$$

where we simplified the expression by assuming spherical particles. The sticking efficiency is parameterised following Cotton et al. (1986)

$$E_{coll} = \min\Big(10^{0.035\cdot(T-T_m)-0.7}, 0.2\Big) \tag{2.68}$$

with a maximum efficiency of 0.2 for $T = 273\,\mathrm{K}$. The mass relation provided in equation (2.5) is not sufficient to characterise the terminal velocity of ice particles since complex shapes and atmospheric turbulence affect the flow field around the particle (Seifert, 2002). The velocity distribution function describes the probability of a ice particle of mass x to have the terminal velocity v'

$$P\big(v'|x\big) = \frac{1}{\sigma_{vel}\sqrt{2\pi}} \exp\left[-\frac{1}{2}\left[\frac{v' - v(x)}{\sigma_{vel}}\right]^2\right] \tag{2.69}$$

with the variance of terminal velocity σ_{vel}.
The absolute velocity difference in the collision kernel would split the integral and impose incomplete gamma functions thus complicating the result. We use the Wisner approximation which assumes characteristic mean values for the terminal velocities that are constant and can hence be separated from the integrand. As proposed in Seifert (2002) integral cross-section is used as a weight

$$\begin{aligned}\overline{v_{ij,k}}^2 = \frac{1}{N_k} \int_{x_i=0}^{\infty} \int_{x_j=0}^{\infty} D_i^2(x_i) D_j^2(x_j) f_i(x_i) f_j(x_j) x_i^k \\ \int_{v_j=-\infty}^{\infty} \int_{v_i=-\infty}^{\infty} \big(v_i'(x_i) - v_j'(x_j)\big)^2 P\big(v_i'|x_i\big) P\big(v_j'|x_j\big) \mathrm{d}x_i \mathrm{d}x_j \mathrm{d}v_i' \mathrm{d}v_j' \\ = \overline{v_i^2}\vartheta_i^k + \overline{v_i v_j}\vartheta_{ij}^k + \overline{v_j}^2 \vartheta_j^0 + 2\sigma_{vel}^2\end{aligned} \tag{2.70}$$

where we used the properties of the Gamma function and the scaling factor

$$N_k = \int_{x_i=0}^{\infty} \int_{x_j=0}^{\infty} D_i^2(x_i) D_j^2(x_j) f_i(x_i) f_j(x_j) x_i^k \mathrm{d}x_i \mathrm{d}x_j \tag{2.71}$$

Integrating equations (2.63) to (2.65) and again using the properties of the Gamma function we finally obtain an analytical solution for the collision rate

$$\begin{aligned}\left.\frac{\partial n_s}{\partial t}\right|_{coll,ij} = -\left.\frac{\partial n_i}{\partial t}\right|_{coll,ij} = -\left.\frac{\partial n_j}{\partial t}\right|_{coll,ij} \\ = \frac{\pi}{4} E_{coll} n_i n_j \Big[\overline{D_i}^2 \delta_i^0 + \overline{D_i D_j} \delta_{ji}^0 + \overline{D_j}^2 \delta_j^0\Big] / \overline{v_{ij,0}}\end{aligned} \tag{2.72}$$

and the change of mass mixing ratios due to aggregation

$$\left.\frac{\partial q_i}{\partial t}\right|_{coll,ij} = -\frac{\pi}{4} E_{coll} q_i n_j \left[\overline{D_i}^2 \delta_i^1 + \overline{D_i D_j} \delta_{ji}^1 + \overline{D_j}^2 \delta_j^0\right] / \overline{v_{ij,1}} \tag{2.73}$$

$$\left.\frac{\partial q_j}{\partial t}\right|_{coll,ij} = -\frac{\pi}{4} E_{coll} q_j n_i \left[\overline{D_i}^2 \delta_i^0 + \overline{D_i D_j} \delta_{ij}^1 + \overline{D_j}^2 \delta_j^1\right] / \overline{v_{ji,1}} \tag{2.74}$$

$$\left.\frac{\partial q_s}{\partial t}\right|_{coll,ij} = -\left.\frac{\partial q_i}{\partial t}\right|_{coll,ij} - \left.\frac{\partial q_j}{\partial t}\right|_{coll,ij} \tag{2.75}$$

See Appendix A.3 for the notation of the coefficients.

3. Idealised simulations

3.1. Introduction

In this chapter we show our first results of employing the ice modes microphysics scheme. We performed idealised simulations to investigate the ice formation pathways in a convective cloud. We will focus on the test of heterogeneous ice nucleation schemes and secondary ice mechanisms. This chapter also serves to evaluate the performance and biases the ice modes microphysics scheme by comparison to a reference simulation done with the standard SB scheme.

3.2. Model setup

Idealised simulations of a deep convective cloud were conducted with the ICON model (Heinze et al., 2017). The Weisman-Klemp setup (Weisman and Klemp, 1982) (WK82) is a suitable test environment to evaluate the ice mode scheme microphysics as all particle classes and associated model routines are active in the simulation and both mixed-phase and pure ice clouds, the latter mostly located in the anvil, are observed.
The vertical profiles of temperature and relative humidity are chosen following Weisman and Klemp (1982) to represent a typical sounding of a deep convection event with a maximum water vapor mixing ratio near the surface of $0.014\,\mathrm{kgkg^{-1}}$ and a surface temperature of 300 K. The horizontal wind u_z varies with altitude from 0 to $U_s = 5\,\mathrm{ms^{-1}}$

$$u_z = U_s \tanh z/z_s \tag{3.1}$$

with $z_s = 3\,\mathrm{km}$. Convection was initiated with a symmetric thermal perturbation of 1400 m vertical extent and 10 000 m diameter with an temperature amplitude of 2 K at the center, that decays to 0 K at the edge of the bubble.
The effective horizontal resolution of the unstructured triangular grid is 1.23 km with 128 vertical levels and a time step of 2 s. The simulation time for each experiment is 240 min.
Experiments with the ice modes scheme in several configurations were performed to evaluate the impact of different heterogeneous nucleation schemes on the distribution of the ice modes and the liquid origin vs in-situ formation pathway. HA, UL and PH label experiments using the nucleation schemes of Hande et al. (2015), Ullrich et al. (2017) and Phillips et al. (2008), respectively. The choice of parameters for the dust aerosol profiles are explained in Section 2.3.4. PH3 refers to a simulation with the Phillips et al. (2008) parametrisation including the soot and biological aerosol modes. The reference

Name	Experiment
HA	HA15 het. ice nucleation
UL	UL18 het. ice nucleation
PH	PH08 het. ice nucleation
PH3	PH08 het. ice nucleation with soot and bio mode
REF	reference simulation with original SB scheme
RS	rime splintering
P17-BR	collisional breakup with PH17
P17-BR_nogrp	same as P17-BR but excluding graupel collisions
P17-BR_noice	same as P17-BR but excluding cloud ice collisions
S18-BR	collisional breakup with SU18
S18-BR_noice	same as S18-BR but excluding cloud ice collisions
S18-BR_org	same as S18-BR but without size-depended scaling of F_{BR}
S18-BR_std_org	same as S18-BR_org but using the standard 2-MOM scheme
P18-DS	droplet fragmentation with PH18
P18-DSc	same as P18-DS but with cold model setup
S18-DS_const	droplet fragmentation with SU18 using constant F_{DF}
S18-DSc_const	same as S18-DS_const but with cold model setup
S18-DSc_poly	same as S18-DSc_const but using polynomial F_{DF}
S18-DSc_sig	same as S18-DSc_const but using sigmodal F_{DF}
P-ALL	using all the parametrisations from RS, P17-BR and P18-DS
S-ALL	using all the parametrisations from RS, S18-BR and S18-DS_const
NO-SEC	no secondary ice mechanisms active

Table 3.1.: List of sensitivity experiments for idealised simulations

simulation (REF) uses the standard SB scheme with the same microphysical parametrisations and assumptions employed as the ice mode microphysics scheme. Thus we can assess the ramifications of using multiple ice classes instead of a single one for the overall cloud evolution.
Table 3.1 lists more sensitivity experiments for different secondary ice parametrisations. PH17 and SU18 refer to the collisionial breakup parametrisations of Phillips et al. (2017b) and Sullivan et al. (2018a), respectively. The droplet fragmentation parametrisation PH18 is from Phillips et al. (2018) with the modifications described in Section 2.4.3. Note that SEC-ALL, P-ALL and NO-SEC specify simulations where all of the respective parametrisations are activated/disabled and are not just an aggregation of individual simulations. All simulations for the secondary ice sensitivities were made with an older ICON version. Thus they are some general differences in the evolution of the convective cloud compared to simulations focused on the heterogeneous ice nucleation schemes (HA, UL, PH, PH3 and REF). However, this part of the study focuses on qualitative results and comparison between the secondary ice mechanisms.

3.3. Ice modes simulation

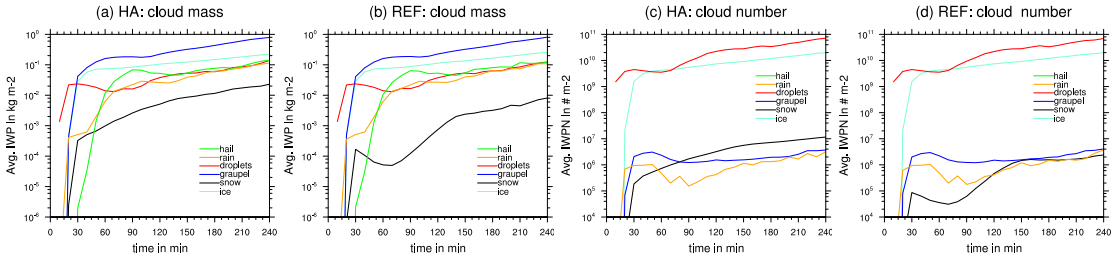

Figure 3.1.: Temporal evolution of the average ice water path for each hydrometeor class for (a) ice modes (HA) and (b) reference SB simulation (REF). Temporal evolution of average integrated number density for (c) HA and (d) REF. ICE is the sum of all ice modes for HA.

Figure 3.1 show the temporal evolution of the different hydrometeor classes as the average (Ice) Water Path (I)WP (a,b) and vertically integrated number densities (I)WPN (c,d) beneath the cloud system. Ice is displayed as the sum of all ice modes. Note that the output interval of the model is 10 min and we only display average Water Path values above $10^{-6}\,\mathrm{kg\,m^{-2}}$. Hence the plots only show the time where hydrometeor classes appear in an 'significant' amount.
First we look at the evolution of the ice modes simulation (HA) in Panel (a). Cloud droplets condense within the first 10 min of the simulation followed by the initiation of the warm rain process. Ice and graupel appear at the same time around 18 min and become quickly the two major contributors to the Water Path. Aggregation occurs shortly after. Strong riming is the last microphysical process to become active with hail first occurring at 30 min. At 60 min simulation time the cell matures. The average water path of each class remains slightly increasing and the cell shows no signs of dissipation within the simulation time. The ratio of the average water path between the classes also remain mostly the same with graupel followed by cloud ice being the dominate classes and hail, rain and cloud droplets showing mostly the same average values. Snow is the weakest hydrometeor class. The mass density of cloud particles is primarily governed by the availability of supersaturation and thus thermodynamics. The number density on the other hand is more varied since it directly depends on the particle formation pathway. Panel (c) in Figure 3.1 shows the average integrated number densities of all hydrometeor classes. We observe a large gap between droplets and ice to the other classes. Droplet numbers are tied to the CCN (cloud condensation nuclei) activation scheme of Hande et al. (2016), which depends mainly on upward vertical velocity and thus produces a large number of droplets in a strong convective case like the Weisman-Klemp setup. However, the scheme is still limited by the number of available CCN. We will discuss the connection between high ice and droplet number densities below.
Figure 3.2 (a) provides insight into the development of each ice mode as average IWP and IWPN. At the beginning, ice consists of frozen cloud droplets where both immersion

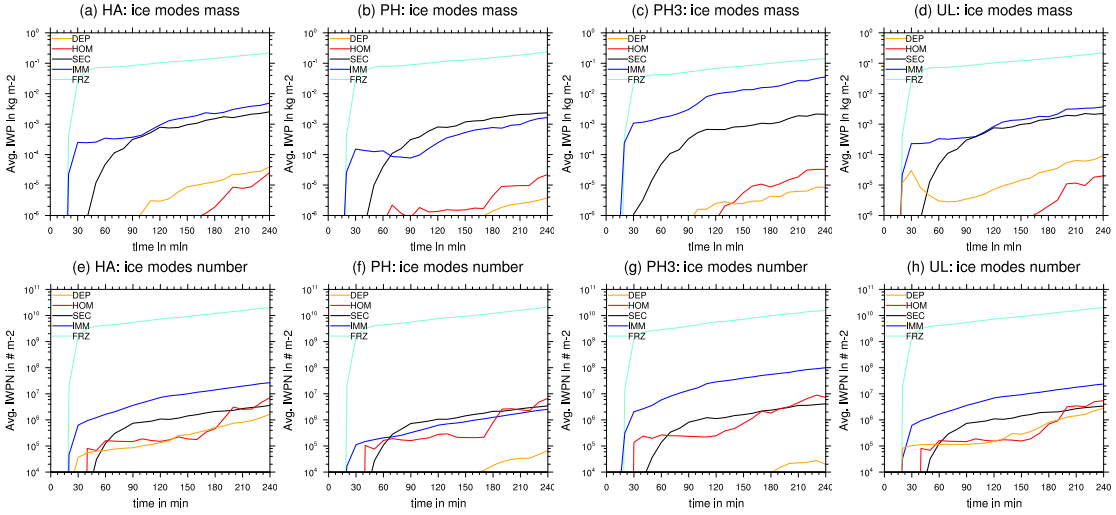

Figure 3.2.: Temporal evolution of the average (ice) water path for each ice for heterogeneous ice nucleation scheme (a) HA, (b) PH, (c) PH3 and (d) UL. Average integrated number density for each ice mode for e) HA, (f) PH, (g) PH3 and (h) UL.

and homogeneous freezing, represented by the IMM and FRZ mode, respectively, are important. The latter, however, becomes the most dominant ice mode by several orders of magnitude. Secondary ice from rime splintering (SEC) occurs with a 20 min offset to the first occurrence of graupel and becomes almost as important as immersion freezing. This is consistent with the findings of Miltenberger et al. (2020), who also performed simulations with the ice mode schemes for the same test case, but utilized lagrangian trajectory analysis to investigate rime splintering and spread of secondary ice through the cloud system. The first occurrence of secondary ice of significant number concentrations ($n_{sec} > 0.1\,\mathrm{L}^{-1}$) was observed after 30 min even for simulations of higher wind shear. They found that riming with graupel that sedimented from higher levels into the Hallett-Mossop temperature zone ($265 < T < 270\,\mathrm{K}$) to be the dominant source of secondary ice.

Ice from homogeneous (HOM) and deposition nucleation (DEP) occurs first from nucleation events in the overshoot starting at 30 min and 40 min for DEP and HOM, respectively. Both types of nucleation events occur multiple times during the simulation and the average IWP of both modes increases over time. The DEP mode is overall stronger in terms of average IWP although the HOM mode catches up. It is also to note while the average IWP of HOM and DEP is weak, their average IWPN is much closer to the other modes, especially secondary ice, as can be seen in Figure 3.2 Panel (e). In general all ice modes except for FRZ show more similar values (in terms of orders of magnitude) when comparing average IWPN than when comparing average IWP. The IWPN of FRZ dominates and thus the total ice number density is strongly tied to the high number of droplets that the CCN activation scheme produces.

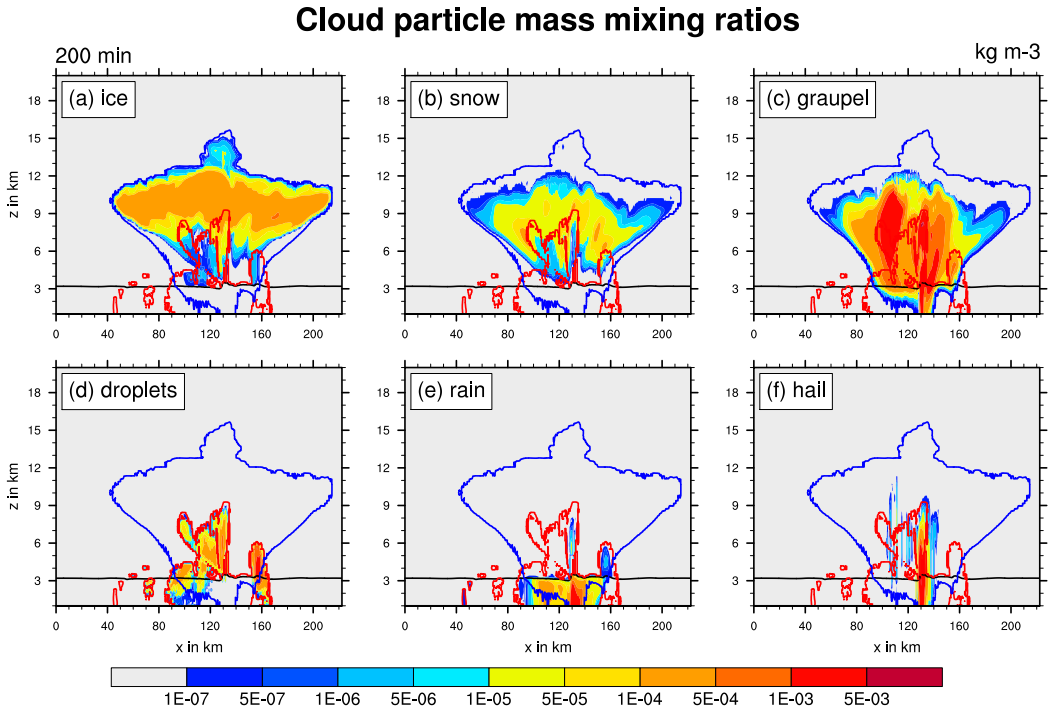

Figure 3.3.: Weisman-Klemp test at 200 min simulation time. Mass mixing ratios of (a) total ice, (b) snow, (c) graupel, (d) cloud droplets, (e) raindrops and (f) hail. The black line indicates the melting temperature level. The red and blue contour show the critical LWC and IWC value of 0.1 mg m^{-3}, respectively.

To investigate the vertical distribution of cloud particles Figure 3.3 shows a vertical slice of the cloud after 200 min simulation time and the mass densities of all hydrometeor classes, where ice is represented as the sum of all ice modes. The red and blue contours show the critical LWC and IWC value of 0.1 mg m^{-3}, respectively. The developed convective cell has an vertical extent of 15 km and developed an anvil. The storm produces heavy (rain) precipitation beneath the cell. Most of the cloud is glaciated with rimed particles, mainly graupel, being the most prevalent in terms of mass. Hail is mostly found in the narrow updraft core where riming rates and resident times are highest. Ice is present in most parts of the cloud above the melting temperature and forms an anvil of (pure) ice with an overshooting top. The mass content of snow depends on the mass density and number concentrations of ice. However, it is heavier than snow and has higher sedimentation rates. Thus snow is mostly located below the maximum ice mass density.
Figure 3.4 shows the same vertical slice as in Figure 3.3 but for the mass mixing ratio for each ice mode after 200 min simulation time. The lower part of the cloud is dominated by secondary ice from rime splintering (SEC) which coincides with the high mass mixing

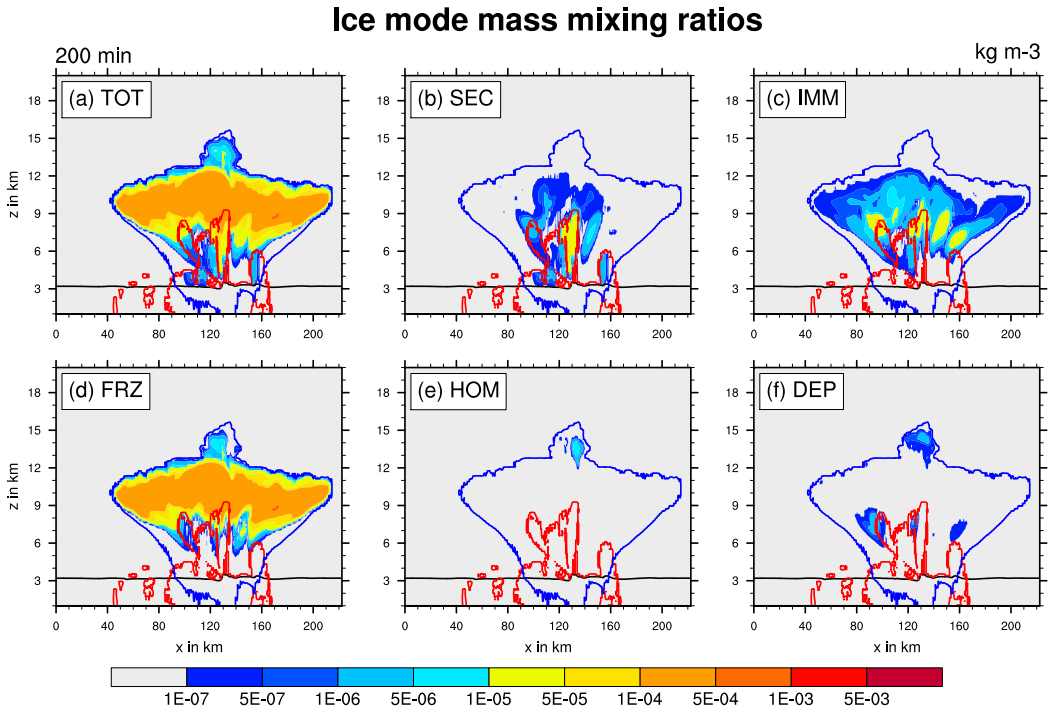

Figure 3.4.: Weisman-Klemp test at 200 min simulation time. Mass mixing ratios of (a) sum of all ice modes, (b) secondary ice, (c) heterogeneously frozen droplets, (d) homogeneously frozen droplets, (e) homogeneous nucleation and (f) deposition nucleation. The black line indicates the melting temperature level. The red and blue contours show the critical LWC and IWC value of 0.1 mg m^3, respectively.

ratios of graupel and hail that we observed in Figure 3.3. The prevalence of secondary ice from rime splintering in this region was also observed by Miltenberger et al. (2020). Ice in an altitude between 6 and 9 km is partially dominated by heterogeneously frozen droplets (IMM), while in the upper part of the cloud homogeneously frozen droplets (FRZ) are prevalent. When cloud droplets are transported upwards into colder regions they freeze first through immersion freezing due to the lower temperature threshold. Once all the INPs are activated, there is still a significant number of cloud droplets left or provided by the constant supply of humidity from convection. At this point homogeneous freezing begins to dominate over immersion freezing. Also, the ice mode schemes only shows the ice formation pathway of the ice observed at this time, it does not track sources and sinks individually. That means that ice from immersion freezing (IMM) could have been converted to snow by aggregation or lost in collisions with graupel and is for that reason not as prevalent as FRZ.
The part of the cloud consisting of ice from FRZ stays structurally mostly the same during the simulation run time, only widening as the anvil expands. However, the cloud

parts where IMM and SEC are present fluctuate with the evolution of the cell. SEC follows the liquid core where riming is occurring. IMM is at the beginning located above the liquid core between the sections were SEC and FRZ are prevalent and later mostly present in the flanks.
Ice from homogeneous nucleation (HOM) is limited to the overshoot, deposition nucleation (DEP) also occurs in small amounts outside the liquid core in the glaciated parts of the cloud between 6 and 9 km.
Overall we notice a mostly clear spatial separation of the ice modes with some overlapping areas where ice of different origin is found. Ice in the upper part of the cloud above 9 km is for the majority of liquid origin, hence consisting of frozen droplets, and stemming from rime splintering below that. This general spatial distribution of the ice modes is also true for the other sensitivity experiments.

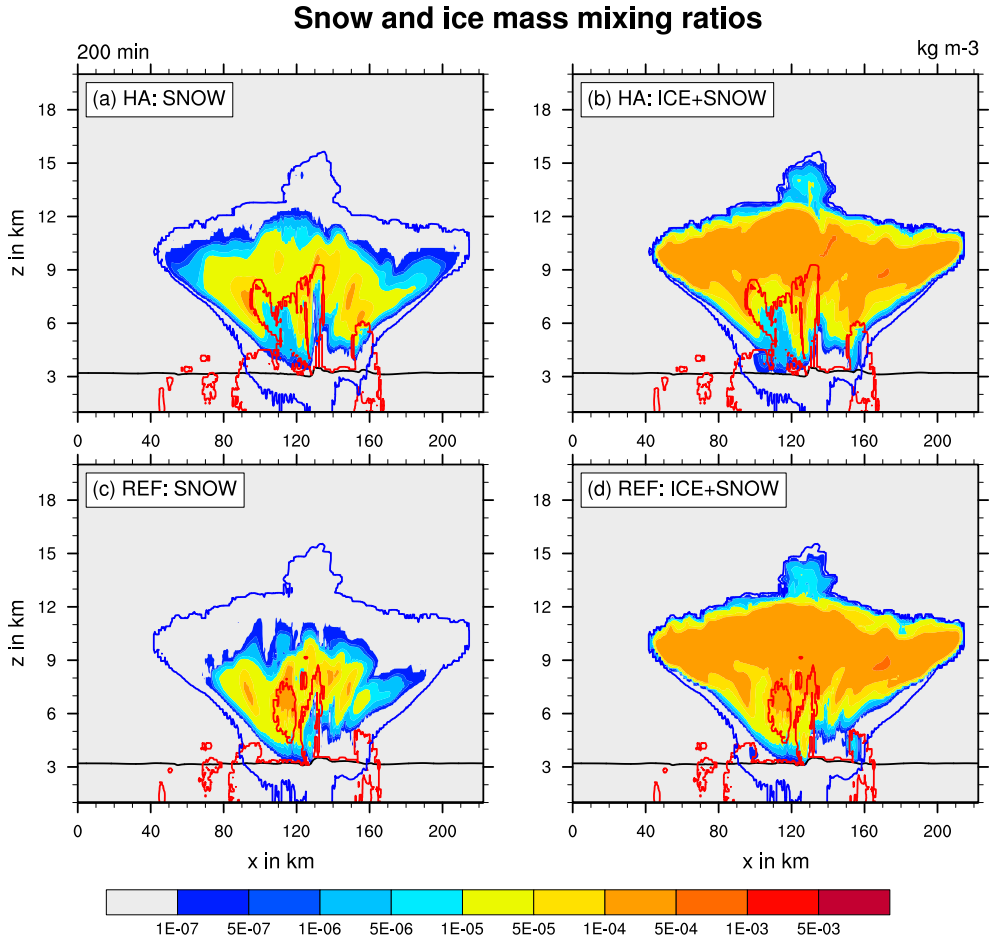

Figure 3.5.: Weisman-Klemp test at 200 min simulation time. Mass mixing ratios of snow for (a) ice modes scheme (HA) and (c) standard SB (REF) as well as the sum of all cloud ice and snow for (b) HA and (d) REF. The black line indicates the melting temperature level. The red and blue contour show the critical LWC and IWC value of 0.1 mg m^{-3}, respectively.

3.4. Comparison - reference simulation

The overall cloud evolution of the reference simulation (REF) is very close to the ice modes scheme. As we can see in Figure 3.1 (b) the evolution of hydrometeors directly related to the liquid phase, that is cloud droplets, rain, graupel and hail, show the same temporal evolution. Even the onset times for cloude ice, where the governing parametrisations of both schemes differ, are are mostly the same. We observe, however, a large difference in the average Water Path of snow which shows an increase of an order of magnitude for the simulation with the ice modes scheme (HA). Although the

difference decreases with time to a factor of ~ 2.5.
This also evident in the vertical slice of the convective cloud. Figure 3.5 shows the vertical slice of the convective cloud at 200 min for snow with (a) the ice modes simulation and (c) the reference simulation. There is significantly more snow present in the ice mode simulation than in the reference simulation. While the maximum snow mass density is still at $10^4\,\mathrm{kgm}^3$, snow is distributed over a wider area of the cloud especially towards the flanks. But comparing the sum of ice and snow for both simulations in panels (b) and (d) shows that there is in general no increase of combined ice particle mass. Rather we notice there is a tendency for the ice mode scheme to shift mass from the ice to the snow class, hence the aggregations rate have to be higher. This is linked to the conceptional differences between both schemes: the SB standard scheme only produces snow by self collection of a single cloud ice class, where in the ice mode schemes, there are five independent cloud ice classes. They not only aggregate snow by self collection, but also by collisions with each other. While the physics of self collection and ice mode - ice mode collision are the same, the increased number of collisions processes leads to higher aggregation rates.
While the shift of ice to snow should affect overall sedimentation rates of ice particles, there seems to be little impact on the cloud evolution and dynamics of the convective cell since the IWC and LWC outlines as well as the general evolution of the cloud observed in Figure 3.1 remains the same. It is also to note that pure ice and especially cirrus clouds will be mostly unaffected by that effect since collision efficiencies are small at low temperatures (see Section 2.5.3). Generally ice number concentrations are also insufficient to produce significant amounts of snow for pure ice clouds. Indeed, we will observe in later sections that snow is mostly insignificant in simulations of cirrus clouds even with the 'bias' of the ice modes scheme. Still we should keep this tendency towards higher snow content in mind when simulating deep convection clouds and consider to scale aggregation rates accordingly.

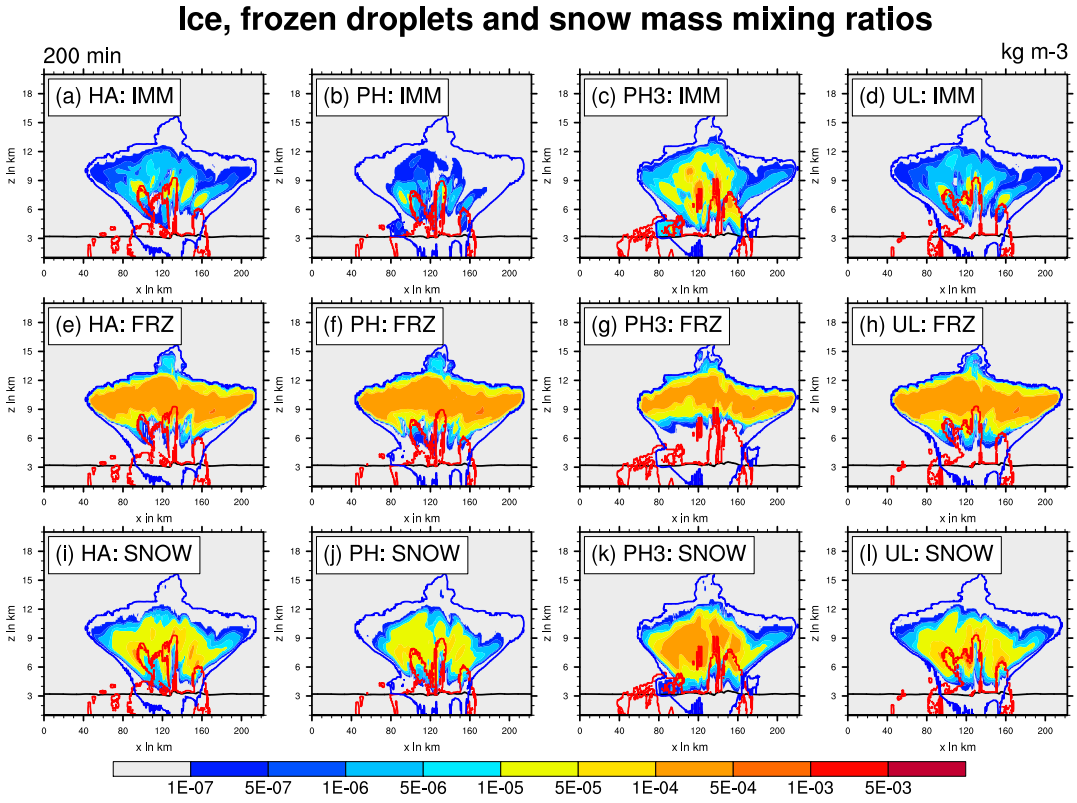

Figure 3.6.: Weisman-Klemp test at 200 min simulation time comparing the fractions of cloud ice stemming from IMM (a-d), FRZ (f-h) and for the experiments HA (a-d), PH (e-h) and UL (i-l). The black line indicates the melting temperature level. The red and blue contour show the critical LWC and IWC value of 0.1 mg m^{-3}, respectively.

3.5. Comparison - heterogeneous ice nucleation

Change of assumptions regarding distribution of INPs or a switch to a different INP activation scheme entirely can have a large impact on the evolution of the ice phase. We compared HA, PH, PH3 and UL. For the general evolution of average Cloud Water Path and Ice Water Path, we do not observe major differences. Hence we will discuss the general evolution of the convective cloud only briefly here. Since the same CCN activation is used for all runs we do not observe much change for the evolution of the liquid phase. The Rain Water Path is slightly lower for PH after the initial warm-rain formation, but catches up later. Hail formation starts sooner for PH but also reaches the same average value as HA. Further we observe a shift towards more snow and slightly less (total) ice for the PH simulation where in general all particle classes are much closer in terms of average Water Path. Thus the overall evolution of the convective clouds are similar.

We will now investigate the spatial and temporal distribution of the ice modes more closely. If we study the evolution of the ice modes average IWP in Figure 3.2 panels (a) to (d) we observe that FRZ and SEC stay mostly the same for all runs. SEC stems from rime splintering and thus depends on the evolution of the graupel and hail class, which again is sensitive to CCN activation and the resulting number of super-cooled droplets. We observed in Section 3.3 that SEC occupies a distinct part of the lower cloud around the updraft core. A change in heterogeneous nucleation scheme seems not to significantly affect the dominance of ice from rime splintering in this region or change the avg. IWP from secondary ice.

FRZ is strongly sensitive to the CCN activation scheme which remains unchanged between the simulations. A weaker IMM mode should affect FRZ since droplets that do not freeze by interacting with INP freeze homogeneously instead unless they are removed by evaporation or collision. Hence both modes are in direct competition for unfrozen cloud droplets. However, FRZ is overall so dominant in this case study, that this effect is not noticeable with regards to averaged mass content and number concentrations.

IMM is weaker in the simulation with the PH scheme both for average IWP and IWPN (Panel b and f), while it stays the same for HA and UL. The latter is not surprising since the assumptions about immersion freezing and the number concentrations of INPs are almost the same. In Section 2.3.4 we chose the dust concentration parameters for the PH parametrisation such that the maximum number of INPs activated for immersion freezing were the same as for the UL and HA schemes. The important difference of the PH to the HA and UL schemes is that immersion freezing occurs at higher temperatures (close to 263 instead of 258 K). Thus in lower and warmer parts of the cloud, where hydrometeor classes other than cloud ice are abundant, e.g. graupel. Collisions with those classes are an efficient sink for the IMM mode. Hence the average IWP and IWPN of IMM are smaller for PH compared to HA and UL.

For PH3 (Panel c and h) we observe higher average IWP of IMM than for all other simulations. Even though we stated in Section 2.3.4 that the maximum amount of active INP is lower with this scheme then for the others, the inclusion of soot and biological aerosols triggers immersion freezing at higher temperatures even close to the melting

temperature level $T_m = 273\,\mathrm{K}$. Where for the PH scheme with the dust only mode, the shift to higher activation temperatures lowered the IMM content, for PH3, with the soot and biological aerosol mode, IMM content is increased. Likely this even 'earlier' activation of INPs changes the cloud evolution such that the IMM mode becomes more important. Indeed, we will note that the cloud shape is different for PH3 when we later present a vertical slice of the cloud.
DEP is in generally weak in this convective case since deposition nucleation events only trigger outside mixed-phase clouds (see Section 2.3.4). In Figure 3.2 we observe different triggering times and strengths of deposition nucleation events. However, these differences are mostly caused by non-linear realisations of the model dynamics and not sensitive to the choice of nucleation scheme.
While DEP is not continuously persistent in the overshoot, there are smaller nucleation events being triggered in the anvil and the flanks of the convective cloud. Also note that output is written only every 10 min, hence not all nucleation events are sampled in the output data and ice from DEP and HOM could be removed by aggregation before they are sampled. When using the PH or PH3 scheme DEP is almost not present at all. This is consistent with our description of the scheme in Section 3.3, where even weak nucleation events are only triggered at high S_i compared to UL and HA. Consequently, the HOM mode is strengthened for PH since homogeneous nucleation events are not suppressed by pre-existing ice from DEP.
Figure 3.6 shows vertical slices of the cloud at 200 min. Plotted are the mass content of ice from immersion freezing (IMM) and homogeneously frozen droplets (FRZ) as well as snow for HA, PH, PH3 and UL (first, second, third and fourth column, respectively). As already discussed, FRZ dominates the upper part of the convective cloud for all heterogeneous nucleation schemes. The structure of vertically layered ice modes described in Section 3.3 holds true for all simulations. As immersion freezing is mostly the same for HA and UL the distribution of ice modes and snow shows only marginal differences between both experiments (first and fourth column).
For PH, however, we found that IMM is much weaker in terms of mass content (and number densities). That also limits its horizontal distribution, which is confined more towards the core of the cloud compared to HA and UL. This directly affects the snow class, which shows lower number densities and less spreading throughout the cloud. This underlines again, that IMM is important for aggregation because it produces ice crystals large enough for efficient collection kernels (see Section 2.5.3).
Using PH3 affects not only the IMM mode but also the overall structure of the cloud. As discussed above, PH3 favors immersion freezing and its biological and soot INP modes show an onset for higher temperatures compared to other heterogeneous ice schemes. We observe the result of INP activation at higher temperatures with a shift of ice mass towards the lower model levels. This can also be observed in the shape of the convective cloud. For example the PH3 cloud shows a lesser developed left flank. Additionally there is a pocket of IMM ice above the melting temperature line which is not present for HA and UL, for which immersion freezing is not possible in this temperature region. While the general structure and layering of ice modes is the same, the shape and location of liquid water zones change (as can be seen from the red LWC outlines) which has a direct

effect on the SEC mode that in general follows the liquid core (where riming occurs) closely. The PH3 simulation also sees an increase in snow underlining the importance of aggregation as a sink for the (in PH3 stronger) IMM mode.

3.6. Liquid origin vs in-situ formation

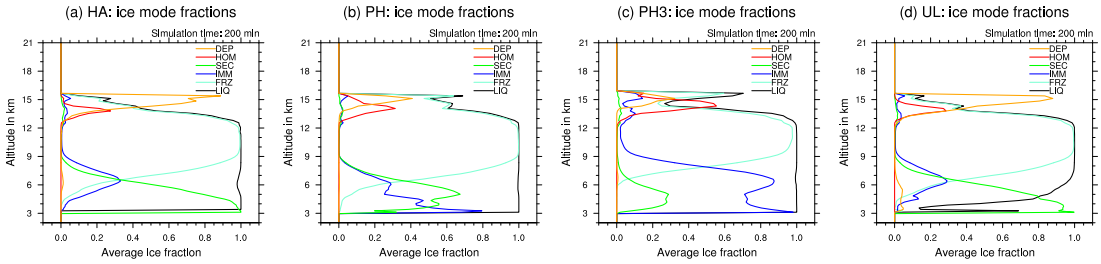

Figure 3.7.: Average liquid origin and ice mode fractions for (a) HA, (b) PH, (c) PH3, (d) UL.

Figure 3.7 shows the average mass fraction for all ice modes at 200 min simulations time. The mass fraction describes the ratio of ice from a particular mode x to the total cloud ice q_{tot} (sum of all ice modes)

$$f_x = \frac{q_x}{q_{tot}} \tag{3.2}$$

LIQ is the liquid origin fraction describing the ratio of cloud ice stemming from liquid origin formation processes

$$f_{liq} = \frac{q_{frz} + q_{imm}}{q_{frz} + q_{imm} + q_{hom} + q_{dep}} \tag{3.3}$$

where HOM and DEP contribute to in-situ formed cirrus and the FRZ and IMM to liquid origin cirrus. Secondary ice is excluded here.
The majority of the fully glaciated parts of the cloud above the secondary ice region between 6 and 12 km is dominated by IMM (for HA, PH and UL) or FRZ (for PH3) classifying the parts of (pure) ice cloud as liquid origin (hence LIQ is close to 1). This includes the anvil of the deep convective cloud. The overshoot is located above 12 km and the liquid origin fraction is determined by the amount of FRZ ice being mixed into this region and the strength of DEP nucleation events. PH and PH3 show a weak DEP mode with incursions from HOM resulting in liquid origin fractions between 0.3 and 0.7. For HA and UL the liquid origin fraction is below 0.4. This makes the overshoot a region where ice stemming from different formation pathways mixes. The dynamic forcing transporting FRZ and IMM ice into the overshoot, the occurrence and strength of HOM and DEP nucleation events and the sedimentation of newly formed ice from the overshoot into the cloud below all affect and change the liquid origin fraction. That the majority of the fully glaciated parts of the deep convection cloud are of liquid origin is in accordance with previous studies (Gasparini et al., 2018).

3.7. Secondary ice

3.7.1. Collisional breakup

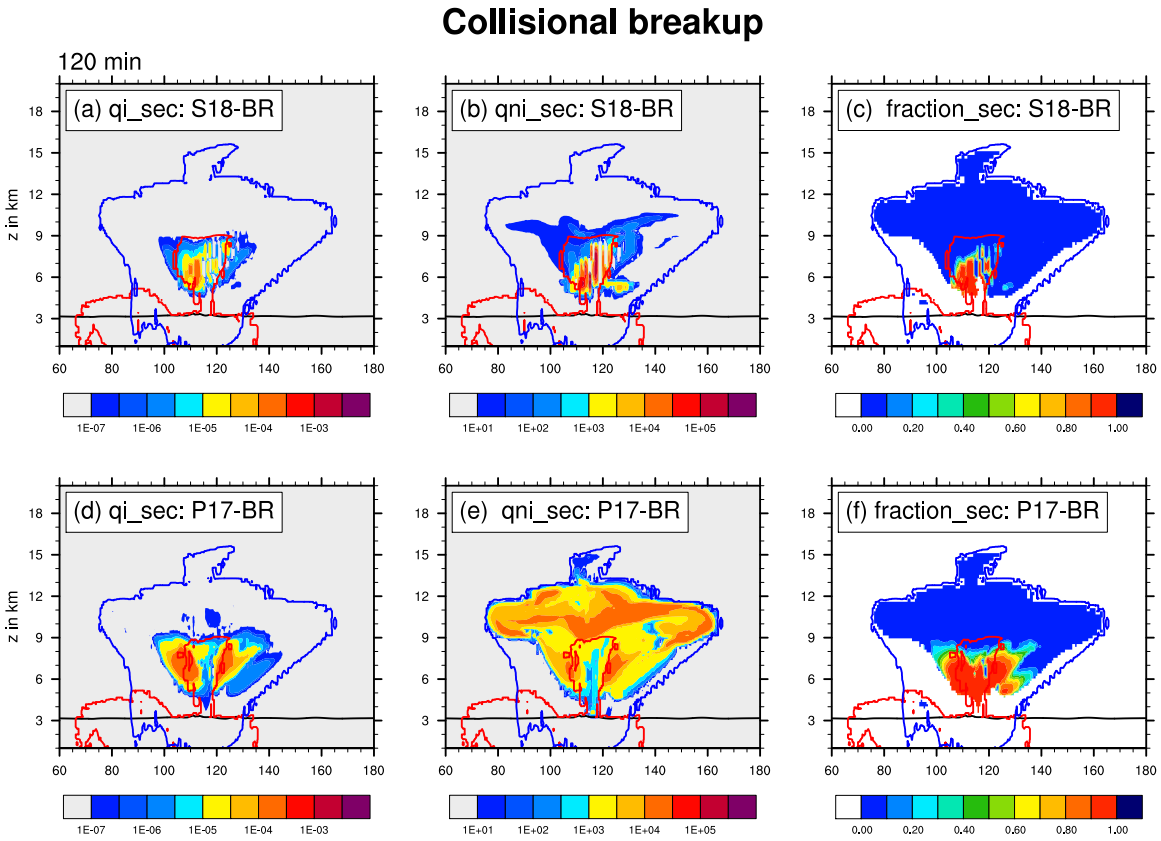

Figure 3.8.: Vertical slice of the convective cloud at 120 min simulation time for the P17-BR and S18-BR collisional breakup simulations. The panels show the mass and number density of secondary ice from collisional breakup as well as the secondary ice fraction f_{sec} for both simulations. The black line indicates the melting temperature level. The red and blue contour show the critical LWC and IWC value of 0.1 mg m^{-3}, respectively.

Figure 3.8 shows a vertical slice of SEC ice number and mass density from collisional breakup for both parametrisations. Panel (c) shows the SEC ice fraction, that is the ratio of SEC to the total cloud ice content cloud (here from collisional breakup) introduced in the previous section. For S18-BR, there is an area near the updraft core between 5 and 8 km that is dominated with a fraction of more than 90 % SEC ice. Panels (a) and (b) show the secondary ice content and number density reaching up to $5 \cdot 10^{-5}$ kgm^{-3} and 10^5 m^{-3}, respectively. The secondary ice distribution is concentrated on a small area and is not symmetrical distributed around the updraft core but instead favors the backside of the cell.

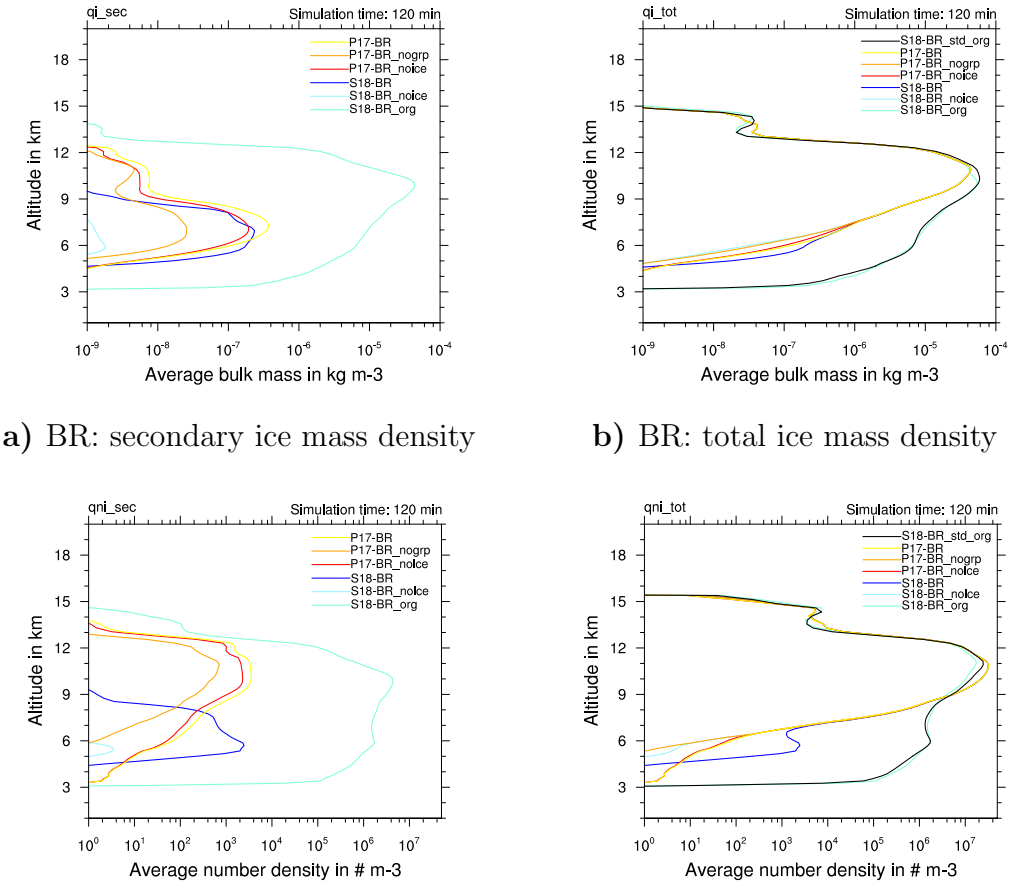

a) BR: secondary ice mass density

b) BR: total ice mass density

c) BR: secondary ice number density

d) BR: total ice number density

Figure 3.9.: Average mass and number density of secondary and total ice with collisional breakup at 120 min simulation time.

The P17-BR simulation on the other hand shows that secondary ice is located in a larger area between 5 and 10 km and distributed more evenly around the updraft core. Here the entire lower part of the cloud is dominated by secondary ice from breakup similar to the RS simulation. Overall there is more SEC ice within the entire cloud than in the S18-BR experiment. However, when comparing panels (b) and (e) we notice that P17-BR never reaches the high number densities of S18-BR but spreads a moderate number of small ice crystals ($< 50\,\mu m$) throughout the entire cloud. These will have little effect on the cloud evolution though since the upper cloud is dominated by ice formed from IMM, which has higher concentrations (compare Section 3.3). In general S18-BR shows a smaller production rate of secondary ice but the splinters grow to larger sizes than in P17-BR. This also means that they are more prone to be removed due to sedimentation into the melting layer and collision with other ice particles.

To test the sensitivity of both schemes to the collision type, we performed several sensitivity simulations where breakup of certain particle types is disabled. Figure 3.9 shows the secondary ice from collisional breakup ((a),(c)) and average ice mass and number densities of total ice, as the sum off all ice modes, ((b),(d)) at 120 min.
If we disable breakup between the collision of ice crystals in the PH17 scheme (P17-BR_noice) we notice a reduction of secondary ice mass density of factor of 2 and even less for the number density. This works as intended as ice crystals are in general to small to be the primary supplicant of secondary ice fragments. Disabling breakup in collisions including graupel however (P17-BR_nogrp) significantly lowers the mass and number density of SEC of up to an order of magnitude, deeming it to be the most important contributor of breakup ice fragments.
Disabling breakup in collisions with ice crystals has a large effect for the SU18 breakup scheme. Comparing the secondary ice densities between S18-BR and S18-BR_noice we notice an immense loss in secondary ice of two orders of magnitude. This strong sensitivity is concerning since, as we see for the PH17 simulations, ice crystals should not be the leading factor in secondary ice from breakup. This sensitivity is also emphasized when using the SU18 simulation without the scaling factors (S18-BR_org) as was originally formulated in Sullivan et al. (2018a). We see an enormous increase in secondary ice and even overall total ice resulting in unrealistic high contribution from BR. The problem is that the S18-BR parametrisation scales to strongly with the bulk collision numbers, which are high for cloud ice. Utilizing the scaling factors from Sotiropoulou et al. (2020) smooths the difference and make the results more consistent with the P17-BR simulations. However, this likely for the wrong reasons since the amount of SEC is is still very sensitive to the cloud ice class and not graupel.
The ice mode scheme introduces multiple ice classes and therefore also more collision routines. This leads to in increase in snow aggregation as was shown in Section 3.4. To test if this increase in ice collision rates is responsible for the high secondary ice density with the SU18 parameterisation, we performed a simulation using only the standard SB scheme in conjunction with the parameterisation (S18-BR_std_org). Since the SB scheme does not allow us to the identify the origin of ice we can only compare the total ice densities in panel (c) and (d). We note that if the original SU18 parameterisation is employed with the SB standard scheme total ice densities are even higher then in the ice modes scheme, hence the problem is enhanced. Thus we do not recommend the use of the SU18 parameterisation including collisions with the cloud ice class and without the scaling factors from Sotiropoulou et al. (2020) in the two-moment bulk scheme of Seifert and Beheng (2006) and derived microphysics schemes.

3.7.2. Droplet fragmentation

Frozen droplet fragmentation (DS) is only active for the rain class in areas below the freezing temperature point and not for cloud droplets, since those are usually too small to produce fragments. This has some important ramifications for the occurrence of secondary ice fragments from DS. The rain class is associated with high sedimentation rates and can quickly sediment out of the temperature zones, where droplet fragmentation is

effective. This is the reason why we barely observe any frozen droplet fragments with the standard WK82 setup. Either the liquid droplets are too small (cloud droplets) or they reside in regions above the temperature melting level ($T > T_f = 270\,\mathrm{K}$). To investigate droplet fragmentation, we would need a model setup with with a colder background temperature profile. In such a setup more raindrops could reside in temperature regions below T_f.

3.7.3. Comparison - secondary ice

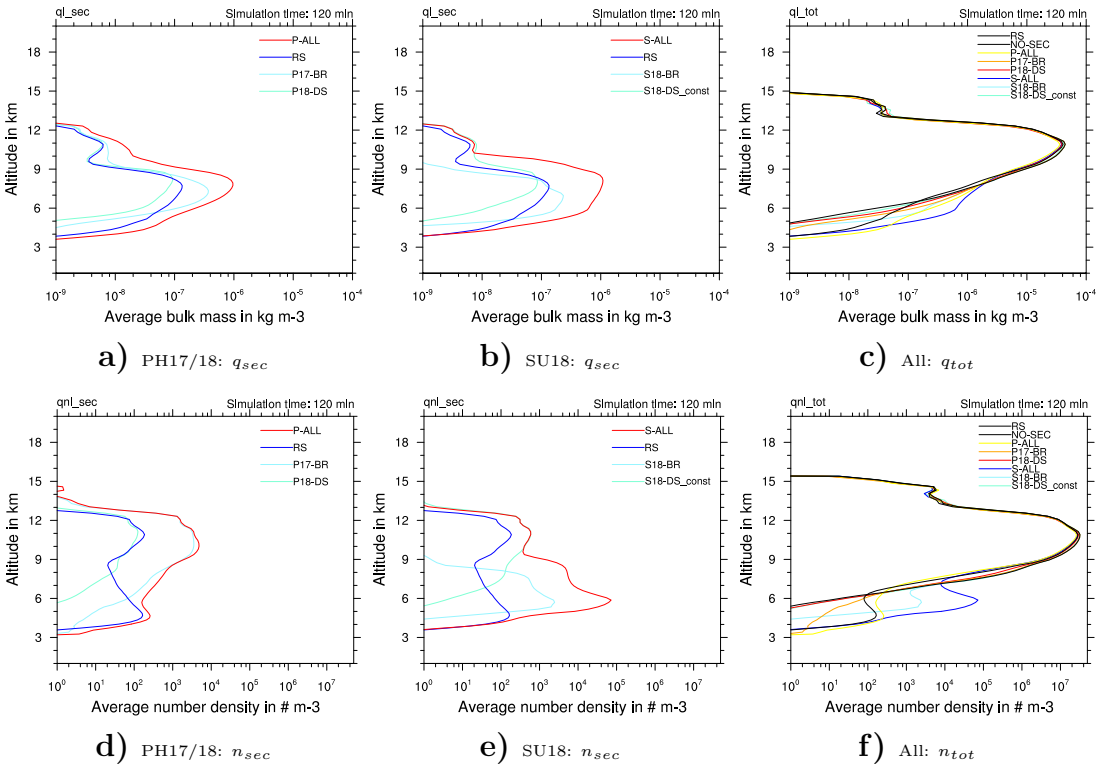

Figure 3.10.: Average mass and number density for all SEC ice sources and total cloud ice at 120 min simulation time.

Figure 3.10 shows an overview of all secondary ice mechanisms as vertical profiles of average cloud properties for simulation time 120 min. We compare two set of parametrisations. In panels (a) and (d) we show parametrisations of PH17/18 for collisionial breakup and droplet fragmentation. In panels (b) and (e) we show a set of SU18 parameterisations. Both include the profiles for RS and the simulations were all the respective parameterisations are active.
For the PH17/18 set (Panel (a) and (d)), breakup is the largest contributor to SEC ice both in terms of mass and number of fragments above 5.5 km. This layering is an effect of

the temperature dependency of rime splintering, which is only active down to 265K, and collisional breakup, which becomes efficient at temperatures below the Hallet-Mossop regime. Despite this difference in onset, SEC ice from both sources does mix. This also underlines the importance of transport process inside a convective cloud. However, the number density of SEC ice is still mainly determined by the secondary ice mechanism locally active. Only droplet fragmentation is too weak to be relevant under the thermodynamic conditions in the WK82 model setup.
We compare now the sets of SU18 and PH17/18 parameterisations. For the average ice mass density (Panels a and b) we see the same general vertical distribution of SEC ice with similar amplitudes. As discussed in section 3.7.1 there is a noticeable shift of collisionial breakup towards lower altitudes that is also reflected when all secondary ice processes active. Droplet fragmentation behaves similar with both parametreisations. However, for average number density (Panels d and e) we observe a larger shift. PH17/18 has a peak between 9 and 13 km and apart form the rime splintering zone the number density is always dominated by collisionial breakup. SU18 has its peak at 6 km with more than an order of magnitude higher SEC ice number densities than PH17/18. Droplet fragmentation actually becomes the dominant supplier for fragments in terms of number of density for altitudes above 10 km. However, we showed the S18-DS_const profile here which does not have a size dependence and is thus less realistic.
Figure 3.10 also shows simulations where all secondary ice mechanisms are active (P-All and S-ALL). We notice that the inclusions of droplet fragmentation and collisionial breakup not only increase the amount of secondary ice but also spreads it over broader and colder parts of the convective cloud. However, we have not discussed the importance of secondary ice with regards to the overall cloud ice content (q_{tot} and n_{tot}). Panels (e) and (f) show the total ice mass and number density for all secondary ice sensitivity studies as well as no secondary ice. We notice that the layer of cloud ice between 3 5 and 7 km are created by secondary ice mechanisms, esp. rime splintering, and do not exist for the NO-SEC run. Above 7 km the NO-SEC profile mostly encloses all the other runs, hence in those regions the total cloud ice content is very similar if no secondary ice mechanisms are enabled. In general secondary ice mechanisms to do not enhance primary ice nucleation but rather create ice crystals in thermodynamic conditions where primary ice nucleation is weak or not active at all.

3.8. Discussion and Summary

In this chapter we showed a first test of the ice modes microphysics scheme. Idealised simulations of an convective cloud, using the Weisman-Klemp setup, were performed to validate the model with an comparison to a reference simulation using the standard SB scheme. It was shown that the ice mode schemes reproduces the same cloud evolution for the dynamics and all particle classes except for snow, where we observed a shift of mass content from ice crystals to snow. This is linked to an increase of collision processes due to introduction of multiple ice classes.
We found that the scheme showed a reasonable distribution of the ice modes with liquid origin ice, formed of homogeneously and immersion frozen droplets, to constitute the majority of ice present in the matured cell. The occurrence of in-situ ice formed of homogeneous and deposition nucleation origin was, compared to other modes, low as it is expected for a convective cloud. Most in-situ ice modes were only present in the overshoot. But even there they mixed with liquid origin ice modes that were transported into the overshoot.
Simulations with four different heterogeneous nucleation parametrisations showed that the ice mode scheme provides the basis for a nuanced analysis to evaluate the impact of parametrisation choice not only on the total ice content and number concentrations but on the competition between ice particle formation pathways as well.
We showed results for several secondary ice mechanisms including rime splintering, collisionial breakup and frozen droplet fragmentation. The relevance of collisionial breakup was strongly depended on the type of colliding ice particles. The parametrisations of PH17 and SU18 also showed large differences, reflecting the uncertainties associated with this secondary ice mechanism. Droplet fragmentation was largely irrelevant due its dependency on low temperatures and the limitation that we only allow fragmentation of raindrops. In a further work we could introduce droplet fragmentation of cloud droplets, but this requires partial integration over the generalized gamma distribution of cloud droplet size.
In general we observed secondary ice mechanism to not really enhance the ice content in the parts of the convective clouds were primary ice formation is active. Rather secondary ice was relevant in thermodynamic regions where primary ice formation is insufficient. Thus it helped to expand cloud ice especially towards higher temperature levels mainly due to the inclusion of rime splintering.
In Section 2.4 we discussed that our understanding of the underlying physics for secondary ice mechanism is lacking. For most simulations in this work we will only employ RS as a secondary ice mechanisms since is the only one that is commonly included in bulk microphysics scheme and in the standard setup of the SB scheme. However, we should note that the importance and high number densities of secondary ice from RS in the lower parts of the cloud (below 7 km) are concerning since the underlying parametrisation of Hallett-Mossop could not be confirmed by recent laboratory studies (Seidel et al., 2024).

4. Liquid vs in-situ classification

4.1. Introduction

In this chapter we introduce the first case study to investigate ice formation in a Warm Conveyor Belt (WCB). We will discuss the composition of ice modes for both the mixed-phase clouds in the ascending WCB and pure ice clouds in the outflow. We are especially interested in the sensitivity of the formation pathway to trajectory ascent times. The cirrus origin classification of the ice modes scheme is compared to classification with the algorithm of Wernli et al. (2016). We evaluate, for both methods, if the cirrus properties, e.g. ice water content and ice number concentrations, along the classified segments fit into the range of observations for the respective cloud types.

4.2. Methods

For this case study we choose a cyclone that was observed during the NAWDEX campaign between the 3th and 6th October 2016 over the North Atlantic (Schäfler et al., 2018). The Icosahedral Nonhydrostatic Weather and Climate Model (ICON) 2.6 is employed in a limited area mode (Zängl et al., 2015) with the ice modes microphysics scheme.

4.2.1. Ice modes scheme

The microphysics scheme used is the ice mode schemes, which is a derivation of the standard 2-mom parametrisation in ICON (Seifert and Beheng, 2006) introduced in Chapter 2. The scheme includes the microphysical classes: cloud droplets, raindrops, snow, graupel and hail. Instead of a single cloud ice class we employ five, each with their distinct formation pathway:

- **HOM**: Homogeneous freezing of solution droplets n_{hom}, q_{hom}
- **FRZ**: Homogeneous freezing of cloud droplets n_{frz}, q_{frz}
- **IMM**: Immersion freezing of cloud and rain droplets n_{imm}, q_{imm}
- **DEP**: Deposition nucleation n_{dep}, q_{dep}
- **SEC**: Secondary ice n_{sec}, q_{sec}

The size distribution of each ice mode x is of the type of a generalized gamma distribution and has its own two prognostic moments, the number n_x and mass densities q_x. Apart from the formation process we assume the same shape, mass-diameter and fallspeed relations for each ice mode. They are also treated equally in advection, depositional growth and can collide with each particle class including itself and other ice

modes. Note that aggregation of any ice mode still contributes only to the same snow class.
Homogeneous freezing of solution droplets (HOM) is governed by the parametrisation of Kärcher and Lohmann (2002), which simulates an adiabatically ascending air parcel during a physics time-step. For homogeneous freezing of cloud droplets (FRZ) the fit of Cotton and Field (2002) is used. Immersion freezing of raindrops (IMM) follows the parametrisation of Bigg (1953).
Heterogeneous nucleation of ice contributes both to the IMM and DEP ice mode and is governed by the number concentration, size distribution and activation scheme of ice nucleating particles (INP). In this study we use the parametrisation of Hande et al. (2015) for dust events over Europe. A detailed description of the ice mode scheme as a whole can be found in Chapter 2. Rime splintering (Hallett-Mossop process) is the only secondary ice mechanism that contributes to the SEC mode in this chapter.

4.2.2. Validation

For validation against observations we compare our model output to the CLAAS-2 (CLoud property dAtAset using SEVIRI, Edition 2) products, in particular Cloud Water Path (CWP) and Cloud Optical Thickness (τ) (Benas et al., 2017), which are interpolated onto the model grid. The retrieval algorithm uses SEVIRI visible and near-infrared measurements to obtain the (total) cloud optical thickness τ and the effective radius of cloud particles (r_{ref}) at cloud top. The formulae of Stephens (1978) is being used to estimate LWP (Liquid Water Path) as well as IWP (Ice Water Path)

$$\mathrm{LWP} = \frac{2}{3}\rho_w r_{ref}\tau \qquad \mathrm{IWP} = \frac{2}{3}\rho_i r_{ref}\tau \qquad \mathrm{CWP} = \mathrm{LWP} + \mathrm{IWP} \tag{4.1}$$

with the cloud optical thickness τ, the effective radius r_{ref} and the liquid water and ice density, ρ_w and ρ_i, respectively. However, only a single value of r_{ref} is used to represent all ice crystals in the entire atmospheric column in CLAAS-2.
The ice mode schemes allows to estimate an effective radius for each hydrometeor class at each model level. On the other hand, optical thickness is estimated with the parametrisation of Fu and Liou (1993), which is simpler than the CLAAS-2 retrieval algorithms

$$\tau = dz\ \mathrm{IWC}\ (-0.291\,721 \cdot 10^{-4} + 2.519\,25/r_{ref}) \tag{4.2}$$

with the thickness of the cloud layer dz, the IWC and the effective radius r_{ref}. When comparing data derived from satellite measurements and simulated observations with the ice mode schemes we have to keep in mind that both use different microphysical assumptions.

4.2.3. Cirrus cloud origin classification

We follow the Krämer et al. (2016) approach of classifying cirrus cloud formation based on the formation process. Liquid origin cirrus forms from freezing droplets that were

transported along the WCB into the cirrus temperature region ($T < T_c = 235\,\mathrm{K}$). Thus it originates from liquid or mixed-phase clouds. Both the ice modes of homogeneous (FRZ) and immersion freezing (IMM) of cloud droplets and rain contribute to liquid origin cirrus. In-situ cirrus is formed directly as ice from the vapor phase onto the surface of ice nucleating particles (INPs). The homogeneous nucleation (HOM) and deposition nucleation (DEP) ice modes contribute to in-situ ice. We define the liquid origin fraction f_{liq} as the ratio of cloud ice content of liquid origin to the total cloud ice content

$$f_{liq} = \frac{q_{frz} + q_{imm}}{q_{frz} + q_{imm} + q_{hom} + q_{dep}} \tag{4.3}$$

Note that we did not include the SEC mode since secondary ice can not be directly associated with either in-situ or liquid origin formation pathway. However, the only secondary ice mechanism included in this simulation, rime splintering, is only active between 265 K and 270 K far below the cirrus temperature level.
Wernli et al. (2016) used a trajectory based categorization algorithm to determine the origin of cirrus clouds. Trajectories were started at all points where a cirrus cloud occurred. They followed the trajectory backwards until the IWC fell below $q_{crit} = 0.1\,\mathrm{mg\,kg^{-1}}$. If the analysed segment contained LWC larger than q_{crit} the cirrus cloud was classified as liquid origin and in-situ otherwise. The trajectories were further selected by applying the typical WCB criterion (see Section 4.2.5)
We adapted this classification scheme (W16 hereafter) with a modification to make it comparable to the liquid origin fraction: only total cloud ice content excluding secondary ice is considered for the IWC criteria. Additionally in this case study we investigate cloud segments of forward calculated WCB trajectories rather than calculating backward trajectories for each cirrus cloud.

4.2.4. Model setup

The ICON configuration follows largely Heinze et al. (2017) in a limited area mode. We use a R03B08 model grid with an effective horizontal resolution of 6.5 km and vertical discretization of 90 levels in a terrain-following coordinate system (SLEVE). The domain extends from 70° W to 50° E and 20° N to 80° N, respectively, thus including most of the Northern Atlantic and Europe. The physics time step is 40 s. Initialisation and boundary data is provided by ECMWF reanalysis data (Bechtold et al., 2008). The start date is the 4th October 2016. The simulation duration is 54 h including a 6 h initialisation phase. Model output is written every 30 min and interpolated from the the icosahedral model to a latitude-longitude grid (0.075°x0.075°).
We include most of the physics parameterisations commonly used in ICON: subgrid scale orographic drag, non-orographic gravity wave drag, vertical diffusion and transfer by turbulence, surface transfer scheme and a radiation transfer model in conjunction with a simple cloud cover parametrisation. Further discussions regarding these configuration can be found in Heinze et al. (2017). Deep convection is treated explicitly. However, we do not use a shallow convection scheme since the assumptions and implementation are not compatible with the ice modes microphysics scheme.

4.2.5. WCB trajectories

Trajectories are calculated offline using LAGRANTO (Sprenger and Wernli, 2015) to characterize the WCB flow in a Lagrangian framework. Trajectories belonging to the WCB are identified by two conditions (Joos and Wernli, 2012; Madonna et al., 2014). First they have to ascend at least 600 hPa in 48 hours. Second they need to start in or cross a cyclone. Cyclones are identified with a newly developed algorithm as two dimensional features in the surface pressure field based on the work of Wernli and Schwierz (2006) (see Appendix A.6).
Trajectories are started 6 h after model initialisation at 4th October 2016 06:00 UTC in a large box around the cyclone from 50°W to 20°W and 30°N to 65°N. One trajectory is started at each point on a 7.5 km equidistant grid and at five altitude levels from the surface up to 1 km.
After selecting trajectories according to WCB criteria we calculate the WCB area index marking the grid cell and model level where a WCB trajectory is present for each time step. This allows to investigate the evolution of (micro-)physical quantities both interpolated on the trajectories as well as in the gridded model data itself.
To characterize the flow and clouds above the WCB additional trajectories were started hourly in large area around the WCB from 50°W to 30°E and 32.5°N to 75°N in an altitude from approximately 7 km up to the tropopause and run backwards towards the start date. Using the WCB area index we selected all trajectories that passed above but did not intersect vertically with the WCB and stayed above 5 km at all times to filter out WCB trajectories.

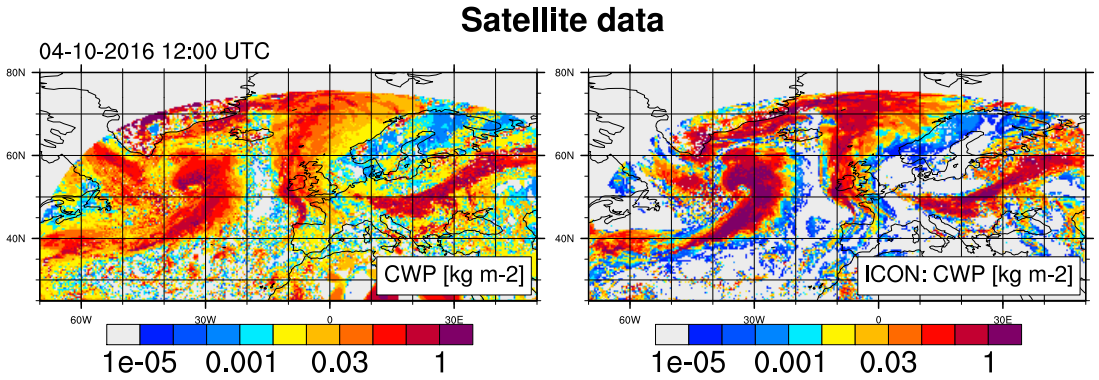

Figure 4.1.: Cloud Water Path (CWP) from CLAAS-2 and the ice modes scheme. Model values are masked when there was no observation available.

4.3. Case study

The surface cyclone began as a weak surface pressure depression at 2th October 2016 at approximately 45 °N and moved over the North Atlantic (Oertel et al., 2023). The cyclone intensified while moving north towards Greenland and showed strong warm and cold sectors with an accompanying WCB from the 4th to 6th October. WCB ascent lead to the development of a vast cloud band with a large cirrus outflow region above Scandinavia. For a detailed discussion regarding the dynamic development of the cyclone and the vertical structure of the associated WCB we refer to the study of Oertel et al. (2023).
Figure 4.1 shows total Cloud Water Path (CWP) for both CLAAS-2 and the ice modes scheme twelve hours after model initialisation at 4th October 12:00 UTC. At this point the cloud band from the WCB ascend was most pronounced (Oertel et al., 2023). While there are multiple small and scattered clouds likely originating from convection that are not present in the simulation, the main features of the cyclone as well as the WCB cloud fields are in good agreement. The model clouds tend to produce higher values of CWP, while the CLAAS-2 data shows a larger spread. Considering the error ranges and difference in physical assumptions of both simulation and observations, the data sets agree well for the WCB cloud band that we are interested in.

4.3.1. Trajectories

Figure 4.2 shows an overview of the LAGRANTO trajectories. We count 40 947 WCB trajectories starting south and east of the cyclone along the warm sector. The WCB air parcel ascend northward as a dense pack (Figure 4.1a). When reaching Greenland the WCB trajectories spread: the majority is deflected westward into an outflow region above Scandinavia, while the other trajectories circle back into the cyclone. High IWC up to $5 \cdot 10^{-3}$ kg/kg is encountered during the ascent phase (Figure 4.1b).

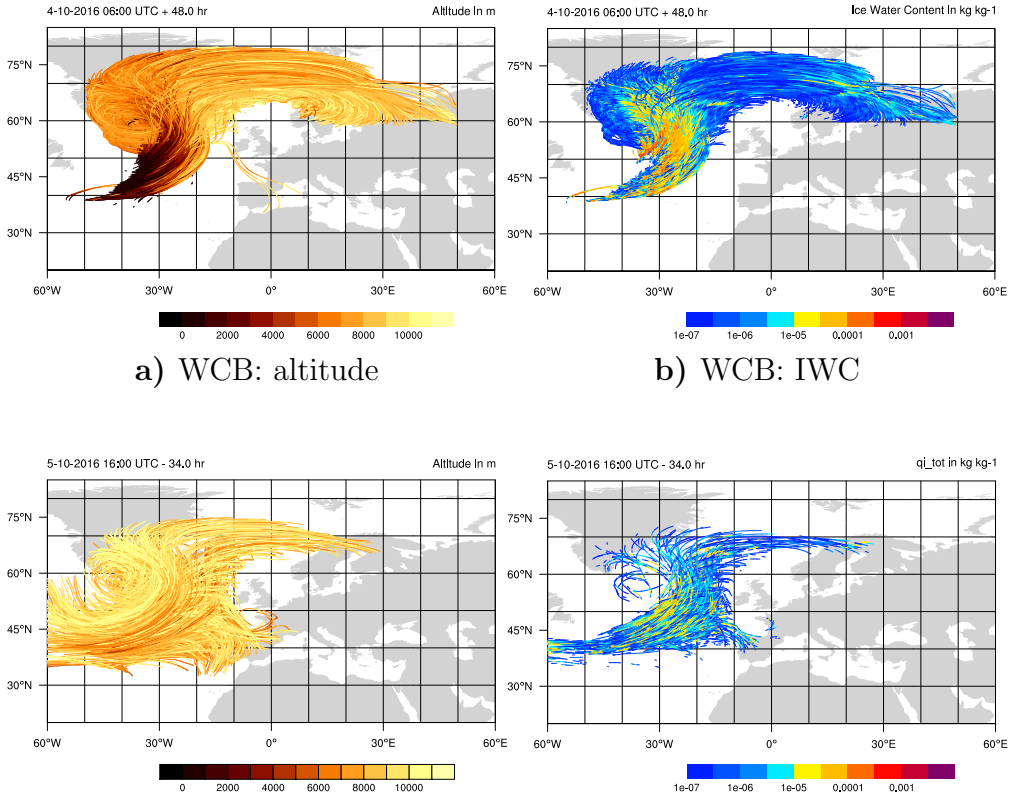

a) WCB: altitude **b)** WCB: IWC

c) Above WCB: altitude **d)** Above WCB: IWC

Figure 4.2.: WCB trajectories starting at 4th October 06:00 UTC (a,b) and backwards trajectories started above the WCB (c,d). Colored according to altitude (a,c) and IWC (b,d), respectively. Only 5 % of all trajectories are shown.

The hourly started backward trajectory files consist on average of 15000 trajectories. Figure 4.2c-d illustrate the air flow above the WCB exemplary for one start date. The air stream starts over the Northern Atlantic and follows the movement of the surface cyclone downstream. The majority of trajectories end above Greenland, where the cyclone stays stationary until its dissipation. A portion of the parcels follow in the WCB outflow region while some disperse early towards Spain. Many of the trajectories show high IWC especially while located above the WCB. This is a first indication that a significant amount of cloud ice is formed above the WCB and its sedimentation into the WCB could be important for the microphysical composition of the cloud band. As we will discuss in Section 4.3.4, the cloud ice stems mostly from the deposition nucleation (DEP). Overall the Lagrangian analysis compares qualitatively well to the case study characteristics described in Oertel et al. (2023).

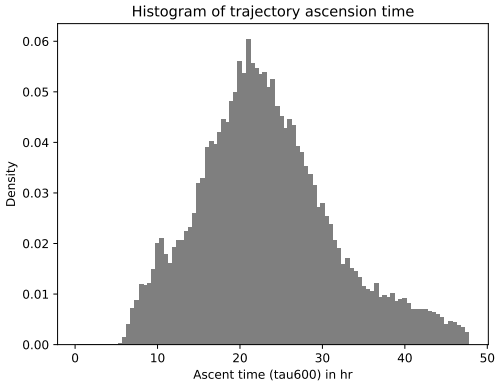

Figure 4.3.: Histogram of WCB (fastest) ascent time τ_{600}.

Figure 4.3 shows a histogram of WCB ascent times defined as the fastest time to complete the 600 hPa ascent (τ_{600}). Note that the histogram excludes trajectories that do not contain a cirrus cloud. Thus it is not a complete picture of the dynamical structure of the WCB.
The mean ascent time is 23.27 h, which is similar to ascent timescales reported in earlier studies (Rasp et al., 2016; Oertel et al., 2021; Oertel et al., 2023). The fastest 5 % of trajectories need 10.5 h or less to ascent and represent convective-like ascents. Forming the tail-end of the distribution are the 5 % slowest trajectories needing at least 31.5 h to ascent representing a slow, gradual ascent.
Oertel et al. (2023) classified trajectories into three subsets: fast ascent (< 18 h), slow ascent (> 30 h) and all times in between as intermediate ascent. This three categories showed different diabatic heating tendencies and varying relevance of different physical processes. In general fast ascent timescales featured stronger heating from liquid phase cloud processes (droplet activation, riming, freezing). Whereas for slow ascending WCB trajectories the deposition onto the ice phase was more pronounced. Since this study only uses offline calculated trajectories we are not able to resolve convection embedded on the gradual WCB ascent. However, Oertel et al. (2023) found that this case only shows a small fraction of embedded convection.

4.3.2. Ice modes

Figure 4.4 shows the bulk mass and number partitioning of mixed phase and cirrus clouds for different ascent times. The label signifies the upper limit of the ascent time bin. The values shown are the ratios an ice mode (or microphysics class) takes of the integrated mass (or number) budget for all trajectories within that bin for the specified cloud regime.
We investigate the distribution of mass between graupel, snow and (cloud) ice, where the latter includes all five ice modes. SEC refers to the secondary ice mode, IMM to the immersion freezing ice mode, FRZ to the homogeneous freezing ice mode, DEP to the

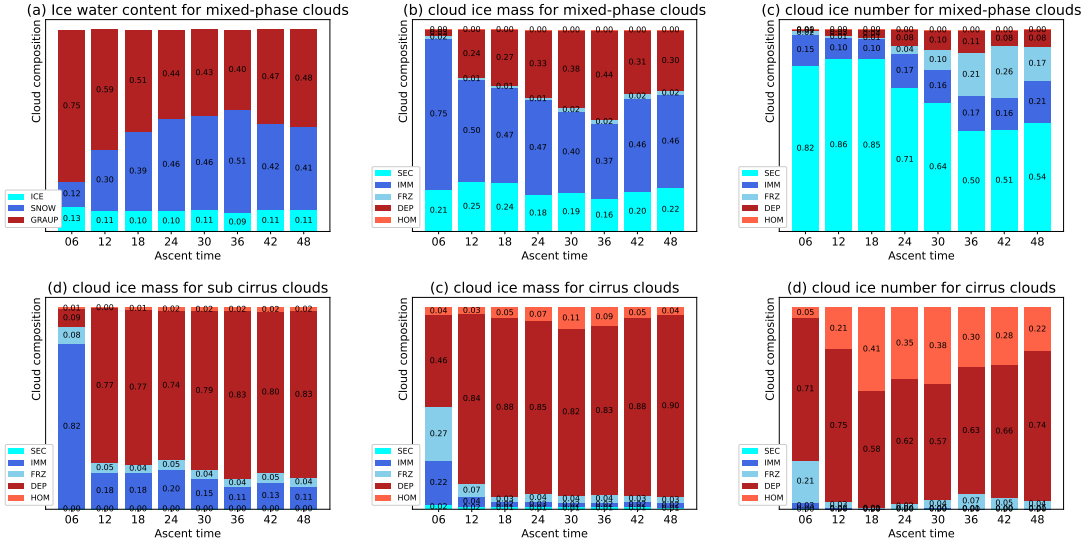

Figure 4.4.: Partitioning for ascent times of (a) ice water content, (b) ice mass and (c) and ice number in in mixed-phase clouds, respectively; (d) ice mass in sub cirrus clouds; (e) ice mass and (f) ice number in cirrus clouds.

deposition nucleation ice mode and HOM to the homogeneous nucleation ice mode.
While the focus of this study is on the microphysical composition of the cirrus outflow, it is still important to investigate the partitioning of the microphysical classes in the mixed-phase clouds of the ascending WCB. After all, the liquid origin pathway is determined by the transport of liquid or already frozen droplets into the cirrus temperature regime. We also included data for pure ice clouds below the cirrus temperature level. This is a cloud layer, where only ice is present but temperatures could in general allow the liquid phase to still coexist. It can be seen as a transition phase between mixed-phase and cirrus clouds. With this distinction we have categorization for all thermodynamic regimes where cloud ice appears.
Panel (a) shows that the majority of the ice particle mass in the ascending mixed phase clouds is concentrated in graupel and snow. The fast ascending trajectories ($\leq 18\,\mathrm{h}$) show a higher ratio of graupel. Oertel et al. (2023) also found that rapidly ascending WCB trajectories of this case study show prolonged residence times of ice particles and enhanced riming. On the other hand depositional growth of ice particles was more important for the slower ascending trajectories. Here, snow is shifted towards lower mass budget ratios for faster ascent times, likely because there is less time for aggregation too occur and snow gets lost in collisions with graupel. The higher graupel content can be explained by increased liquid water contents and enhanced riming in fast ascending trajectories.
Panel (b) and (c) show the ice mode statistics of mixed phase clouds for the mass and number budgets, respectively. As expected and consistent with our findings in Chapter 3 for mixed-phase clouds, frozen droplets (IMM and FRZ) provide the majority

of cloud ice mass in this regime. However, FRZ takes up only a small portion of the mass budget. The IMM and FRZ mode compete for available cloud droplets. However, immersion freezing (IMM) is more efficient and triggers at higher temperatures than homogeneous freezing (FRZ). In this case study there are enough INP available from the heterogeneous ice nucleation scheme to freeze cloud droplets by immersion freezing before they are advected into temperature zones where homogeneous freezing of cloud droplets becomes relevant. Trajectories that ascent within 6 h show the largest amount of IMM. However, the sample size is small with them only representing 0.001 % of all trajectories. In general, IMM ratios decreases for lower ascent times. This correlates with the increase in snow content, thus supporting our hypothesis from Chapter 3 that aggregation is a major sink for ice of the IMM mode.
Secondary ice takes up about 20 % of the mass and the majority of the number budget for all ascent times. Though the latter decreases for slower ascending trajectories. Secondary ice in this study is only provided by rime splintering ('Hallet-Mossop process'). Panel (a) already showed a high graupel content and implied that riming rates are large in this case study. However, recent reviews of secondary ice processes have determined that physical understanding of rime splintering is severely lacking (Korolev et al., 2020) and no rime splintering was observed in recent laboratory studies (Seidel et al., 2024). Thus the amount of rime splinters is likely overestimated. In the previous chapter we showed that secondary ice from rime splinters was the prevalent ice mode in the Hallet-Mossop temperature range ($265 < T < 270\,\mathrm{K}$) forming the lowermost layer of ice in a convectivly driven cloud. However, for this case study the dominance of secondary ice from rime splintering is largely irrelevant since the SEC mode does not reach the cirrus temperature regime.
A surprising finding of the mixed-phase cloud mass budget is the high ratio of ice stemming from DEP. Deposition nucleation can not occur within mixed-phase clouds. Hence this ice mode needs to sediment into the mixed-phase clouds from model levels above the WCB. We also notice that while the mass budget of DEP is high, the number budget (Panel (c)) is comparatively low. This indicates that the DEPs mean size is large, which consequently leads to high fall-speeds and sedimentation rates.
The HOM mode is not present within the mixed-phase clouds since homogeneous nucleation only occurs at high supersaturations wrt ice ($S_i > 1.35$) and low temperatures. That is outside the thermodynamic regimes of mixed-phase clouds. Although it is still possible for HOM to sediment into a mixed-phase clouds, the homogeneous nucleation events above the WCB are mostly suppressed by DEP nucleation as we will discuss later.
Panel (d) shows the cloud composition of pure ice clouds below the cirrus temperature level ('sub cirrus clouds') in the WCB. Comparing the ascent times shows a weak trend: DEP shows the highest contribution for the slower and frozen droplet modes (FRZ and IMM) for the faster ascent times. Only the few trajectories in the 6 h ascent time bin stand out with a high amount of IMM. In general FRZ is slightly more relevant compared to the mixed-phase cloud regime. In Chapter 3 we observed that for ascending clouds, FRZ can become more important than IMM as soon as the INP necessary for immersion freezing are depleted. While deposition nucleation is possible in this regime, its is likely that the mode is still influenced by sedimentation from clouds in higher model levels.

We even observe the first onset (or sedimentation) of homogeneous nucleation (HOM). Finally panel (e) and (f) show the composition of the cirrus clouds in the WCB outflow. We see the trends from the mixed phase and sub cirrus regimes continue: the cloud composition of fast ascending trajectories ($\leq 12\,\mathrm{h}$) are still influenced by ice of liquid origin (IMM + FRZ). Overall though all bins are dominated by ice formed through in-situ formation pathways (DEP + HOM). DEP and HOM are in direct competition for available supersaturation. Since deposition nucleation has an earlier onset (higher T, lower S_i) than homogeneous nucleation it triggers first, provided INP are available. DEP ice can then suppress further (homogeneous) nucleation events by depleting the supersaturation. In this case DEP dominates over HOM, especially with regard to the cloud ice mass budget. Intermediate ascent times (18 to 30 h) show a higher ratio of HOM than the faster or slower ascent time regimes. The parametrisation of homogeneous nucleation scales directly with the vertical upward velocity (Kärcher et al., 2006) and thus should be depended on the ascent time. However, more likely HOM is stemming from nucleation events above the WCB trajectories and thus not directly related to the ascent times.
Overall we observe the importance of DEP ice mode for all cloud regimes and ascent times. In-situ ice is thus the main constituent of the cirrus in the outflow. Fast ascending trajectories show stronger mixed-phase cloud processes (e.g. riming) and higher ratios of liquid origin ice in the resulting cirrus clouds. We will further investigate the liquid origin vs in-situ competition in Section 4.4.2.

4.3.3. Vertical cross-section along a sample trajectory

Figure 4.5 shows the ice modes mass content in a vertical cross section moving along a sample trajectory, which encounters all ice modes. Noteworthy are the fall streaks of sedimentating ice especially of the DEP mode. We also observe a strong presence of DEP ice above the trajectory. Overall we find a similar vertical layering of the ice modes as for the deep convection case in the previous chapter. SEC ice resides in the lowest mixed-phase cloud layer within and around the Hallet-Mossop temperature range in conjunction with the occurrence of graupel. Frozen (cloud) droplets primarily stemming from IMM form the ice phase in the cloud layer above. Following the cloud (evolution) further upward we encounter a layer of ice consisting of cloud droplets that froze homogeneously (FRZ). In general the FRZ mode is weaker for the WCB than for the deep convection case. For the latter we observed a higher concentration of cloud droplets that ware available for freezing, however, the profile of INPs (for immersion freezing) was still the same as in this study. Thus more cloud droplets froze homogeneously because all available INP were already activated. Then lastly we encounter a layer of DEP and HOM ice in the cirrus temperature regime. For the deep convection case this layer was weak and only relevant in the overshoot (see Section 3.3).

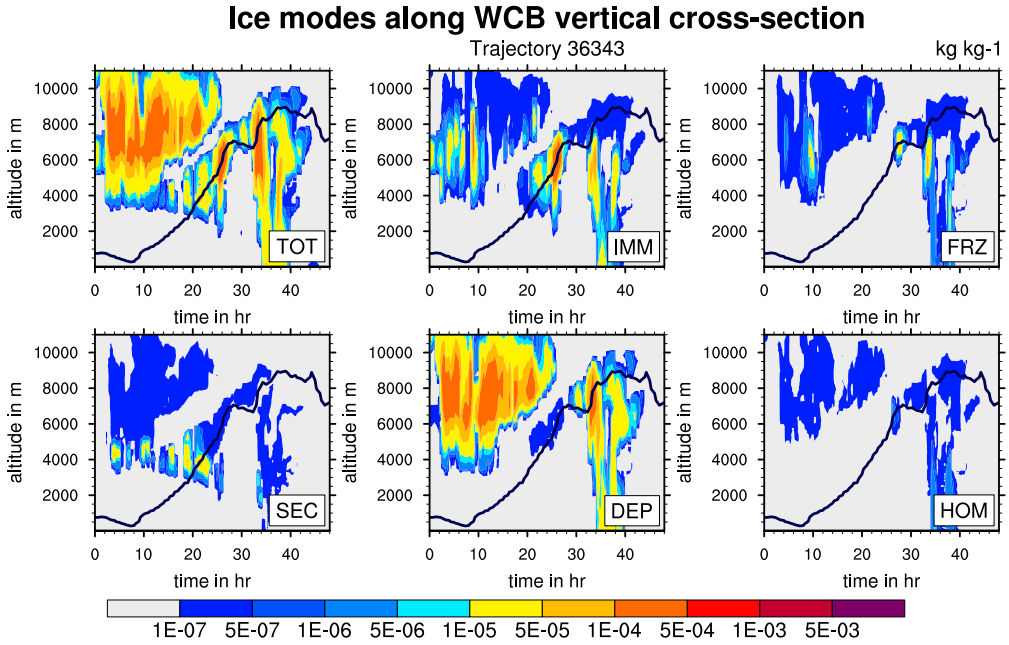

Figure 4.5.: Vertical cross-section of the WCB along a sample trajectory. Cloud ice mass content for the five ice modes as well as the sum of all ice modes (q_{tot})

4.3.4. Clouds above WCB

Figure 4.6 shows statistics characterizing the microphysical and thermodynamic properties of the air stream above the WCB. As introduced in Section 4.2.5 the backward trajectories from the WCB outflow region were chosen such that they cross at least one WCB trajectory horizontally but never intersect them. Additionally the have to stay at an altitude higher than 5 km. For the statistics we further only include data points that are above a WCB trajectory at that time step. As a surrogate coordinate for altitude we chose temperature as it is an important parameter for microphysical processes.
Ice from HOM and FRZ modes is mostly irrelevant for the clouds above the WCB. The IMM mode however is present at temperatures lower than 235 K. This suggest that some mixed-phase clouds are pushed upwards by the WCB and glaciate. Most prominent though is the DEP mode (Panel (a)). Comparing it to the total cloud ice content (Panel (e)) shows that the bulk of the cloud ice stems from DEP.
The median of upwards vertical velocity (Panel (h)) lies mostly between 0.6 and 0.8 cm s^{-1} with the 75th percentile being larger than 1 cm s^{-1}. This represents a slow updraft lower than the average upwards vertical velocity of the WCB trajectories (1.1 cm s^{-1}). Following Krämer et al. (2020) this slow updrafts should lead to cirrus with few but large ice crystals from heterogeneous nucleation. Panel (g) shows that most of the relative humidity wrt ice is between 100 and 110 %. This corresponds to a typical existence phase

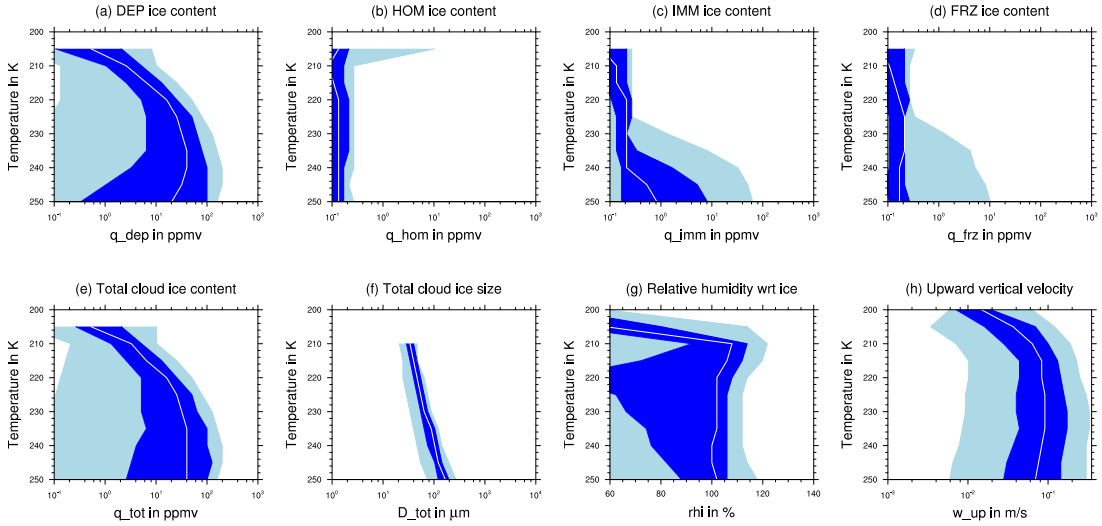

Figure 4.6.: Statistics of the ice modes q_{dep}, q_{hom}, q_{imm}, q_{frz}, the total cloud ice content q_{tot}, mean cloud ice size D_{tot}, relative humidity wrt ice and upward vertical velocity as a function of temperature. With the median as the white line, the 25th to 75th percentile are shaded in dark blue and the 5th to 95th percentile in light blue.

for cirrus, where ice crystals can slowly grow (Krämer et al., 2020). Its also a thermodynamic region where deposition nucleation of the heterogeneous ice scheme Hande et al., 2015 is active, but still far below the critical supersaturation needed for homogeneous nucleation (see Section 2.3.3).
Mean cloud ice diameter (D_{tot}) increases with decreasing altitude (increasing temperature). Hence larger ice crystals (mean size $> 100\,\mu m$) sediment from the regime suitable for deposition nucleation into the WCB below. The median of DEP ice content also increases until 240 K forming a bell-curve. Such a profile is typical for gravitational sorting of hydrometeors due to size depended sedimentation velocities (Wacker and Seifert, 2001). Overall this statistics show that DEP ice is present above the WCB showing high mean mass content and strong signatures associated with sedimentation.

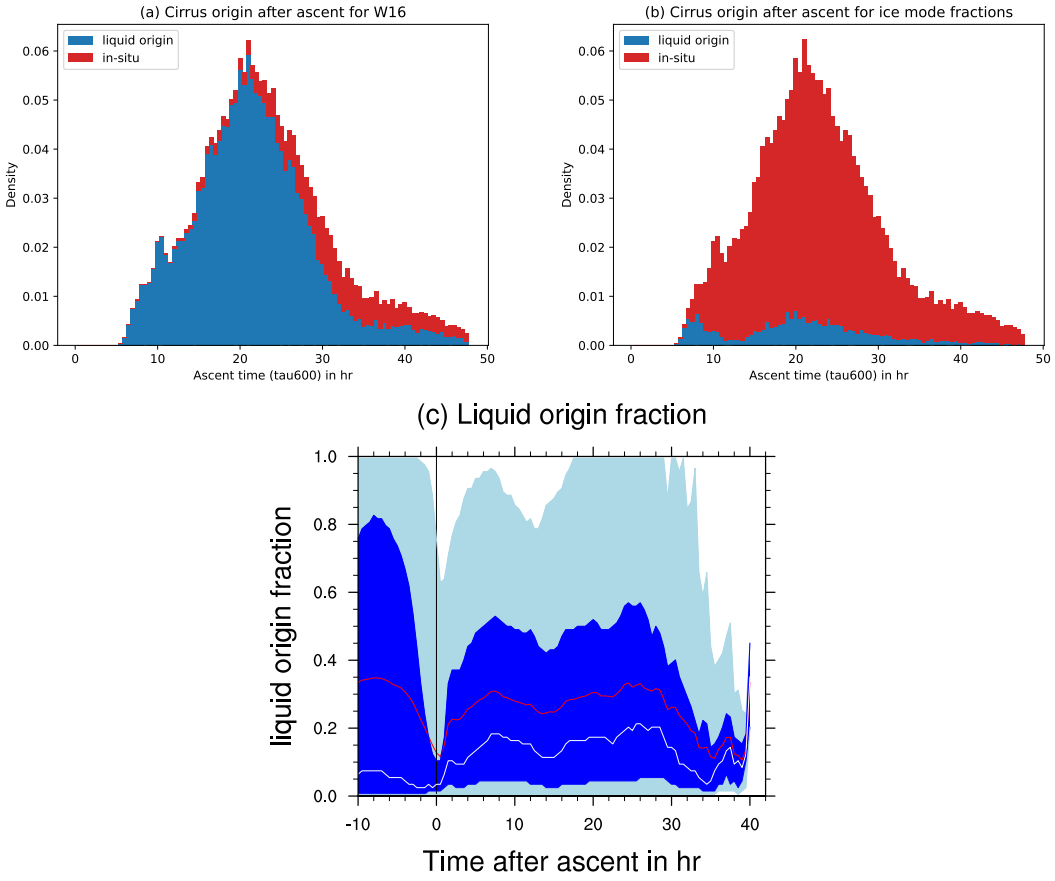

Figure 4.7.: Histogram of WCB (fastest) ascent times with identification of cirrus cloud origin for (a) W16 and (b) ice modes, respectively. Panel (c) shows the liquid origin fraction as a function of time after ascent with the mean in red, the median in white, the 25/75th percentile shaded in blue and 5/95th percentile in light blue.

4.4. In-situ vs liquid origin

Classification	Ascent		All	
	liquid origin	in-situ	liquid origin	in-situ
Ice modes	10 %	90 %	16 %	84 %
W16	84 %	16 %	64 %	36 %

Table 4.1.: Cirrus cloud composition following the ice modes and W16 classification. Ascent only includes the first type of cirrus encountered after WCB ascent (τ_{600}). All includes all points of the WCB trajectory where cirrus is present.

4.4.1. Cloud segments

Cloud segments are defined as intervals of the (forward) trajectory where total cloud ice content is continuously above the critical threshold q_{crit}. Wernli et al. (2016) found that the length of clouds segments in their analysis of ERA-Interim data varied from between 6 h to 5 days. However, we limit our analysis to WCB trajectories and only cloud segments, which are below cirrus temperature level T_c. As such the segments will be considerably shorter compared to Wernli et al. (2016).
64 % of all trajectories containing cirrus cloud ice featured more than one cloud segment. They are split between trajectories with more than one liquid origin segment (8 %) and more than one in-situ segment (33 %). A majority of trajectory (52 %) contained both in-situ and liquid origin segments.
The average length of cirrus cloud segments is 8.9 h. Of the 36 % trajectories that only contain a single continuous cloud the average length is high with 15.65 h. For trajectory with multiple cloud segments the average length is only 6.2 h. Since the cirrus cloud disappeared through sedimentation or evaporation, nucleation events or sedimentation of ice from above is necessary for another cloud segment to occur. This leads to overall shorter segments for this type of trajectories.
Liquid origin segments are in general double the length of in-situ segments (13 h vs 6 h). Trajectories containing in-situ and liquid origin segments are also show in general shorter with segments 6 h. This suggests that liquid origin cirrus persist longer then in-situ cirrus. However, the latter appear at later times in the trajectory and are often cut off. Letting trajectories run for more than 48 h might reveal that on average in-situ cloud segments would have a similar or even longer lifetime than liquid origin segments.

4.4.2. Comparison of cirrus classification

Figure 4.7 shows a histogram of WCB (fastest) ascent times τ_{600}. Colored are the first type of cirrus cloud encountered by the trajectory after fulfilling the 600 hPa ascent criterion. For W16 this corresponds to the classification of the cloud segment wherein τ_{600}

is fulfilled. For the ice modes schemes this corresponds to the liquid origin fraction f_{liq} at the time step where τ_{600} is fulfilled. $f_{liq} > 0.5$ is considered a liquid origin cloud and in-situ cloud otherwise. If there is no cirrus cloud present at ascent, but later on a cloud forms ($q_{tot} \geq q_{crit} = 0.1\,\mathrm{mg\,kg^{-1}}$), the cloud type is projected back to the original ascent time.

Panel (a) in Figure 4.7 shows that W16 identifies the majority (84 %) of WCB cloud segments at ascent (as a function of τ_{600}) as liquid origin. In-situ trajectories are mostly identified at high ascent times ($> 25\,\mathrm{h}$) and in the tail-end of the distribution. That shows that most liquid origin cloud segments survive, without q_{tot} dropping below q_{crit}, from the mixed-phase into the cirrus cloud regime.

Panel (b) shows the cirrus origin after ascent as determined by its microphysical composition obtained from the ice modes scheme. The fraction of liquid origin cirrus is very low with 10 % in stark contrast to the 84 % of the W16 algorithm. The few liquid origin trajectories are favoured among the fast ascent regime ($< 18\,\mathrm{h}$) but also appear in the intermediate ascent regime. This is consistent with our earlier findings in Section 4.3.2 that fast ascending trajectories show significant mixed-phase processes (esp. riming) and higher mass fractions of frozen droplets (IMM and FRZ). From W16 we determined that many cloud segments show a continuous cloud from the mixed-phase deep into the cirrus regime. However, as noted in Section 4.3.4, DEP ice is sedimentating from clouds above into the WCB. This makes DEP the predominant ice mode leading to an in-situ classification.

So far we have only considered the liquid origin and in-situ classification of the cloud segment directly after fulfilling the (fastest) ascent criterion. Table 4.1 shows the classification including all cloud segemtns where cirrus clouds are present in the WCB trajectories. The ice modes classification only differs slightly with an 6 % shift from liquid origin to in-situ cirrus. Hence ice from DEP and HOM mode dominate the cirrus composition during (almost) all times. W16 sees an increase of 20 % in-situ cirrus as it also considers the transition from liquid origin to in-situ segments. Still there remains a large 'disagreement' with the ice modes scheme.

In Section 4.2.3 we introduced the liquid origin (mass) fraction f_{liq}, that states to which degree a (cirrus) cloud is made from ice stemming of in-situ or liquid origin formation processes. Where a liquid origin fraction close to 1 classifies the cirrus as liquid-origin and close to 0 as in-situ. Panel (c) in Figure 4.7 shows the statistical distribution of the cirrus liquid origin fraction of clouds as a function of time before and after ascent. Before ascent (black line) most of the trajectories are dominated by in-situ formed ice (median close to 0.). However, the 75h percentile extends up to 0.8, hence there are also a lot of WCB trajectories where cloud ice of liquid origin is important. The liquid origin fraction rapidly drops at ascent ($t = 0$), where the distribution is very narrow. Liquid origin ice has likely sedimented out of the trajectory at this point and in-situ ice formation processes within or above the WCB dominate the microphysical composition of the cirrus cloud. This also agrees with the results from Panel (b) which also show the dominance of in-situ formed ice at the time of ascent.

We observe that almost none of the WCB trajectories reach liquid origin fractions close to 1 after ascent. However, the liquid origin in general increases. For the majority of

the time mean liquid origin fraction (red line) varies around 0.3. After the initial liquid origin phase the median (white line) is even lower with a maximum of 0.2. Both, the 25th and 5th percentiles, shaded in blue and light blue, receptively, are also close to 0. Hence majority of the cirrus outflow remains clearly dominated by ice stemming from the in-situ formation pathway. This tendency to was already apparent in Section 4.3.2 when we noticed that for (almost) all ascent times the majority of the cirrus cloud ice stems from the DEP mode.
However, we encounter regions of mixed origin with liquid origin fractions up to 0.45 in the 75th percentile. These regions often represent very thin cirrus where only a small amount ($0.1 < q_{tot} < 1\,\mathrm{mg\,kg^{-1}}$) of cloud ice remains. A likely explanation is that liquid origin ice from convection is transported into the upper troposphere and mixes with cloud ice in the WCB trajectories. The mixing might occur due to sedimentation or turbulent mixing.
In summary the trajectory based algorithm W16 and the ice modes schemes do not agree in its classification. However, we also have to consider the definition of in-situ and liquid origin. In this work the liquid origin fraction is determined entirely by the formation mechanism of the ice particle. It might be that the microphysical processes encountered by the trajectory are actually more important, which would is only indirectly linked to ice particle formation mechanism itself. If the trajectory passed trough a mixed-phased clouds it was thus subject to riming, aggregation and strong depositional growth (Wernli et al., 2016), which might lead to higher IWC and larger ice particles than for cirrus clouds that only experience the thermodynamic environment of the upper troposphere. In that case the W16 trajectory based algorithm is useful in determining which cirrus clouds recently experienced mixed-phase cloud processes.

4.4.3. Statistics along in-situ and liquid origin

We will now investigate the microphysical properties of cirrus along the formation pathways determined by both W16 and the ice modes classification and check if we observe typical values of these cloud types. Figure 4.8 shows statistics of the total ice content, the total ice number concentration and the liquid origin fraction as a function of time after ascent for segments of W16 liquid origin (a,e,i), ice modes liquid origin (b,f,j), W16 in-situ (c,g,k) and ice modes in-situ (d,h,l), respectively. The ice modes (IM) segments are classified as liquid origin if the f_{liq} is greater than 0.5 and as in-situ otherwise.
The total cloud ice content q_{tot} for the W16 liquid origin segments shows a peak $-5\,\mathrm{h}$ before ascent is completed. At it is peak the median q_{tot} is at 20 ppmv which is within the expected range for liquid origin cirrus (Krämer et al., 2020). The ice content quickly falls off below 10 ppmv after the ascent. However, it shows a broad distribution with the 25th to 75th percentile extending over two orders of magnitude. Overall q_{tot} is decreasing with time. In Panel (e) we note that the mean ice number concentration n_{tot} is with $0.02\,\mathrm{cm^{-3}}$ below expected values for (idealized) liquid origin cirrus ($0.05 - 2\,\mathrm{cm^{-3}}$) (Krämer et al., 2020). n_{tot} does not show the sharp decrease after ascent as q_{tot}. As we discussed in Section 4.4.1 W16 classifies most clouds segments as liquid origin. Panel (i) shows the liquid origin fraction f_{liq} along the liquid origin segments of W16 is low

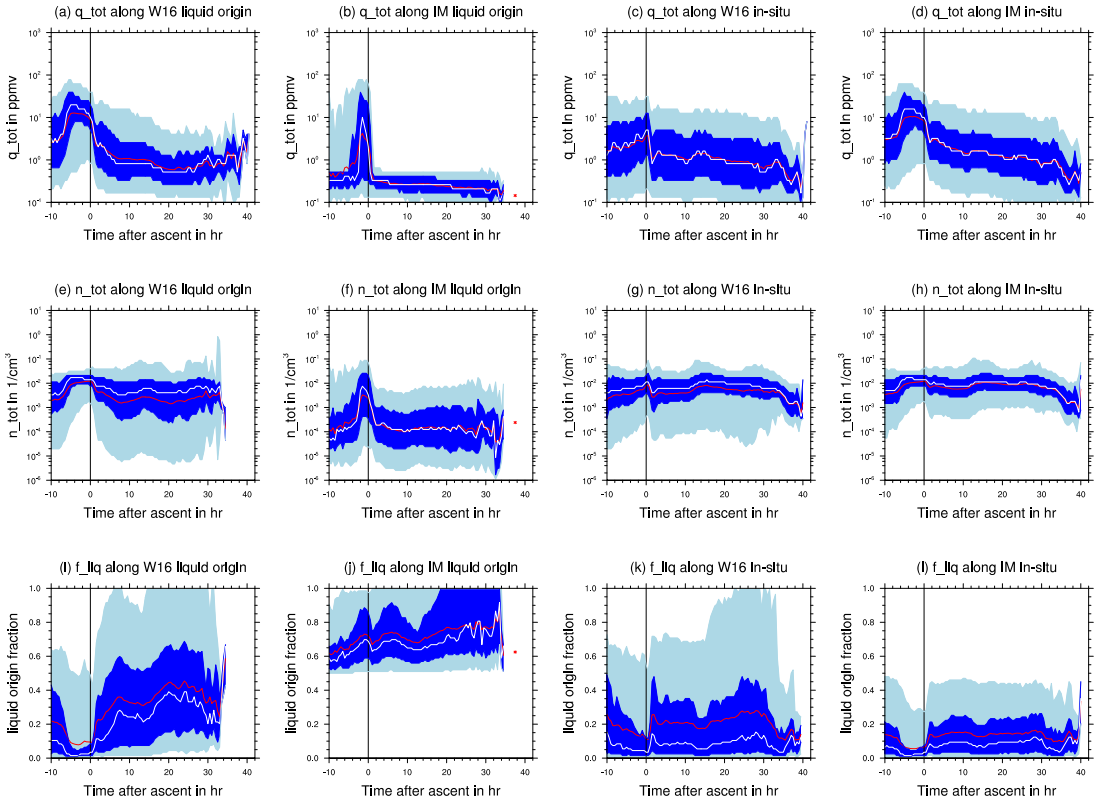

Figure 4.8.: Statistics of total ice content, total ice number density and liquid origin fraction along liquid origin and in-situ sections of W16 and ice modes . Median as the white line, the 25th to 75th percentile in dark blue and the 5th to 95th percentile in light blue. Red represents the mean.

between −6 and 0 h. This correlates with the the peak of q_{tot} in Panel (a). Hence where the WCB trajectory carries a signature of liquid origin cirrus properties, the ice actually stems from in-situ formation processes. Now the question remains if this in-situ formed ice was subject to processes of mixed-phase cloud and thus carries the signature of liquid origin cirrus. After ascent f_{liq} increases again, showing regions of mixed origin as discussed in Section 4.4.2. The as liquid origin classified segments are affected by sedimentation of liquid origin ice out of and insertion of in-situ ice into the segments due to subsequent nucleation or sedimentation from above.
For the IM classification the total ice content of liquid origin cirrus (Panel (b)) starts at slightly lower values as W16 at around 10 ppmv. However, mean q_{tot} falls more rapidly below 1 ppmv and remains two orders of magnitude below the start value for the entirety of the trajectories lifetime in the outflow. This also underlines the observation of the ice modes scheme from the last section, that liquid origin cirrus is very thin for this case study. n_{tot} (Panel (f)) peaks at similar values than the W16 liquid origin segments (compare Panel (e)) and is such still at the lower end of ice number concentrations as expected from observations Krämer et al. (2020). Like q_{tot}, n_{tot} decreases rapidly, but shows a broader distribution after ascent. Panel (j) shows f_{liq} along IM liquid origin segments. By construction all f_{liq} values are above 0.5 for IM liquid origin classified segments. However, as can be seen at the median (white line) at least 50 % of these segments show mixing with in-situ formed ice ($f_{liq} < 0.6$).
Panels (c,g,k) characterise the cirrus cloud properties along W16 in-situ segments. q_{tot} (Panel (c)) varies mostly (25th to 75h percentile) from 0.04 to 8 ppmv with a significant decrease after ascent. The peak of q_{tot} is located at ascent rather than before it as it was the case for the liquid origin segments. Median of n_{tot} (Panel (g)) shows mostly the same values as for the W16 liquid origin segments and its range stays fairly constant. The mean of n_{tot} is in the range expected for slow updraft cirrus and below the median of ice crystal number concentrations (Krämer et al., 2020). Panel (k) shows that most as W16 in-situ classified segments contain ice that stems from in-situ ice formation processes. Again we notice that before the ascent f_{liq} is at a minimum. With increasing time in the outflow, more liquid origin ice mixes into the in-situ segments.
Lastly panels (d,h,l) show the cirrus cloud properties along those segments, which are classified as in-situ with the ice modes scheme. q_{tot} (Panel (d)) starts with a liquid origin signatures close to 10 ppmv. The peak occurs again 4 to 6 h before ascent and shows a signature of high IWC as expected from liquid origin cirrus (Krämer et al., 2020). After ascent, q_{tot} shows in general higher values for IM in-situ than for W16 in-situ segments. However, q_{tot} decreases with time as the cirrus outflow ages and dissipates by sedimentation and evaporation. Actually the profile of q_{tot} for IM in-situ is close the profiles of W16 liquid origin segments. This is due to the effect, that W16 classifies the large majority of cloud segments as liquid origin where as IM classifies the majority as in-situ based on their origin (see Section 4.4.2). Hence there is a large overlap between both samples. n_{tot} though stays consistent within a narrow band centered at 0.01 cm^{-3} before and after ascent. This ice number concentrations expected for slow-updraft in-situ cirrus from observations and idealized scenarios Krämer et al. (2020). f_{liq} is by construction below 0.5 and stays for the majority of the IM in-situ segments between 0 and 0.2. Thus

it shows little to no mixing with liquid origin classified ice.
Overall both W16 and the ice modes scheme capture the initial occurrence and IWC signals as expected of liquid origin cirrus. However, this signal occurs before the WCB trajectories complete their ascent (determined by the 600 hPa ascend criterion). W16 continues to identify most trajectories as liquid origin after ascent despite them neither showing typical liquid origin properties nor them being primarily composed of ice stemming from liquid origin formation processes. For in-situ ice both classifications agree better at least for the ice number concentrations which are fairly stable for the duration of the simulation.

4.5. Discussion and Summary

In this study we employed the ice mode schemes introduced in Chapter 2 to investigate ice formation pathways in a WCB case. The ice mode schemes allowed us to distinguish between cloud ice from homogeneous nucleation, homogeneous freezing, heterogeneous nucleation (immersion freezing, deposition nucleation) and secondary ice. During the WCB ascent immersion freezing of liquid droplets and secondary ice were prevalent. However, sedimentation of large ice crystal from deposition nucleation above the core WCB band affected even the composition of mixed-phase clouds. Ice from deposition nucleation was also the most dominant ice mode in the cirrus cloud of the WCB outflow. Contributions of homogeneous nucleation and homogeneous freezing of cloud droplets were overall minor.
The ice modes scheme also allowed us to investigate the liquid origin vs in-situ formation pathways. As the cirrus cloud ice was primarily formed by deposition nucleation, most of the ice in the cirrus outflow was stemming from in-situ formation processes. Ice stemming from liquid origin formation in terms of integrated mass content was mostly only relevant for fast ascending WCB trajectories. However, they were also significant parts of the outflow that were of liquid origin or where ice from both formation pathways mixed. Although these clouds were usually thin, hence showing low IWC and ice number concentrations.
We compared the cirrus origin classification of the ice modes scheme (IM) to the trajectory based algorithm of Wernli et al. (2016) (W16). W16 classified most of the cirrus segments as liquid origin because they continuously contained ice from the mixed-phase into the cirrus cloud regime. In contrast, IM classified most trajectories as in-situ origin as most of the ice (in terms of mass) was stemming from deposition nucleation that sedimented into the WCB trajectories. Wernli et al. (2016) also demonstrated that for two WCB case studies, the cirrus of the WCB outflow were embedded in a slow ascending air mass, where ice formed in-situ. In the interface between these two air masses sedimentation could possible 'confuse' their scheme as sedimentation cannot be considered in their cirrus origin classification. The ice modes schemes confirms that such an interaction between an ascending WCB and enveloping air mass is occurring for this WCB case. In-situ formed ice, mainly from heterogeneous ice formation, is sedimentating into the otherwise liquid origin WCB trajectories.

However, the question remains if in-situ formed ice, that sediments into the ascending WCB trajectories, is for a sufficiently long time subject to mixed-phase cloud processes, so that they attain the microphysical properties of liquid origin cirrus. Generally, it is expected that the differences between the cirrus types are most pronounced shortly after cloud formation and get blurred with increasing lifetime in the outflow due to various cloud processes Gasparini et al., 2018; Krämer et al., 2020. This study confirms this effect at least for this WCB case and especially for liquid origin cirrus.
We summarize the key results as

1. Sedimentation plays an important role for the cirrus evolution and should be considered in cloud classification schemes

2. WCB liquid origin cirrus properties are sensitive to (fast) ascent times

3. Trajectory based cirrus classifications are useful but microphysical signatures of the cloud types occur before a 600 hPa ascent is completed and are lost quickly

This study has several limitations. Heterogeneous ice nucleation is sensitive to choice of parametrisation. Changing the size distribution and number concentrations of ice nucleating particles (INP) will strongly affect deposition nucleation (DEP) and immersion freezing (IMM) modes. Additionally the activation of INPs as a function of temperature and supersaturation wrt ice differs strongly between parametrisations (see Section 2.3.4). DEP ice was the prevalent ice mode in this case study, naturally it would be strongly affected by changes to the heterogeneous ice nucleation scheme. In the next chapter we will test the sensitivity of liquid origin vs in-situ formation to choice of ice formation parametrisations.
The sedimentating DEP ice in this study formed (partly) in a slow rising air stream enveloping the WCB. This indicates that these dynamical structures of the WCB not identified by WCB trajectories are important for the formation and composition of the WCB cirrus outflow. However, this is only a single case study. Other WCB cases might not show this dynamical feature. In Chapter 6 we will investigate and compare liquid origin and in-situ formation pathways between several WCB cases using the ice modes scheme and model setup of this study.

5. Sensitivity studies

5.1. Introduction

In Chapter 4 we investigated dominant ice formation pathways in a WCB case study. We found that ice from deposition nucleation (DEP) was dominating the cirrus cloud regime and even sedimented into the mixed-phase clouds of the ascending WCB. Homogeneous nucleation (HOM) was overall weak, likely being suppressed by DEP. The cloud ice number concentrations were also overall low compared to global cirrus climatologies (Krämer et al., 2020).
We demonstrated in Chapter 3 that the ice mode microphysics scheme is useful for investigating the impact of changing ice formation parametrisations on the distribution of ice modes and general cloud evolution. In this chapter we employ the three heterogeneous ice nucleation schemes introduced in Section 2.3.4 with several configuration of aerosol modes and INP concentrations. Especially, we want investigate the impact of the choice parametrisation on the ice formation pathways (liquid origin and in-situ), the distribution of ice modes and the cloud ice number concentrations. Additionally we will test two of the new secondary ice parametrisations introduced in Section 2.4.

5.2. Methods

For this case study we chose the same cyclone as in Chapter 4, that was observed during the NAWDEX campaign between the 3th and 6th October 2016 over the North Atlantic (Schäfler et al., 2018). The Icosahedral Nonhydrostatic Weather and Climate Model (ICON) 2.6 is employed in a limited area mode (Zängl et al., 2015) with the ice modes microphysics scheme.

5.2.1. Ice modes scheme

The summary and setup of the ice modes schemes were also explained in the last chapter and are repeated here for convenience. However, additional information was added regarding parametrisations that were not used for the simulations presented in Chapter 4 but are relevant for this chapter.
The microphysics scheme is the ice mode schemes, which is a derivation of the standard 2-mom parametrisation in ICON (Seifert and Beheng, 2006) (SB). The scheme includes the microphysical classes: cloud droplets, raindrops, snow, graupel and hail. Instead of a single cloud ice class we employ five, each with their distinct formation pathway:

- Homogeneous freezing of solution droplets n_{hom}, q_{hom}
- Homogeneous freezing of cloud droplets n_{frz}, q_{frz}
- Immersion freezing of cloud and rain droplets n_{imm}, q_{imm}
- Deposition nucleation n_{dep}, q_{dep}
- Secondary ice n_{sec}, q_{sec}

The size distribution of each ice mode x is of the type of a generalized gamma distribution and has its own two prognostic moments, the number n_x and mass densities q_x. Apart from the formation process we assume the same shape, mass-diameter and fallspeed relations for each ice mode. They are also treated equally in advection, depositional growth and can collide with each particle class including itself and other ice modes. Note that aggregation of any ice mode still contributes only to same snow class.
Homogeneous freezing of solution droplets (HOM) is governed by the parametrisation of Kärcher and Lohmann (2002), which simulates an adiabatically ascending air parcel during a physics time-step. For homogeneous freezing of cloud droplets (FRZ) the fit of Cotton and Field (2002) is used. Immersion freezing of raindrops (IMM) follows the parametrisation of Bigg (1953).
Heterogeneous nucleation of ice contributes both to the IMM and DEP ice mode and is governed by the number concentration, size distribution and activation scheme of ice nucleating particles (INP). There are several choices of INP parametrisations available in the ice modes scheme: Hande et al. (2015) (HA15), Phillips et al. (2008) (P08) with modifications and Ullrich et al. (2017) (UL17). The nature of this modifications will be discussed in Section 5.2.6. A detailed description of the ice mode scheme as a whole can be found in Chapter 2.
For cloud condensation nuclei (CCN) activation there are also two parametrisations available. The scheme of Hande et al. (2016) (HA16) is often used in combination with the HA15 heterogeneous ice nucleation parametrisations in many experimental set-ups. The CCN scheme of Segal and Khain (2006) (SK06) is also implemented.
There are many possible secondary ice mechanisms that might have an impact on the evolution of clouds (Korolev and Leisner, 2020). Commonly included in two moment bulk schemes is a parametrisation of rime splintering (RS). The implementation is based on the laboratory study of Hallett and Mossop (1974) setting the number of secondary ice fragments in relation to temperature and rime mass. However, several choices of parametrisations for two other secondary ice mechanisms, collisional breakup (BR) and frozen droplet fragmentation (DF), are available for the ice modes scheme. Collisional breakup describes the breaking and fragmentation of dendrite branches upon collisions of ice particles, esp. graupel and snow. Droplet fragmentation describes the ejection of ice splinters during freezing and potential shattering of the frozen droplet. In this study we will use the formulation of Sullivan et al. (2018a) with the scaling coefficients of Sotiropoulou et al. (2020) for collisional breakup and the parametrisation of Phillips et al. (2018) for frozen droplet fragmentation. Details regarding these parametrisations, their performance and impact on the evolution of the ice modes can be found in Section 2.4.

5.2.2. Ice mode fractions

To characterize the contribution of an ice mode j to the total cloud ice content we define ice fractions as the ratio

$$f_j = \frac{q_j}{q_{tot}} \tag{5.1}$$

with the sum of all ice modes q_{tot}. Similar we define the number fraction of ice mode j as

$$fn_j = \frac{n_j}{n_{tot}} \tag{5.2}$$

with the total ice number density n_{tot}. However, when calculating ice mode fraction we only consider grid and trajectory points where a cloud containing ice is present, i.e. the total cloud ice content exceeds the critical value $q_{tot} > q_{crit} = 0.1\,\mathrm{mg\,kg^{-1}}$. This threshold value is often used to define cloud regions (see, e.g., Wernli et al., 2016). Otherwise ice fraction statistics would be distorted by regions where only insignificant traces of ice remain.
Further we distinguish between three cloud types. Mixed phase clouds containing both Liquid Water Content (IWC) and Ice Water Content (LWC) both exceeding the critical mass content q_{crit}. Cirrus clouds are defined as pure ice clouds in the cirrus temperature region ($T < T_c = 235\,\mathrm{K}$). 'Sub cirrus' clouds are pure ice clouds below the cirrus temperature. Ice mode fractions are calculated for all three cloud types.

5.2.3. Cloud ice origin classification

We follow the Krämer et al. (2016) approach of classifying cirrus cloud formation based on the formation process. Liquid origin cirrus forms from freezing droplets that were transported along the WCB into regions below the cirrus temperature T_c. This temperature represents the homogeneous freezing temperature threshold below which all liquid droplets are frozen. Thus the ice originates from liquid or mixed-phase clouds. Both, the FRZ and IMM ice mode contribute to liquid origin cirrus. In-situ cirrus is formed directly as ice deposition from the vapor phase onto an INP. Both, the HOM and DEP ice modes contribute to in-situ cirrus. We define the liquid origin fraction as the ratio of cloud ice content of liquid origin to the total cloud ice content

$$f_{liq} = \frac{q_{frz} + q_{imm}}{q_{frz} + q_{imm} + q_{hom} + q_{dep}} \tag{5.3}$$

Note that we did not include the SEC mode since secondary ice can not be directly associated with either in-situ or liquid origin. Collisional breakup is a secondary ice mechanism that can occur both within mixed-phase and pure ice clouds.
Wernli et al. (2016) used a trajectory based categorization algorithm to determine the origin of cirrus clouds. Trajectories were started at all points where a cirrus cloud occurred. They followed the trajectory backwards until the IWC fell below $q_{crit} = 0.1\,\mathrm{mg\,kg^{-1}}$. If the analysed segment contained LWC larger than q_{crit} the cirrus cloud was classified as liquid origin and in-situ otherwise. The trajectories were further selected by applying the typical WCB criterion (see Section 4.2.5)

We adapted this classification scheme (W16 hereafter) with a modification to make it comparable to the liquid origin fraction: only total cloud ice content excluding secondary ice is considered for the IWC criteria. Additionally in this case study we investigate cloud segments of forward calculated WCB trajectories rather than calculating backward trajectories for each cirrus cloud.
Another useful diagnostic quantity is the heterogeneous ice fraction f_{het} as the ratio of ice content formed by heterogeneous nucleation to the total cloud ice content

$$f_{het} = \frac{q_{imm} + q_{dep}}{q_{frz} + q_{imm} + q_{hom} + q_{dep}} \tag{5.4}$$

We again omit secondary ice as it is formed neither by homogeneous nor heterogeneous nucleation.

5.2.4. Model setup

The ICON configuration follows largely Heinze et al. (2017) in a limited area mode setup. We use a R03B08 model grid with an effective horizontal resolution of 6.5 km and vertical discretization of 90 levels in a terrain-following coordinate system (SLEVE). The domain extends from 70° W to 50° E and 20° N to 80° N, respectively, thus including most of the Northern Atlantic and Europe. The physics time step is 40 s. Initialisation and boundary data is provided by ECMWF reanalysis data (Bechtold et al., 2008). The simulation duration is 54 h including a 6 h initialisation phase. Model output is written every 30 min and interpolated from the the icosahedral model to a latitude-longitude grid (0.075°x0.075°).
We include most of the physics parameterisations commonly used in ICON: subgrid scale orographic drag, non-orographic gravity wave drag, vertical diffusion and transfer by turbulence, surface transfer scheme and a radiation transfer model in conjunction with a simple cloud cover parametrisation. Further discussions regarding these configuration can be found in Heinze et al. (2017). Deep convection is treated explicitly. However, we do not use a shallow convection scheme since the assumptions and implementation are not compatible with the ice modes microphysics scheme.
All experiments in this chapter use the same model setup as in Chapter 4 apart from the differences described in Section 5.2.6.

5.2.5. WCB trajectories

Trajectories are calculated offline using LAGRANTO (Sprenger and Wernli, 2015) to characterize the WCB flow in a Lagrangian framework. Trajectories belonging to the WCB are identified by two conditions (Joos and Wernli, 2012; Madonna et al., 2014). First they have to ascend at least 600 hPa in 48 hours. Second they need to start in or cross a cyclone. Cyclones are identified with a newly developed algorithm as two dimensional features in the surface pressure field based on the work of Wernli and Schwierz (2006) (see Appendix A.6).
Trajectories are started 6 h after model initialisation at 4th October 2016 06:00 UTC in

Name	Experiment
R6	6.5 km grid resolution
R13	13.5 km grid resolution
UL	UL18 het. ice nucleation
PH	PH08 het. ice nucleation
PH3	PH08 het. ice nucleation with soot and bio mode
PHSK	PH08 het. ice nucleation and SK06 CCN activation
DF	DF instead of RS for secondary ice
BR	BR instead of RS for secondary ice
ASEC	all secondary ice processes (RS, DF & BR)
AxBy	ensemble simulation with sensitivity values
	x and y for A and B, respectively

Table 5.1.: List of sensitivity experiments

a large box around the cyclone from 50°W to 20°W and 30°N to 65°N. One trajectory is started at each point on a 7.5 km equidistant grid and at five altitude levels from the surface up to 1 km. After selecting trajectories according to WCB criteria we calculate the WCB area index marking the grid cell and model level where WCB trajectory is present for each time step. This allows to investigate the evolution of (micro-)physical quantities both interpolated on the trajectories as well as on the gridded model data itself.
All experiments in this chapter calculate WCB trajectories the same way.

5.2.6. Experiments

Several experiments have been performed to investigate the impact of different model assumptions on the ice modes and cirrus cloud formation. Table 5.1 provides a list of all sensitivity experiments. R6 labels the reference simulation of this study and unless otherwise noted each experiment uses the standard setup with a 6.5 km effective grid resolution, HA15 INP and HA16 CCN activation.
R13 uses a coarser model grid (R03B07) with an 13.5 km effective resolution. UL and PH experiments employ the INP activation parametrisation of Ullrich et al. (2017) and Phillips et al. (2008), respectively. Note that the parameters of both parametrisations have been adjusted so that the immersion freezing rates are closest to HA15. See Section 2.3.4 for details. PH3 not only considers dust but also soot and biological aerosols as INPs. PHSK uses the PH3 setup in conjunction with SK06 CCN activation.
Secondary ice mechanisms are investigated with three additional experiments. Rime splintering (RS) is active in all experiments except the ones dedicated to droplet fragmentation (DF) and collisional breakup (BR), respectively. In ASEC all three secondary ice parameterisations are active.
Additionally we perform an ensemble of simulations to investigate the impact of the heterogeneous ice nucleation scheme. The HA15 scheme estimates INPs from Saharan dust events over Europe. HA15 performed mesoscale aerosol simulations and employed

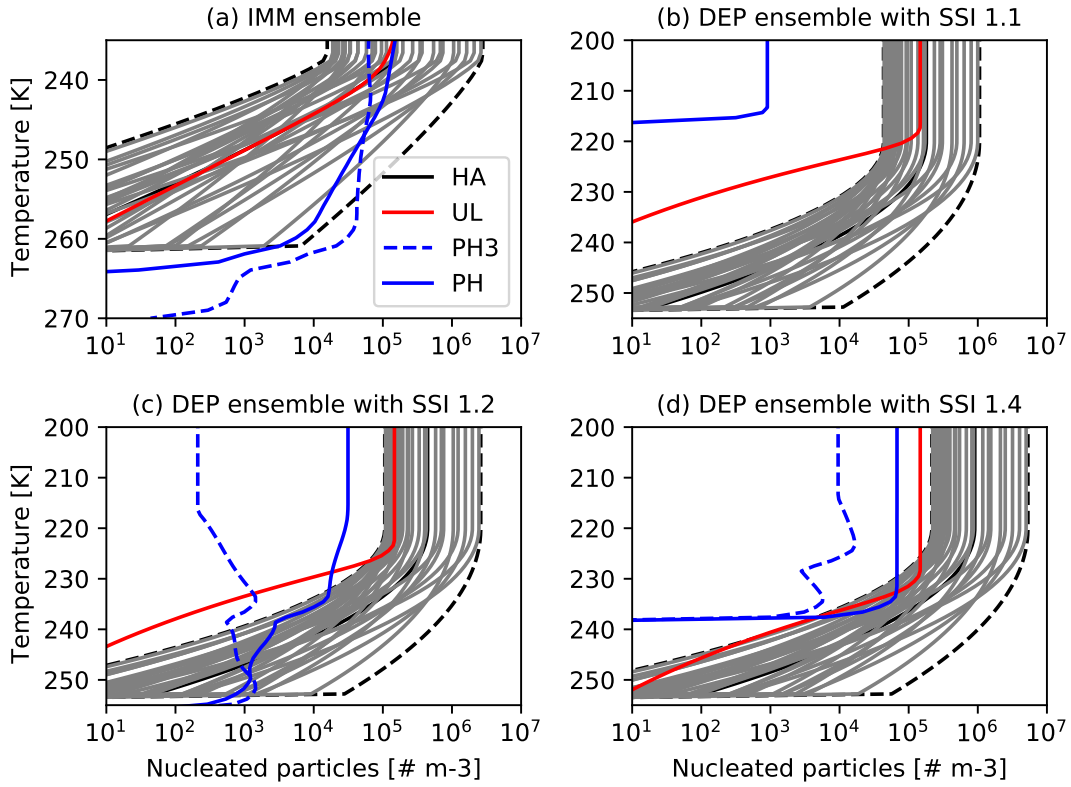

Figure 5.1.: Number density of activated INPs for (a) immersion freezing and (c) to (d) deposition nucleation with supersaturation wrt ice for (b) 1.1, (c) 1.2, (d) 1.3. Shown are the profiles for the HA, UL and PH parameterisations. The profiles of the ensemble members are shown in grey.

laboratory-based nucleation parameterisations to obtain seasonal INP profiles for Europe (Hande et al., 2015). The potential INPs increase exponentially with decreasing temperature T

$$n_{\mathrm{INP}}(T) = N_{0,\mathrm{INP}} \exp[-\beta(T - T_0)^{\gamma}] \tag{5.5}$$

where the parameters $N_{0,\mathrm{INP}}$, β, γ and T_0 are chosen depending on the mode (immersion freezing or deposition nucleation) and season. The deposition mode uses an additional term to describe the dependence on supersaturation wrt ice (S_i). In our microphysics scheme immersion freezing occurs only at water saturation and thus INP activation only depends on temperature.

For the sensitivity analysis we vary two important parameters of the HA15 parametrisation. Scaling $N_{0,\mathrm{INP}}$ impacts the overall dust concentration and availability of INPs. Changing β affects the shape of the the profiles. Let A and B be our sensitivity parameters

$$N_{0,\mathrm{INP}} = A_0 + A(A_1 - A_0) \qquad \beta = B_0 + B(B_1 - B_0) \tag{5.6}$$

with $A, B \in [0, 1]$. We choose the 5th and 95th percentile scaling factors from Hande et al. (2015) for A_0 and A_1, respectively. These values represent strong and weak dust events over Europe. b is simply scaled as $B_0 = 0.5\,\beta$ and $B_1 = 1.5\,\beta$. For the ensemble we choose 30 pairs of sensitivity parameters by latin hypercube sampling. A is sampled logarithmly as the dust concentrations span multiple orders of magnitude and B is sampled linearly. The maximum concentration of active INP fits well with observations of strong Saharan dust events from Brunner et al. (2021) measured at the High Altitude Station Jungfraujoch in Switzerland.
The resulting ensemble profiles are shown in Figure 5.1. Together both sensitivity parameters span a large space of possible profiles (in grey) to be sampled in the ensemble. The dashed black lines indicates the two extreme profiles of the ensemble ($A = 0$, $B = 1$ and $A = 1$, $B = 0$), receptively. The standard HA15 parametrisation (black curve) is in the middle of the ensemble. By design the profile of UL17 is very close to HA15 for immersion freezing (see Section 2.3.4). However, P08 extends the temperature range of active INPs to higher temperatures. For deposition nucleation (panel c to d) the three parameterisations show large discrepancies. This is related to different assumptions of INP activation and implementation in microphysics schemes.
Note that immersion freezing is still limited by the availability of cloud droplets. Also for both, IMM and DEP ice modes, the number of activated INPs n_{niact} is tracked as a scalar field and subtracted from the number of available INPs during subsequent nucleation events. n_{niact} is advected along with the cloud variables and relaxes back to zero in a cloud free environment on a time scale of 10 min. In addition the PH3 configuration of the PH08 heterogeneous nucleation scheme tracks potential (dust) INPs n_{nipot}.

5.3. Ice phase of the WCB

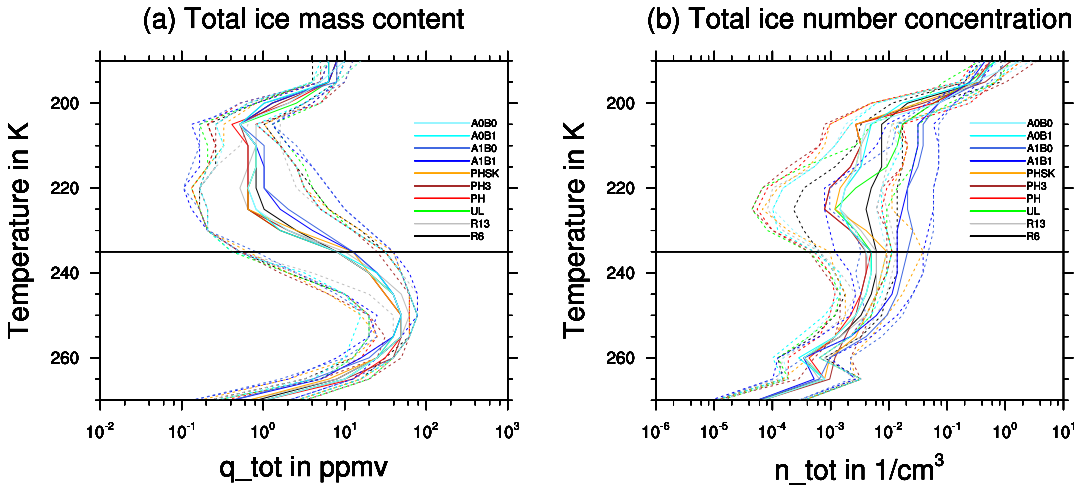

Figure 5.2.: Temperature profiles of mean (solid) and 25th/75h percentile (dashed) for (a) total cloud ice content q_{tot} and (b) total cloud ice number concentration n_{tot}, respectively. The black horizontal line donates the cirrus temperature level T_c.

The experiments in this study use different assumptions and parametrisations that influence heterogeneous ice nucleation and secondary ice production. Before we compare their effects on the relative compositions of the ice modes, we first establish how the total cloud ice content (q_{tot}) is affected. We compare the statistics of those properties for all WCB trajectories and all times. Figure 5.2 (a) shows the statistics of q_{tot} for each experiment as a function of temperature. The mean as well as the the 25/75th percentile profiles (dashed) are similar for each experiment, only deviating by a factor of 2 from the reference simulation R6 (in black) at most. This is due to the fact that ice mass is thermodynamically constrained by the availability of water vapor. When ice is formed it will consume the available supersaturation until saturation is reached. Since the WCB dynamics are very similar for each experiment the cloud experience mostly the same thermodynamic environments. The differences between the experiments arises from different assumptions regarding the INP activation sensitivity to temperature and supersaturation. Thus the time at which cloud ice is formed during the ascent and the resulting ice number density are affected. The latter also directly influences mean ice mass and thus sedimentation rates, which changes the vertical distribution of ice.
Overall q_{tot} increases as the WCB ascends and more ice formation pathways become active. The maxima lay in the mixed-phase temperature ($T > T_c = 235\,\mathrm{K}$) region with about 50 ppmv. Below 240 K the mean ice content decreases to 2 ppmv as the WCB trajectories enter the cirrus temperature regime ($T \leq T_c$). At 200 K we observe a peak caused by homogeneous nucleation events, that produce a high number concentration of ice crystals. Since all experiments use the same HOM parametrisation the signals look

mostly the same.
There are some (small) differences to note between the experiments. During the ascent phase at temperatures above 255 K the PH and PH3 simulations (in reds) show a small peak of q_{tot} since immersion freezing onset for these parametrisations extends towards higher temperatures (see Section 2.3.4). The lower resolution experiment (R13) shows the highest mean q_{tot} during ascent reaching up to 100 ppmv. Because R6 and R13 use the same INP assumptions the differences between both experiments arises from the less well resolved dynamics for the coarser grid resolution.
Above the cirrus temperature line we observe that the high INP (A1B*) experiments (dark blues) show higher mean q_{tot} than the reference, R6, but also an overall larger spread (as can be seen from the 25/75th percentiles). The PH and low INP (A0B*) experiments (light blues) show less q_{tot} than R6 for most of the cirrus temperature range.
Figure 5.2 (b) shows the mean total cloud ice number concentration n_{tot} and its distribution for each experiment. Immediately, we note a much larger spread between the experiments especially above the cirrus temperature line. n_{tot} is more strongly related to the parametrisations of the ice formations pathways and less limited by the thermodynamic forcing than the ice content. This is also apparent on the 25th and 75h percentile lines, where the profiles of the experiments are not as aligned as for q_{tot}. In general n_{tot} is increasing with decreasing temperature. However, especially in the mixed-phase temperature region below 240 K, collision processes with graupel and snow play an important role in removing cloud ice. This sink for IMM was investigated in Chapter 3.
In general we observe the same trend for inter-experiment variability for n_{tot} as for q_{tot}. The high INP experiments (A1B*) shows as much as 10 higher n_{tot} than the reference, R6. The PH* and A0B* experiments show overall lower n_{tot} than R6. This is caused by the lower number concentration of INPs (for A0B*) or the more thermodynamical constrained activation of INP (for PH*). UL first follows the evolution of the PH* experiments and but then overtakes R6 for temperatures below 210 K. In Section 2.3.4 we showed that deposition nucleation rates for UL are lower than for HA at temperatures higher than 210 K, but catch up for moderately high ice supersaturation ($S_i \approx 1.1$). R13, with the lower spatial resolution, also shows reduced n_{tot}. Changing the spatial resolution has a similar impact on n_{tot} in cirrus clouds as lowering the INP by several orders of magnitude.
In summary the evolution and distribution of totaled cloud ice properties (as the some of all ice modes) follows the same pattern for each experiment especially for the (thermodynamically constrained) cloud ice mass content q_{tot}.

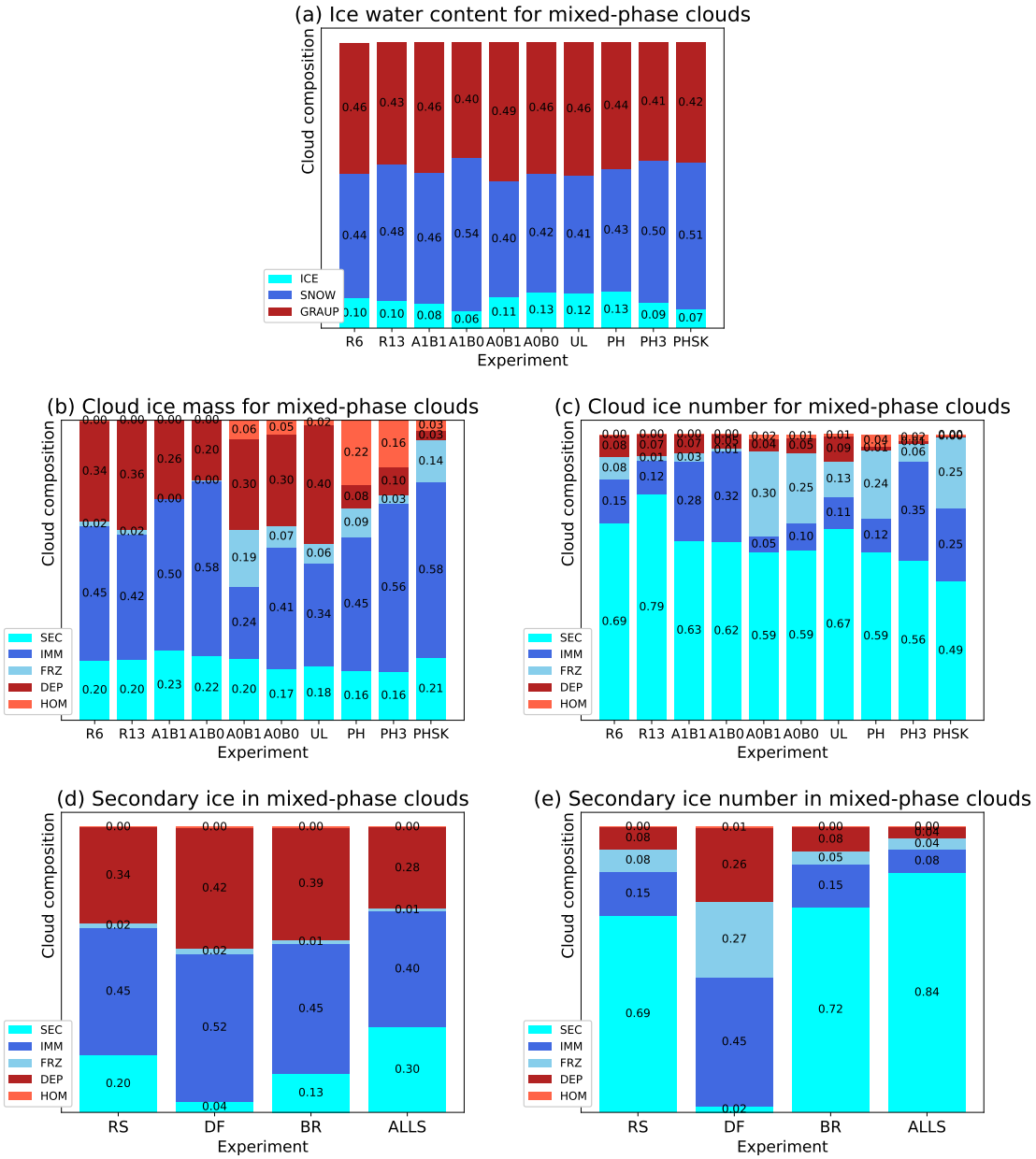

Figure 5.3.: Cloud (ice) compositions of mixed-phase clouds in the WCB.

5.3.1. Mixed-phase clouds

Figure 5.3 shows the compositions of ice water content (a), cloud ice mass content (b) and cloud ice number concentrations (c) for mixed-phase clouds in the WCB trajectories. These plots show the ratio (or 'budget') of a particular class or ice mode mass content (or number concentration) to the integrated mass content (or number concentration) of all ice particle classes or ice modes. The compositions are further split into cloud regimes (mixed-phase, pure ice clouds below cirrus temperature level and cirrus).
The first panel shows that ice particle mass is mostly contained within the graupel and snow classes. Hence riming is one of the major microphysical processes in the mixed-phase clouds of the rising WCB, although not strong enough to produce hail. Aggregation is effective enough to make snow mostly as dominant as graupel. Ice (as the sum of all ice modes) only makes up around 10 % of the mass budget. We only observe marginal shifts of the ice particle compositions between the experiments.
The experiments with the P08 heterogeneous ice nucleation including all aerosol types (PH3 and PHSK) favour snow at the cost of graupel and ice. We observe a similar shift for the HA15 simulation with high INP but shallow dust concentration profile (A1B0). In Section 3.3 we found that the higher aggregation rates are related to an increase of ice content of the immersion freezing ice mode (IMM) in the mixed-phase parts of (convective) clouds. Here we observe the same relation. PH3, PHSK and A1B0 all show high IMM and high snow ratios in terms of mass (compare Panel (a) and (b)).
The R13 experiment also increases the snow content at cost of graupel, likely because riming is depended on the strength of updrafts and those are not resolved as well at a lower grid resolution. Low INP experiments (A0B*), UL and PH trend towards higher ice and lower snow mass content ratios.
All experiments retain similar mass ratios for the major ice particle classes. As for total cloud ice mass in Section 5.3, different experiment setups do not change the general cloud evolution significantly. This makes this part of the study more robust and we can focus on the differences of the experiments with regard to the partitioning of ice modes.
Panel (b) and (c) in Figure 5.3 show the composition of the ice modes for mixed-phase clouds as the total mass and number ratios, respectively. First we look at the reference simulation R6 for the general characteristics. The immersion freezing mode (IMM) with 45 %, deposition mode (DEP) with 34 % and secondary ice mode from rime splintering (SEC) with 20 % are the strongest modes with regards to ice mass. Note that the parametrisations of homogeneous and deposition nucleation are inactive at water saturation (see Section 2.3), so nucleation events have to be triggered outside mixed-phase clouds and sediment into it. This also evident when looking at the number ratio, where DEP only makes up to 8 %, hinting that ice from this mode has a large mean size and thus high sedimentation velocity. In Chapter 4 we found that DEP ice of this WCB case stems from a slow ascending cloud on top of the WCB. Especially noteworthy is that SEC dominates the total ice number ratio for R6, hence rime splintering as the standard secondary mechanism in all simulations, creates small ice crystals with high number concentrations. The homogeneously frozen droplet mode (FRZ) for R6 is rather weak with regards to mass (2 %) but shows a higher number ratio (8 %).

In general we find the same vertical structure of the ice modes in the mixed-phase cloud as in our idealised studies of a convective cloud (see Section 3.3) and in the previous chapter (see Section 4.3.3): SEC ice from rime splintering dominates the lowest part of the cloud especially in the Hallet-Mossop temperature zone around 268 K, the next layer consists of heterogeneously frozen droplets (IMM) and any liquid droplets left after immersion freezing and riming freeze homogeneously (FRZ) once they temperatures close to the homogeneous freezing temperature T_f. This leads to a direct competition for availability of cloud droplets between IMM and FRZ, stemming from a heterogeneous and a homogeneous freezing mechanism respectively. If environmental conditions or microphysical assumptions change, e.g. by modifying the heterogeneous ice nucleation scheme, one of those modes is weakened, the other one is strengthened. A similar 'rivalry' applies for DEP and HOM ice modes although they do not compete for cloud droplets but for supersaturation, which we will discuss in Section 5.3.4.
The next 5 experiments are R13, with its lowered grid resolution, and four ensemble experiments AxBy, which also use the HA15 nucleation scheme but with different scaling and slope parameters. Ice mode composition shows that the lower resolution experiment (R13) features mostly the same partitioning as R6. High INP concentrations experiments (A1B*) favour the IMM mode at the cost of even less droplets freezing homogeneously (FRZ) than for the other experiments. As expected low INP concentration experiments (A0B*) show FRZ to be more relevant. Similar, but less notable than for PH* experiments, DEP is also weakened leading to more HOM nucleation events above the WCB that sediment into the mixed-phase clouds. The experiment with the stepper INP profiles (A*B1) show less IMM mass and number ratios. Since more INPs are activated at higher temperatures, they are more likely removed by aggregation, collision with graupel and sedimentation below the melting temperature level.
Next we look at UL featuring the UL17 heterogeneous nucleation scheme. UL shows mostly the same features as the reference simulation R6. This is to be expected as the INP activated for immersion freezing are basically the same for both parametrisations. However, the differ in their activation of INPs for deposition nucleation. So the composition of ice modes in the mixed-phase cloud composition is indirectly affected by weakening of DEP and strengthening of HOM modes.
In Section 2.3.4 we found that using PH08 heterogeneous nucleation scheme (PH, PH3 and PHSK) weakens DEP since the required supersaturations wrt ice for the onset of deposition nucleation are higher than for UL and HA. Since deposition nucleation above the mixed-phase clouds is weaker for this parametrisation, it allows homogeneous nucleation to occur and ice from the HOM mode to sediment into the cloud. Again, as for DEP in the other experiments, HOM shows only a low number ratio which is consistent with the earlier observation for DEP. The ice crystals have to be large in order to sediment into the mixed-phase cloud as the HOM nucleation zones have to be located far above the mixed-phase clouds since homogeneous nucleation requires low temperatures and high supersaturations.
IMM is more prominent, both, for mass and number ratios for PH3 and PHSK. These parametrisations use biological aerosol and soot in addition to dust. Immersion freezing is activated at higher temperatures for this aerosol modes (see Section 3.3). We also

noted the spike in (total) cloud ice content in Section 5.3 for these temperature levels. For PHSK we changed the CCN activation scheme to SK06, which shifts the partition of the ice modes even more. In addition to IMM, FRZ is more prominent and equally represented with regards to number ratio as IMM. Ice from deposition and homogeneous nucleation is mostly irrelevant within the mixed-phase cloud. This is caused by the increased CCN activation due to SK06, which leads to much higher cloud droplet number concentrations that can (potentially) freeze contributing to both IMM and FRZ.

5.3.2. Secondary ice

Panel (d) and (e) in Figure 5.3 show the ice mode distribution for the secondary ice sensitivity experiments. We found that SEC ice from rime splintering is very dominant, however, it is only present in mixed-phase and not in pure ice clouds (see Section 5.3.4) and mostly in the Hallet-Mossop temperature zone within the lowest parts of the cloud. Using collisional breakup (BR) instead of rime splintering as the secondary ice mechanism lowers the SEC ice mass ratio by 7 % but increases the number ratio by 3 %. So even if we use BR instead of RS, SEC is still the strongest mode with regards to ice number ratios. Droplet fragmentation (DF) shows low mass and very low number ratios for mixed-phase clouds making it the weakest of the three secondary ice mechanisms. Note that droplet fragmentation in the model only occurs for raindrop freezing since cloud droplets are too small to eject a significant amount of splinters. In this case study rain is mostly present in the warm temperature zone above 270 K where freezing and the DF parametrisation are very weak (see Section 2.4.2). When using all three secondary ice mechanisms (ALLS) SEC becomes the second strongest ice mode with regards to mass with 30 %. However, it is also evident that the three mechanisms are not additive. Rather they expand the temperature range where secondary ice mechanisms are active and thus strengthen the SEC ice mode as a whole. Collisional breakup adds to and makes the SEC ice mode more prevalent for the mixed-phase clouds of this WCB case. But even without additional secondary ice mechanism, SEC ice from rime splintering by itself dominates in mixed-phase clouds of the WCB.

5.3.3. Sub cirrus clouds

Figure 5.4 shows the composition of the sub cirrus clouds in terms of ice mode mass (a) and number ratios (b). These pure ice clouds are a transition stage between the mixed-phase clouds and cirrus clouds. As such they show trends and characteristics of both regimes. Secondary ice is almost completely absent being only relevant for the very beginning of the ascent phase. For experiments using the HA15 heterogeneous nucleation (all but UL, PH, PH3 and PHSK) deposition nucleation reigns as the dominant ice mode with remnants from mixed-phase clouds in the form of IMM and FRZ modes remaining. The later are more prominent for the low INP experiments (A*B0). This is partly a carry over from the mixed-phase clouds, however, FRZ stands out here. Cloud droplets that did not freeze in the mixed-phase regime due to lack of INPs have to freeze homogeneously in this thermodynamic regime. The FRZ mode is distinct by its high

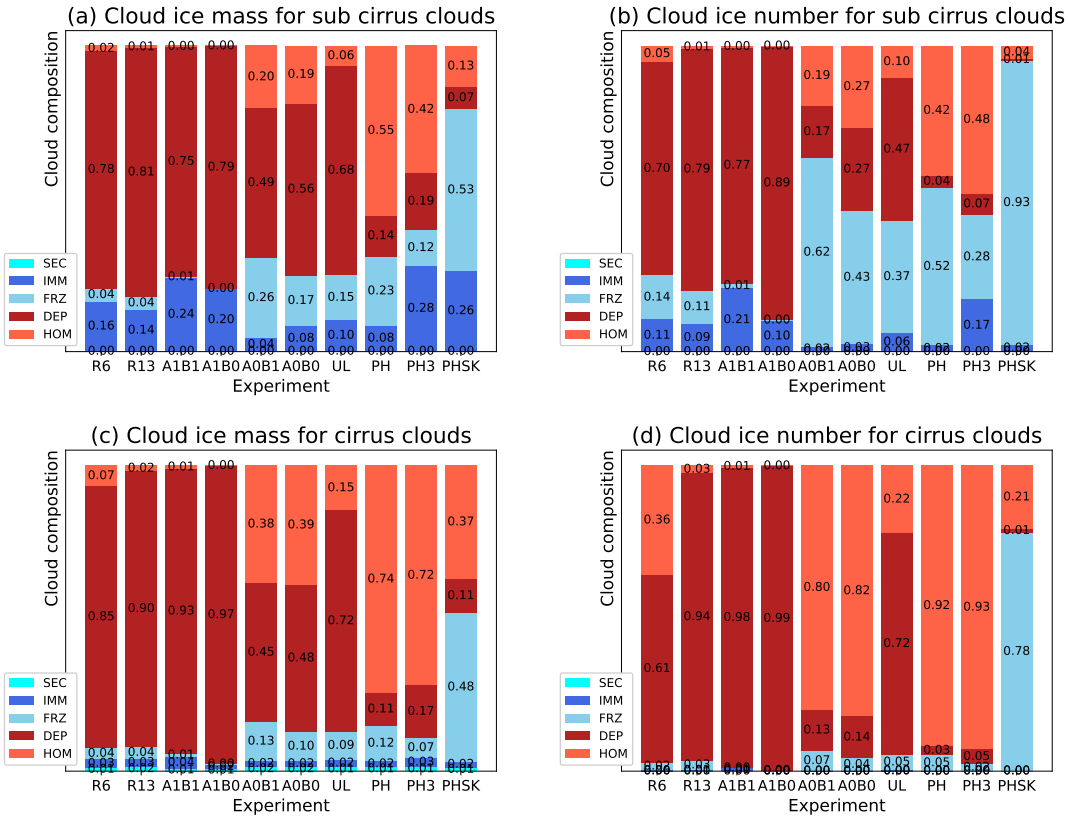

Figure 5.4.: Ice mode compositions for sub cirrus (a,b) and cirrus clouds (c,d).

number concentrations (and low mean size) even for the R6 and R13 experiments. The high INP experiments (A1B*) also carry on as expected from the mixed-phase regimes: strong DEP and IMM modes with homogeneous freezing and nucleation barely occurring.

The UL experiment also shows a strong DEP mode in terms of mass. However, the number ratios are more even between the ice modes with FRZ being prominent as well as HOM being twice as strong as for the R6 experiment. That UL shows a higher number ratio but lower mass ratio for FRZ than R6 and the low INPs experiments (A0B*) is curious. The immersion freezing profile is basically the same as for R6 (see Section 2.3). So any differences have to arise from the assumptions about the onset of deposition nucleation.

Concerning PH* experiments we already noted that for mixed-phase clouds HOM was more important and DEP weaker than for experiments HA15 and UL17 parametrisations. Deposition nucleation rates are generally weak for the PH08 parametrisation, which consequently leads to high mass and number ratios of FRZ and HOM. PHSK stands out as having a very strong presence of the FRZ mode. The SK06 CCN activation produces such a high number of cloud droplets, that we obtain a pure ice cloud

almost entirely consisting of homogeneously frozen droplets.

5.3.4. Cirrus clouds

Panels (c) and (d) in Figure 5.4 shows the composition of ice modes in the cirrus outflow with regards to mass and number ratios, respectively. In general we see the trends from the sub cirrus transition regime continuing but even more pronounced.
For the reference experiment R6, ice from deposition nucleation (DEP) dominates the mass ratios strongly with 85 % and the number ratio with 61 % similar to the statistics for pure ice clouds below the cirrus level (compare panels (a,b)). Ice that stems from frozen droplets (FRZ and IMM) is even less relevant. Ice stemming from homogeneous nucleation HOM takes up a large partition of the number ratios, consistent with the observation that homogeneous nucleation produces a large number of small ice crystals and heterogeneous (deposition) nucleation produces less but larger ice crystals (Krämer et al., 2020).
For the lower resolution experiment R13, HOM is almost not present and its 'share' is taken by the competitor mode, DEP. The parametrisation of HOM directly depends on the strength of the vertical updraft, which is less well resolved for the coarser grid experiment. This impacts the HOM mode significantly.
The four edge members of the ensemble (AxBy) show also an expected result: for the high INP experiment A1B* HOM is almost complete gone as the homogeneous nucleation events are being suppressed by DEP, while A0B* makes DEP weaker and thus leads to higher supersaturations S_i, which give HOM nucleation events the opportunity to occur. This makes both modes comparable in terms of mass and showing much higher number rations for HOM. The impact of the steepness of the INP profile (sensitivity parameter B*) on the ice mode is almost completely gone.
The distribution of ice modes for the UL experiment is in between the high and low INP concentration experiments, A1* and A0*, respectively. UL17 parametrisation features similar dust concentrations as the reference simulation R6, but uses different assumptions for the INP activation (see Section 2.3.4). In Section 5.3 we already remarked on the later onset of DEP nucleation in the evolution of the mean cloud ice mass. This leads to a weaker DEP and stronger HOM mode compared to R6, but with the FRZ and IMM modes still being insignificant for the cirrus cloud regime.
Although A0B* experiments represent cases where the number concentrations of dust INPs (in the HA15 scheme) are (extremely) low, changing the parametrisation (and thus the thermodynamic onset conditions of DEP nucleation) to the PH08 scheme has a larger impact. DEP is even weaker in the PH and PH3 experiments and HOM now also dominates the mass ratios. The experiment with the SK06 CCN activation scheme (PHSK) shows the largest differences to the reference simulation R6. Again, as for pure ice clouds below the cirrus temperature level, homogeneously frozen droplets (FRZ) making up almost half of the cirrus ice mass and even 78 % of the number ratio. The remaining cloud ice mostly stems from HOM.

5.3.5. Ensemble

The Panel (a) and (b) in Figure 5.5 show the mean total cloud ice content and cloud ice number concentrations, respectively, for all ensemble experiments as a function of temperature. Both profiles show the same general structure as discussed in Section 5.3. The mean total cloud ice content of all ensemble members stays tightly packed and shows less variation than in between the other sensitivity experiments (compare to Figure 5.2). We observe the largest spread above the cirrus temperature line where deposition nucleation is strong. As noted in Section 5.3 the ice mass is strongly controlled by the thermodynamic environment. Even if a specific formation pathway is weaker (e.g. due to lower INP concentrations), the pre-existing or otherwise formed ice crystals compensate by consuming more water vapor per particle and thus grow larger.
For the cloud ice number density we observe a larger differences up to a factor of ~ 5 between the ensemble members for temperatures lower than 250 K. Above that temperature the difference is small since secondary ice is still dominant in that region and not (directly) depended on changes of immersion freezing rates. Also there are likely still enough INPs available for all ensemble experiments, hence immersion freezing is not limited. For the transition zone between mixed-phase and cirrus clouds ($250 > T > 235$ K) as well as for experiments in the cirrus regime, experiments with lowered INP concentrations tend to show higher cloud ice number concentrations. Likely due to the effect that if immersion freezing is stronger, more droplets freeze earlier (at higher temperatures) and are easily removed by aggregation and sedimentation.
Panels (c) to (f) show the total heterogeneous ice mass and number fractions for mixed-phase and cirrus clouds, respectively, as a function of the sensitivity parameters. The total heterogeneous mass/number fraction states how much of the overall integrated cloud ice mass/number for that cloud regime stems from homogeneous (HOM+FRZ) or heterogeneous (DEP+IMM) formation pathways (see Section 5.2.2). The trend for the scaling sensitivity parameter A is clear: the larger A, the higher the INP concentrations. Thus the total heterogeneous ice mass and number fractions are higher. The mass fraction is ranging from ~ 50 to over 90 % for both cloud regimes, whereby the mixed-phase regime shows a lower range. The number fraction though ranges from almost 0 to 90 % and shows a steeper increase for high A and a large area in the parameter space with low ice number fractions. Hence heterogeneously formed ice is always relevant in terms of mass content but might show low number concentrations for low INP concentrations. The influence of the rate parameter B is harder to interpret and overall weak. For high A there is a small increase in heterogeneous ice fractions for lower B values. We also noted for the experiments with extreme slopes of the ensemble (A*B1), that FRZ got stronger. Likely a steeper INP profile causes higher IMM ice concentrations at higher temperatures, where this heterogeneous ice mode gets easier removed by the typical suspects: aggregation and sedimentation. As we do not track sinks of ice modes, we can only draw conclusions from abundance or absence of ice modes. Overall there is no notable trend for variation of the slope parameter.

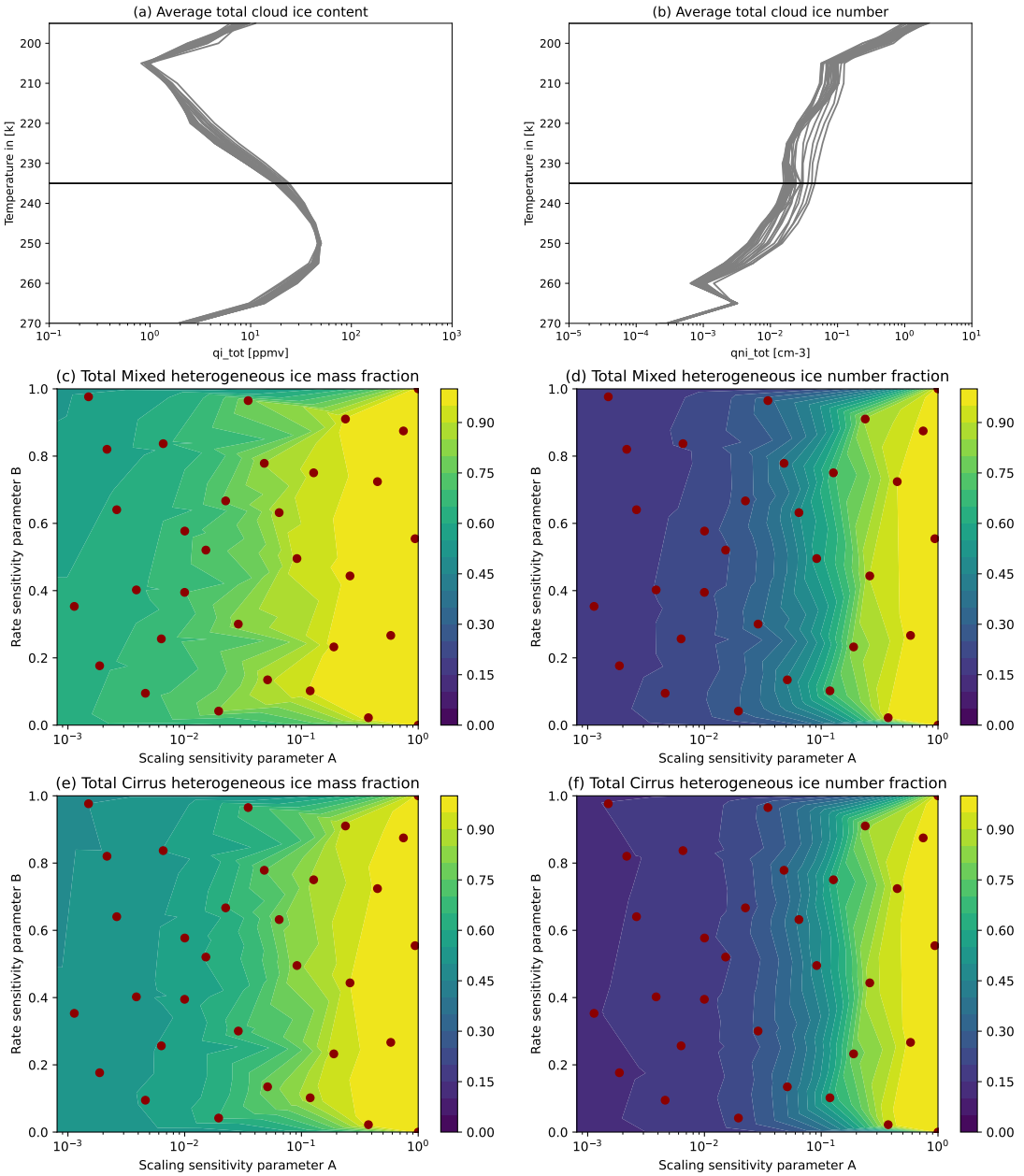

Figure 5.5.: Temperature ensemble profiles of mean (a) total cloud ice content and (b) total cloud ice number, respectively. The black horizontal line donates the cirrus temperature level. Total heterogeneous ice mass fraction and number fraction for mixed-phase (c,d) and cirrus clouds (e,f) in the ensemble parameter space, respectively. Red dots denote the sensitivity parameters of the experiments.

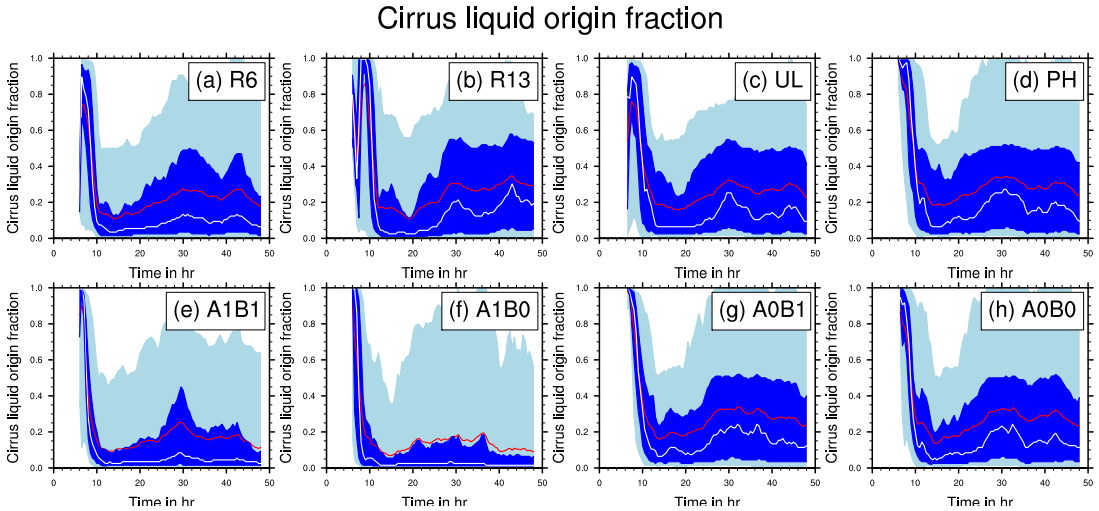

Figure 5.6.: Temporal evolution of f_{liq} four eight experiments. Median as the white line, the 25th to 75th percentile in dark blue and the 5th to 95th percentile in light blue. Red represents the mean.

5.4. In-situ vs liquid origin

Figure 5.6 shows the evolution of the liquid origin mass fraction f_{liq} for eight experiments (see Table 5.1). The characteristics of the reference case R6 have been discussed in detail in Chapter 4. Here we do not plot f_{liq} as a function of outflow time, but of time since trajectory start. This provides a better insight into the temporal evolution of the outflow while we can still make some statements about the ascent times. Trajectories that show cirrus at low trajectory times have to ascend fast (small τ_{600}). However, trajectories that contribute data points to the statistics for later trajectory times could ascend fast or slow depending on the time they began their ascent.
To summarize our findings for the R6 reference case here: we notice high f_{liq} for the fast ascent trajectories contributing to a spike of f_{liq} for $t < 10\,\mathrm{h}$ followed by a sharp decrease of liquid origin formed ice. Mean f_{liq} increase with time up to ~ 0.2, although the majority of trajectories ($> 50\,\%$) are still strongly dominated by in-situ ice ($f_{liq} < 0.1$). There are regions where in-situ and liquid origin ice mixes leading to f_{liq} values from 0.3 up to 0.4. This influxes of liquid origin formed ice correspond with peaks at 32 and 44 h. Regions of mixed origin are often thin cirrus ($0.1 < q_{tot} < 1\,\mathrm{mg\,kg^{-1}}$), where only traces of cloud ice remain (see Section 4.4.3). This is also apparent when comparing f_{liq} to the ice modes statistics in Figure 5.4. The latter shows the contribution of the particular ice mode to the total cloud ice mass integrated over the entirety of the specified cloud regime. f_{liq} only considers how much an ice mode contributes to the cirrus at each point as long as the total cloud ice content is above $q_{crit} = 0.1\,\mathrm{mg\,kg^{-1}}$. Hence, the composition of (very) thin cirrus clouds are more pronounced in the f_{liq} statistics.
R13 (Panel (b)) shows a broader distribution of f_{liq} than the reference case, R6, with

regions of mixed origin being more prominent. The median rises after the initial ascent to values of 0.2 and the 75th percentile region extends towards 0.5. However, from Section 5.3.4 we know that both R13 and R6 contain the same ratios of in-situ (HOM+DEP) and liquid origin (FRZ+IMM) cirrus ice. With this additional information we can conclude, that R13 sees a larger spread of very thin cirrus, where in-situ and liquid origin ice mixed. The lower spatial grid resolution likely leads to less vertical mixing and more (very) thin cirrus being carried along in the WCB.
UL (Panel (c)) shows similar to R13 a broader spread of cirrus, where liquid origin and in-situ ice mixed, after the initial ascent phase. But in contrast to R13, the increase in f_{liq} indeed correspond to an increased amount of IMM ice (compare Figure 5.4). The drop in f_{liq} between 10 and 20 h is less pronounced than for R6 and R13.
The PH experiment shows, like UL, a higher mean f_{liq} and broader distribution with some outliers even reaching f_{liq} up to 1. The more limited onset of DEP nucleation in the PH08 parametrisation allows liquid origin formation pathways to be more relevant even though HOM partly compensates for the reduced DEP ice content.
The extreme cases of the high INP (A1B*) experiments for the ensemble (Panels e-f) show results that are to be expected from the (even stronger) dominance of the DEP mode due to increased INP concentrations. The median of f_{liq} is very close to 0 and even the upper 75th percentile does not exceed 0.2. The A1B1 experiment with the steeper slope of INP profiles show more liquid origin ice since the IMM mode is strengthened (compare Figure5.4). The extremely low INP concentrations experiments A0B* (Panels g-h) show results that are similar to the PH simulation with a f_{liq} median ranging from 0.05 to 0.2 after the initial ascent and a 95th percentile area extending towards $f_{liq} = 1$. That means that changing the dust INP concentrations by several orders of magnitude has the same effect on f_{liq} statistics as changing the parameterisations of deposition nucleation onset entirely (while keeping the INPs concentration roughly the same).
We can also analyze the statistics of liquid origin by considering the ice mode number concentration instead of the ice mode mass content. However, the number concentrations are much stronger affected by the ice formation pathway than the mass content (see Section 5.3). Hence the liquid origin number fractions are even stronger skewed towards in-situ cirrus than the mass fractions.

5.4.1. Comparison of classification schemes

Table 5.2 shows the percentage of liquid origin and in-situ classified trajectories for each of the sensitivity experiments. The 'ice modes' classification uses the liquid origin mass fraction as described in Section 5.2.3. Liquid origin fraction $f_{liq} > 0.5$ classifies a liquid origin and $f_{liq} < 0.5$ an in-situ cirrus cloud. As discussed in Section 4.4.2 for the R6 experiment, the ice modes scheme identifies the WCB as mostly in-situ (84 %) with the sedimentation of DEP ice from clouds above the WCB having a large impact on the microphysical composition.
In contrast, W16 classifies the WCB as mostly liquid origin (64 %). The algorithm does not take sedimentation into account. Instead it follows a trajectory and checks if in a continuous existing cirrus cloud ($q_{tot} > q_{crit}$) LWC was present and classifies the

Experiment	Ice modes		W16	
	liquid origin	in-situ	liquid origin	in-situ
R6	16 %	84 %	64 %	36 %
R13	22 %	78 %	76 %	24 %
A1B1	11 %	89 %	60 %	40 %
A1B0	9 %	91 %	53 %	47 %
A0B1	19 %	81 %	66 %	34 %
A0B0	19 %	81 %	67 %	33 %
UL	20 %	80 %	67 %	33 %
PH	21 %	79 %	67 %	33 %
PH3	21 %	79 %	61 %	39 %
PHSK	42 %	58 %	55 %	45 %

Table 5.2.: Cirrus cloud origin following the ice modes and W16 classification for each experiment.

segment as liquid origin or in-situ otherwise. We discussed in Section 4.4.1 that this WCB case shows many cloud segments with a long life time (~ 13 h), which extend from the mixed-phase into the cirrus regime. Thus W16 classifies them as liquid origin cirrus, although they are strongly affected by sedimentation of in-situ ice formed above the WCB. However, this does not mean that the W16 classification is wrong as its focused on the impact cloud processes in mixed-phase clouds have on the cloud properties. See Section 4.4.3 for a detailed discussion.

This results holds true for all sensitivity experiments. R13 shows 6 % more liquid origin clouds classified by the ice modes scheme, but also increases the W16 liquid origin clouds by 12 %. As discussed in the previous section, the high INP experiments (A1B*) show the lowest amount of liquid origin ice (only $9-11$ %) and consequently W16 also classifies more trajectories as in-situ. However, the bias towards liquid origin classification is still there with 53/60 % of the trajectories being classified as liquid origin. The low INP experiments (A0B*) show just minor variations from R6 in favour of liquid origin for both ice modes and W16 classification.

The two experiments with different INP activation schemes, UL and PH, show $4-5$ % more liquid origin ice and proportionally W16 also classifies 3 % more of the trajectories as liquid origin. PH3, with its inclusion of soot and biological INPs, shows the same overall amount of liquid origin ice as the PH experiment with only the dust aerosol mode. This is to be expected as these additional aerosol modes are mainly active at high temperatures outside the cirrus regime (see Section 5.2.6). However, the segments with continuous cloud ice from the mixed-phase into the cirrus regime are more often interrupted, leading to the effect that W16 labels more trajectories as in-situ. We showed in Section 5.3.4 that the changes to the CCN activation in PHSK had the largest impact on the partitioning of ice modes, mostly strengthening the FRZ mode. This also reflected in the classification statistics. 42 % and 55 % are classified as liquid origin for ice modes

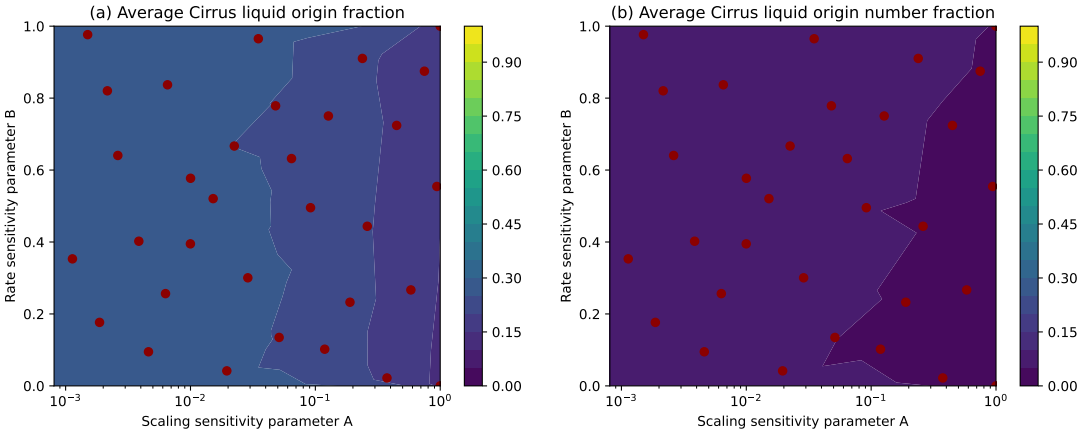

Figure 5.7.: Cirrus liquid origin mass and number fractions as function of the ensemble sensitivity parameters.

and W16, respectively. So W16 matches the classification when the ice modes scheme identifies a trajectory segment as liquid origin, but the inverse is not true.

5.4.2. Ensemble

Figure 5.7 shows the cirrus liquid origin mass and number fractions for the ensemble parameter space. Obviously neither the choice of scaling coefficient nor rate parameter has a large impact on the mean liquid origin fraction with only the mass fraction increasing by a few percent for low A. This is consistent with the previously discussed results, that the heterogeneous ice nucleation scheme has a low impact on weighing the liquid origin or in-situ formation pathway.

5.5. Discussion and Summary

The total cloud ice content q_{tot} was only marginally affected by the choice of heterogeneous nucleation parametrisation as this cloud variable is constrained by the initialised thermodynamic environment. The total cloud ice number concentration n_{tot} in the cirrus regime was more strongly affected, especially by changing the INP concentration. In general though homogeneous freezing mechanisms partly compensate for lowered heterogeneous nucleation rates. n_{tot} is overall low for the cirrus clouds compared to a global climatology (Krämer et al., 2020)
Secondary ice from rime splintering and collisional breakup were both almost equally important for the ascending mixed-phase clouds. Although using both processes enhanced secondary ice content, they are not fully additive. Droplet fragmentation was weak, but this might partially be due to its implementation. A partial integration over cloud droplet spectra (for $D_c \geq 65\,\mu m$) or inclusion of a 'drizzle' class is likely required for the inclusion of this process in bulk schemes. For pure ice clouds, all secondary ice

mechanisms were irrelevant.
We performed experiments with three different heterogeneous ice nucleation schemes: HA15, UL17 and PH08. Additionally we performed an ensemble of 34 experiments for different configurations of the HA15 scheme, where we changed the INP concentration by several orders of magnitude and the steepness of the INP-altitude profile. These changes affected n_{tot} especially in the cirrus regime. Higher INP concentrations for HA15 lead to enhanced n_{tot} and q_{tot}. The enhancement is larger for the ice concentrations n_{tot} than for the ice mass content, as the latter is constrained by the thermodynamic initialisation of the simulation. High INP concentrations strengthened the heterogeneous ice modes: immersion freezing (IMM) and deposition nucleation (DEP). Especially in the cirrus regime, DEP got even more dominant compared to other ice modes both with regards to mass content and number concentrations.
In general, lowered INP concentrations strengthen the ice modes of homogeneous freezing of cloud droplets (FRZ) and homogeneous nucleation (HOM). However, changing the INP activation scheme while keeping the concentration of INPs roughly constant, affected the ice modes on the same magnitude. This underlines the large uncertainties regarding the onset of nucleation for INPs and larger discrepancies between the heterogeneous nucleation schemes. Overall homogeneous and heterogeneous ice modes show compensating effects. Lower immersion freezing rates leads to more droplets freezing homogeneously. Higher INP concentrations (or deposition nucleation onsets on lower S_i) suppress homogeneous nucleation. Of course, these changes in the heterogeneous nucleation scheme still affect the temperature levels on which ice formation occurs.
While the distribution of ice modes were strongly sensitive to the choice of parametrisation, the competition of liquid vs in-situ formation was not. This supports our theory from the previous chapter that the ice formation pathway is mostly determined by dynamical forcing and less by the microphysical parameters. In this WCB case the cloud laying on top of the WCB strongly affects the ice phase in the ascending WCB trajectories as well as their outflow by sedimentation of in-situ formed ice.

6. WCB ensemble

6.1. Introduction

In Chapter 4 we found that the cirrus outflow of the Warm Conveyor Belt (WCB) was dominated by in-situ formed ice. Even more, in-situ ice, mostly stemming from deposition nucleation (DEP), sedimentating from clouds enveloping the WCB was strongly affecting even the ice mode composition of the ascending mixed-phase clouds. In Chapter 5 we investigated the impact of dust concentrations and INP activation schemes on the ice formation pathways. Even for low dust concentrations or more limited INP activation schemes, in-situ formed ice was still dominating the case study as homogeneously nucleated ice (HOM) concentrations got larger, if DEP ice concentrations got weaker. Thus the ice formation pathway is mostly determined by dynamic forcing and not by the number concentrations of INPs and choice of INP activation scheme.
In this chapter we want to investigate an ensemble of case studies to explore if the domination of in-situ formation pathways was just a feature of a single WCB event or if it is indicative for a larger trend. We already noted in Chapter 4 that the (fastest) ascent time τ_{600} can strongly influence the ice formation pathways, esp. that of liquid origin cirrus. We want to investigate if we can find a link between ice formation pathways and the thermodynamic starting conditions of WCB trajectories.
Observations indicate that liquid origin and in-situ cirrus show characteristic microphysical properties (Krämer et al., 2016). In general liquid origin cirrus in WCBs are expected to show a higher ice water content (IWC) than in-situ cirrus. The idea is to choose WCB case ensemble members from a climatology of the IWC at the time of (fastest) ascent. To achieve that we need WCB trajectory data for multiple years, an algorithm to find WCB outflow regions and (model) data of cloud properties, e.g. IWC. Then we can attempt to find WCB outflow features and characterize them by their average IWC (or rather the IWP as we discuss later). We can then choose an ensemble of WCB cases with different characteristic values of their cirrus outflow and investigate if those properties can be linked to the ice formation pathway. We limit ourselves to WCB events in the same domain as the main case study of this work. So they need to occur over the Northern Atlantic and Europe.
In Section 6.2 we will discuss the methodology of finding WCB outflow features and present the results of the climatology. We will also discuss fundamental issues of this method and its implementation. Section 6.3 provides an overview of the 10 ensemble experiments. In Section 6.4 we will discuss the ice mode composition and evaluate the competition between liquid origin and in-situ formation. Finally Section 6.5 contains the sensitivity analysis of the ice formation pathway to the environmental starting conditions of the WCB trajectories.

6.2. Cirrus outflow climatology

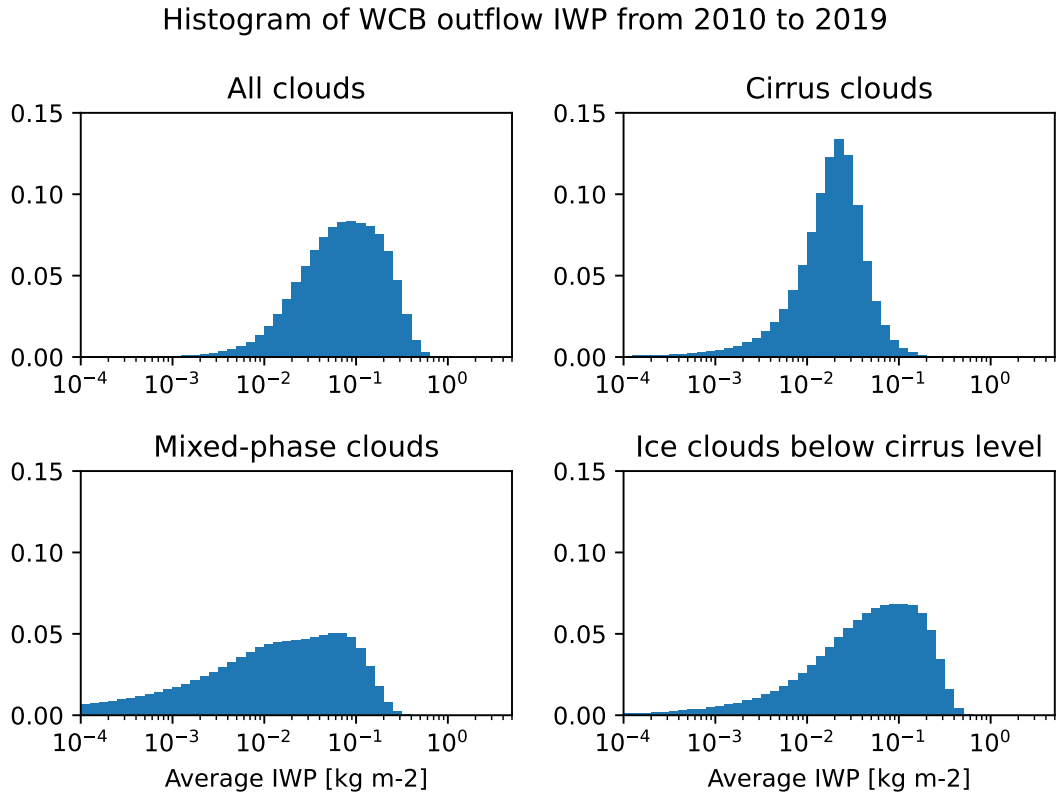

Figure 6.1.: Histograms of IWP for WCB outflow features found between the years 2010 to 2019 in the Europe and North Atlantic domain.

The data basis of this climatology is work done by A. Miltenberger and Z. Guo for the DFG funded project TPChange. They calculated 48 hour forward trajectories starting on the Northern Hemisphere from the years 2010 to 2019, driven by the ECMWF Reanalysis v5 (ERA5) dataset. LAGRANTO was used to calculate the trajectories and WCB selection was done by applying the usual requirements: ascent of 600 hPa and intersection with a surface cyclone (Joos and Wernli, 2012; Madonna et al., 2014). Surface cyclones were detected using the algorithm introduced in Section A.1 with modifications to allow cyclic boundary conditions. For each WCB trajectory the fastest ascent time (τ_{600}) was determined. The coordinates and time of the completed ascent were used to obtain a WCB outflow flag for the ERA5 dataset. The outflow mask is only applied for the single grid point where ascent is completed and not for the entire stretch of the trajectories lifetime after ascent. We reproduced the algorithm in Python 3 and applied it for WCB simulations performed with the atmospheric model ICON and the ice modes microphysics scheme.

ERA5 only uses a single moment microphyiscs scheme, thus only predicts the mass content of ice particles. Hence there are two cloud properties, which characterize the (cirrus) cloud at the WCB outflow: IWC (Ice Water Content) and IWP (Ice Water Path). IWC provides a snapshot of the (cloud) ice mass at ascent and, as explained earlier, should be a indication of the ice formation pathway. IWP includes a representation of the cloud ice above and below the outflow point by vertical integration. In Chapter 3 we showed the significance of sedimentation for the microphysical composition of the ascending WCB cloud band. In that sense IWP might provide a better representation of the outflow region. Additionally for IWP, we do not need information about the model level on which the WCB trajectories completed their ascent. In this work we chose IWP as a signature parameter for the WCB outflow climatology.
We calculated IWP by vertical integration of IWC assuming hydrostatic equilibrium. For ICON data we integrate over the geometric altitude and for ERA5 data over pressure levels. IWC is provided as a parameter in ERA5. For our ice modes microphysics scheme in ICON we calculate IWC by summing over all ice particle classes: the five ice modes as well as snow, graupel and hail. We utilize masks to obtain IWP that only considers specific cloud types. By only including grid points where liquid water is present ($\mathrm{LWC} > 0.1\,\mathrm{mg\,kg^{-1}}$), we obtain mixed-phase IWP. Only including grid points where temperature is below the cirrus temperature level ($T < T_c = 235\,\mathrm{K}$) we obtain cirrus IWP. The latter is especially useful for the WCB outflow climatology since the (total) IWP also considers ice content below the outflow which can be caused by other synoptic and local events and is not necessarily representative for the WCB outflow.

6.2.1. Climatology

Figure 6.1 shows histograms of IWP for WCB outflows masked for different cloud regimes. The data is obtained as explained in the previous section for the ERA5 dataset from the years 2010 to 2019 limited to the North Atlantic and Europe domain. The IWP bins start at 10^{-6} and extend logarithmically in 60 steps to $1\,\mathrm{kg\,m^{-2}}$. Cirrus IWP shows a log-normal distribution centered at $2 \cdot 10^{-2}\,\mathrm{kg\,m^{-2}}$ with a slightly longer tail towards lower IWP.
The mixed-phase cloud IWP does not show a distinct distribution type with values extending from 10^{-4} to $10^{-1}\,\mathrm{kg\,m^{-2}}$. This is not surprising since the outflow points of WCB are usually at an altitude where the temperature is to low for the liquid phase to (co-)exist. Hence these mixed-phase clouds are below the cirrus outflow. While sedimentation might affect the mixed-phase clouds below the WCB outflow, there are likely mostly influenced by local events such as convection or synoptic events and thus only weakly related to the WCB.
The histogram for the (pure) ice clouds below cirrus temperature level is more relevant. We are usually interested in the cirrus clouds. However, in the previous chapters we already established the importance of the cloud layer between mixed-phase and cirrus clouds. It can be seen as a transition phase, carrying signatures, in terms of ice mode composition, from the mixed-phase and cirrus regime. In this temperature region ($253 - 235\,\mathrm{K}$) we can expect the onset of in-situ ice nucleation. Sedimentation of (cirrus)

cloud ice from above can also affect the composition here. However, note that ERA5 only uses a 1-moment bulk scheme and as such does not resolve sedimentation and size sorting well (Wacker and Seifert, 2001). More importantly though this sub cirrus temperature region ($T < 235\,\mathrm{K}$) might be the altitude where a large portion of the WCB trajectories complete their 600 hPa ascent and only with subsequent rising do they reach the cirrus temperature level. This of course also depends on the definition of the outflow. We can simply use the pressure (or altitude) level where the trajectory completed the 600 hPa ascent. However, the trajectory might still continue to ascend. For that reason one can shift the outflow point to a later time step as long as the trajectory is continuously ascending by at least $8\,\mathrm{hPa\,s^{-1}}$. Even that definition has its issues since some trajectories might dip for a short while and than ascend again. Overall it might be better to only consider the IWP of all pure ice clouds without a subdivision of cirrus and 'sub cirrus'.

6.2.2. Outflow feature tracking

The WCB outflow mask provides the coordinates and time where a WCB trajectory fulfills the τ_{600} criterion, but it does not provide a relationship between the outflow points. This algorithm is an attempt to find outflow features that belong to a single WCB event. We try to achieve this by clustering the outflow points with regards to their spatial coordinates and time. We iterate through all grid points marked as outflow in the ERA5 files. They are provided as hourly data from the year 2010 to 2019. First we group all outflow points that are adjacent to each other and save their average IWP as well as their coordinates and number of outflow points as a feature object. We consider both the (total) IWP and cirrus IWP. If the average IWP is too low ($< q_{crit}$), indicating that no or only few clouds are present, the feature is discarded.
Now we iterate over all features and check if other outflow features are occurring within a threshold time step. Next we check if they are within clustering distance. The distance is calculated with the haversine formula between the focal points of the two features. If both checks are true the features are added to the same WCB event object and marked as used. If there are no more outflow features to be found that fulfill the requirements the WCB event is saved with the average (cirrus) IWP, upper and lower limit of the IWP and the coordinates of outermost outflow points. The WCB events were sorted first by year and second by their average IWP. The latter is attributed to a mass bin within the range introduced for the climatology in Section 6.2.1.
The threshold values for associated outflow features were 1 h between start and end of the respective features and 2000 km for the great-circle distance between the focal points. Of course, these values are highly subjective and were chosen based on the clustering of outflow features for only few example cases.
While employing the outflow tracking we encountered several issues with this method and for the comparison of WCB outflow features in ERA5 and ICON. We will elaborate on these problems in the next sections.

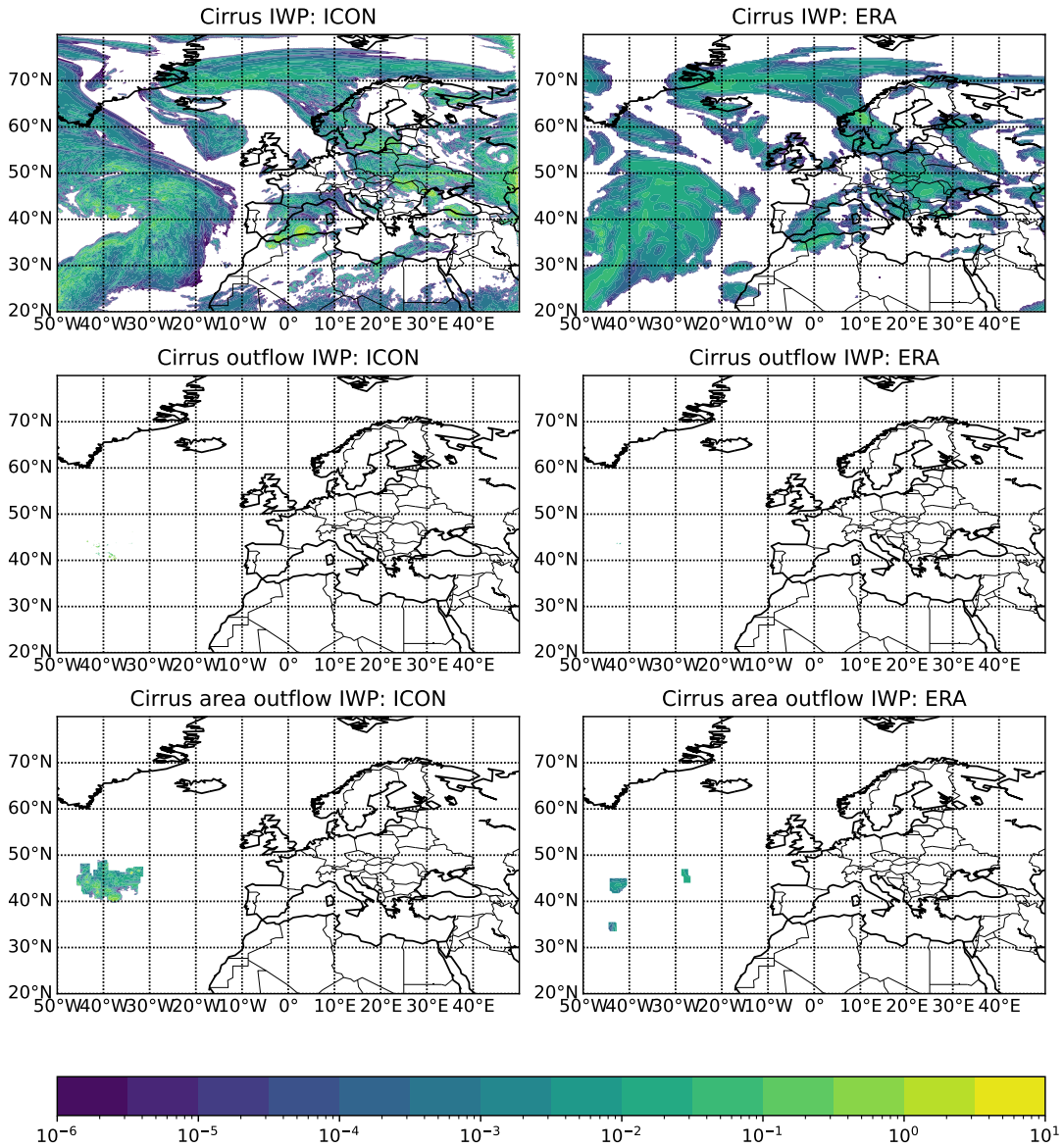

Figure 6.2.: Comparison of cirrus IWP [$\mathrm{kg\,m^{-2}}$] between ICON and ERA5 for the 'Bin 52' case at 2011-06-09 23:00 UTC. The panels in the second and third row mask IWP by the WCB outflow and area around the WCB outflow, respectively.

6.2.3. Outflow sampling

Table 6.1 lists the 10 experiments of this study. For this section we will focus on the average IWP of the outflow in ERA5 and ICON. Figure 6.2 shows the cirrus IWP in comparison between ICON and ERA5 for experiment 'Bin 52'. The panels in the second row show the IWP for all points in the outflow region and the panels in the third row for all points in an area of 0.75°x0.75° (latitude/longitude) around the outflow points.
The second row in Fig. 6.2 shows the IWP for all grid points where an WCB outflow was detected in the ERA5 and ICON data. Apparently, there is not much to see. On closer observation we note some outflow points between 40°N and 50°N at 40°W. For this snap shot we observe more outflow points for the ICON, but for other dates the opposite is true. In general we found that outflow masks rarely form a coherent region neither in space nor time. This is problematic for feature tracking since it makes it harder to define which small collection of, often singular, outflow points belong to the same WCB. While plotting the entire (or even just partial) package of WCB trajectories reveals a coherent air stream (see, e.g., Figure 6.3), the time step at and grid point in which singular trajectories complete their ascent varies strongly.
The next problem is the grid resolution. Naturally a coarser grid can lead to a larger area being marked as WCB outflow since a single ascending trajectory is enough to mark the grid point no matter is size. On the other hand multiple trajectories marking the same grid point by completing the ascent during the same time step in a small area do not increase its relevance. Overall utilizing finer grid resolutions and starting an appropriately amount of trajectories (e.g. at each grid point) should alleviate this problem to some degree.
The output files for ICON are only available every 30 min and for ERA5 every 60 min. Similar to the problem with spatial grid resolution, the time step to which the ascent is attributed can thus vary. In this study we attributed the ascent to the model output step closest to the ascent time. However, even for our ICON data this means that the ascent can be up attributed to a time step up to 15 min earlier/later than the time when the trajectory actually completed their ascent. In this study we use a physical time step of 40 s for the ice mode microphysics scheme in ICON. Many microphysics processes operate on that or even shorter time scales. Hence the cloud properties can change significantly between the time where the trajectory actually completes its ascent and the time it is recorded (and model data is available).

6.2.4. Comparison between ERA5 and ICON

Table 6.1 lists the average IWP of the outflow for each case study in ERA5 and ICON. The average outflow IWP in ICON is mostly between 2 and 5 times larger than that of the WCB outflow in ERA5. For experiment 'Bin 52' and 'Bin 55' even 13 and 15 times larger, respectively. In general we can not proclaim that the inter-case variability is smaller than the difference between ERA5 and ICON of a singular case.
This could be caused by several issues. The grid horizontal resolution of the ICON dataset (0.075°) is finer than that of the ERA5 dataset (0.25°). For comparison it would

be better to regrid ICON data to the ERA5 grid. However, the third row in Figure 6.2 shows an area of 0.75° around the outflow masks and still both masks do not match even closely. Hence regridding would solve this issue only partly.
With the large discrepancy in grid resolution and time steps, we can hardly expect that ERA5 and ICON share the same realisation of atmospheric dynamics. Even if the general evolution of WCB trajectories of the ERA5 and ICON runs look (mostly) the same, the ascent criteria marking the outflow are still to specific and highly variable as to expect that both models would mark similar regions at the same time step.
Another problem gets apparent when we compare the domain wide IWP of both simulations as shown exemplary in the first row of Fig. 6.2. The WCB outflow region for Experiment 'Bin 52' extends from 32.5°N to 55°N and 45°W to 10°W. The general outline of the cloud fields roughly matches for both models, but ICON shows a significant gap of clouds where the cold sector is located. The structure of ICON clouds is also more finely resolved, showing regions of high IWP near the cyclone center and low IWP on the outer edges of the cloud band. The cloud field of ERA5 is more homogeneous.
Due to the large differences of both the atmospheric and especially the (micro-)physics model components of ERA5 and ICON, we did not expect the WCB outflow properties do closely match. Though, there was hope that they are closely related enough, that the inter-case variability is larger than the variability between the models. However, we can still use ERA5 data to find promising WCB cases for (high-resolution) ICON studies by studying the trajectory data and not just the outflow points themselves. Similar we could extend the analysis of the outflow from ascent until the end of the trajectory lifetime as long as the trajectory does not significantly descent. Adding other statistical properties like standard deviation might also help with the classification of outflow features.

6.3. WCB ensemble

Table 6.1 contains a list of all 10 ensemble member labeled as the bin in which the average IWP of the initial outflow for the ICON simulation lies in. The ensemble member were chosen from the list of WCB events obtained with the feature tracking in Section 6.2.2. The timestamps listed as date show the beginning and end of the WCB outflow feature. All WCB cases occurred between the years 2011 and 2012, mostly in summer and autumn. Region labels the corner points of an (rectangular) box that fully covers the WCB outflow region. The average IWP of the cirrus clouds at the time and point of ascent is calculated for all start times for the ERA5 and ICON datasets. The outflow time and region for both ERA5 and ICON was calculated by using the algorithm introduced in the previous section.

6.3.1. Model setup

We use the same R03B08 grid in limited area mode as described in Section 4.2.4, which covers most of the North Atlantic and Europe up to 50°E. The physics time step also remains the same with 40 s. However, the simulation duration varies for each experiment.

Name	Avg. IWP [kg m^{-2}]		Date	Region
	ERA5	ICON		
Bin 44	1.44e-02	2.96e-02	2011-09-01 09 + 17 hr	40°W 12.5°E 47.5°N 55°N
Bin 45	1.98e-02	3.33e-02	2012-09-03 22 + 14 hr	30°W 40°E 60°N 75°N
Bin 46	2.38e-02	4.87e-02	2012-09-24 03 + 19 hr	22.5°W 40°E 45°N 65°N
Bin 47	1.85e-02	6.12e-02	2012-06-26 05 + 12 hr	10°E 50°E 45°N 75°N
Bin 49	3.45e-02	8.06e-02	2012-12-21 00 + 24 hr	40°W 0°E 12.5°N 62.5°N
Bin 50	2.26e-02	9.52e-02	2011-06-03 03 + 19 hr	45°W 5°E 32.5°N 70°N
Bin 52	1.57e-02	2.00e-01	2011-06-10 12 + 18 hr	45°W 10°W 32.5°N 55°N
Bin 53	3.46e-02	2.46e-01	2012-11-13 02 + 14 hr	20°W 10°E 25°N 50°N
Bin 54	5.75e-02	2.91e-01	2012-09-30 03 + 27 hr	45°W 15°E 30°N 75°N
Bin 55	2.12e-02	3.26e-01	2012-04-10 13 + 28 hr	5°W 50°E 30°N 70°N

Table 6.1.: List of all ensemble member with average IWP for cirrus outflow at ascent for ERA5 and ICON. Included are the date range and corner point of the outflow region.

The start time was chosen such that we begin 48 h prior the earliest date of the outflow feature with an additional 4 to 6 h initialisation phase. The latter depends on a convenient start date available from the IFS model, which is only provided in 6 h increments. As for the other ICON simulations in this work, IFS is used as initial and boundary data. The shortest and longest simulation run for 66.5 and 84.5 h, respectively.
The choice of physical parametrisations is also the same as described in Section 4.2.4. Hence only rime splintering is used as secondary ice mechanism and heterogeneous nucleation is governed by the parametrisation of Hande et al. (2015). The boundaries of the cyclones and cirrus outflow regions vary between the ensemble member from 45° to 50°W and from 12.5° to 75°N. While it would be more realistic to choose an dust INP profile appropriate for the geographic region (Atlantic Ocean vs Continental Europe and North Africa) and season (Summer vs Autumn / early Winter) we chose to use the standard ICON setup for the two-moment scheme as described in Section 2.3.4. The main reason for this choice is to make the results directly comparable to our work in Chapter 4 and the sensitivity analysis in Chapter 5. The differences in the distribution of the ice modes will then mainly be governed by the different (thermo-)dynamical drives of each WCB case.

6.3.2. Trajectories selection

The trajectories were again calculated offline with LAGRANTO (Sprenger and Wernli, 2015). For each case a broad outflow area was chosen based on the WCB outflow features described in Section 6.2.2. We checked for each case if a distinct cloud band was visible in the Meteosat level 1.5 data products (Meteosat Visible and Infrared Imager for 12:00 UTC) archived as EUMETSAT Data. Additionally we confirmed with archived DWD surface analysis products (surface pressure isolines with front analysis) that there was

indeed a cyclone with frontal activity located inside the model domain. In many cases we applied additional selection criteria to exclude trajectories that belong to other WCB or convective events, which intersected with the only broadly defined outflow regions in Table 6.1.
Trajectories were started inside a rectangular box around the outflow area (with corner points provided in Table 6.1) on a equidistant grid of 13 km on each of 8 altitude levels ranging from 6976 to 10 782 m. Trajectories were started each hour within the outflow time range (see Table 6.1) and ran backwards for 48 h. We applied the established WCB criteria: ascending 600 hPa and crossing a surface cyclone (Joos and Wernli, 2012; Madonna et al., 2014). Additionally we excluded all trajectories that passed through domain boundaries.

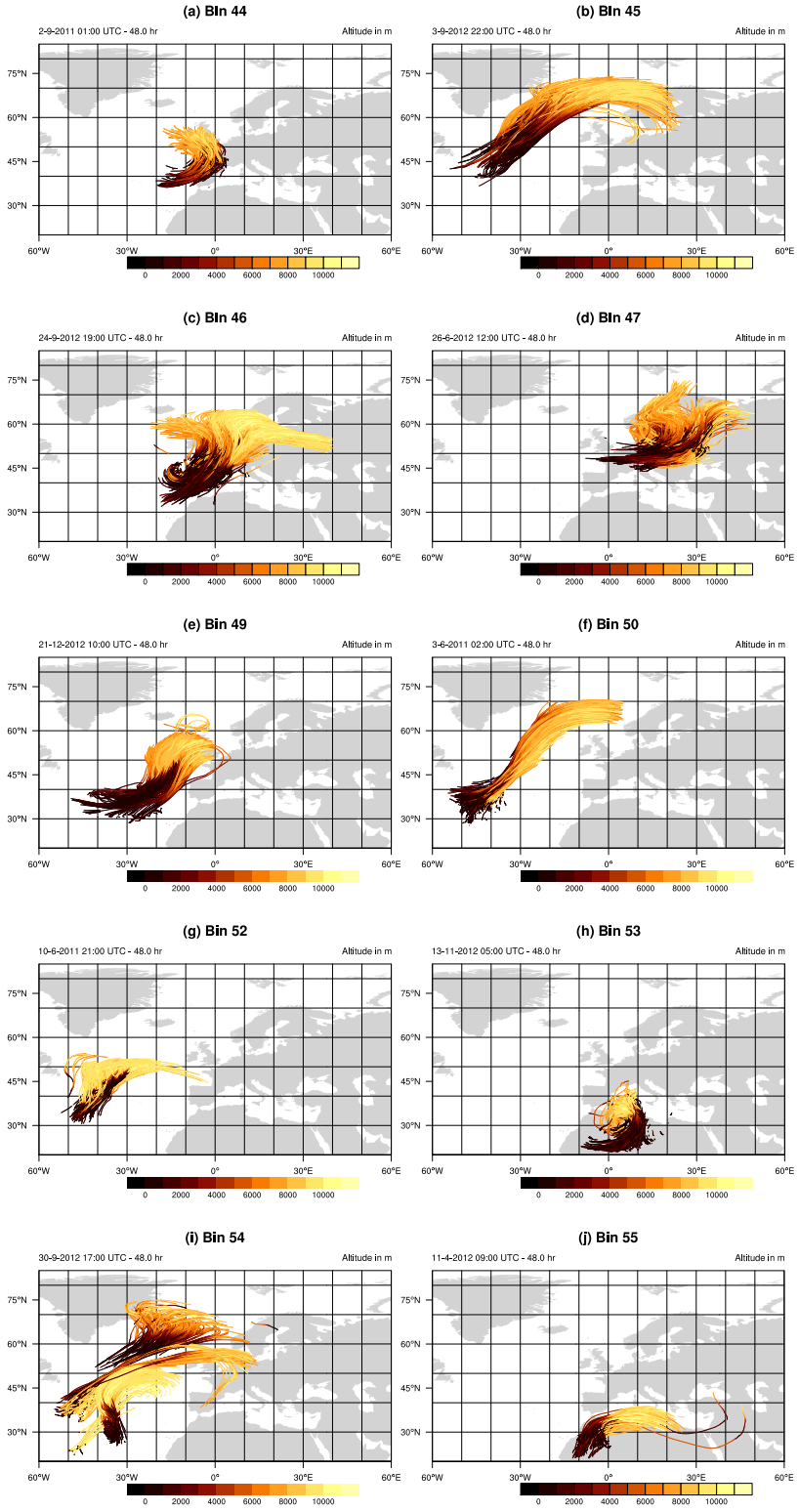

Figure 6.3.: Overview of representative WCB trajectories for each experiment.

6.3.3. WCB trajectories overview

Figure 6.3 shows an impression of the temporal evolution of WCB parcels for each ensemble member. The start dates with the most trajectories were chosen for this representation and only 5 % of those evenly sampled trajectories are displayed. The purpose of this overview is not to provide an in-depth insight of each synoptic situation and the cyclone life cycle preceding the WCB event. Rather we want to highlight the position of the WCBs and there associated cyclones as well as the origin of their ascending air streams and outflow regions.
The first case, 'Bin 44', shows only a small horizontal extension of the WCB in comparison to the other ensemble members. The start region of the ascent is located east of Spain. The WCB was caused by an extended occluded front caused by a strong cyclone located at Iceland. The cyclone was stemming from an extra-tropical transition of Hurricane Irene, which had devastating impacts on the Caribbean and the United States.
In early September 2012 a strong cyclone located at Iceland caused strong lifting of air masses from the North Atlantic to an outflow region above the Greenland Sea and Norwegian Sea as well as Scandinavia. The trajectories of case 'Bin 45' form a tightly packed band typical for WCBs. The cloud field of the cyclone is also distinctly visible in the Meteosat images of the 3th September 12 UTC.
In case 'Bin 46' sees the cyclone is located above the Atlantic Ocean west of Spain and North Africa. It developed as a secondary cyclone of the former hurricane 'Nadine', which was located above the Azores at that time. Nadine is famous for being one of the longest living tropical storms in weather records with a life time of 24 days. Nadine did undergo multiple transitions from tropical storm to hurricane, to an extra-tropical cyclone and again regeneration to a tropical storm. The secondary cyclone formed by Nadine showed strong WCB activity with a vast outflow region stretching from the British Isles to Scandinavia and Eastern Europe.
In case 'Bin 47' two cyclones were present: one located above the North Atlantic and another above the North Sea. Both cyclones showed strong frontal activity with extended warm sectors. We will focus on the cyclone located above the North Sea, where the passage of the occluded front caused a strong lifting of air masses with three WCB outflow regions: over Scandinavia, Northeastern Europe and one air stream is circled back into the ascent region. The other cyclone also produced a WCB with its occluding cold front. The latter WCB had its outflow located partly above the ascent region of the eastward cyclone. We investigate the latter cyclone here. It is likely that sedimentation of ice from the west-most WCB will impact the microphysical composition of the WCB of interest.
The case of 'Bin 49' was dominated by a large cloud field covering the North Atlantic, the British Isles and most of Northern Europe. As such we could not detect the WCB cloud band easily by using satellite images. However, the trajectory analysis reveals a WCB caused by a cyclone, which center moved along 45°N towards Spain, where it dissipated. The outflow region was mostly located above the British Isles.
The synoptic situation for case 'Bin 50' was governed by a persistent and large high pressure system above Europe, which blocked cyclones and deflected them northward.

One such cyclone caused air masses to rise in the Northern Atlantic and, grazing the boundaries of the high pressure system, pushed them to an outflow region over the Norwegian Sea.
The WCB in the 'Bin 52' case was caused by a low intensity cyclone jammed between two large high pressure systems over the Northern Atlantic and Greenland, respectively. Frontal activity pushed air from the center of the Atlantic high pressure system rapidly into the upper troposphere where it was deflected eastward. Both the WCB and it is outflow region were entirely located above the ocean.
The next case, 'Bin 53', describes a cyclone that was situated above Northern Africa. The trajectories stayed in the planetary boundary layer for a longer time until they ascended rapidly. The outflow was located close to the cyclone center with a distinct cloud band following the cyclones contours in a Meteosat satellite image. Our algorithm also identified an additional air stream rising quickly above the North Atlantic at 45°W, that is directed into the outflow region, likely caused by a frontal passage from a more northern cyclone. We excluded the latter air stream from this analysis.
In case study 'Bin 54', two cyclones of interest moved along the 60th circle of latitude from Canada towards Northern Europe. The WCB can be attributed to the later cyclone and its occlusion began early on the 30th September when the central pressure minima was located at 45°W. The cyclone center stopped at Iceland and stayed there until dissipation. Two WCB trajectory packages are associated with this case. A slowly ascending WCB forced by the occluded front with an outflow region above the Norwegian and North Seas. Notably, the average outflow altitude of the outflow is in general lower compared to the other cases. An additional package of rapidly ascending air parcels, that fulfill the WCB criterion, was located in the warm sector at 30° N. These trajectories stay fully above the Atlantic Ocean.
Case study 'Bin 55' showed strong cyclonic activity in the entire Continental Europe domain for early-mid April. A cluster of cyclones lead to multiple fronts being detected simultaneously causing the occurrence of 3 WCBs. The outflow regions of WCBs were partly overlapping so we selected trajectories such that (mostly) only a single distinct and dense WCB trajectory package remained. The chosen trajectory package starts above North Africa and has its outflow area above the Mediterranean sea.
Of all the WCB cases five of the ascending air masses are oceanic, two start over North Africa, one over Central Europe and the last two are partly oceanic and partly continental.

6.4. Ice phase in the WCB ensemble

6.4.1. Mixed-phase clouds

Figure 6.4 and Figure 6.5 show the cloud composition of mixed-phase clouds for each experiment and each start time with respect to integrated mass content and integrated number concentrations, respectively.
Experiment 'Bin 44' (Panel (a)) shows a high mass ratios of SEC ($\sim$ 22 %), IMM ($\sim$ 40 %) and DEP ice ($\sim$ 35 %) with only traces of FRZ ($\sim$ 2 %). These ratios are mostly independent of the start time. The cloud ice number shows high fractions for SEC and FRZ and low ratios for IMM and DEP. They show a larger variation with start time than the mass ratios. We note that DEP shows high mass and low number ratios, which hints that the DEP mode has a large mean size and thus high sedimentation rates. This overall cloud composition is very similar to the main case study of this work, introduced in Chapter 4. The DEP ice has to stem from clouds above the WCB as deposition nucleation does not trigger within mixed-phase clouds (see Section 2.3.4). The occurrence of low FRZ mass to high FRZ number ratios was discussed in Chapter 5. IMM has strong sinks in aggregation, riming and removal by sedimentation. The dominance of SEC from rime splintering was discussed for idealised simulations (see Chapter 3) and in comparison to different secondary ice mechanisms (see Sections 3.7.3 and 5.3.2). Since the structure of the mixed-phase clouds in all ensemble cases are similar, will we use experiment 'Bin 44' as a reference for the others and mostly highlight the differences.
Experiment 'Bin 45' (Panels (b)) shows mostly the same ratios as 'Bin 44' with SEC is making up $\sim$ 25 % of the mass budget, IMM contribution is larger with $\sim$ 65 % and DEP is less important with 5 to 12 %. For cloud ice number ratios, SEC shows even larger ratios, while FRZ contribution's are mostly small in terms of number ratios.
The mass and number ratios for experiment 'Bin 46' (Panels (c)) shows a temporal evolution with DEP ratios becoming larger and IMM smaller for later start dates. The majority of the cloud ice number budget stems from FRZ with a maximum in ratios of up to 66 %.
Experiment 'Bin 47' (Panels (d)) shows for all start times a consistent amount of DEP with number ratios of up to 12 %. Steady sedimentation of DEP ice into the mixed-phase clouds might be a result of the WCB outflow of another cyclone that overlaps with the ascending trajectories as described in Section 6.3.3. As for 'Bin 45' the SEC ice mode again takes the majority of the cloud ice number budget.
Experiment 'Bin 49' (Panels (e)) sees a strong increase of DEP ice with later start dates and features overall the highest number budgets of SEC ($\sim$ 65 %) and IMM ($\sim$ 23 %) with FRZ being largely irrelevant.
Experiment 'Bin 50' (Panels (f)) similar to 'Bin 47' is being characterized by high ratios of DEP in terms of mass (up to $\sim$ 55 %) while SEC and FRZ are the most prominent ice modes with regard to cloud ice number ratios.
Experiment 'Bin 52' (Panels (g)) is the first of the ensemble member where FRZ is consistently contributing more than $\sim$ 75 % to the cloud ice number budget. However, the majority of the mass budget is comprised of the IMM mode. SEC is also weak in terms

of cloud ice number ratios, but still relevant in terms of mass ratios.
Experiment 'Bin 53' (Panels (h)) shows low DEP and SEC ratios (for mass and number budgets) but higher IMM and especially FRZ ratios. The low SEC ratios are hard to explain as graupel ratios are similarly large as for other ensemble member (not shown here). It might the case that riming mostly occurs outside the Hallet-Mossop temperature zone. Sedimentation of DEP seems to be less important for this case, which is also interesting as 'Bin 53' shows one of shortest WCB clouds band and mostly stays stationary close the cyclone center before ascending. We might assume that for such a case, there would be more time and opportunity for ice to sediment from clouds above the WCB ascent region. However, this is not the case here.
Experiment 'Bin 54' (Panels (i)) returns to more typical distributions of ice modes for mixed-phase clouds found in these ensemble. Although SEC cloud ice number ratios are still lower than for the first six ensemble member.
Experiment 'Bin 55' (Panels (i)) features the most start dates and is noteworthy for IMM being consistently the most dominant ice mode with respects to the mass ratios, and FRZ with respect to number ratios. The latter contributes more than 80 % to the number ratios for all start dates.
It is inherently difficult to link the distribution of the ice modes in the mixed-phase clouds to the geographic start region, extension of the cloud band or duration of the WCB ascent. However, all ensemble member show the same general cloud compositions of the mixed-phase clouds as found in the previous WCB case study. Like the previous case study, all ensemble member show signatures of DEP ice nucleation above the ascending WCB, which sediments into the mixed-phase clouds. Riming is active in all cases leading to SEC dominating the cloud ice number ratios in 5 cases. Similarly the FRZ mode is characterized by low mass, but high number ratios. This too is consistent with our findings in Chapters 3 and 4.

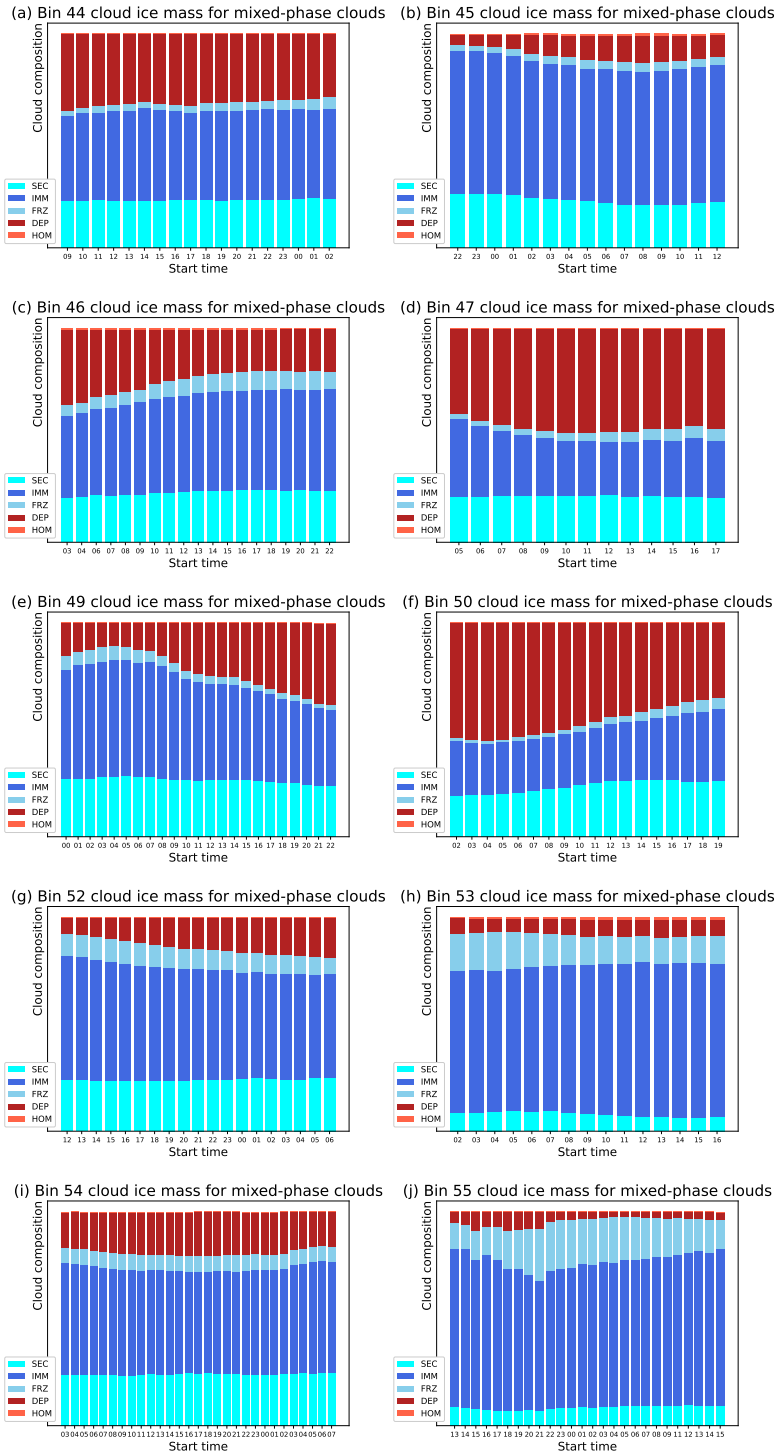

Figure 6.4.: Cloud (mass) compositions for mixed-phase clouds. Shown are all trajectories of the respective start date.

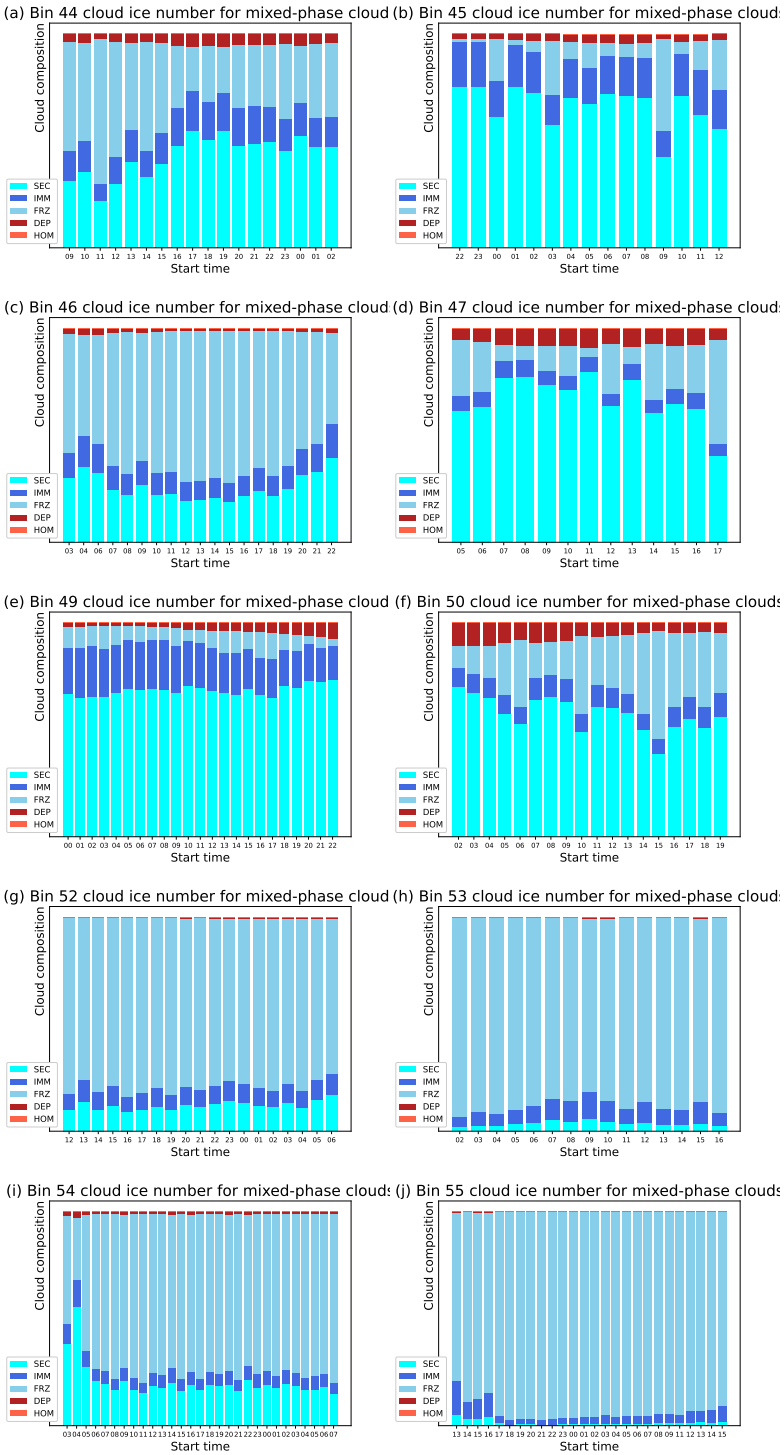

Figure 6.5.: Cloud (mass) compositions for mixed-phase clouds. Shown are all trajectories of the respective start date.

6.4.2. Cirrus clouds

Figure 6.6 and 6.7 show the cloud composition of cirrus clouds for each experiment and each start time with respect to mass content and to number concentrations, respectively. This plots represent integrated cloud ice mass content or number concentrations for each start date in the cirrus regime. Thus the ratios give an impression how much each ice mode contributes relatively to the cloud ice mass and number budgets in the cirrus outflow. While all WCB cases show the same general structure for their mixed-phase clouds, the cirrus clouds present a larger variation in cloud composition.
DEP is relevant for all WCB cases with respect to mass ratios. 'Bin 45', 'Bin 47', 'Bin 49' and 'Bin 50' (Panels b, d, e and f) show both high DEP mass and number ratios. 'Bin 45' and 'Bin 47' show consistently more than 80 % contribution of DEP to the total ice mass budget. 'Bin 49' and 'Bin 50' reach similar values but they increase or decrease, respectively, with time. The cloud ice number ratios are also high for this four ensemble members. Although they show more variation and, in general, lower ratios for cloud ice number than for mass budgets. All other ensemble members show overall intermediate (20 %) to high (> 60 %) mass ratios of DEP as well. But DEP ice number ratios are much smaller (< 5 %). Hence for many ensemble members even in the cirrus regime, DEP still shows typical signatures of sedimentation: high mass, but low number ratios, which hint at large mean sizes and thus high sedimentation rates. That may be caused by nucleation and subsequent sedimentation of DEP ice in nucleation zones located above the outflow, in regions that are not associated with WCB trajectories.
Ratios of HOM for both, mass and number budgets, are overall low. This ice mode is only really relevant in terms of overall contribution to the cirrus clouds for the four ensemble members where DEP was dominant ('Bin 45', 'Bin 47', 'Bin 49' and 'Bin 50') with number ratios up to 25 % in one case but mostly below 5 % for all other cases and start dates. Higher HOM ratios seems to be favoured for ensemble members, where in-situ ice formation pathway for cirrus clouds in general is favored. Hence, in such cases where DEP is already the dominant ice mode. DEP nucleation is limited by the availability of INPs. If INP are depleted HOM nucleation can trigger if ice supersaturations S_i are sufficiently high and there was no opportunity for INP concentrations to reset under cloud free conditions (see Section 2.3.3 for details). In all other cases where HOM is not present, there are likely enough INP available for DEP and other (liquid origin) ice modes to deplete S_i before the homogeneous nucleation threshold is reached.
IMM is present in all ensemble members with mass fractions ranging from ~ 5 % to ~ 25 %. The number ratios though are very low for all cases and all times (usually < 1 %). These are likely residuals of the mixed-phase cloud regime, where IMM already showed low number ratios. Although it is also possible that IMM gets mixed into the WCB outflow by convection and turbulent mixing.
FRZ is an important ice mode for all ensemble member especially with respect to number ratios. This ice mode strongly dominates the number ratios for 6 cases: 'Bin 44', 'Bin 46' as well as 'Bin 52' through 'Bin 55'. The importance of FRZ was also apparent in our idealised simulations of deep convection in Chapter 3. There the heterogeneous nucleation scheme produced not enough INP to freeze all cloud droplets heterogeneously,

leading to a large number of droplets being frozen homogeneously. They were also located mostly in the pure ice parts of the cloud above the mixed-phase layer but below the cirrus temperature level. FRZ in our main case study (see Chapter 4) was mostly present in the transition regime between mixed-phase and cirrus clouds.
SEC, here only included as secondary ice from rime splintering, is as expected absent from the cirrus clouds despite its high mass and number ratios for the mixed-phase regime. Rime splintering only occurs in the Hallet-Mossop temperature regime and is removed from the WCB trajectories through sedimentation and other sinks before the trajectories complete their ascent and further reach the cirrus regime.
Based on the integrated cloud ice mass contents in this section, we can evaluate how much of the overall cloud ice stems from each formation pathway. For three cases, 'Bin 52', 'Bin 53' and 'Bin 55', the cloud ice mostly stems from liquid origin ice modes (IMM and FRZ), with FRZ showing a higher contribution. Three other cases, 'Bin 44', 'Bin 46' and 'Bin 54', show a split around 30 to 50 % between liquid origin and in-situ ice modes. 'Bin 45', 'Bin 47' and 'Bin 50', feature mostly ice from in-situ formation pathways, especially from DEP. 'Bin 49' shows more liquid origin ice for early start dates, but shifts to mostly in-situ ice modes for the later start dates.
Though, we have to emphasize that these mass and number ratios do not present information of the absolute amount of cloud ice from each formation pathway. Neither do they provide information about the coverage and spatial distribution of the ice modes. We will discuss these properties in the next sections.

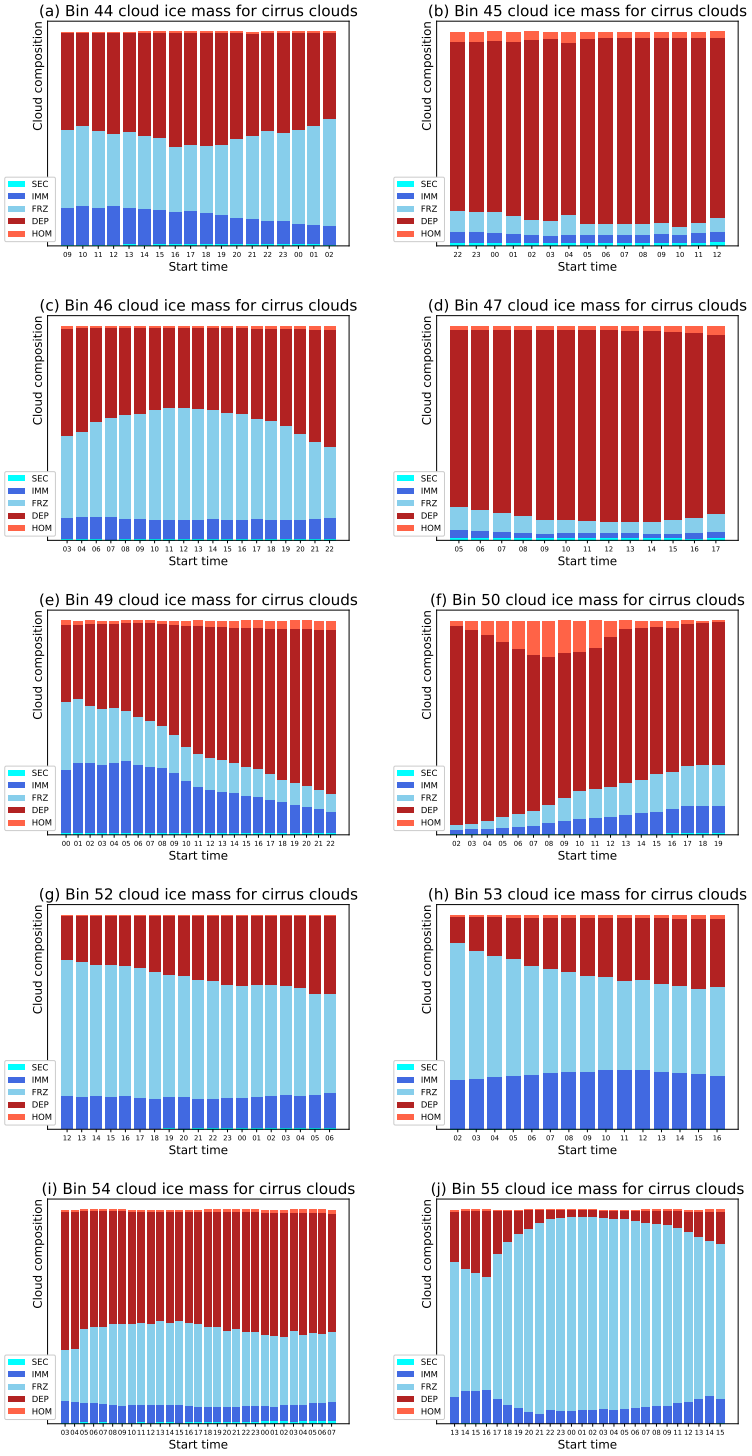

Figure 6.6.: Cloud (mass) compositions for cirrus clouds

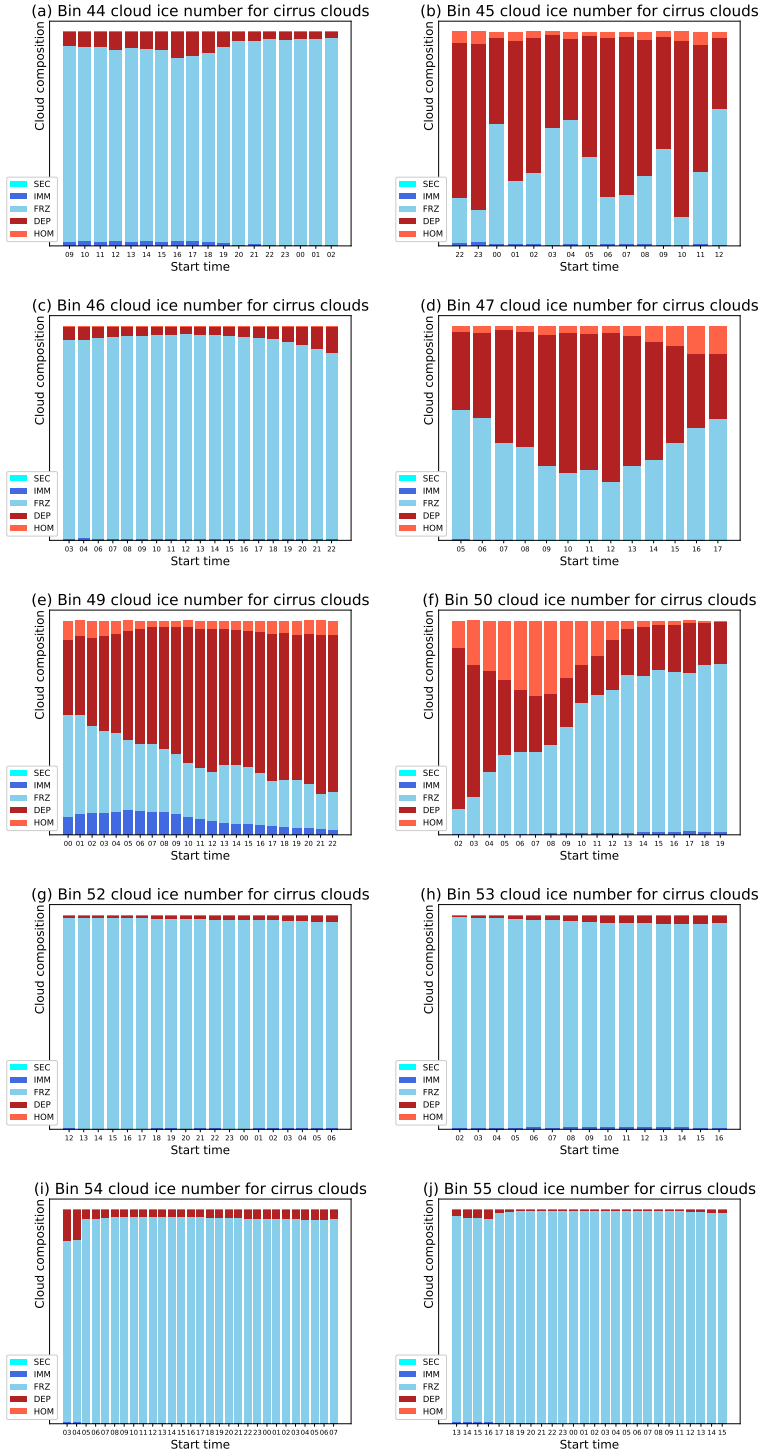

Figure 6.7.: Cloud (mass) compositions for cirrus clouds

Experiment	LIQ	NLIQ	HET	IMM	FRZ	DEP	HOM
Bin 44	32	19	74	10	18	58	5
Bin 45	19	5	81	8	8	67	8
Bin 46	30	21	72	7	20	60	5
Bin 47	19	4	82	8	9	69	7
Bin 49	28	13	79	11	13	60	5
Bin 50	16	7	84	6	7	73	7
Bin 52	38	27	67	10	25	53	5
Bin 53	50	44	60	14	33	41	5
Bin 54	27	12	76	9	14	62	6
Bin 55	65	65	39	7	56	31	3
R6	20	5	79	8	8	64	9

Table 6.2.: List of average cirrus mass fractions for each experiment in %. LIQ donates the liquid origin fraction f_{liq}. NLIQ donates liquid origin number fraction fn_{liq}. HET donates the heterogeneous ice fraction f_{het}.

6.4.3. Liquid origin and heterogeneous ice fractions

Table 6.2 lists the average liquid origin and heterogeneous cirrus ice mass fractions for each experiment as well as the individual average mass fractions of each ice mode (except SEC). In contrast to the distribution of ice modes in Figures 6.6 and 6.7, this table lists the average and not the ratios of integrated mass content and number densities. Hence, it gives a representation of how much of the cirrus cloud volume stems from each formation pathway, without weighing the statistics by the 'thickness' of the clouds. The ice mode fractions are defined in Section 5.2.2. The main case study of Chapters 4 and 5 is included with the label 'R6' for reference. 'R6' uses the same model setup as the experiments of the WCB ensemble in this chapter. Appendix A.7 contains histograms of the ice modes within the cirrus outflow as function of temperature.
Of the 10 ensemble member in this chapter, 7 (marked in red) show that cirrus in the outflow mostly stems from the in-situ formation pathway ($LIQ < 33\,\%$). As discussed before the liquid origin number fraction (NLIQ) is more strongly inclined towards an extreme than the mass fraction. These 7 in-situ cases show similar statistics as the WCB case from the previous chapters, 'R6'. The cirrus cloud ice stems to a large majority from the DEP mode with contributions of IMM and FRZ being small. 'Bin 54' is an interesting case in that average fn_{liq} is small ($NLIQ = 12\,\%$) although the FRZ mode was dominating in terms of number ratios (compare Figure 6.7 (i)). This means that a large number concentration of cloud ice stemming from FRZ, which makes up the majority of the integrated cloud ice number ratios ($f_{frz} > 90\,\%$), is focused on a overall small percentage of the cloud volume ($V_{frz} < 14\,\%$).
3 WCB cases ('Bin 44', 'Bin 46' and 'Bin 52') lean towards in-situ ice formation, but show also show a large amount of ice that stems from liquid origin formation pathways as well. 'Bin 53' is evenly split between cirrus that contains (mostly) in-situ and liquid origin formed ice. Of the liquid origin ice modes, IMM contributes usually one third

up to half and FRZ provides the majority of liquid origin formed ice. This fits to the previous findings in this chapter, that homogeneous freezing of cloud droplets is the more important formation process for liquid origin (parts of) cirrus.
Only one case, 'Bin 55', is mostly influenced by the liquid origin formation pathway in terms of overall cloud coverage (marked in blue). FRZ with 56 % makes up the majority of the cirrus clouds in this WCB outflow, although DEP is also still important with 31 %. This makes 'Bin 55' also the only case where less than half of the clouds are formed by heterogeneous ice formation ($HET = 39\,\%$). All other cases including 'R6' show that a majority of the clouds stem from heterogeneous ice formation ($HET \geq 60\,\%$). Mostly deposition nucleation is responsible for the high heterogeneous ice fractions as can be concluded from the high DEP fractions.
We now have seen that most WCB cases contain both clouds with a split between in-situ and liquid origin fractions. The conceptually model is that cirrus cloud of liquid origin are overlayed with in-situ formed clouds (Wernli et al., 2016). However, if we look at the vertical structure of the liquid origin fraction f_{liq} (with temperature as a parameter for altitude) in Figure A.5, we note that in six cases (a, b, c, e, g and i) f_{liq} actually increases with decreasing temperature (and thus 'altitude'). Figure A.3 shows that DEP, the main contributor to in-situ formed ice, shows the inverse trend for these ensemble members. f_{dep} increasing with temperature. Again, we note that sedimentation is a important process of distributing ice modes within the clouds. While liquid origin formed ice stemming mostly from FRZ (and to a lesser degree from IMM) is transported upward with the WCB, in-situ ice from DEP is sedimentating through the WCB outflow towards lower model levels. Only one WCB case is not significantly affected by this process, the case 'Bin 53', where ice of liquid and in-situ origin mixed. That case shows overall a more expected layering of clouds stemming from DEP ice over clouds stemming from FRZ.
Many of the WCB cases in this ensemble show an inversion of f_{liq} in the topmost, thin temperature layer, This inversion is likely caused either by deposition nucleation (see e.g. panels a, b and c in Figure A.3) or by homogeneous nucleation (see e.g. panels d, e and f in Figure A.4). The latter three cases show increasing f_{hom} with decreasing temperature and were also among the as in-situ labeled cases in Table 6.2.

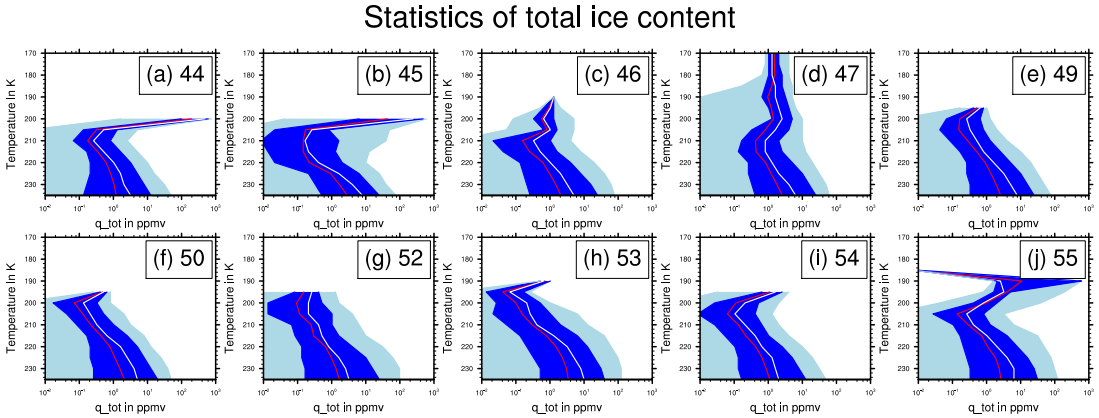

Figure 6.8.: q_{tot} histogram as function of temperature. The white line is the median. The 25th to 75th percentile are shaded in dark blue and the 5th to 95th percentile in light blue. Red represents the mean.

6.4.4. Cirrus properties

Figures 6.8 and 6.9 show histograms of total cloud ice content q_{tot} and number concentrations n_{tot}, respectively, as a function above temperature for each ensemble member. We limit our analysis to the cirrus regime ($T < T_c$).
The total mass content of cloud ice is limited by the availability of water vapor q_v and the resulting supersaturation wrt ice S_i. This was the reason that in Chapter 5 q_{tot} showed similar statistics for each of the sensitivity experiments, where we investigated the impact of various heterogeneous ice nucleation schemes and assumptions of INP concentrations on the ice modes. For this WCB ensemble we expect more variance between ensemble member as each case has a different initialisation of q_v. They also show different dynamical characteristics of WCB ascent.
All ensemble start with the q_{tot} median and mean showing values between 1 and 10 ppmv. This is already lower than the average q_{tot} starts with in the cirrus regime for the case study in the previous chapters. However, the general structure with decreasing temperature is the same: q_{tot} decrease with temperature with a spike caused by HOM (or DEP) nucleation at the highest model level with cirrus. Although the number of data points in these nucleation zones are low as can be concluded from the narrow distribution of percentiles (shaded areas). The median (and mean) decreases for most ensemble members below 1 but stays above 0.1 ppmv. For the temperature range from 200 to 220 K, these values are within the IWC core band and close to the median of observed cloud ice content for cirrus (Krämer et al., 2020). The general decline of q_{tot} with decreasing temperature is also present in observations (Krämer et al., 2020).
For most ensemble members the statistics end at $200 - 195$ K as the WCB trajectories do not reach higher altitudes (with in general lower temperatures). Only two ensemble members, 'Bin 55' and 'Bin 47', reach temperatures of 185 and even 170 K, respectively. Interestingly 'Bin 55' is the only case that we classified as 'liquid origin' during the last

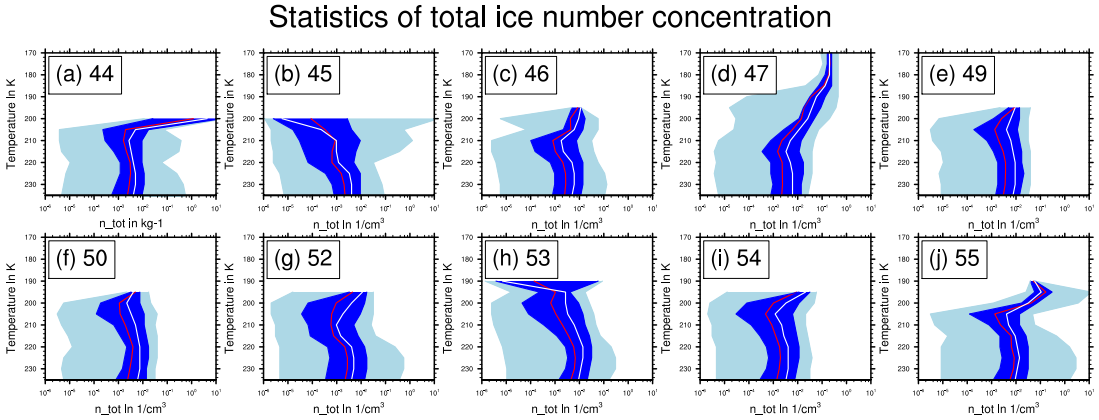

Figure 6.9.: n_{tot} histogram as function of temperature. The white line is the median. The 25th to 75th percentile are shaded in dark blue and the 5th to 95th percentile in light blue. Red represents the mean.

section. And in general we would suspect that cirrus outflows that extend towards lower temperatures contain mainly in-situ formed ice as nucleation rates are higher for colder temperatures at constant supersaturation (see Section 2.3.4). This highlights the issue that we can not really link the cirrus properties to an ice formation pathway in this broad statistical sense presented here. In Chapter 4 we discussed that signatures of the ice formation pathway in term of mass content are 'only' noticeable for a short duration after (or even just before) the WCB ascent criteria are fulfilled.
In the previous chapters we noted that n_{tot} was overall low compared to the climatology from observations. There are overall similar low for these WCB cases with median values mostly moving between 0.001 and 0.01 cm^{-3}. These values are around the 25th percentile of observed ice number concentrations (Krämer et al., 2020). As for the observations, the statistical distribution of n_{tot} shows only a small dependence on temperature. Only for the lowest temperatures, does n_{tot} in general increase. This fits our assumption that in these regions nucleation occurs, leading to high ice number concentrations. The peak is larger for n_{tot} than for q_{tot} in the cases where the trajectories reached temperature levels below 200 K (Panels d and j).

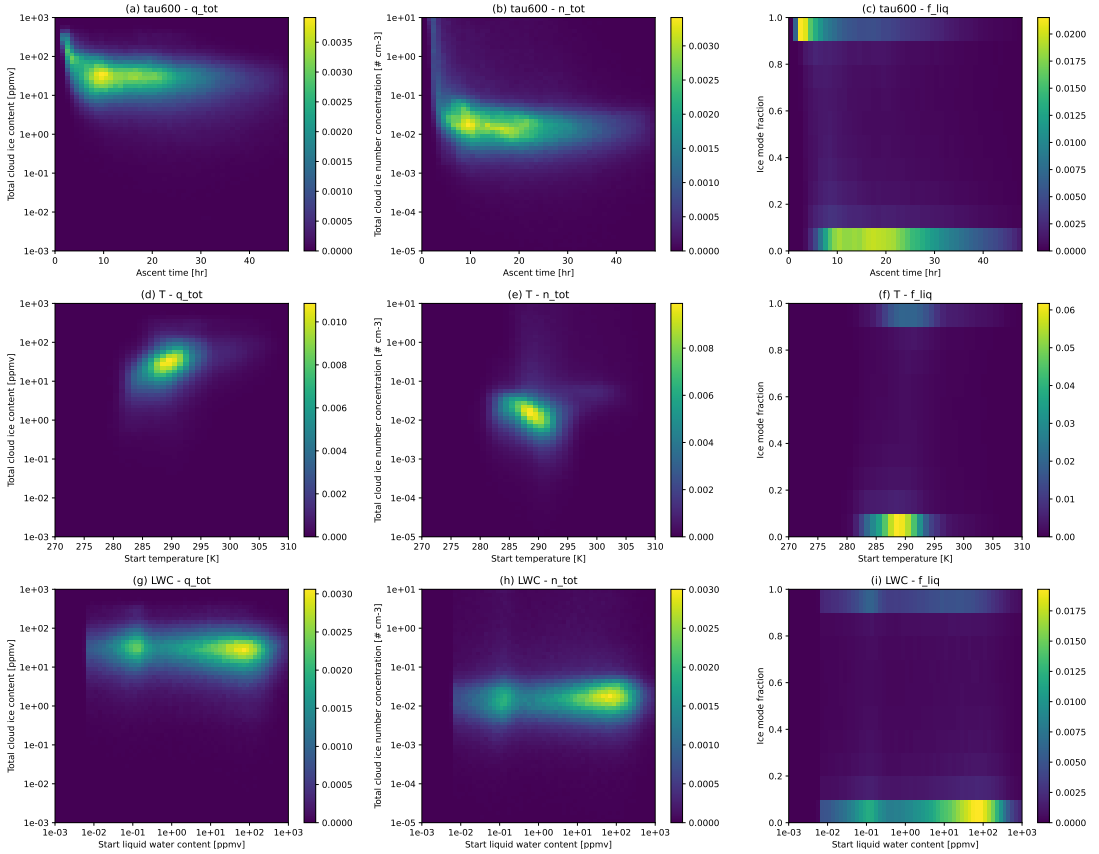

Figure 6.10.: 2-D Histograms of q_{tot} (a,d,g), n_{tot} (b,e,h) and f_{liq} (c,f,i) at ascent as function of start temperature, start LWC or ascent time.

6.5. Dependence on environmental conditions

Figure 6.10 shows 2-D histograms of q_{tot}, n_{tot}, and f_{liq} at ascent as functions of T, LWC or τ_{600} at start. 'Ascent point' is defined as the time step of fastest ascent, hence the earliest time step where a WCB trajectory fulfilled the 600 hPa ascent criteria and is no longer ascending ($\frac{\partial p}{\partial t} < -8\,\mathrm{hPa/h}$). 'Start point' is defined as the latest time step where the pressure difference to the ascent point is still equal or larger than 600 hPa. The start point is shifted towards earlier time steps for as long as the trajectory is already ascending ($\frac{\partial p}{\partial t} < -8\,\mathrm{hPa/h}$). Data of trajectories from all ensemble member and all start dates were included in these histograms.
Panels (a-c) show q_{tot}, n_{tot}, and f_{liq} as function of (fastest) ascent time (τ_{600}). There is a clear trend of larger q_{tot} (from 5 to 150 ppmv) for convective-like ascent times ($\tau_{600} < 8\,\mathrm{h}$). For intermediate to long ascent times, there seems to be no clear relation to q_{tot}. n_{tot} sees a an increase for convective-like ascent times as well, but the the values are scattered above multiple orders of magnitude, which makes the trend less clear than for q_{tot}. There is, however, a strong signal that most of the cloud ice in cirrus from convective-like WCB

trajectories is stemming from liquid origin formation processes (see high f_{liq} for low τ_{600} in Panel (c)). We already discussed the connection of peaks in q_{tot} and high f_{liq} for fast ascent times in Chapter 4 and see these findings confirmed here for an ensemble of WCB cases. However, for intermediate and slow ascent times, we do not observe statistical trends.
The next three panels (d-f) in Figure 6.10 show the effect of starting temperature on the cloud properties at the outflow. The majority of starting temperatures is in the range from 280 to 300 K. The total cloud ice content q_{tot} shows an increase from 10 to 100 ppmv with increasing start temperature. The total cloud ice concentration shows an inverse trend: n_{tot} decreases from 0.05 to 0.008 cm^{-3}. Its unclear if this trend is significant since the ensemble consists only of ten members. We checked if the start temperature is related to fast ascent times, which may explain an increase of q_{tot}, as q_{tot} was higher for fast ascent times ($\tau_{600} < 8\,\mathrm{h}$). This was not the case. However, in literature there are indications that Sea Surface Temperature (SST) strongly modifies the WCB ascent and the precipitation structure. The ice mode fraction f_{liq} (shown in Panel (c)) seems to be mostly unaffected by start temperature. In the last section we noted that f_{liq} is overall low for most ensembles because sedimentation of DEP dominates the lower model levels of the WCB outflow. As such the distribution of f_{liq} mostly follows the overall start temperature distribution specific to each case study without a relation to a favored ice formation pathway. A larger WCB ensemble might reveal a clearer trend.
One assumption concerning cirrus clouds of liquid origin is, that the cloud processes in mixed-phase clouds affect the cloud ice in such a way, that it leads to on average larger IWC compared to in-situ formed ice clouds. As such we could expect a relation between the LWC in an ascending WCB and the IWC of the cirrus outflow at ascent. However, there seems to be no relation of start LWC to q_{tot}, n_{tot}, or f_{liq}. Panels (g) to (i) mostly show the distribution of start LWC for the ensemble members with a peak at 0.01 and 100 ppmv but without a strong relation to the variables at the y-axis. It might be that enhanced LWC primarily modifies precipitation and riming rates. The latter mostly benefit the rimed particle classes, graupel and hail, and indirectly SEC as rime splintering is increased. Our results of previous chapters have shown though that SEC usually does not reach the cirrus regime in significant quantity as it quickly sediments out of the WCB or is otherwise lost in aggregation. Total water content including LWC, IWC and water vapor content q_v might be a more promising parameter to find a relation between its values at the start to cloud-relevant properties at the end of WCB ascent.

6.6. Discussion and summary

We found that the distribution of the mixed-phase clouds of each ensemble member follows the general structure found in the previous case studies. Riming was active in all cases and thus SEC ice from rime splintering present. The high number ratios again hint that the from Hallet-Mossop derived parametrisation is very impactful, although the physical understanding of the mechanisms is lacking (see, Korolev et al., 2020; Seidel et al., 2024). Sedimentation of DEP ice into the mixed-phase clouds of the ascending

WCB was also present and relevant in all cases.
Ice modes from heterogeneous nucleation (DEP and IMM) showed overall large mass but smaller number ratios for both mixed-phase and cirrus cloud regimes. Ice modes from homogeneous freezing, mostly stemming from FRZ, showed overall high number but low mass ratios. The HOM mode was mostly irrelevant for most parts of the cirrus outflow of all WCB cases. Only WCB cases with strong deposition nucleation (and thus high in-situ ice fractions) showed parts of the WCB outflow constituting of the HOM ice mode. This was likely due to the effect that in this strong in-situ fraction cases, INPs are depleted and ice from DEP sediments out, which give homogeneous nucleation the opportunity to trigger. This underlines our findings from Chapter 5 that the implementation of heterogeneous nucleation scheme of Hande et al. (2015) while using its standard coefficients often suppresses homogeneous nucleation.
Cloud ice number concentrations were again, as for the case study of the previous chapters, below the median of global cirrus observations. This occurred for all ensemble members, which featured different dynamical structures and initialisation. This raises the question, if low ice number concentrations are a general issue in the ice modes and SB scheme. Especially, when utilizing the deposition nucleation of Hande et al. (2015) with its standard configuration. This might also be related to the poor resolution of homogeneous nucleation, as it is expected hat homogeneous nucleation forms many small ice crystals, where heterogeneous (in-situ) nucleation forms few but large ice crystals (Krämer et al., 2020). The latter also agrees with strong signatures of DEP sedimentation, which only occur if the DEP ice mode has a large mean size. We will discuss possible causes and solutions for this 'issue' in the last chapter.
We found no clear relation between the ice formation pathway and cirrus properties at ascent to the environmental starting conditions of the WCB trajectories. However, they are several limitations with our analysis. 10 WCB cases might not be enough to obtain clear statistical trends as the cirrus cloud properties at ascent are affected by many factors, e.g., by sedimentation of hydrometeors from above clouds above the WCB cloud band. We also might obtain better results if we investigate other parameters such as total water content instead of liquid water content. And lastly relations between parameters at start point and end point of ascent might not be significant. The ascent criterion of 600 hPa ascent within 48 h is strong for general selection of WCB trajectories (Madonna et al., 2014), but this does not mean that this static value is adequate for characterising the starting conditions of cirrus outflow. For example, in Section 4.4.3 we noticed that the peak of q_{tot} was usually located before completion of 600 hPa ascent. In that sense it might be advantageous to characterize the outflow properties by searching for the maximum value of the respective property within a certain time range or by taking the average of the respective property around the end point of ascent.
We attempted to create a climatology of IWP for WCB outflow features for ERA5 dataset and compared it to WCB simulations done with ICON and the ice modes scheme. However, our feature tracking was insufficient to characterize the WCB outflow. A machine learning approach might yield better results. However, this would require a comprehensive definition of what substitutes a WCB outflow region in time and space and how one might distinguish between two nearby or overlapping outflow regions orientating from

different WCBs. It might be a problem that a singular outflow point is not a significant marker for the properties of the cirrus outflow as we obtained mostly inconclusive statistics in Section 6.5 using the same definition for marking end of ascent points.

7. Summary and outlook

7.1. Summary

In this thesis we introduced the 'ice mode' microphysics, an adaption of the standard two-moment scheme employed in the atmospheric model ICON (Seifert and Beheng, 2006). The ice modes scheme allows to identify the formation process, cloud ice in model simulations is stemming from. We utilized this new microphysics scheme to investigate ice formation in idealised deep convection (Chapter 3) and in mixed-phase and cirrus clouds of Warm Conveyor Belts (WCB) (Chapters 4 and 6). In Chapter 5 we compared the impact of a selection of heterogeneous ice nucleation parametrisations and ensemble of INP profiles to the cloud compositions. The major research topic of this thesis was to investigate the competition between two ice formation pathways of cirrus clouds: liquid origin (freezing of liquid droplets close to water saturation) and in-situ (ice formation directly from the vapour phase below water saturation).
Ice from deposition nucleation (DEP) was dominant in all cases and even being relevant for mixed-phase clouds. The latter was caused by high sedimentation rates due to DEP ice often showing large mean sizes. Ice number concentrations were overall below the median of climatologies from observations for all WCB cases. This might be connected to the overall infrequent occurrence of ice from homogeneous nucleation (HOM). The physical parameterisation for homogeneous nucleation is strongly depended on vertical updraft (Kärcher et al., 2006) and thus on grid resolution of the general circulation model. While we noticed an increase of HOM ice content for higher resolution grids, the main issue was that ice from deposition nucleation was suppressing homogeneous nucleation events by depleting supersaturation. Since deposition nucleation events have a lower supersaturation thresholds to trigger, they can inhibit homogeneous nucleation events effectively.
We found that reducing the number concentration of INPs by several orders of magnitudes was less impactful than changing the heterogeneous ice nucleation scheme entirely. This emphasizes the uncertainty regarding the activation of INPs especially for deposition nucleation. The dominance of the DEP ice mode in most studies presented in this thesis is likely caused by the choice of heterogeneous nucleation scheme. Hande et al., 2015 activates INP for deposition nucleation even at minor supersaturations wrt ice and is thus very dominant as an in-situ formation process. The onset of deposition nucleation for Phillips et al., 2008 and Ullrich et al., 2017 occurs at higher supersaturations and thus gives homogeneous nucleation more opportunities to trigger. In general, homogeneous and heterogeneous formation processes show compensating effects. Lower immersion freezing rates lead to more droplets freezing homogeneously. Higher INP concentrations (or deposition nucleation onsets on lower supersaturations) suppress homogeneous nu-

cleation.
We found that secondary ice from rime splintering and collisional breakup is very dominant in parts of mixed-phase clouds where graupel is present for both convective (idealised) clouds and WCBs. Most notable was the high number densities of secondary ice. However, especially rime splintering in convective clouds rather expanded the thermodynamic regimes where cloud ice is is present, than enhancing primary nucleation. Still it is concerning that the rime splintering parametrisation has such an large impact despite our understanding of the physical process being limited and the experimental results on which the parameterisation is based on not being reproducible (see Korolev et al., 2020; Seidel et al., 2024).
We investigate the liquid origin vs in-situ research question in multiple case studies. For (idealised) deep convection clouds, we found that most of the pure ice clouds in the anvil and outflow were of liquid origin. Only parts of the overshoot formed with in-situ formation.
The mixed-phase clouds of all WCB cases showed similar compositions of ice modes. For the cirrus outflow though, the results differed between the case studies. In terms of integrated ice mass contents, in-situ formed ice, mostly stemming from deposition nucleation, dominated the cloud compositions. However, even for those cases, they were often large but thin cirrus clouds of liquid origin present. In WCB outflows where liquid origin ice showed the largest integrated mass contents, ice from homogeneously frozen droplets dominated the cloud compositions.
We compared the cirrus origin classification of our ice modes scheme (IM) to the algorithm of Wernli et al., 2016 (W16). We found that W16 classified most parts of the WCB trajectories as liquid origin, where IM classified them as in-situ. This mismatch was caused by sedimentation of in-situ formed ice into trajectories that ascend from mixed-phase clouds.
The characteristic properties of liquid origin and in-situ cirrus expected from observations, were (if present) only found shortly before ascent and only noticeable for a short time. This also highlights the issues that while the choice of the 600 hPa ascent criterion is very useful for the selection of WCB trajectories, it might not necessarily be the right choice for finding the relevant time step that highlights the cirrus outflow properties.
Overall we found that the choice of heterogeneous ice nucleation scheme and profiles of INPs did not strongly affect the competition of liquid origin and in-situ formation pathways. The dynamical structure of the WCB and the properties of the air mass that the WCB is embedded seem to be the more important. Especially slow ascending clouds above the WCB, which are not identified by Lagrangian analysis starting from the boundary layer, seem to impact the cloud composition of the WCB outflow significantly. We also found no relation between the ice formation pathway and cirrus properties to the environmental starting conditions of the ascending WCB trajectories.

7.2. Outlook

In this thesis we have mostly conducted model studies with few comparisons to observations. The ice modes scheme would be useful in studies combining observations and modelling. In particular airborne measurements often require analysis of cloud origin and accompanying microphysics simulations to interpret the data. For example, in Chapter 1 we referenced multiple secondary ice studies that try to link observed ice and INP concentrations to (secondary) formation processes. The ice mode schemes does lend itself naturally to such an analysis as we can directly track the origin of ice.
We noted that cloud ice concentrations n_i were fairly low for cirrus clouds compared to observations. This was true for all case studies. Krämer et al., 2020 presented a 10 year climatology of n_i from global observations utilizing satellite products in particular DARDAR-Nice (Sourdeval et al., 2018). We could perform ice mode simulations complementary to the DARDAR-Nice product to attribute observations to ice formation pathways (in particular homogeneous vs heterogeneous nucleation). We can also employ the ice modes scheme to test which ice formation parametrisations are under- or over-performing by using the DARDAR-Nice dataset as validation.
For the model side, we can also consider several additions to the ice mode microphysics scheme. Currently we only use a simple aerosol model. However, our sensitivity analysis in Chapter 5 showed that aerosol concentrations have a large impact on cloud compositions in particular on homogeneous vs heterogeneous freezing modes. The implementation of the ice modes scheme into the ICON-ART infrastructure would give us more control over the availability, distribution and types of INP (Schröter et al., 2018).
The ice mode schemes also included new parameterisation developments for secondary ice, specifically for droplet fragmentation and collisional breakup. However, droplet fragmentation rates were very low. This might be due to its implementation into the bulk scheme. Cloud droplets are in a size range, which is in general too small to produce ice splinters (Lauber et al., 2018). Thus we enabled droplet fragmentation only for raindrops. Though in Chapter 3 we found that raindrops quickly leave the relevant temperature zone by sedimentation. It would be interesting to expand the parameterisation to include larger cloud droplets by partial integration over the droplet size spectra. Drizzle droplets occupy a size range ($> 100\,\mu m$) where droplet fragmentation is active, but are not as large raindrops and thus there sedimentation rates are lower. Hence they would be able to remain longer in temperature regions where droplet fragmentation is active. So a better representation of 'drizzle' droplets, e.g. as inclusion as a third liquid droplet class, could be beneficial to investigate frozen droplet fragmentation [see, e.g., Sant et al., 2013; Sant et al., 2015 for implementations].
The ice mode model does not allows us to investigate sources and sinks individually, we only obtain how much ice from each formation pathway remains. Especially for the IMM mode, we suspected that aggregation and riming removes a large portion of IMM ice. To improve interpretation of our results we could implement tracking of microphysical process rates as additional variables to more directly asses major sinks of the ice modes. Similar we could track nucleation rates, e.g., integrated between the output time steps, to find the zones where ice nucleation is occurring to get a more complete idea of the

spatial development of each ice mode.
In Chapter 6 we showed the results of ice modes simulations for an ensemble of WCB cases. While the results gave us an impression of ice formation pathways for various WCB starting conditions and environments, the sample size is still small. To obtain more robust results an extended climatology is needed. Such a project might need a revised model setup and more automated postprocessing, but is in general doable with ICON and the ice modes microphysics scheme. Special care should be taken in developing new criteria for choosing WCB cases. A case selection criteria that characterizes the dynamical evolution of the WCB would be best as one of the conclusion in this work is that the ice formation pathway is likely mainly depended on dynamic forcing. Such criteria could include the starting position of the WCB in relation to the cyclone center, stage of the cyclone lifecycle, ascent behavior, outflow altitude, geographic location and season (Binder et al., 2020).
We found a relation of WCB (fastest) ascent times to the ice formation pathway in Chapter 4. Additionally we noted that even for WCB outflows dominated by in-situ formed ice, liquid origin ice was mixed in, likely being transported into the upper troposphere by convection. Studies found that convection embedded onto the WCB can significantly affect the PV structure of a WCB and impact the mesocale precipitation patterns [see, e.g., Oertel et al., 2020; Oertel et al., 2021]. It would be interesting to investigate the ice formation pathways along embedded convection using the ice modes scheme. Such a study would require high resolution simulations and thus we would need to employ convection-permitting grid resolutions and calculation of online trajectories.
In the introduction we emphasized that one motivation of this work is that radiative characteristics of cirrus clouds and their relation to the ice formation pathway are still not fully understood. However, apart from Section 4.3, we did not discuss the radiative properties of simulated clouds further. One straightforward way to investigate the radiative impact in the ice modes is to calculate the optical thickness for each ice mode using the parametrisation of Fu and Liou, 1993. Then we can attribute the contribution of each ice mode to the overall cloud optical thickness in relation to the model level. The options for coupling the radiative properties of clouds to the radiation scheme are limited in the standard version of ICON. Of all the cloud variables, only cloud cover fraction, is used as an input for the 1-D RRTM scheme of Mlawer et al., 1997. Cloud cover fraction does not allow for a nuanced investigation as it takes only the integrated mass content of all ice particle classes (including cloud ice, graupel, snow and hail) into account. To investigate the interaction of the ice modes in WCB with radiation diagnostically we could use vertical profiles along the WCB trajectories (see e.g. Section 4.3.3) and employ the radiation transfer model from Fusina and Spichtinger, 2010. Such a study could also be compared with suitable remote sensing cloud data from satellite observations or a ground-based campaign.
In nature subsequent nucleation events can produce bimodal cloud ice size distributions in cirrus (Lüttmer, 2017). Bulk microphysics scheme in general assume unimodal size distributions for their hydrometeor classes (see Section 1.4). Hence multimodal size distributions are not resolved in bulk models and would better be investigated by employing spectral models. However, the ice mode microphysics scheme can actually

simulate multimodal size distributions by overlaying different ice modes. This is limited by the requirement that ice has to stem from different formation pathways (such as deposition nucleation and homogeneous nucleation), while spectral models can simulate multimodal distributions stemming from a single formation pathway. Krämer et al., 2020 even suggested that different cirrus subclasses (like liquid origin and in-situ cirrus) occurring in succession can lead to bimodal ice size distributions. It would be interesting to investigate if we can see such bimodal distributions caused by different ice formation processes in our data. However, we would likely encounter issues. For most grid points containing cloud ice, one ice mode usually dominates the others by several orders of magnitude in terms of number concentrations, thus obscuring contributions from other ice modes. Also, in order to resolve multimodal distributions we might need to adjust the shape parameter of the ice crystal size distribution and the minimal ice crystal size.

A. Appendix

A.1. Generalized Gamma distribution

In cloud physics the generalized gamma distribution is often used to describe the mass or size distribution of a cloud particle class

$$f(x) = Ax^{\nu} \exp(-\lambda x^{\mu}) \tag{A.1}$$

where we use the particle mass x as the variable and the shape and scale parameters ν and μ are prescribed. λ and A are linked to the prognostic distribution moments, the zeroth and first moment, corresponding to the number density $M^0 = n$ and mass mixing ratio $M^1 = q$, respectively. To obtain the n-th mass weighed moment of the generalized gamma distribution M^n we multiply equation (A.1) with x^n and integrate over the entire domain which yields

$$\begin{aligned} M^n &= \int_0^{\infty} f(x) x^n \,\mathrm{d}x = \int_0^{\infty} A x^{\nu+n} \exp(-\lambda x^{\mu}) \,\mathrm{d}x \\ &= \frac{A}{\mu} \int_0^{\infty} y^{\frac{\nu+n+1}{\mu}-1} \exp(-\lambda y) \,\mathrm{d}y \\ &= \frac{A}{\mu \lambda^{\frac{\nu+n+1}{\mu}}} \Gamma\left(\frac{\nu+n+1}{\mu}\right) \end{aligned} \tag{A.2}$$

where we used the substitution $y = x^{\mu}$ and the relation of the gamma function $\int_0^{\infty} y^{\zeta} \exp(-\eta y) \,\mathrm{d}y = \Gamma(\zeta+1)\eta^{-(\zeta+1)}$ for $\zeta > -1$, which can be reduced to Euler's definition of the gamma function with the use of a suitable substitution. Prescribing constant values for ν and μ we can now solve equation (A.2) for A and λ

$$\lambda = \left(\frac{n}{q} \frac{\Gamma\left(\frac{\nu+2}{\mu}\right)}{\Gamma\left(\frac{\nu+1}{\mu}\right)} \right)^{\mu} \tag{A.3}$$

$$A = \frac{\mu n}{\Gamma\left(\frac{\nu+1}{\mu}\right)} \lambda^{\frac{\nu+1}{\mu}} = \frac{\mu n}{\Gamma\left(\frac{\nu+1}{\mu}\right)} \left(\frac{n}{q} \frac{\Gamma\left(\frac{\nu+2}{\mu}\right)}{\Gamma\left(\frac{\nu+1}{\mu}\right)} \right)^{\nu+1} \tag{A.4}$$

and so we can finally describe the distribution function as a function of particle mass and the two prognostic moments

$$f(x,q,n) = \left[\frac{x}{\overline{x}}\right]^{\nu} \frac{n}{\mu \overline{x} \Gamma\left(\frac{\nu+1}{\mu}\right)} \left[\frac{\Gamma\left(\frac{\nu+2}{\mu}\right)}{\Gamma\left(\frac{\nu+1}{\mu}\right)} \right]^{\nu+1} \exp\left(- \left[\frac{x}{\overline{x}} \frac{\Gamma\left(\frac{\nu+2}{\mu}\right)}{\Gamma\left(\frac{\nu+1}{\mu}\right)} \right]^{\mu} \right) \tag{A.5}$$

with the mean particle mass $\overline{x} = q/n$.

A.2. Derivation of collisions growth equations

The collision processes between two ice classes f_i and f_j leads to the formation of snow f_s and can formally be described as

$$\left.\frac{\partial f_i(x)}{\partial t}\right|_{coll,ij} = -\int_0^\infty f_i(x) f_j\big(x'\big) K_{ij}\big(x, x'\big)\,\mathrm{d}x' \tag{A.6}$$

$$\left.\frac{\partial f_j(x)}{\partial t}\right|_{coll,ij} = -\int_0^\infty f_i\big(x'\big) f_j(x) K_{ij}\big(x, x'\big)\,\mathrm{d}x' \tag{A.7}$$

$$\left.\frac{\partial f_s(x)}{\partial t}\right|_{coll,ij} = \int_0^\infty \int_0^\infty f_i\big(x'\big) f_j\big(x''\big) K_{ij}\big(x', x''\big)\delta\big(x - \big(x' + x''\big)\big)\,\mathrm{d}x'\,\mathrm{d}x'' \tag{A.8}$$

where we used the properties of the Dirac-delta function to simplify the result in Equation (A.8). The collision kernel K_{ij} is defined as

$$K_{ij}(x_i, x_j) = A_{ij}(x_i, x_j) E_{ij}(x_i, x_j) |v_i(x_i) - v_j(x_j)| \tag{A.9}$$

where A_{ij} is the cross section of the sweep out volume, E_{ij} is the collection efficiency and $v_{i,j}$ are the sedimentation velocities. Let D_i and D_j donate the maximum diameters of ice crystals and we obtain for A_{ij}

$$A_{ij}(x_i, x_j) = \epsilon (D_i(x_i) + D_j(x_j))^2 \tag{A.10}$$

with $\epsilon = \frac{\pi}{4}$ for spherical particle and $\epsilon = 6\sqrt{3}$ for hexagonal plates. Although expressions for more complicated ice forms like columns exist they would make integration more complicated and we will restrict our derivation on spherical particles for now.
Sedimentation velocities and mass-diameter relationships are parameterised as power laws

$$v_k(x) = \alpha_k x^{\beta_k} \tag{A.11}$$

$$D_k(x) = a_k x^{b_k} \tag{A.12}$$

where a_k, b_k, α_k and β_k are constants.
We do not have a suitable parametrisation for the collisions efficiency $E_{i,j}$ and approximate it as a constant mean value

$$E_{i,j}(x_i, x_j) = \overline{E_{ij}} \tag{A.13}$$

The absolute of the velocity difference in the collision kernel (A.9) would force us to split the integral. However, this would lead to incomplete gamma functions which we want to avoid. Hence we need a suitable approximation. We will just assume a mean value $\overline{v_{ij}}$ for the velocity difference. Integrating equations (A.6) and (A.8) over x from zero to infinity and inserting (A.9) as well as (A.10) yields prognostic equations for the zeroth moment, the number mixing ratio n

$$\left.\frac{\partial n_i}{\partial t}\right|_{coll,ij} = -\epsilon\overline{E_{ij}}\overline{v_{ij}} \int_0^\infty \int_0^\infty \big(D_i(x') + D_j(x)\big)^2 f_i(x') f_j(x)\,\mathrm{d}x\,\mathrm{d}x' \tag{A.14}$$

$$\left.\frac{\partial n_j}{\partial t}\right|_{coll,ij} = \left.\frac{\partial n_i}{\partial t}\right|_{coll,ij} \tag{A.15}$$

$$\begin{aligned}\left.\frac{\partial n_s}{\partial t}\right|_{coll,ij} &= \int_0^\infty \int_0^\infty \int_0^\infty f_i(x') f_j(x'') K_{ij}(x', x'') \delta\big(x - (x' + x'')\big)\,\mathrm{d}x\,\mathrm{d}x'\,\mathrm{d}x'' \\ &= \int_0^\infty \int_0^\infty f_i(x') f_j(x'') K_{ij}(x', x'')\,\mathrm{d}x'\,\mathrm{d}x'' \\ &= -\left.\frac{\partial n_i}{\partial t}\right|_{coll,ij}\end{aligned} \tag{A.16}$$

and for the first moment, the mass mixing ratio q

$$\left.\frac{\partial q_i}{\partial t}\right|_{coll,ij} = -\epsilon\overline{E_{ij}}\overline{v_{ij}} \int_0^\infty \int_0^\infty \big(D_i(x') + D_j(x)\big)^2 x' f_i(x') f_j(x)\,\mathrm{d}x\,\mathrm{d}x' \tag{A.17}$$

$$\left.\frac{\partial q_j}{\partial t}\right|_{coll,ij} = -\epsilon\overline{E_{ij}}\overline{v_{ij}} \int_0^\infty \int_0^\infty \big(D_i(x) + D_j(x')\big)^2 x' f_i(x) f_j(x')\,\mathrm{d}x\,\mathrm{d}x' \tag{A.18}$$

$$\begin{aligned}\left.\frac{\partial q_s}{\partial t}\right|_{coll,ij} &= \int_0^\infty \int_0^\infty \int_0^\infty f_i(x') f_j(x'') K_{ij}(x', x'') \delta\big(x - (x' + x'')\big) x\,\mathrm{d}x\,\mathrm{d}x'\,\mathrm{d}x'' \\ &= \int_0^\infty \int_0^\infty f_i(x') f_j(x'') K_{ij}(x', x'') (x' + x'')\,\mathrm{d}x'\,\mathrm{d}x'' \\ &= \epsilon\overline{E_{ij}}\overline{v_{ij}} \int_0^\infty \int_0^\infty f_i(x') f_j(x'') \big(D_i(x) + D_j(x')\big)^2 (x' + x'')\,\mathrm{d}x'\,\mathrm{d}x'' \\ &= -\left(\left.\frac{\partial q_i}{\partial t}\right|_{coll,ij} + \left.\frac{\partial q_j}{\partial t}\right|_{coll,ij}\right)\end{aligned} \tag{A.19}$$

A.2.1. Solving prognostic equations

For solving equation (A.17) we expand the quadratic expression, split the integral into a sum, insert the parametrisation for the diameter (A.12) and find suitable substitutions so that the integrals can be solved using the relation of the gamma function. Then using

the expressions for the distribution parameters (A.3) and (A.4) we arrive at

$$
\begin{aligned}
\left.\frac{\partial q_i}{\partial t}\right|_{coll,ij} &= -\epsilon\overline{E_{ij}}\,\overline{v_{ij}}\int_0^\infty\int_0^\infty \big(D_i(x') + D_j(x)\big)^2 x' f_i(x') f_j(x)\,\mathrm{d}x\,\mathrm{d}x' \\
&= -\epsilon\overline{E_{ij}}\,\overline{v_{ij}}[\int_0^\infty f_j(x)\,\mathrm{d}x\int_0^\infty a_i^2 x'^{2b_i+1+\nu_i} A_i \exp\big(-\lambda_i x'^{\mu_i}\big)\,\mathrm{d}x' \\
&\quad +2\int_0^\infty a_j x^{b_j} f_j(x)\,\mathrm{d}x\int_0^\infty a_i x'^{b_i+1+\nu_i} A_i \exp\big(-\lambda_i x'^{\mu_i}\big)\,\mathrm{d}x' \\
&\quad +\int_0^\infty a_j^2 x^{2b_j+\nu_j} A_j \exp(-\lambda_j x^{\mu_j})\,\mathrm{d}x\int_0^\infty x' f_i(x')\,\mathrm{d}x'] \\
&= -\epsilon\overline{E_{ij}}\,\overline{v_{ij}}[N_j \frac{A_i a_i^2}{\mu_i \lambda_i^{\frac{2b_i+2+\nu_i}{\mu_i}}}\Gamma\left(\frac{2b_i+2+\nu_i}{\mu_i}\right) \\
&\quad +2\frac{a_i a_j A_i A_j}{\mu_i\mu_j \lambda_i^{\frac{b_i+2+\nu_i}{\mu_i}} \lambda_i^{\frac{b_j+1+\nu_j}{\mu_j}}}\Gamma\left(\frac{b_i+2+\nu_i}{\mu_i}\right)\Gamma\left(\frac{b_j+1+\nu_j}{\mu_j}\right) \\
&\quad +q_i \frac{A_j a_j^2}{\mu_j \lambda_j^{\frac{2b_j+1+\nu_j}{\mu_j}}}\Gamma\left(\frac{2b_j+1+\nu_j}{\mu_j}\right)] \\
&= -\epsilon\overline{E_{ij}}\,\overline{v_{ij}}[\frac{q_i^{2b_i+1} n_j}{n_i^{2b_i}} a_i^2 \frac{\Gamma\left(\frac{2b_i+2+\nu_i}{\mu_i}\right)}{\Gamma\left(\frac{\nu_i+1}{\mu_i}\right)}\left(\frac{\Gamma\left(\frac{\nu_i+1}{\mu_i}\right)}{\Gamma\left(\frac{\nu_i+2}{\mu_i}\right)}\right)^{2b_i+1} \\
&\quad +\frac{q_i^{b_i+1} q_j^{b_j}}{n_i^{b_i} n_j^{b_j-1}} 2a_i a_j \frac{\Gamma\left(\frac{b_i+2+\nu_i}{\mu_i}\right)}{\Gamma\left(\frac{\nu_i+1}{\mu_i}\right)}\frac{\Gamma\left(\frac{b_j+1+\nu_j}{\mu_j}\right)}{\Gamma\left(\frac{\nu_j+1}{\mu_j}\right)}\left(\frac{\Gamma\left(\frac{\nu_i+1}{\mu_i}\right)}{\Gamma\left(\frac{\nu_i+2}{\mu_i}\right)}\right)^{b_i+1}\left(\frac{\Gamma\left(\frac{\nu_j+1}{\mu_j}\right)}{\Gamma\left(\frac{\nu_j+2}{\mu_j}\right)}\right)^{b_j} \\
&\quad +\frac{q_i q_j^{2b_j}}{n_j^{2b_j-1}} a_j^2 \frac{\Gamma\left(\frac{2b_j+1+\nu_j}{\mu_j}\right)}{\Gamma\left(\frac{\nu_j+1}{\mu_j}\right)}\left(\frac{\Gamma\left(\frac{\nu_j+1}{\mu_j}\right)}{\Gamma\left(\frac{\nu_j+2}{\mu_j}\right)}\right)^{2b_j}] \\
&= -\epsilon\overline{E_{ij}}\,\overline{v_{ij}} q_i n_j [D_i^2(\overline{x_i})\frac{\Gamma\left(\frac{2b_i+2+\nu_i}{\mu_i}\right)}{\Gamma\left(\frac{\nu_i+1}{\mu_i}\right)}\left(\frac{\Gamma\left(\frac{\nu_i+1}{\mu_i}\right)}{\Gamma\left(\frac{\nu_i+2}{\mu_i}\right)}\right)^{2b_i+1} \\
&\quad +D_i(\overline{x_i})D_j(\overline{x_j})\frac{\Gamma\left(\frac{b_i+2+\nu_i}{\mu_i}\right)}{\Gamma\left(\frac{\nu_i+1}{\mu_i}\right)}\left(\frac{\Gamma\left(\frac{\nu_i+1}{\mu_i}\right)}{\Gamma\left(\frac{\nu_i+2}{\mu_i}\right)}\right)^{b_i+1}\frac{\Gamma\left(\frac{b_j+1+\nu_j}{\mu_j}\right)}{\Gamma\left(\frac{\nu_j+1}{\mu_j}\right)}\left(\frac{\Gamma\left(\frac{\nu_j+1}{\mu_j}\right)}{\Gamma\left(\frac{\nu_j+2}{\mu_j}\right)}\right)^{b_j} \\
&\quad +D_j^2(\overline{x_i})\frac{\Gamma\left(\frac{2b_j+1+\nu_j}{\mu_j}\right)}{\Gamma\left(\frac{\nu_j+1}{\mu_j}\right)}\left(\frac{\Gamma\left(\frac{\nu_j+1}{\mu_j}\right)}{\Gamma\left(\frac{\nu_j+2}{\mu_j}\right)}\right)^{2b_j}] \\
&= -\epsilon\overline{E_{ij}}\,\overline{v_{ij}} q_i n_j [D_i^2(\overline{x_i})\delta_i^1 + D_i(\overline{x_i})D_j(\overline{x_j})\delta_{ji}^1 + D_j^2(\overline{x_i})\delta_j^0]
\end{aligned}
\tag{A.20}
$$

with δ_{ij}^k and δ_l^k being shortcut notations (see equations (A.33) and (A.34)).
The integration of (A.14) yields similiary

$$\begin{aligned}\left.\frac{\partial n_i}{\partial t}\right|_{coll,ij} &= -\epsilon\overline{E_{ij}}\overline{v_{ij}}[\frac{q_i^{2b_i}n_j}{n_i^{2b_i-1}}a_i^2\frac{\Gamma\left(\frac{2b_i+1+\nu_i}{\mu_i}\right)}{\Gamma\left(\frac{\nu_i+1}{\mu_i}\right)}\left(\frac{\Gamma\left(\frac{\nu_i+1}{\mu_i}\right)}{\Gamma\left(\frac{\nu_i+2}{\mu_i}\right)}\right)^{2b_i} \\ &+\frac{q_i^{b_i}q_j^{b_j}}{n_i^{b_i-1}n_j^{b_j-1}}2a_ia_j\frac{\Gamma\left(\frac{b_i+1+\nu_i}{\mu_i}\right)}{\Gamma\left(\frac{\nu_i+1}{\mu_i}\right)}\frac{\Gamma\left(\frac{b_j+1+\nu_j}{\mu_j}\right)}{\Gamma\left(\frac{\nu_j+1}{\mu_j}\right)}\left(\frac{\Gamma\left(\frac{\nu_i+1}{\mu_i}\right)}{\Gamma\left(\frac{\nu_i+2}{\mu_i}\right)}\right)^{b_i}\left(\frac{\Gamma\left(\frac{\nu_j+1}{\mu_j}\right)}{\Gamma\left(\frac{\nu_j+2}{\mu_j}\right)}\right)^{b_j} \\ &+\frac{n_iq_j^{2b_j}}{n_j^{2b_j-1}}a_j^2\frac{\Gamma\left(\frac{2b_j+1+\nu_j}{\mu_j}\right)}{\Gamma\left(\frac{\nu_j+1}{\mu_j}\right)}\left(\frac{\Gamma\left(\frac{\nu_j+1}{\mu_j}\right)}{\Gamma\left(\frac{\nu_j+2}{\mu_j}\right)}\right)^{2b_j}] \\ &= -\epsilon\overline{E_{ij}}\overline{v_{ij}}n_in_j[D_i^2(\overline{x_i})\delta_i^0+D_i(\overline{x_i})D_j(\overline{x_j})\delta_{ji}^0+D_j^2(\overline{x_j})\delta_j^0]\end{aligned} \tag{A.21}$$

A.2.2. Approximation for mean velocity difference

For two particle classes with significant different mean velocities, like graupel and cloud droplets, we can simply neglect the velocity of the smaller particles and use the so called continuous model which simplifies the equation for the collision kernel and yields an analytic solution for the differential equations

$$|v_i(x_i)-v_j(x_j)| \approx v_i(x_i) = \alpha_i x_i^{\beta_i} \tag{A.22}$$

for $v_i >> v_j$.
However, for collision between particles that have similar mean velocities, like between ice crystals and snow, the continuous model is not a suitable approximation.
Instead one can use the Wisner approximation which assumes characteristic mean values for the sedimentation velocities which are constant and can hence be separated from the integrand. The characteristic mean values are can either be number- or mass weighed means. Alternatively we can use a the cross sectional area as weight

$$\begin{aligned}\overline{v_i} &= \frac{\int_0^\infty v_i(x_i)D_i^2(x_i)f_i(x_i)\mathrm{d}x_i}{\int_0^\infty D_i^2(x_i)f_i(x_i)\mathrm{d}x_i} \\ &= \alpha_i\overline{x_i}^{\mu_i\beta_i}\frac{\Gamma\left(\frac{2b_i+\beta_i+\nu_i+1}{\mu_i}\right)}{\Gamma\left(\frac{2b_i+\nu_i+1}{\mu_i}\right)}\left[\frac{\Gamma\left(\frac{\nu_i+1}{\mu_i}\right)}{\Gamma\left(\frac{\nu_i+2}{\mu_i}\right)}\right]^{\mu_i\beta_i}\end{aligned} \tag{A.23}$$

and the collision kernel can be approximated as

$$K_{ij}(x_i,x_j) = \overline{E_{ij}}|\overline{v_i}-\overline{v_j}|(D_i(x_i)+D_j(x_j))^2 = \overline{E_{ij}}\overline{v_{ij}}(D_i(x_i)+D_j(x_j))^2 \tag{A.24}$$

with $\overline{E_{ij}}$ and $\overline{v_{ij}}$ being constant. A problem with the Wiesner approximation occurs when characteristic velocities of both populations are equal since the collision kernel

would vanish and the collision growth would be zero. This, however, is physically only correct for monodisperse size distributions.
In Seifert (2002) a improved Wiesner approximation is proposed. Using the integral cross-section weighed variance

$$\begin{aligned}
\overline{v_{ij}} &= \left[\frac{1}{N}\int_0^\infty\int_0^\infty (v_i(x_i)-v_j(x_j))^2 D_i^2(x_i)D_j^2(x_j)f_i(x_i)f_j(x_j)x_i\mathrm{d}x_i\mathrm{d}x_j\right]^{\frac{1}{2}} \\
&= \left[\frac{1}{N}\int_0^\infty\int_0^\infty \left(v_i^2(x_i)+2v_i(x_i)v_j(x_j)+v_j^2(x_j)\right)D_i^2(x_i)D_j^2(x_j)f_i(x_i)f_j(x_j)x_i\mathrm{d}x_i\mathrm{d}x_j\right]^{\frac{1}{2}} \\
&= \frac{1}{N^{\frac{1}{2}}}\left[\int_0^\infty\int_0^\infty \left(\alpha_i^2 x_i^{2\beta_i}+2\alpha_i x_i^{\beta_i}\alpha_j x_j^{\beta_j}+\alpha_j^2 x_j^{2\beta_j}\right)a_i^2 x_i^{2b_i}a_j^2 x_j^{2b_j}f_i(x_i)f_j(x_j)x_i\mathrm{d}x_i\mathrm{d}x_j\right]^{\frac{1}{2}} \\
&= \frac{1}{N^{\frac{1}{2}}}[\int_0^\infty a_j^2 x_j^{2b_j}f_j(x_j)\mathrm{d}x_j\int_0^\infty a_i^2\alpha_i^2 x_i^{2b_i+1+2\beta_i}f_i(x_i)\mathrm{d}x_i \\
&\quad +2\int_0^\infty a_j^2\alpha_j x_j^{2b_j+\beta_j}f_j(x_j)\mathrm{d}x_j\int_0^\infty a_i^2\alpha_i x_i^{2b_i+1+\beta_i}f_i(x_i)\mathrm{d}x_i \\
&\quad +\int_0^\infty a_j^2\alpha_j^2 x_j^{2b_j+2\beta_j}f_j(x_j)\mathrm{d}x_j\int_0^\infty a_i^2 x_i^{2b_i+1}f_i(x_i)\mathrm{d}x_i]^{\frac{1}{2}}
\end{aligned} \tag{A.25}$$

and further solving the integrals and then simplfying

$$
\begin{aligned}
&\overline{v_{ij}} = \\
&= \frac{1}{N^{\frac{1}{2}}}[n_j D_j^2(\overline{x_j})\delta_j^0 D_i^2(\overline{x_i}) q_i v_i^2(\overline{x_i}) \frac{\Gamma\left(\frac{\nu_i+2b_i+1+2\beta_i+1}{\mu_i}\right)}{\Gamma\left(\frac{\nu_i+1}{\mu_i}\right)} \left(\frac{\Gamma\left(\frac{\nu_i+1}{\mu_i}\right)}{\Gamma\left(\frac{\nu_i+2}{\mu_i}\right)}\right)^{2b_i+1+2\beta_i} \\
&+2n_j D_j^2(\overline{x_j}) v_j(\overline{x_j}) \frac{\Gamma\left(\frac{\nu_j+2b_j+\beta_j+1}{\mu_j}\right)}{\Gamma\left(\frac{\nu_j+1}{\mu_j}\right)} \left(\frac{\Gamma\left(\frac{\nu_j+1}{\mu_j}\right)}{\Gamma\left(\frac{\nu_j+2}{\mu_j}\right)}\right)^{2b_j+\beta_j} \\
&q_i D_i^2(\overline{x_i}) v_i(\overline{x_i}) \frac{\Gamma\left(\frac{\nu_i+2b_i+1+\beta_i+1}{\mu_i}\right)}{\Gamma\left(\frac{\nu_i+1}{\mu_i}\right)} \left(\frac{\Gamma\left(\frac{\nu_i+1}{\mu_i}\right)}{\Gamma\left(\frac{\nu_i+2}{\mu_i}\right)}\right)^{2b_i+1+\beta_i} \\
&+n_j D_j^2(\overline{x_j}) v_j^2(\overline{x_j}) \frac{\Gamma\left(\frac{\nu_j+2b_j+2\beta_j+1}{\mu_j}\right)}{\Gamma\left(\frac{\nu_j+1}{\mu_j}\right)} \left(\frac{\Gamma\left(\frac{\nu_j+1}{\mu_j}\right)}{\Gamma\left(\frac{\nu_j+2}{\mu_j}\right)}\right)^{2b_j+2\beta_j} q_i D_i^2(\overline{x_i}) \delta_i^1]^{\frac{1}{2}} \\
&= [\frac{v_i^2(\overline{x_i})}{\delta_i^1} \frac{\Gamma\left(\frac{\nu_i+2b_i+1+2\beta_i+1}{\mu_i}\right)}{\Gamma\left(\frac{\nu_i+1}{\mu_i}\right)} \left(\frac{\Gamma\left(\frac{\nu_i+1}{\mu_i}\right)}{\Gamma\left(\frac{\nu_i+2}{\mu_i}\right)}\right)^{2b_i+1+2\beta_i} \\
&+\frac{2v_j(\overline{x_j})v_i(\overline{x_i})}{\delta_j^0\delta_i^1} \frac{\Gamma\left(\frac{\nu_j+2b_j+\beta_j+1}{\mu_j}\right)}{\Gamma\left(\frac{\nu_j+1}{\mu_j}\right)} \left(\frac{\Gamma\left(\frac{\nu_j+1}{\mu_j}\right)}{\Gamma\left(\frac{\nu_j+2}{\mu_j}\right)}\right)^{2b_j+\beta_j} \frac{\Gamma\left(\frac{\nu_i+2b_i+1+\beta_i+1}{\mu_i}\right)}{\Gamma\left(\frac{\nu_i+1}{\mu_i}\right)} \left(\frac{\Gamma\left(\frac{\nu_i+1}{\mu_i}\right)}{\Gamma\left(\frac{\nu_i+2}{\mu_i}\right)}\right)^{2b_i+1+\beta_i} \\
&+\frac{v_j^2(\overline{x_j})}{\delta_j^0} \frac{\Gamma\left(\frac{\nu_j+2b_j+2\beta_j+1}{\mu_j}\right)}{\Gamma\left(\frac{\nu_j+1}{\mu_j}\right)} \left(\frac{\Gamma\left(\frac{\nu_j+1}{\mu_j}\right)}{\Gamma\left(\frac{\nu_j+2}{\mu_j}\right)}\right)^{2b_j+2\beta_j}]^{\frac{1}{2}} \\
&= [v_i^2(\overline{x_i}) \frac{\Gamma\left(\frac{\nu_i+2b_i+1+2\beta_i+1}{\mu_i}\right)}{\Gamma\left(\frac{2b_1+1+\nu_i+1}{\mu_i}\right)} \left(\frac{\Gamma\left(\frac{\nu_i+1}{\mu_i}\right)}{\Gamma\left(\frac{\nu_i+2}{\mu_i}\right)}\right)^{2\beta_i} \\
&+2v_j(\overline{x_j})v_i(\overline{x_i}) \frac{\Gamma\left(\frac{\nu_j+2b_j+\beta_j+1}{\mu_j}\right)}{\Gamma\left(\frac{2b_j+1+\nu_j}{\mu_j}\right)} \left(\frac{\Gamma\left(\frac{\nu_j+1}{\mu_j}\right)}{\Gamma\left(\frac{\nu_j+2}{\mu_j}\right)}\right)^{\beta_j} \frac{\Gamma\left(\frac{\nu_i+2b_i+1+\beta_i+1}{\mu_i}\right)}{\Gamma\left(\frac{2b_i+1+\nu_i+1}{\mu_i}\right)} \left(\frac{\Gamma\left(\frac{\nu_i+1}{\mu_i}\right)}{\Gamma\left(\frac{\nu_i+2}{\mu_i}\right)}\right)^{\beta_i} \\
&+v_j^2(\overline{x_j}) \frac{\Gamma\left(\frac{\nu_j+2b_j+2\beta_j+1}{\mu_j}\right)}{\Gamma\left(\frac{2b_j+1+\nu_j}{\mu_i}\right)} \left(\frac{\Gamma\left(\frac{\nu_j+1}{\mu_j}\right)}{\Gamma\left(\frac{\nu_j+2}{\mu_j}\right)}\right)^{2\beta_j}]^{\frac{1}{2}} \\
&= \left[v_i^2(\overline{x_i})\vartheta_i^1 + v_j(\overline{x_j})v_i(\overline{x_i})\vartheta_{ji}^1 + v_j^2(\overline{x_j})\vartheta_j^0\right]^{\frac{1}{2}}
\end{aligned}
\tag{A.26}
$$

with the scaling factor

$$N = \int_0^\infty D_j^2(x_j) f_j(x_j) \mathrm{d}x_j \int_0^\infty D_i^2(x_i) f_i(x_i) x_i \mathrm{d}x_i \\ = n_j D_j^2(\overline{x_j}) \delta_j^0 D_i^2(\overline{x_i}) q_i \delta_i^1 \tag{A.27}$$

for the characteristic velocity difference weighted with the mass of particle i. Note that we have to use particle mass j as weight and scaling factor when calculating the mass rates for that respective class, hence we change the indicies i and j in equation (A.26). Similar for the collision rate we use the number concentration as a weight

$$\overline{v_{ij}} = \left[\frac{1}{N} \int_0^\infty \int_0^\infty \left(v_i(x_i) - v_j(x_j)\right)^2 D_i^2(x_i) D_j^2(x_j) f_i(x_i) f_j(x_j) \mathrm{d}x_i \mathrm{d}x_j \right]^{\frac{1}{2}} \\ = \left[v_i^2(\overline{x_i}) \vartheta_i^0 + v_j(\overline{x_j}) v_i(\overline{x_i}) \vartheta_{ji}^0 + v_j^2(\overline{x_j}) \vartheta_j^0 \right]^{\frac{1}{2}} \tag{A.28}$$

A.2.3. Collision rates

Finally we arrive at the complete collision growth equations approximating the particles as spheres

$$\left.\frac{\partial n_i}{\partial t}\right|_{coll,ij} = \left.\frac{\partial n_j}{\partial t}\right|_{coll,ij} = -\left.\frac{\partial n_s}{\partial t}\right|_{coll,ij} \\ = -\frac{\pi}{4} \overline{E_{ij}} n_i n_j [D_i^2(\overline{x_i}) \delta_i^0 + D_i(\overline{x_i}) D_j(\overline{x_j}) \delta_{ji}^0 + D_j^2(\overline{x_j}) \delta_j^0] \\ \left[v_i^2(\overline{x_i}) \vartheta_i^0 + v_j(\overline{x_j}) v_i(\overline{x_i}) \vartheta_{ji}^0 + v_j^2(\overline{x_j}) \vartheta_j^0 \right]^{\frac{1}{2}} \tag{A.29}$$

$$\left.\frac{\partial q_i}{\partial t}\right|_{coll,ij} = -\frac{\pi}{4} \overline{E_{ij}} q_i n_j [D_i^2(\overline{x_i}) \delta_i^1 + D_i(\overline{x_i}) D_j(\overline{x_j}) \delta_{ji}^1 + D_j^2(\overline{x_i}) \delta_j^0] \\ \left[v_i^2(\overline{x_i}) \vartheta_i^1 + v_j(\overline{x_j}) v_i(\overline{x_i}) \vartheta_{ji}^1 + v_j^2(\overline{x_j}) \vartheta_j^0 \right]^{\frac{1}{2}} \tag{A.30}$$

$$\left.\frac{\partial q_j}{\partial t}\right|_{coll,ij} = -\frac{\pi}{4} \overline{E_{ij}} q_j n_i [D_i^2(\overline{x_i}) \delta_i^0 + D_i(\overline{x_i}) D_j(\overline{x_j}) \delta_{ij}^1 + D_j^2(\overline{x_i}) \delta_j^1] \\ \left[v_i^2(\overline{x_i}) \vartheta_i^0 + v_j(\overline{x_j}) v_i(\overline{x_i}) \vartheta_{ij}^1 + v_j^2(\overline{x_j}) \vartheta_j^1 \right]^{\frac{1}{2}} \tag{A.31}$$

$$\left.\frac{\partial q_s}{\partial t}\right|_{coll,ij} = -\left.\frac{\partial q_i}{\partial t}\right|_{coll,ij} - \left.\frac{\partial q_j}{\partial t}\right|_{coll,ij} \tag{A.32}$$

See Appendix A.3 for the shorthand notations.

A.3. Shorthand notations

These shorthand notations are used for the coefficients in the analytical results of the collision integrals in Section 2.5.3 and can be calculated beforehand since they only contain fixed parameters

$$\delta_i^k = \frac{\Gamma\left(\frac{2b_i+1+\nu_i+k}{\mu_i}\right)}{\Gamma\left(\frac{\nu_i+1}{\mu_i}\right)} \left(\frac{\Gamma\left(\frac{\nu_i+1}{\mu_i}\right)}{\Gamma\left(\frac{\nu_i+2}{\mu_i}\right)}\right)^{2b_i+k} \tag{A.33}$$

$$\delta_{ji}^k = \frac{\Gamma\left(\frac{b_i+1+\nu_i+k}{\mu_i}\right)}{\Gamma\left(\frac{\nu_i+k}{\mu_i}\right)} \left(\frac{\Gamma\left(\frac{\nu_i+1}{\mu_i}\right)}{\Gamma\left(\frac{\nu_i+2}{\mu_i}\right)}\right)^{b_i+1} \frac{\Gamma\left(\frac{b_j+1+\nu_j}{\mu_j}\right)}{\Gamma\left(\frac{\nu_j+1}{\mu_j}\right)} \left(\frac{\Gamma\left(\frac{\nu_j+1}{\mu_j}\right)}{\Gamma\left(\frac{\nu_j+2}{\mu_j}\right)}\right)^{b_j} \tag{A.34}$$

$$\vartheta_i^k = \frac{\Gamma\left(\frac{\nu_i+2b_i+1+2\beta_i+k}{\mu_i}\right)}{\Gamma\left(\frac{2b_1+1+\nu_i+k}{\mu_i}\right)} \left(\frac{\Gamma\left(\frac{\nu_i+1}{\mu_i}\right)}{\Gamma\left(\frac{\nu_i+2}{\mu_i}\right)}\right)^{2\beta_i} \tag{A.35}$$

$$\vartheta_{ji}^k = \frac{\Gamma\left(\frac{\nu_j+2b_j+\beta_j+1}{\mu_j}\right)}{\Gamma\left(\frac{2b_j+1+\nu_j}{\mu_j}\right)} \left(\frac{\Gamma\left(\frac{\nu_j+1}{\mu_j}\right)}{\Gamma\left(\frac{\nu_j+2}{\mu_j}\right)}\right)^{\beta_j} \frac{\Gamma\left(\frac{\nu_i+2b_i+1+\beta_i+k}{\mu_i}\right)}{\Gamma\left(\frac{2b_i+1+\nu_i+k}{\mu_i}\right)} \left(\frac{\Gamma\left(\frac{\nu_i+1}{\mu_i}\right)}{\Gamma\left(\frac{\nu_i+2}{\mu_i}\right)}\right)^{\beta_i} \tag{A.36}$$

A.4. Truncated moments of the generalized gamma distribution

We want to obtain the result of a partial integration over a generalized gamma distribution with x^n (n-th truncated moment). First we rewrite equation (A.1) to the commonly used form of the generalized gamma distribution with $\beta = \frac{1}{\lambda}$, $\alpha = \frac{\nu+1}{\mu}$ and $A = \frac{\mu N}{\Gamma\left(\frac{\nu+1}{\mu}\right)} \lambda^{\frac{\nu+1}{\mu}} = \frac{\mu N}{\beta^\alpha \Gamma(\alpha)}$

$$f(x) = \frac{\mu N}{\beta^\alpha \Gamma(\alpha)} x^{\alpha\mu-1} \exp\left(-\frac{x^\mu}{\beta}\right) \tag{A.37}$$

This distribution is normalized for $N = 1$. We can transform (A.37) to a 3-parameter gamma distribution using the power transformation $y = x^\mu$ with $\mathrm{d}x = \frac{\mathrm{d}y}{\mu} y^{\frac{-\mu+1}{\mu}}$

$$\begin{aligned} f(y)\,\mathrm{d}y &= f(x)\,\mathrm{d}x \\ f(y) &= \frac{\mu N}{\beta^\alpha \Gamma(\alpha)\mu} y^{\frac{\alpha\mu-1}{\mu}} y^{\frac{-\mu+1}{\mu}} \exp\left(-\frac{y}{\beta}\right) \\ &= \frac{N}{\beta^\alpha \Gamma(\alpha)} y^{\alpha-1} \exp\left(-\frac{y}{\beta}\right) \end{aligned} \tag{A.38}$$

We obtain the n-th truncated moment of the 4-parameter gamma distribution in the interval from l to u using the power transformation and adapting the results from Jawitz, 2004 for gamma distributions

$$\begin{aligned} m_n &= N \int_l^u x^n \frac{\mu}{\beta^\alpha \Gamma(\alpha)} x^{\alpha\mu-1} \exp\left(-\frac{x^\mu}{\beta}\right) \mathrm{d}x \\ &= N \int_{l^\mu}^{u^\mu} y^{\frac{n}{\mu}} \frac{1}{\beta^\alpha \Gamma(\alpha)} y^{\alpha-1} \exp\left(-\frac{y}{\beta}\right) \mathrm{d}y \\ &= N \frac{\beta^{\frac{n}{\mu}}}{\Gamma(\alpha)} \left[\gamma\left(\frac{n}{\mu}+\alpha, \frac{u^\mu}{\beta}\right) - \gamma\left(\frac{n}{\mu}+\alpha, \frac{l^\mu}{\beta}\right)\right] \end{aligned} \tag{A.39}$$

with the lower incomplete gamma function $\gamma(\alpha, x) = \int_0^x t^{\alpha-1} \exp(-t)\, \mathrm{d}t$ which is defined for all real positive α and x.

A.5. Generalized Gauss–Laguerre quadrature

We want to solve the double integral of function g with two generalized gamma distribution f_i and f_j of two classes i and j over their spectra of x_i and x_j

$$\begin{aligned} &\int_0^\infty \int_0^\infty f_i(x_i) f_j(x_j) g(x_i, x_j)\, \mathrm{d}x_i\, \mathrm{d}x_j = \\ &= \int_0^\infty A_i x_i^{\nu_i} \exp(-\lambda_i x_i^{\mu_i})\, \mathrm{d}x_i \int_0^\infty A_j x_j^{\nu_j} \exp\left(-\lambda_j x_j^{\mu_j}\right) g(x_i, x_j)\, \mathrm{d}x_j \\ &= \int_0^\infty y_i^{\frac{\nu_i-\mu_i+1}{\mu_i}} \exp(-y_i)\, \mathrm{d}y_i \int_0^\infty y_j^{\frac{\nu_j-\mu_j+1}{\mu_j}} \exp(-y_j) \frac{A_i A_j}{\lambda_i^{\frac{\nu_i}{\mu_i}-1} \lambda_j^{\frac{\nu_j}{\mu_j}-1} \mu_i \mu_j} g(x_i, x_j)\, \mathrm{d}y_j \\ &= \int_0^\infty y_i^{\alpha_i} \exp(-y_i)\, \mathrm{d}y_i \int_0^\infty y_j^{\alpha_j} \exp(-y_j) g'\left(\left(\frac{y_i}{\lambda_i}\right)^{1/\mu_i}, \left(\frac{y_j}{\lambda_j}\right)^{1/\mu_j}\right) \mathrm{d}y_j \\ &\approx \sum_k w_k \sum_l w_l g'(y_{i_k}, y_{j_l}) \end{aligned} \tag{A.40}$$

where we used the power transformations $y_i = \lambda_i x_i^{\mu_i}$ and $y_j = \lambda_j x_j^{\mu_j}$ with $\mathrm{d}x = \frac{\mathrm{d}y}{\lambda\mu} y^{\frac{-\mu+1}{\mu}}$.

A.6. Cyclone identification

We developed an algorithm in Python 3 to detect cyclones in pressure fields on a regular grid. An object oriented programming approach lends itself to the identifying of features. The principles are based on the work of Wernli and Schwierz, 2006 (WS06). However, we do not include cyclone tracking as we are merely interested in the area where a cyclone is present at any given time. Similar to WS06, the algorithm is based on the analysis of pressure contours and minima. But instead of starting from a (local) minima and consecutively calculating closed contours encapsulating it, we calculate all

isobars and filter them by various criteria until we obtain the largest closed contour enclosing a local minima.
The algorithm requires a pressure field and a topography file as input. When identifying a cyclone on surface level it is recommended to use already to mean sea level reduced data, but otherwise there is a (simple) pressure reduction option available in the program. At first minima in the pressure field are detected by simple comparison to its neighbours. The number of adjacent points taken into account depends on the resolution of the grid so that the search range is 5°. In a limited area mode points near the domain boundary are ignored. For global data a cyclic boundary data mode is available. Values that are unrealistic for a surface level cyclone such as minima below 900 hPa are discarded. Similar minima that are located 1.5 km above sea level are filtered out.
Contours are calculated as isobars in 2 hPa intervals. All non-closed contours are discarded, which limits the applicability of the algorithm in a limited area mode if the cyclone feature of interest is located close to the domain boundary. Especially for model data with high spatial resolution there will be numerous closed contours that are connected to non-cyclones features like landmasses. So we additionally filter out contours that are to short (< 200 km) or only enclose a small area ($< 100\,000\,\mathrm{km}^2$) , where for the latter we transform contour coordinates to a sinusoidal equal-area map projection and use Green's theorem for closed curves.
Next the contours are associated with minima that they enclose. Any minima without enclosing contours or contours without associated minima are discarded. The minima are now characterized depending on their distance to each other, their depth and if they share enclosing contours. Minima within the clustering distance (< 2000 km) and with a shared contour are attributed to the same cyclone with the deepest minima being labeled as the primary and the others as secondary minima. Contours that enclose multiple minima outside clustering distance are discarded so that they are classified as different cyclones. At last we take the largest contour enclosing a (deepest) minima and label every point within as being inside a cyclone. Note that the values of all selection criteria should be adjusted and tested for the specifics of the chosen dataset. Especially the spatial resolution and smoothness of the surface pressure vary strongly between atmospheric circulation models. The algorithm was tested on ICON data with effective grid resolutions of 7.5 and 13 km as well as for ERA5 data with a resolution of 0.25°.

A.7. Ice mode fractions of WCB ensemble

Ice mode fractions as function of temperature for the 10 ensemble cases of Chapter 6. In all figures is median the white line. The 25th to 75th percentiles are represented by dark blue and the 5th/95th percentiles by light blue shading, respectively.

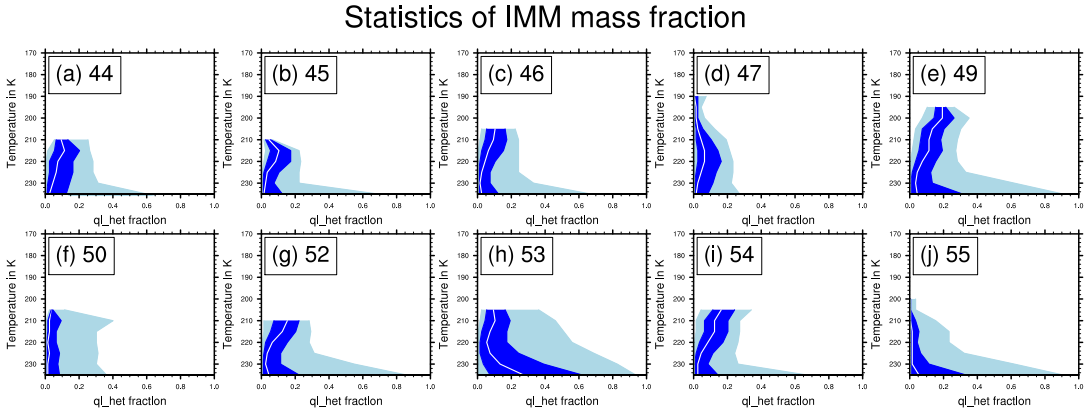

Figure A.1.: f_{imm} histogram as function of temperature.

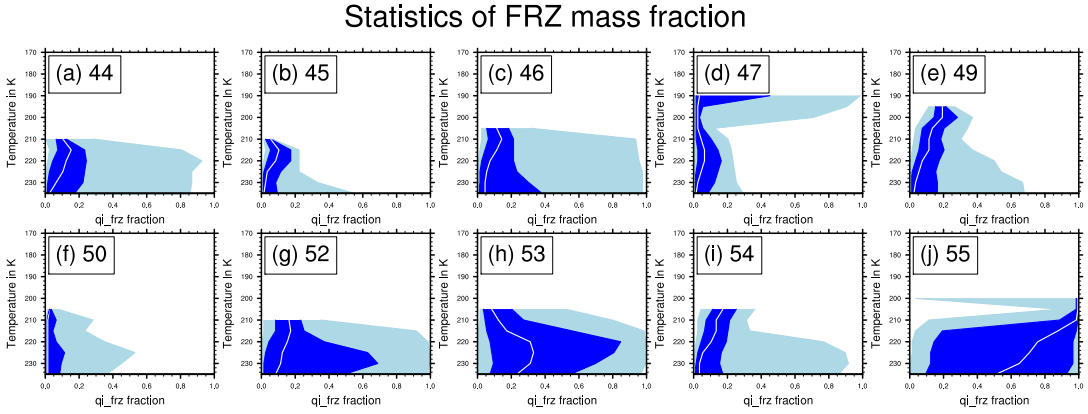

Figure A.2.: f_{frz} histogram as function of temperature.

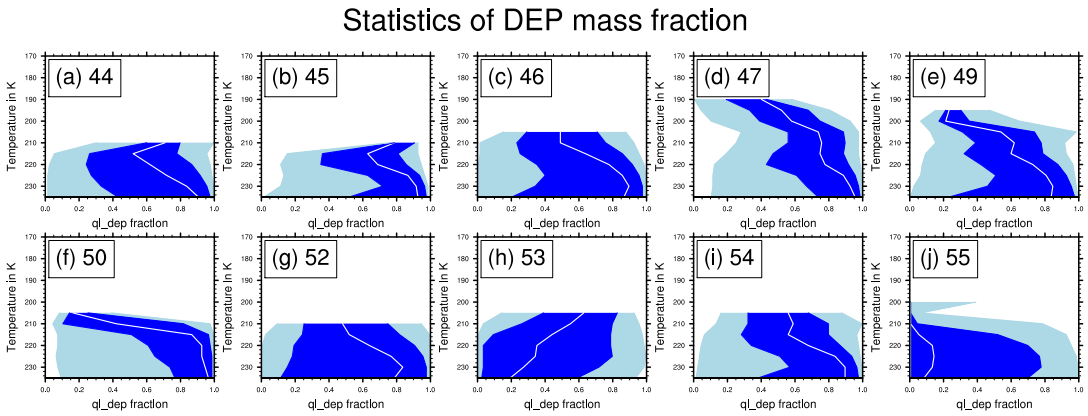

Figure A.3.: f_{dep} histogram as function of temperature.

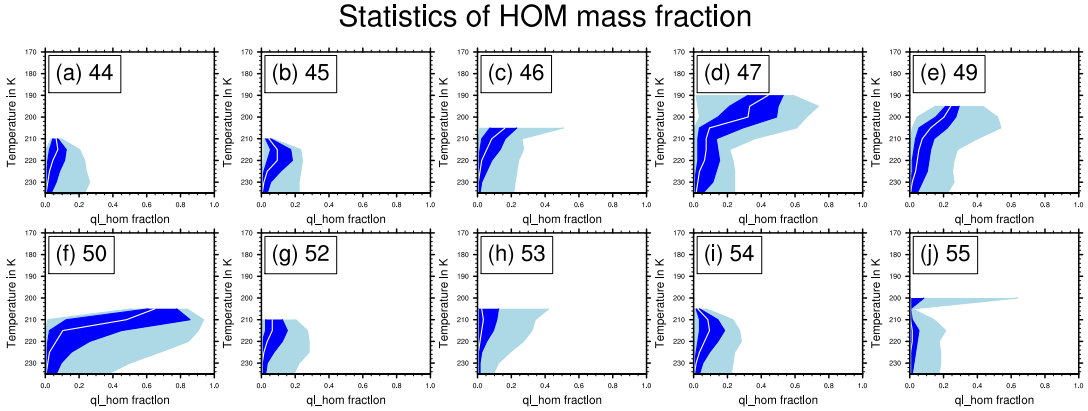

Figure A.4.: f_{hom} histogram as function of temperature.

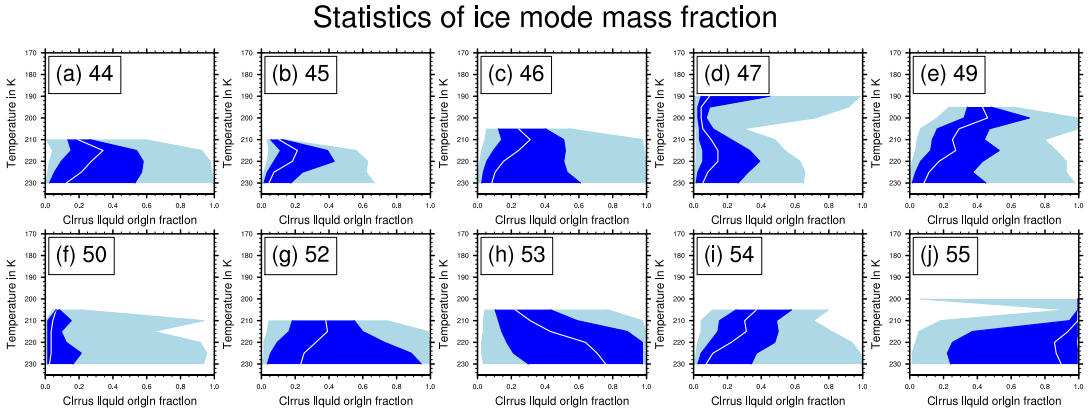

Figure A.5.: f_{liq} histogram as function of temperature.

List of Symbols

Table A.1.: Selection of physical constants and parameters in parametrisations.

Notation	Description	Value
α_i	constant in terminal velocity relation	$27.7\ \mathrm{m\,s^{-1}\,kg^{-\beta_i}}$
β_i	constant in terminal velocity relation	0.21579
λ_i	slope parameter in Γ-distribution for ice	
μ_i	shape parameter in Γ-distribution for ice	$\frac{1}{3}$
ν_i	shape parameter in Γ-distribution for ice	0
σ_{vel}	variance of ice terminal velocity	0.05
a_i	constant in ice shape relation	$0.835\ \mathrm{m\,kg^{-b_i}}$
b_i	constant in ice shape relation	0.39
$e_{sat,i}$	water vapor saturation pressure wrt ice	Pa
k_b	Boltzmann constant	$1.381 \cdot 10^{-23}\ \mathrm{J\,kg^{-1}}$
A_i	scale parameter in Γ-distribution for ice	
D_v	diffusion coefficient	$\mathrm{m^2 s^{-1}}$
E_{coll}	mean sticking efficiency	
F_v	ventilation coefficient	
K_a	thermal conductivity of air	$\mathrm{W\,m^{-1}\,K^{-1}}$
L_s	latent heat of sublimation	$\mathrm{J\,kg^{-1}}$
M_a	molar mass of dry air	$0.029\ \mathrm{kg\,mol^{-1}}$
M_i^k	kth-moment of ice mode i	
M_w	molar mass of water	$0.018\ \mathrm{kg\,mol^{-1}}$
R	ideal gas constant	$8.314\ \mathrm{J\,kg^{-1}\,K^{-1}}$
S_{cr}	critical super saturation for hom. nucleation	
T_f	homogeneous freezing temperature	235 K
T_c	cirrus temperature level	235 K
T_m	equilibrium melting temperature	273.16 K

Table A.2.: List of important Variables.

Notation	Description	Unit
f_{het}	heterogeneous ice fraction	
f_{liq}	liquid origin mass fraction	
fn_{liq}	liquid origin number fraction	
f_x	mass fraction of ice mode x	
n_{hom}	number concentration of homogeneous ice	cm^{-3}
n_{imm}	number concentration of immersion ice	cm^{-3}
n_{frz}	number concentration of homogeneously frozen droplets	cm^{-3}
n_{dep}	number concentration of deposition ice	cm^{-3}
n_{sec}	number concentration of secondary ice	cm^{-3}
n_{tot}, n_i	number concentration of sum of all ice modes	cm^{-3}
m_j	mass of hydrometeor j	kg
q_c	mass content of cloud droplets	$\mathrm{kg\,kg}^{-1}$
q_g	mass content of graupel	$\mathrm{kg\,kg}^{-1}$
q_h	mass content of hail	$\mathrm{kg\,kg}^{-1}$
q_i	mass content of cloud ice	$\mathrm{kg\,kg}^{-1}$
q_r	mass content of raindrops	$\mathrm{kg\,kg}^{-1}$
q_s	mass content of snow	$\mathrm{kg\,kg}^{-1}$
q_v	mass content of water vapor	$\mathrm{kg\,kg}^{-1}$
q_{hom}	mass content of homogeneous ice	$\mathrm{kg\,kg}^{-1}$
q_{imm}	mass content of immersion ice	$\mathrm{kg\,kg}^{-1}$
q_{frz}	mass content of homogeneously frozen droplets	$\mathrm{kg\,kg}^{-1}$
q_{dep}	mass content of deposition ice	$\mathrm{kg\,kg}^{-1}$
q_{sec}	mass content of secondary ice	$\mathrm{kg\,kg}^{-1}$
q_{tot}, q_i	mass content of sum of all ice modes	$\mathrm{kg\,kg}^{-1}$
v_x	terminal velocity of particle x	$\mathrm{m\,s}^{-1}$
w	vertical wind speed	$\mathrm{m\,s}^{-1}$
D_j	maximum diameter of particle j	m
IWC	ice water content	$\mathrm{kg\,kg}^{-1}$
IWP	ice water path	$\mathrm{kg\,m}^{-2}$
LWC	liquid water content	$\mathrm{kg\,kg}^{-1}$
S_i	super saturation wrt ice	
T	(air) temperature	K
x_j	mean mass of class j	$\mathrm{kg\,kg}^{-1}$

List of Figures

List of Tables

Bibliography

Allen, J. T., I. M. Giammanco, M. R. Kumjian, H. Jurgen Punge, Q. Zhang, P. Groenemeijer, M. Kunz, and K. Ortega (2020). "Understanding Hail in the Earth System". In: *Reviews of Geophysics* 58.1. e2019RG000665 10.1029/2019RG000665, e2019RG000665.

Barklie, R. H. D. and N. R. Gokhale (1959). "The freezing of supercooled water drops". In: *Stormy Weather Group, McGill Univ., Sci. Rep.* MW-30, pp. 43–64.

Bechtold, P., M. Köhler, T. Jung, F. Doblas-Reyes, M. Leutbecher, M. J. Rodwell, F. Vitart, and G. Balsamo (2008). "Advances in simulating atmospheric variability with the ECMWF model: From synoptic to decadal time-scales". In: *Quarterly Journal of the Royal Meteorological Society* 134.634, pp. 1337–1351.

Benas, N., S. Finkensieper, M. Stengel, G.-J. van Zadelhoff, T. Hanschmann, R. Hollmann, and J. F. Meirink (2017). "The MSG-SEVIRI-based cloud property data record CLAAS-2". In: *Earth System Science Data* 9.2, pp. 415–434.

Bigg, E. (1953). "The formation of atmospheric ice crystals by the freezing of droplets". In: *Quarterly Journal of the Royal Meteorological Society* 79.342, pp. 510–519.

Binder, H., M. Boettcher, H. Joos, M. Sprenger, and H. Wernli (2020). "Vertical cloud structure of warm conveyor belts – a comparison and evaluation of ERA5 reanalysis, CloudSat and CALIPSO data". In: *Weather and Climate Dynamics* 1.2, pp. 577–595.

Brdar, S. and A. Seifert (2018). "McSnow: A Monte-Carlo Particle Model for Riming and Aggregation of Ice Particles in a Multidimensional Microphysical Phase Space". In: *Journal of Advances in Modeling Earth Systems* 10.1, pp. 187–206.

Brunner, C., B. T. Brem, M. Collaud Coen, F. Conen, M. Hervo, S. Henne, M. Steinbacher, M. Gysel-Beer, and Z. A. Kanji (2021). "The contribution of Saharan dust to the ice-nucleating particle concentrations at the High Altitude Station Jungfraujoch (3580 m a.s.l.), Switzerland". In: *Atmospheric Chemistry and Physics* 21.23, pp. 18029–18053.

Choularton, T., J. Latham, and B. J. Mason (1978). "A possible mechanism of ice splinter production during riming". In: *Nature* 274.5673, pp. 791–792.

Cotton, R. and P. Field (2002). "Ice nucleation characteristics of an isolated wave cloud". In: *Quarterly Journal of the Royal Meteorological Society: A journal of the atmospheric sciences, applied meteorology and physical oceanography* 128.585, pp. 2417–2437.

Cotton, W. R., G. J. Tripoli, R. M. Rauber, and E. A. Mulvihill (1986). "Numerical Simulation of the Effects of Varying Ice Crystal Nucleation Rates and Aggregation Processes on Orographic Snowfall". In: *Journal of Climate and Applied Meteorology* 25.11, pp. 1658–1680.

Dedekind, Z., A. Lauber, S. Ferrachat, and U. Lohmann (2021). "Sensitivity of precipitation formation to secondary ice production in winter orographic mixed-phase clouds". In: *Atmospheric Chemistry and Physics Discussions* 2021, pp. 1–27.

Emersic, C. and P. Connolly (2017). "Microscopic observations of riming on an ice surface using high speed video". In: *Atmospheric Research* 185, pp. 65–72.

Forster, P., T. Storelvmo, K. Armour, W. Collins, J.-L. Dufresne, D. Frame, D. Lunt, T. Mauritsen, M. Palmer, M. Watanabe, M. Wild, and H. Zhang (2021). "The Earth's Energy Budget, Climate Feedbacks, and Climate Sensitivity". In: *Climate Change 2021: The Physical Science Basis. Contribution of Working Group I to the Sixth Assessment Report of the Intergovernmental Panel on Climate Change*. Ed. by V. Masson-Delmotte, P. Zhai, A. Pirani, S. Connors, C. Péan, S. Berger, N. Caud, Y. Chen, L. Goldfarb, M. Gomis, M. Huang, K. Leitzell, E. Lonnoy, J. Matthews, T. Maycock, T. Waterfield, O. Yelekçi, R. Yu, and B. Zhou. Cambridge, United Kingdom and New York, NY, USA: Cambridge University Press, pp. 923–1054.

Fu, Q. and K. N. Liou (1993). "Parameterization of the Radiative Properties of Cirrus Clouds". In: *Journal of Atmospheric Sciences* 50.13, pp. 2008–2025.

Fusina, F. and P. Spichtinger (2010). "Cirrus clouds triggered by radiation, a multiscale phenomenon". In: *Atmospheric Chemistry and Physics* 10.11, pp. 5179–5190.

Gasparini, B., A. Meyer, D. Neubauer, S. Münch, and U. Lohmann (2018). "Cirrus Cloud Properties as Seen by the CALIPSO Satellite and ECHAM-HAM Global Climate Model". In: *Journal of Climate* 31.5, pp. 1983–2003.

Gasparini, B. and U. Lohmann (2016). "Why cirrus cloud seeding cannot substantially cool the planet". In: *Journal of Geophysical Research: Atmospheres* 121.9, pp. 4877–4893.

Grams, C. M., L. Magnusson, and E. Madonna (2018). "An atmospheric dynamics perspective on the amplification and propagation of forecast error in numerical weather prediction models: A case study". In: *Quarterly Journal of the Royal Meteorological Society* 144.717, pp. 2577–2591.

Grams, C. M., H. Wernli, M. Böttcher, J. Čampa, U. Corsmeier, S. C. Jones, J. H. Keller, C.-J. Lenz, and L. Wiegand (2011). "The key role of diabatic processes in modifying the upper-tropospheric wave guide: a North Atlantic case-study". In: *Quarterly Journal of the Royal Meteorological Society* 137.661, pp. 2174–2193.

Hallett, J. and S. C. Mossop (1974). "Production of secondary ice particles during the riming process". In: *Nature* 249, pp. 26–28.

Hande, L. B., C. Engler, C. Hoose, and I. Tegen (2015). "Seasonal variability of Saharan desert dust and ice nucleating particles over Europe". In: *Atmospheric Chemistry and Physics* 15.8, pp. 4389–4397.

— (2016). "Parameterizing cloud condensation nuclei concentrations during HOPE". In: *Atmospheric Chemistry and Physics* 16.18, pp. 12059–12079.

Heinze, R., A. Dipankar, C. C. Henken, C. Moseley, O. Sourdeval, S. Trömel, X. Xie, P. Adamidis, F. Ament, H. Baars, et al. (2017). "Large-eddy simulations over Germany using ICON: A comprehensive evaluation". In: *Quarterly Journal of the Royal Meteorological Society* 143.702, pp. 69–100.

Hoose, C. and O. Möhler (2012). "Heterogeneous ice nucleation on atmospheric aerosols: a review of results from laboratory experiments". In: *Atmospheric Chemistry and Physics* 12.20, p. 9817.

Houze, J. and A. Robert (2012). "Orographic effects on precipitating clouds". In: *Reviews of Geophysics* 50.1.

Houze, R. A. (2018). "100 Years of Research on Mesoscale Convective Systems". In: *Meteorological Monographs* 59, pp. 17.1–17.54.

Huo, J., Y. Tian, X. Wu, C. Han, B. Liu, Y. Bi, S. Duan, and D. Lyu (2020). "Properties of ice cloud over Beijing from surface Ka-band radar observations during 2014–2017". In: *Atmospheric Chemistry and Physics* 20.22, pp. 14377–14392.

Jaruga, A. and H. Pawlowska (2018). "libcloudph++ 2.0: aqueous-phase chemistry extension of the particle-based cloud microphysics scheme". In: *Geoscientific Model Development* 11.9, pp. 3623–3645.

Jawitz, J. (Mar. 2004). "Moments of truncated continuous univariate distributions". In: *Advances in Water Resources - ADV WATER RESOUR* 27, pp. 269–281.

Jeffery, C. and P. Austin (1997). "Homogeneous nucleation of supercooled water: Results from a new equation of state". In: *Journal of Geophysical Research: Atmospheres* 102.D21, pp. 25269–25279.

Joos, H. and H. Wernli (2012). "Influence of microphysical processes on the potential vorticity development in a warm conveyor belt: a case-study with the limited-area model COSMO". In: *Quarterly Journal of the Royal Meteorological Society* 138.663, pp. 407–418.

Joos, H. (2019). "Warm Conveyor Belts and Their Role for Cloud Radiative Forcing in the Extratropical Storm Tracks". In: *Journal of Climate* 32.16, pp. 5325–5343.

Kärcher, B., J. Hendricks, and U. Lohmann (2006). "Physically based parameterization of cirrus cloud formation for use in global atmospheric models". In: *Journal of Geophysical Research: Atmospheres* 111.D1.

Kärcher, B. (2018). "Formation and radiative forcing of contrail cirrus". In: *Nature communications* 9.1, p. 1824.

Kärcher, B. and U. Lohmann (2002). "A parameterization of cirrus cloud formation: Homogeneous freezing of supercooled aerosols". In: *Journal of Geophysical Research: Atmospheres* 107.D2, AAC–4.

Keinert, A., D. Spannagel, T. Leisner, and A. Kiselev (July 2020). "Secondary ice production upon freezing of freely falling drizzle droplets". In: *Journal of the Atmospheric Sciences*.

Kessler, E. (1969). "On the Distribution and Continuity of Water Substance in Atmospheric Circulation". In: *Meteorological Monographs* 10.32, p. 88.

Khain, A., K. Beheng, A. Heymsfield, A. Korolev, S. Krichak, Z. Levin, M. Pinsky, V. Phillips, T. Prabhakaran, A. Teller, et al. (2015). "Representation of microphysical processes in cloud-resolving models: Spectral (bin) microphysics versus bulk parameterization". In: *Reviews of Geophysics* 53.2, pp. 247–322.

Khvorostyanov, V. (1995). "Mesoscale processes of cloud formation, cloud-radiation interaction, and their modelling with explicit cloud microphysics". In: *Atmospheric Research* 39.1, pp. 1–67.

Kobayashi, T. (1967). "On the Variation of Ice Crystal Habit with Temperatur". In: *Physics of Snow and Ice: proceedings* 1.1, pp. 95–104.

Köhler, C. G. and A. Seifert (Jan. 2015). "Identifying sensitivities for cirrus modelling using a two-moment two-mode bulk microphysics scheme". In: *Tellus B: Chemical and Physical Meteorology*.

Koop, T., B. Luo, A. Tsias, and T. Peter (2000). "Water activity as the determinant for homogeneous ice nucleation in aqueous solutions". In: *Nature* 406.6796, pp. 611–614.

Korolev, A., I. Heckman, M. Wolde, A. S. Ackerman, A. M. Fridlind, L. A. Ladino, R. P. Lawson, J. Milbrandt, and E. Williams (2020). "A new look at the environmental conditions favorable to secondary ice production". In: *Atmospheric Chemistry and Physics* 20.3, pp. 1391–1429.

Korolev, A. and T. Leisner (2020). "Review of experimental studies of secondary ice production". In: *Atmospheric Chemistry and Physics* 20.20, pp. 11767–11797.

Krämer, M., C. Rolf, A. Luebke, A. Afchine, N. Spelten, A. Costa, J. Meyer, M. Zöger, J. Smith, R. L. Herman, B. Buchholz, V. Ebert, D. Baumgardner, S. Borrmann, M. Klingebiel, and L. Avallone (2016). "A microphysics guide to cirrus clouds – Part 1: Cirrus types". In: *Atmospheric Chemistry and Physics* 16.5, pp. 3463–3483.

Krämer, M., C. Rolf, N. Spelten, A. Afchine, D. Fahey, E. Jensen, S. Khaykin, T. Kuhn, P. Lawson, A. Lykov, L. L. Pan, M. Riese, A. Rollins, F. Stroh, T. Thornberry, V. Wolf, S. Woods, P. Spichtinger, J. Quaas, and O. Sourdeval (2020). "A microphysics guide to cirrus – Part 2: Climatologies of clouds and humidity from observations". In: *Atmospheric Chemistry and Physics* 20.21, pp. 12569–12608.

Lamb, D. and J. Verlinde (2011). *Physics and chemistry of clouds*. Cambridge University Press.

Lauber, A., A. Kiselev, T. Pander, P. Handmann, and T. Leisner (2018). "Secondary ice formation during freezing of levitated droplets". In: *Journal of the Atmospheric Sciences* 75.8, pp. 2815–2826.

Lawson, R. P., S. Woods, and H. Morrison (2015). "The microphysics of ice and precipitation development in tropical cumulus clouds". In: *Journal of the Atmospheric Sciences* 72.6, pp. 2429–2445.

Libbrecht, K. G. (2005). "The physics of snow crystals". In: *Reports on progress in physics* 68.4, p. 855.

Lin, Y.-L., R. D. Farley, and H. D. Orville (1983). "Bulk parameterization of the snow field in a cloud model". In: *Journal of climate and applied meteorology* 22.6, pp. 1065–1092.

Luebke, A. E., A. Afchine, A. Costa, J.-U. Grooss, J. Meyer, C. Rolf, N. Spelten, L. M. Avallone, D. Baumgardner, and M. Kraemer (2016). "The origin of midlatitude ice clouds and the resulting influence on their microphysical properties". In: *Atmospheric Chemistry and Physics* 16.9, pp. 5793–5809.

Lüttmer, T. (2017). "Einfluss der Mikrophysik auf Eiskristallgrößenverteilungen". Master Thesis. Johannes Gutenberg-Universität Mainz.

Macklin, W. (1960). "The production of ice splinters during riming". In: *Nubila* 3, pp. 30–33.

Madonna, E., H. Wernli, H. Joos, and O. Martius (2014). "Warm Conveyor Belts in the ERA-Interim Dataset (1979–2010). Part I: Climatology and Potential Vorticity Evolution". In: *Journal of Climate* 27.1, pp. 3–26.

Magono, C. and C. W. Lee (1966). "Meteorological classification of natural snow crystals". In: *Journal of the Faculty of Science, Hokkaido University. Series 7, Geophysics* 2.4, pp. 321–335.

Milbrandt, J. A. and H. Morrison (2016). "Parameterization of Cloud Microphysics Based on the Prediction of Bulk Ice Particle Properties. Part III: Introduction of Multiple Free Categories". In: *Journal of the Atmospheric Sciences* 73.3, pp. 975–995.

Miltenberger, A. K., T. Lüttmer, and C. Siewert (2020). "Secondary Ice Formation in Idealised Deep Convection—Source of Primary Ice and Impact on Glaciation". In: *Atmosphere* 11.5, p. 542.

Ming, C., Z. Chen, and F. Roux (Feb. 2010). "Analysis of gravity-waves produced by intense tropical cyclones". In: *Annales Geophysicae* 28.

Mlawer, E. J., S. J. Taubman, P. D. Brown, M. J. Iacono, and S. A. Clough (1997). "Radiative transfer for inhomogeneous atmospheres: RRTM, a validated correlated-k model for the longwave". In: *Journal of Geophysical Research: Atmospheres* 102.D14, pp. 16663–16682.

Morrison, H., J. Curry, and V. Khvorostyanov (2005). "A new double-moment microphysics parameterization for application in cloud and climate models. Part I: Description". In: *Journal of the atmospheric sciences* 62.6, pp. 1665–1677.

Morrison, H., M. van Lier-Walqui, A. M. Fridlind, W. W. Grabowski, J. Y. Harrington, C. Hoose, A. Korolev, M. R. Kumjian, J. A. Milbrandt, H. Pawlowska, D. J. Posselt, O. P. Prat, K. J. Reimel, S.-I. Shima, B. van Diedenhoven, and L. Xue (2020). "Confronting the Challenge of Modeling Cloud and Precipitation Microphysics". In: *Journal of Advances in Modeling Earth Systems* 12.8. e2019MS001689 2019MS001689, e2019MS001689.

Morrison, H. and J. A. Milbrandt (2015). "Parameterization of Cloud Microphysics Based on the Prediction of Bulk Ice Particle Properties. Part I: Scheme Description and Idealized Tests". In: *Journal of the Atmospheric Sciences* 72.1, pp. 287–311.

Murphy, D. M. and T. Koop (2005). "Review of the vapour pressures of ice and supercooled water for atmospheric applications". In: *Quarterly Journal of the Royal Meteorological Society* 131.608, pp. 1539–1565.

Niemand, M., O. Möhler, B. Vogel, H. Vogel, C. Hoose, P. Connolly, H. Klein, H. Bingemer, P. DeMott, J. Skrotzki, and T. Leisner (2012). "A Particle-Surface-Area-Based Parameterization of Immersion Freezing on Desert Dust Particles". In: *Journal of the Atmospheric Sciences* 69.10, pp. 3077–3092.

Oertel, A., M. Boettcher, H. Joos, M. Sprenger, and H. Wernli (2020). "Potential vorticity structure of embedded convection in a warm conveyor belt and its relevance for large-scale dynamics". In: *Weather and Climate Dynamics* 1.1, pp. 127–153.

Oertel, A., A. K. Miltenberger, C. M. Grams, and C. Hoose (2023). "Interaction of microphysics and dynamics in a warm conveyor belt simulated with the ICOsahe-

dral Nonhydrostatic (ICON) model". In: *Atmospheric Chemistry and Physics* 23.15, pp. 8553–8581.

Oertel, A., M. Sprenger, H. Joos, M. Boettcher, H. Konow, M. Hagen, and H. Wernli (2021). "Observations and simulation of intense convection embedded in a warm conveyor belt – how ambient vertical wind shear determines the dynamical impact". In: *Weather and Climate Dynamics* 2.1, pp. 89–110.

Parmar, R. S., M. Welling, M. O. Andreae, and G. Helas (2008). "Water vapor release from biomass combustion". In: *Atmospheric Chemistry and Physics* 8.20, pp. 6147–6153.

Pfahl, S., E. Madonna, M. Boettcher, H. Joos, and H. Wernli (2014). "Warm Conveyor Belts in the ERA-Interim Dataset (1979–2010). Part II: Moisture Origin and Relevance for Precipitation". In: *Journal of Climate* 27.1, pp. 27–40.

Phillips, V. T. J., M. Formenton, A. Bansemer, I. Kudzotsa, and B. Lienert (2015). "A Parameterization of Sticking Efficiency for Collisions of Snow and Graupel with Ice Crystals: Theory and Comparison with Observations". In: *Journal of the Atmospheric Sciences* 72.12, pp. 4885–4902.

Phillips, V. T. J., S. Patade, J. Gutierrez, and A. Bansemer (Aug. 2018). "Secondary Ice Production by Fragmentation of Freezing Drops: Formulation and Theory". In: *Journal of the Atmospheric Sciences* 75.9, pp. 3031–3070.

Phillips, V. T., P. J. DeMott, and C. Andronache (2008). "An empirical parameterization of heterogeneous ice nucleation for multiple chemical species of aerosol". In: *Journal of the atmospheric sciences* 65.9, pp. 2757–2783.

Phillips, V. T., J.-I. Yano, M. Formenton, E. Ilotoviz, V. Kanawade, I. Kudzotsa, J. Sun, A. Bansemer, A. G. Detwiler, A. Khain, et al. (2017a). "Ice Multiplication by Breakup in Ice–Ice Collisions. Part II: Numerical Simulations". In: *Journal of the Atmospheric Sciences* 74.9, pp. 2789–2811.

Phillips, V. T., J.-I. Yano, and A. Khain (2017b). "Ice multiplication by breakup in ice–ice collisions. Part i: Theoretical formulation". In: *Journal of the Atmospheric Sciences* 74.6, pp. 1705–1719.

Plougonven, R. and F. Zhang (2014). "Internal gravity waves from atmospheric jets and fronts". In: *Reviews of Geophysics* 52.1, pp. 33–76.

Price, C., J. Penner, and M. Prather (1997). "NOx from lightning: 1. Global distribution based on lightning physics". In: *Journal of Geophysical Research: Atmospheres* 102.D5, pp. 5929–5941.

Pruppacher, H. R. and J. D. Klett (1998). *Microphysics of clouds and precipitation*. Taylor and Francis.

Pruppacher, H., J. Klett, H. Pruppacher, and J. Klett (2010). "Microstructure of atmospheric clouds and precipitation". In: *Microphysics of clouds and precipitation*, pp. 10–73.

Rasp, S., T. Selz, and G. C. Craig (2016). "Convective and Slantwise Trajectory Ascent in Convection-Permitting Simulations of Midlatitude Cyclones". In: *Monthly Weather Review* 144.10, pp. 3961–3976.

Reed, R. J., M. T. Stoelinga, and Y.-H. Kuo (1992). "A Model-aided Study of the Origin and Evolution of the Anomalously High Potential vorticity in the Inner Region of a

Rapidly Deepening Marine Cyclone". In: *Monthly Weather Review* 120.6, pp. 893–913.

Ren, C. and A. MacKenzie (2005). "Cirrus parametrization and the role of ice nuclei". In: *Quarterly Journal of the Royal Meteorological Society: A journal of the atmospheric sciences, applied meteorology and physical oceanography* 131.608, pp. 1585–1605.

Rodwell, M., R. Forbes, and H. Wernli (2018 2018). *Why warm conveyor belts matter in NWP*. eng.

Sandvik, M., A. Sorteberg, and R. Rasmussen (Jan. 2018). "Sensitivity of historical orographically enhanced extreme precipitation events to idealized temperature perturbations". In: *Climate Dynamics* 50.

Sant, V., R. Posselt, and U. Lohmann (2015). "Prognostic precipitation with three liquid water classes in the ECHAM5–HAM GCM". In: *Atmospheric Chemistry and Physics* 15.15, pp. 8717–8738.

Sant, V., U. Lohmann, and A. Seifert (2013). "Performance of a Triclass Parameterization for the Collision–Coalescence Process in Shallow Clouds". In: *Journal of the Atmospheric Sciences* 70.6, pp. 1744–1767.

Saunders, C. P. R. (1993). "A Review of Thunderstorm Electrification Processes". In: *Journal of Applied Meteorology and Climatology* 32.4, pp. 642–655.

Schäfler, A., G. Craig, H. Wernli, P. Arbogast, J. D. Doyle, R. McTaggart-Cowan, J. Methven, G. Rivière, F. Ament, M. Boettcher, et al. (2018). "The North Atlantic Waveguide and Downstream Impact Experiment". In: *Bulletin of the American Meteorological Society* 99.8, pp. 1607–1637.

Schröter, J., D. Rieger, C. Stassen, H. Vogel, M. Weimer, S. Werchner, J. Förstner, F. Prill, D. Reinert, G. Zängl, M. Giorgetta, R. Ruhnke, B. Vogel, and P. Braesicke (2018). "ICON-ART 2.1: a flexible tracer framework and its application for composition studies in numerical weather forecasting and climate simulations". In: *Geoscientific Model Development* 11.10, pp. 4043–4068.

Segal, Y. and A. Khain (2006). "Dependence of droplet concentration on aerosol conditions in different cloud types: Application to droplet concentration parameterization of aerosol conditions". In: *Journal of Geophysical Research: Atmospheres* 111.D15.

Seidel, J. S., A. A. Kiselev, A. Keinert, F. Stratmann, T. Leisner, and S. Hartmann (2024). "Secondary ice production – no evidence of efficient rime-splintering mechanism". In: *Atmospheric Chemistry and Physics* 24.9, pp. 5247–5263.

Seifert, A. (2002). "Parametrisierung wolkenmikrophysikalischer Prozesse und Simulation konvektiver Mischwolken." PhD thesis. Institut für Meteorologie und Klimaforschung, Universität Karlsruhe/Forschungszentrum Karlsruhe.

Seifert, A. and K. D. Beheng (2006). "A two-moment cloud microphysics parameterization for mixed-phase clouds. Part 1: Model description". In: *Meteorology and atmospheric physics* 92.1-2, pp. 45–66.

Shima, S.-i., K. Kusano, A. Kawano, T. Sugiyama, and S. Kawahara (2009). "The super-droplet method for the numerical simulation of clouds and precipitation: A particle-based and probabilistic microphysics model coupled with a non-hydrostatic model". In: *Quarterly Journal of the Royal Meteorological Society: A journal of the atmo-*

spheric sciences, applied meteorology and physical oceanography 135.642, pp. 1307–1320.

Siler, N. and G. Roe (2014). "How will orographic precipitation respond to surface warming? An idealized thermodynamic perspective". In: *Geophysical Research Letters* 41.7, pp. 2606–2613.

Sölch, I. and B. Kärcher (2010). "A large-eddy model for cirrus clouds with explicit aerosol and ice microphysics and Lagrangian ice particle tracking". In: *Quarterly Journal of the Royal Meteorological Society* 136.653, pp. 2074–2093.

Solomon, S., S. Borrmann, R. R. Garcia, R. Portmann, L. Thomason, L. R. Poole, D. Winker, and M. P. McCormick (1997). "Heterogeneous chlorine chemistry in the tropopause region". In: *Journal of Geophysical Research: Atmospheres* 102.D17, pp. 21411–21429.

Sotiropoulou, G., S. Sullivan, J. Savre, G. Lloyd, T. Lachlan-Cope, A. M. L. Ekman, and A. Nenes (2020). "The impact of secondary ice production on Arctic stratocumulus". In: *Atmospheric Chemistry and Physics* 20.3, pp. 1301–1316.

Sourdeval, O., E. Gryspeerdt, M. Krämer, T. Goren, J. Delanoë, A. Afchine, F. Hemmer, and J. Quaas (2018). "Ice crystal number concentration estimates from lidar–radar satellite remote sensing – Part 1: Method and evaluation". In: *Atmospheric Chemistry and Physics* 18.19, pp. 14327–14350.

Spichtinger, P., K. Gierens, and A. Dörnbrack (2005). "Formation of ice supersaturation by mesoscale gravity waves". In: *Atmospheric Chemistry and Physics* 5.5, pp. 1243–1255.

Spichtinger, P., P. Marschalik, and M. Baumgartner (2023). "Impact of formulations of the homogeneous nucleation rate on ice nucleation events in cirrus". In: *Atmospheric Chemistry and Physics* 23.3, pp. 2035–2060.

Spichtinger, P. and K. M. Gierens (2009). "Modelling of cirrus clouds – Part 1a: Model description and validation". In: *Atmospheric Chemistry and Physics*.

Sprenger, M. and H. Wernli (2015). "The LAGRANTO Lagrangian analysis tool – version 2.0". In: *Geoscientific Model Development* 8.8, pp. 2569–2586.

Steinke, I., C. Hoose, O. Möhler, P. Connolly, and T. Leisner (2015). "A new temperature- and humidity-dependent surface site density approach for deposition ice nucleation". In: *Atmospheric Chemistry and Physics* 15.7, pp. 3703–3717.

Stephens, G. L. (1978). "Radiation Profiles in Extended Water Clouds. II: Parameterization Schemes". In: *Journal of Atmospheric Sciences* 35.11, pp. 2123–2132.

Sullivan, S., C. Barthlott, J. C., I. Zhukov, A. Nenes, and C. Hoose (2018a). "The effect of secondary ice production parameterization on the simulation of a cold frontal rainband". In: *Atmospheric Chemistry and Physics* 18.22, pp. 16461–16480.

Sullivan, S., C. Hoose, A. Kiselev, T. Leisner, and A. Nenes (2018b). "Initiation of secondary ice production in clouds". In: *Atmospheric Chemistry and Physics* 18.3, pp. 1593–1610.

Sullivan, S., C. Hoose, and A. Nenes (2017). "Investigating the contribution of secondary ice production to in-cloud ice crystal numbers". In: *Journal of Geophysical Research: Atmospheres* 122.17, pp. 9391–9412.

Takahashi, C. (1975). "Deformations of Frozen Water Drops and Their Frequencies". In: *Journal of the Meteorological Society of Japan. Ser. II* 53.6, pp. 402–411.

Takahashi, T., Y. Nagao, and Y. Kushiyama (Dec. 1995). "Possible High Ice Particle Production during Graupel–Graupel Collisions". In: *Journal of the Atmospheric Sciences* 52.24, pp. 4523–4527.

Thomas, J., A. Barrett, and C. Hoose (2023). "Temperature and cloud condensation nuclei (CCN) sensitivity of orographic precipitation enhanced by a mixed-phase seeder–feeder mechanism: a case study for the 2015 Cumbria flood". In: *Atmospheric Chemistry and Physics* 23.3, pp. 1987–2002.

Tost, H., P. Jöckel, A. Kerkweg, R. Sander, and J. Lelieveld (2006). "Technical note: A new comprehensive SCAVenging submodel for global atmospheric chemistry modelling". In: *Atmospheric Chemistry and Physics* 6.3, pp. 565–574.

Ullrich, R., C. Hoose, O. Möhler, M. Niemand, R. Wagner, K. Höhler, N. Hiranuma, H. Saathoff, and T. Leisner (2017). "A New Ice Nucleation Active Site Parameterization for Desert Dust and Soot". In: *Journal of the Atmospheric Sciences* 74.3, pp. 699–717.

Unterstrasser, S. and I. Sölch (2010). "Study of contrail microphysics in the vortex phase with a Lagrangian particle tracking model". In: *Atmospheric Chemistry and Physics* 10.20, pp. 10003–10015.

Urbanek, B., S. Groß, A. Schäfler, and M. Wirth (2017). "Determining stages of cirrus evolution: a cloud classification scheme". In: *Atmospheric Measurement Techniques* 10.5, pp. 1653–1664.

Vali, G., P. J. DeMott, O. Möhler, and T. F. Whale (2015). "Technical Note: A proposal for ice nucleation terminology". In: *Atmospheric Chemistry and Physics* 15.18, pp. 10263–10270.

Vardiman, L. (1978). "The generation of secondary ice particles in clouds by crystal–crystal collision". In: *Journal of the Atmospheric Sciences* 35.11, pp. 2168–2180.

Wacker, U. and A. Seifert (June 2001). "Evolution of rain water profiles resulting from pure sedimentation: Spectral vs. parameterized description". In: *Atmospheric Research - ATMOS RES* 58, pp. 19–39.

Weisman, M. L. and J. B. Klemp (1982). "The Dependence of Numerically Simulated Convective Storms on Vertical Wind Shear and Buoyancy". In: *Monthly Weather Review* 110.6, pp. 504–520.

Wernli, H., M. Boettcher, H. Joos, A. K. Miltenberger, and P. Spichtinger (2016). "A trajectory-based classification of ERA-Interim ice clouds in the region of the North Atlantic storm track". In: *Geophysical Research Letters* 43.12, pp. 6657–6664.

Wernli, H. and H. C. Davies (1997). "A Lagrangian-based analysis of extratropical cyclones. I: The method and some applications". In: *Quarterly Journal of the Royal Meteorological Society* 123.538, pp. 467–489.

Wernli, H. and C. Schwierz (2006). "Surface Cyclones in the ERA-40 Dataset (1958–2001). Part I: Novel Identification Method and Global Climatology". In: *Journal of the Atmospheric Sciences* 63.10, pp. 2486–2507.

Wildeman, S., S. Sterl, C. Sun, and D. Lohse (2017). "Fast dynamics of water droplets freezing from the outside in". In: *Physical review letters* 118.8, p. 084101.

Wolf, V., T. Kuhn, M. Milz, P. Voelger, M. Krämer, and C. Rolf (2018). "Arctic ice clouds over northern Sweden: microphysical properties studied with the Balloon-borne Ice Cloud particle Imager B-ICI". In: *Atmospheric Chemistry and Physics* 18.23, pp. 17371–17386.

Yano, J.-I. and R. Plant (2012). "Interactions between Shallow and Deep Convection under a Finite Departure from Convective Quasi Equilibrium". In: *Journal of the Atmospheric Sciences* 69.12, pp. 3463–3470.

Zängl, G., D. Reinert, P. Rípodas, and M. Baldauf (2015). "The ICON (ICOsahedral Non-hydrostatic) modelling framework of DWD and MPI-M: Description of the non-hydrostatic dynamical core". In: *Quarterly Journal of the Royal Meteorological Society* 141.687, pp. 563–579.

Curriculum Vitae

Danksagung